

NANOCELLULOSE: PREPARATION, CHARACTERIZATION, SUPRAMOLECULAR MODELING, AND ITS LIFE CYCLE ASSESSMENT

Qingqing Li

Dissertation submitted to the faculty of
Virginia Polytechnic Institute & State University
in partial fulfillment of the requirements for the degree of

Doctor of Philosophy

in

Forest Products

Scott H. Renneckar, Chair
Justin R. Barone
Kevin J. Edgar
Maren Roman
Audrey G. Zink-Sharp

August 29, 2012

Blacksburg, Virginia

Keywords: TEMPO-mediated oxidation, cellulose, molecularly thin, MT nanocellulose,
microfibrils, supramolecular structure, modeling, life cycle assessment

Copyright 2012 Qingqing Li

NANOCELLULOSE: PREPARATION, CHARACTERIZATION, SUPRAMOLECULAR MODELING, AND ITS LIFE CYCLE ASSESSMENT

Qingqing Li

Abstract

Nanocellulose is a nascent and promising material with many exceptional properties and a broad spectrum of potential applications; hence, it has drawn increasing research interests in the past decade. A new type of nanocellulose – with mono- or bi-layer cellulose molecular sheet thickness – was synthesized through a combined chemical-mechanical process (TEMPO-mediated oxidation followed by intensive sonication), and this new material was named molecularly thin nanocellulose (MT nanocellulose). The overarching objective of this study was to understand the formation and supramolecular structure of MT nanocellulose and contribute to the knowledge of native cellulose structure.

The research involved four major bodies of study: preparation of MT nanocellulose, characterization of MT nanocellulose, modeling wood pulp-derived cellulose microfibril cross section structure, and a comparative life cycle assessment (LCA) of different nanocellulose fabrication approaches. The results revealed that MT nanocellulose with mono- to bi-layer sheet thickness (~0.4-0.8 nm), three to six chain width (~2-5 nm), and hundreds of nanometers to several microns length, can be prepared through TEMPO-mediated oxidation followed by 5-240 min intensive sonication. The thickness, width, and length of MT nanocellulose all decreased with extended sonication time and leveled off after 1 or 2 h sonication. Crystallinity, hydrogen bonding, and glycosidic torsion angles were evaluated by XRD, FTIR, Raman, and NMR. These experiments revealed systematic changes to structure with sonication treatments. A microfibril “cross section triangle scheme” was developed for the microfibril

supramolecular modeling process and a 24-chain hexagonal/elliptical hybrid model was proposed as the most credible representation of the supramolecular arrangement for wood pulp-derived cellulose I β microfibril. Comparative LCA of the fabrication of nanocellulose indicated that nanocellulose presented a significant environmental burden markup on its precursor, kraft pulp, and the environmental hotspot was attributed to the mechanical disintegration process. Yet, overall nanocellulose still presented a prominent environmental advantage over other nanomaterials like single-walled carbon nanotubes, due to its relative low energy consumption.

Overall, this research developed a facile approach to produce a new type of nanocellulose, the MT nanocellulose, provided new insights about the supramolecular structure of cellulose microfibrils, and evaluated the environmental aspects of the fabrication process of nanocellulose.

Dedicated to my dearest parents *Xichun (father)* and *Qi (mother)*, who always support and love me unconditionally, in good and bad times.

Acknowledgements

First and foremost, I would like to express my sincerest gratitude to my advisor Dr. Scott Renneckar, for his extremely generous support in my study, research, personal and career development during the past five years. Dr. Renneckar has been the most important and reliable source of inspiration as I overcame all the obstacles in completion of this dissertation.

I would like to thank the rest of my committee members, Dr. Justin Barone, Dr. Kevin Edgar, Dr. Maren Roman, Dr. Audrey Zink-Sharp, as well as non-voting committee member Dr. Mahajan, for their insightful input and intriguing questions during the past meetings as well as from their lectures. I also appreciate their various contributions to this research through granting me access to their expensive research equipment.

My special thanks go to Dr. Sean McGinnis and Anthony Wong for their assistance in developing the LCA chapter, as well as Dr. McGinnis' contribution in manuscript preparation.

I am very grateful for the financial support and various opportunities I received from ICTAS, VTSuN, and my home department, Sustainable Biomaterials, which enabled me to focus on research while living a fulfilling life.

I would also take this opportunity to acknowledge the invaluable help and support I received from my fellow (past and present) colleagues in S.A.M.I.L. group, Department of Sustainable Biomaterials, College of Natural Resources and Environment, as well as professors, research specialists, administrative staff members, and colleagues from other groups and departments across the campus.

Last, but by no means least, I feel so indebted for all the emotional support and encouragement I received from my family and friends, past and present roommates, colleagues and friends from ACSS, CPAG, Consulting Club, Table Tennis Club, Greater DC CSSA, and China Wood-based Panels Magazine.

Table of Contents

ABSTRACT	II
ACKNOWLEDGEMENTS	V
LIST OF FIGURES	IX
LIST OF TABLES	XV
GLOSSARY OF SYMBOLS AND TERMS	XVII
CHAPTER 1 INTRODUCTION	1
1. BACKGROUND AND MOTIVATION	1
2. SCOPE AND COVERAGE	2
2.1. <i>Preparation (chapter 3)</i>	2
2.2. <i>Characterization (chapter 3, 4, and 5)</i>	3
2.3. <i>Supramolecular modeling (chapter 5)</i>	6
2.4. <i>Life cycle assessment (LCA) (chapter 6)</i>	7
3. SIGNIFICANCE	8
REFERENCES	9
CHAPTER 2 LITERATURE REVIEW	12
1. CELLULOSE OVERVIEW	12
1.1. <i>Sources</i>	13
1.2. <i>Basic properties and applications of cellulose</i>	13
2. CELLULOSE BIOSYNTHESIS PROCESS	15
2.1. <i>Cellulose biosynthesis in bacteria</i>	15
2.2. <i>Cellulose biosynthesis in higher plants</i>	17
3. SUPRAMOLECULAR STRUCTURE, CRYSTALLINITY, HYDROGEN BONDING, AND EXISTENCE IN WOOD CELL WALL	19
3.1. <i>Supramolecular structure of cellulose</i>	19
3.2. <i>Cellulose crystalline nature</i>	22
3.3. <i>Cellulose hydrogen bonding</i>	24
3.4. <i>Existence of cellulose in wood cell wall</i>	26
4. NANOCELLULOSE AND ITS PREPARATION	28
4.1. <i>Nanocellulose</i>	28
4.2. <i>Preparation methods</i>	31
4.3 <i>Additional information on the top-down approach TEMPO-mediated oxidation followed by sonication</i>	35
REFERENCES	36
CHAPTER 3 MOLECULARLY THIN NANOPARTICLES FROM CELLULOSE: ISOLATION OF SUB-MICROFIBRILLAR STRUCTURES*	48
ABSTRACT	48
1. INTRODUCTION	49
2. MATERIALS AND METHODS	50
2.1. <i>Materials</i>	50
2.2. <i>Methods</i>	51

3. RESULTS	52
4. DISCUSSION	56
5. CONCLUSIONS	58
APPENDIX	59
REFERENCES	60
CHAPTER 4 SUPRAMOLECULAR STRUCTURE CHARACTERIZATION OF MOLECULARLY THIN CELLULOSE I NANOPARTICLES*	62
ABSTRACT	62
1. INTRODUCTION	63
2. MATERIALS AND METHODS	65
3. RESULTS	68
3.1. <i>Yield</i>	68
3.2. <i>AFM</i>	68
3.3. <i>XRD</i>	69
3.4. <i>Raman Spectroscopy</i>	71
3.5. <i>FTIR</i>	76
4. DISCUSSION	80
4.1. <i>Fibril surface oxidation vs sonication</i>	80
4.2. <i>Destruction of the microfibril structure</i>	80
4.3. <i>Hydrogen bonding and C6 conformation alternations</i>	81
4.4. <i>Cellulose Iβ crystalline model and microfibrils delamination mechanism</i>	82
5. CONCLUSIONS	85
APPENDIX-- SUPPORTING INFORMATION	86
REFERENCES	92
CHAPTER 5 UNDERSTANDING THE SUPRAMOLECULAR STRUCTURE OF CELLULOSE MICROFIBRILS VIA MOLECULARLY THIN NANOCELLULOSE— PERSPECTIVES FROM TEM AND NMR INVESTIGATIONS	97
ABSTRACT	97
1. INTRODUCTION	98
2. EXPERIMENTAL	102
3. RESULTS AND DISCUSSION	104
3.1. <i>TEM results-- MT nanocellulose width profile</i>	104
3.2. <i>NMR results-- crystallinity, molecular conformation, chain conformation</i>	106
3.3. <i>Reflections on cellulose microfibril supramolecular structure</i>	115
4. CONCLUSIONS	123
APPENDIX	125
<i>Appendix 1. Tests of statistical significance for TEM width distributions</i>	125
<i>Appendix 2. Calculation of the dimensions of different chain packing arrangements</i>	129
REFERENCE	132
CHAPTER 6 NANOCELLULOSE LIFE CYCLE ASSESSMENT	138
ABSTRACT	138
1. INTRODUCTION	139
2. MATERIALS AND METHODS	143
2.1. <i>Scope definition</i>	143
2.2. <i>Nanocellulose (MFC) fabrication process description</i>	144

2.3. Key assumptions	146
2.4. Life cycle inventory analysis (LCI)	147
3. RESULTS.....	148
3.1. Eco-Indicator 99 assessment method.....	148
3.2. Comparison between the chemical processes	149
3.3. Comparison between the mechanical processes	151
3.4. Overall comparison based on functional unit (scenario I)	152
3.5. Overall comparison based on single batch (scenario II).....	153
3.6. Nanocellulose vs kraft pulp	154
3.7. Nanocellulose vs carbon nanotubes	156
4. CONCLUSIONS.....	157
APPENDIX.....	159
Appendix 1. Life cycle inventory raw data.....	159
REFERENCES.....	162
CHAPTER 7 SUMMARY AND CONCLUSIONS.....	166
MT NANOCELLULOSE PREPARATION.....	166
CHARACTERIZATION.....	167
SUPRAMOLECULAR MODELING	168
LIFE CYCLE ASSESSMENT OF NANOCELLULOSE	169

List of Figures

--- CHAPTER 1 ---

- Figure 1.1.** Nanocellulose was prepared by a combined chemical-mechanical approach...3
- Figure 1.2.** Left: thickness measurement statistics from AFM indicates that substantial portion of the MT nanocellulose presents a thickness value of 0.4-0.8 nm, related to cellulose monolayer or bilayer molecular sheet. Right: schematic drawing of the cross section view of a 36-chain cellulose $I\beta$ microfibril, indicating the thickness of a monolayer molecular sheet is 0.39 nm.....4
- Figure 1.3.** Schematic representation of intra-sheet hydrogen bonds, inter-sheet hydrogen bonds, and van der Waals interaction in cellulose $I\beta$ crystalline structure. Diffraction planes (200) are highlighted.....5
- Figure 1.4.** Schematic drawings represent cellulose torsion angles Φ , Ψ , and X (left) and three possible conformations at cellulose C6 position (right).....6
- Figure 1.5.** **Left:** the “cross section triangle” diagram highlights the primary data acquisition approaches and the interrelationships among cross section dimensions, cross section shape, and chain packing numbers, which collectively determine the microfibril cross section structure. **Right:** Schematic drawing of the refined 24-chain hexagonal/elliptical hybrid cross section model for cellulose $I\beta$ microfibril.....7
- Figure 1.6.** Nanocellulose fabrication process flow in lab setting for LCA, four comparable fabrication routes are indicated by arrows with designated colors.....8

--- CHAPTER 2 ---

- Figure 2.1.** Glucose, cellobiose, and cellulose linear molecular chain.....13
- Figure 2.2.** Left: one cellulose terminal complex (TC) is composed of six (three different kinds of) cellulose synthases (CesA). Right: one “rosette” structure is composed of six such TCs....17
- Figure 2.3.** Schematic drawing of cellulose synthase rosette in plasma membrane: orientation of

microtubules controlling the orientation of cellulose in the cell wall where the microtubules act as tracks to guide the cellulose enzymes floating in the cell membrane.....	19
Figure 2.4. A schematic drawing showing fringed micelle structure.....	21
Figure 2.5. Unit cell structure of cellulose $I\alpha$ and $I\beta$ (viewed along the fiber direction).....	23
Figure 2.6. Hydrogen bonding system in native cellulose crystalline structure: OH—O bonds dominate the intra-sheet interaction, CH—O and van der Waals collectively are responsible for the inter-sheet interaction.....	25
Figure 2.7. Three possible conformations at C6 primary hydroxyl group.....	26
Figure 2.8. Schematic drawing of the hierarchical structure of wood polysaccharides and lignin in secondary cell wall of softwood tracheids.....	27
Figure 2.9. Simplified speculative schematic drawing of the assembly process (top down) of cellulose microfibril bundle, hemicelluloses, and lignin with their estimated dimension in wood cell wall S2 layer.....	28
Figure 2.10. Images of different types of nanocelluloses.....	29
Figure 2.11. Classification of nanocellulose fabrication approaches.....	32

--- CHAPTER 3 ---

Figure 3.1. Typical AFM height images of nanocellulose on mica surface as a function of sonication time.....	52
Figure 3.2. Measurements related to nanocellulose thickness. A) Thickness measurements arranged in ascending order for fibrils (each Y-value value corresponds to the average of three measurements on a single fibril). All Y-Axis values are plotted with the same scale and the number of layers related to proposed	54
Figure 3.3. Measurements related to nanocellulose length. A) A histogram plot showing the frequency of measurement for each size. B) Box plot indicating the distribution of measurement values, line in center indicates median, while star in center indicates average.....	55
Figure 3.4. a) AFM height image of non-centrifuged and mechanically blended particle with microfibrils unwinding, and b) digitally zoomed AFM height image of sonicated sub-microfibrils shearing.....	57

--- CHAPTER 4 ---

- Figure 4.1.** AFM height images of cellulose microfibril with height profiles below. Points A, D, E and F are related to cellulose mono-layer sheet thickness, whereas point B is related to a three-layer sheet thickness, point C is related to a bi-layer sheet thickness.....64
- Figure 4.2.** Schematic drawing of hydrogen bonding directions and the layered structure in cellulose $I\beta$, diffraction planes (200) are highlighted.....65
- Figure 4.3.** Left: AFM height image shows one large cellulose bundle being disintegrated into individual nanofibrils upon 5 min sonication. Right: 5 min sonication sample, only fractional portion of the nanofibrils shows thickness related to cellulose mono- or bi-layer, as indicated in the height profile, units of picometers.....69
- Figure 4.4.** XRD diffractogram of cellulose samples with reflection planes labeled. WP-- wood pulp; WT-- TEMPO-mediated oxidized cellulose; WTS30, 60, 120-- oxidized cellulose sonication for 30 min, 60 min, and 120 min respectively.....70
- Figure 4.5.** Raman spectra for CH_2 and CH related peaks (underlined by $\underline{\quad}$) and OH related peaks (underlined by $\blacklozenge\rightarrow$).....73
- Figure 4.6.** Raman spectra for COC deformation related peaks (underlined by $\underline{\quad}$) and ring deformation related peaks (underlined by $\blacklozenge\rightarrow$).....75
- Figure 4.7.** Overlaid Raman spectra at different band regions, all spectra are normalized at band ca. 1090 cm^{-1}76
- Figure 4.8.** FTIR spectra in $3700\text{-}2700\text{ cm}^{-1}$ range, Happ-Genzel apodization function applied to deconvolute the peaks; inset shows the intensity decrease at band $3375\text{-}3340\text{ cm}^{-1}$78
- Figure 4.9.** FTIR spectra in range of $1800\text{-}500\text{ cm}^{-1}$. Insets contain overlaid spectra.....79
- Figure 4.10.** Schematic drawing of cellulose $I\beta$ microfibril 36-chain model, cross section view (chain direction perpendicular to paper plain). The thick dotted lines represent the intermolecular (intra sheet) hydrogen bonding; the thin broken lines represent the intersheet hydrogen bonding. This model is modified and combined based on previous models and calculations by Ding et al., Finkenstadt et al., Vietor et al, and Nishiyama.....84
- Figure 4.11.** Schematic detailing molecularly thick sheets fragmenting along the (200) plane: Intact cellulose microfibril (left) has the intersheet CH--O bonds and van der Waals bonds broken (right) after intensive sonication.....85

SI Figure 4.1. Cellulose nanofibrils yield as a function of sonication time. Sonication started to produce nanofibrils as soon as 5min (yield 12%), and the yield finally reached 87% at 240 min sonication. The yield was calculated based on averages of three replications for each level.....	89
SI Figure 4.2. Raman spectra in 1600-50 cm^{-1} range, peaks normalized on ca. 1090 cm^{-1} . WP-- wood pulp, WT-- oxidized pulp, WTS30-- oxidized pulp sonication 30 min, WTS60-- oxidized pulp sonication 60 min, WTS120-- oxidized pulp sonication 120 min.....	90
SI Figure 4.3. FTIR spectra in 4000-500 cm^{-1} range, peaks normalized on ca. 1161 cm^{-1}	91

--- CHAPTER 5 ---

Figure 5.1. Cellulose microfibril delaminates along the (200) plane under intensive sonication, reproduced from Li and Renneckar 2011.....	98
Figure 5.2. Schematic drawings represent cellulose torsion angles Φ , Ψ , and X (left) and three possible conformations at cellulose C6 position.....	100
Figure 5.3. Left: Nanocellulose width distribution from TEM indicates average fibril width leveled off after 60 min sonication and the width cut-off value is ca. 2 nm across all levels regardless of the sonication time. Right: TEMPO-Oxidized cellulose undergone 5 min of sonication, ribbon shape fibrils and twisting features are revealed (representative twisting features were indicated with arrows).....	106
Figure 5.4. Right: (CP/MAS) ^{13}C NMR spectra of WP, WT, WT30, WT60, and WT120 in 55-125 ppm region; Left: expansion of the carboxylate group chemical shift region, indicating that i) carboxylate group peak emerges after oxidation, and ii) the carboxylate peak shifts ca. 1 ppm towards upfield upon sonication.....	107
Figure 5.5. (CP/MAS) ^{13}C NMR spectrum of kraft wood pulp. Inset demonstrates the area based crystallinity index (CI) calculation: $\text{CI}=\text{C}/(\text{C}+\text{A})$	109
Figure 5.6. (CP/MAS) ^{13}C NMR spectra of the peak shifts for C1 and C4 under oxidation and different sonication treatment levels.....	112
Figure 5.7. (CP/MAS) ^{13}C NMR spectra of the peak shifts for C6 under oxidation and different	113
Figure 5.8. (CP/MAS) ^{13}C NMR spectra of the peak shifts for C2, C3, and C5 under oxidation and different sonication treatment levels.....	115

Figure 5.9. The “Dimension-shape-packing numbers” triangle scheme indicates primary information acquisition approaches and the interrelationships among cross section dimensions, cross section shape, and chain packing numbers, which collectively determine the microfibril cross section structure.....	117
Figure 5.10. Schematic drawing of the refined 24-chain hexagonal-elliptical hybrid model for cellulose $I\beta$ microfibril. Top left figure represents the cross section view of the paracrystalline region where the two core chains are in crystalline state (blue) and the outer layers are in non-crystalline state (green); top right figure represents cross section view of the crystalline region where all the chains are in crystalline state; bottom figure is the corresponding 3D view along the microfibril longitudinal direction, where the left half is in paracrystalline state and the right half is in crystalline state.....	122
SI Figure 5.1. Cellulose $I\beta$ unit cell geometry.....	131

--- CHAPTER 6 ---

Figure 6.1. Images of different types of nanocelluloses.....	140
Figure 6.2. Cradle-to-gate LCA system boundary (indicated by the dashed line box) of lab-scale nanocellulose fabrication.....	143
Figure 6.3. Cellulose MFC fabrication process flow, with colored arrows indicating 4 distinct path ways: red—TOSO, yellow—CESO, green—TOHO, and blue—CEHO.....	144
Figure 6.4. EI99 single score results for the chemical processes: CE and TO.....	150
Figure 6.5. EI99 single score break down for chloroacetic acid etherification and TEMPO mediated oxidation processes based on major contributing sources, indicating the difference in overall impact is from the use of isopropanol of the CE process. Note, chloroacetic acid did not have measurable impact (<1 mPt) based on the functional unit of 10g of pulp.....	151
Figure 6.6. EI99 single score results for the mechanical and purifying processes.....	152
Figure 6.7. EI99 single score for four candidate nanocellulose fabrication routes, functional unit of 10 g equivalent dry nanocellulose. The colored arrows are corresponding to the fabrication routes defined in Figure 6.3.....	153
Figure 6.8. EI99 single score for four candidate nanocellulose fabrication routes, per batch basis. The colored arrows are corresponding to the fabrication routes defined in Figure 6.3.....	154

Figure 6.9. EI99 impact score comparison between kraft pulping process and nanocellulose fabrication processes.....156

Figure 6.10. Energy consumption for producing 1 kg of material of nanocellulose and SWNT in lab setting, TOHO and TOSO refers to two fabrication routes for nanocellulose.....157

List of Tables

--- CHAPTER 1 ---

Table 1.1. Cross section dimensions of cellulose microfibrils from various sources.....	4
--	---

--- CHAPTER 3 ---

Table 3.1. Dimensions of cellulose microfibrils from various sources.....	50
Table 3.2. Statistical values for length, thickness, and aspect ratios of nanocellulose as a function of sonication time.....	53

--- CHAPTER 4 ---

Table 4.1. Crystallinity index and crystalline region thickness evaluated by XRD diffraction peaks on plane (200) according to Scherrer equation.....	71
Table 4.S-1. Assignments for vibrational Raman bands of allomorphs cellulose $I\beta$	86
Table 4.S-2. Assignments for FTIR bands for cellulose.....	88

--- CHAPTER 5 ---

Table 5.1. Crystallinity index (CI) value calculated by peak integration method.....	108
Table 5.2. Experimentally determined wood cellulose microfibril lateral dimensions from different techniques (unit nm).....	119
Table 5.3. Calculated cellulose $I\beta$ microfibril cross sectional dimensions under different combinations of chain packing numbers and cross section shapes.....	121

--- CHAPTER 6 ---

Table 6.1. The environmental impact categories considered in Eco-Indicator 99.....	149
Table 6.2. Impact categories (fossil fuel depletion and respiratory inorganics pollution) involved in the chemical modification processes.....	150

SI Table 6.1. LCI TEMPO-oxidation and sonication data.....	159
SI Table 6.2. LCI chloroacetic acid etherification data.....	160
SI Table 6.3. LCI homogenization data.....	161

Glossary of Symbols and Terms

MT nanocellulose: molecularly thin nanocellulose

TC: terminal complex

CesA: cellulose synthase catalytic subunit

CelS: cellulose synthase complex

UDP-Glc: uridine diphosphate glucose

TEMPO: 2,2,6,6-Tetramethylpiperidin-1-oxyl

Φ , Ψ , X : torsion angles

gt, *tg*, *gg*: cellulose C6 position conformations

LCA: life cycle assessment

TO: TEMPO-oxidation

CE: chloroacetic acid etherification

SO: sonication

HO: homogenization

CP: centrifuge purifying

AFM: atomic force microscopy

TEM: transmission electron microscopy

XRD: X-ray diffraction

FTIR: Fourier transform infrared spectroscopy

Raman: Raman spectroscopy

NMR: nuclear magnetic resonance

CHAPTER 1

Introduction

1. Background and motivation

Cellulose is a critical material used in our industrialized society that facilitated mass communication (newspapers), enabled information archiving (books), reduced the spread of diseases (personal hygienic materials), initiated the textile industry, and changed armed conflict (nitrocellulose). The chemical structure of cellulose was first identified in 1838 by French chemist A. Payen.¹ A little less than a decade later (1846), Schönbein developed the process for one of the first commercial derivatives of cellulose—nitrocellulose; many other industrialized chemicals like cellulose acetate and carboxymethylcellulose were also created from cellulose afterwards.² With its chemical composition known, much work centered on its native structure and in 1913 the first X-ray scattering pattern showed cellulose had a certain degree of molecular symmetry (crystalline order).³ Additional study to the structure of cellulose, Rånby was first to report cellulose “micelles” that were obtained after acid hydrolysis of the more accessible regions of the fiber.⁴ This work was the initial characterization studies of isolated cellulose in its nanoscale form. Soon after, Patel in 1951 reported the oxidation of fibers in sodium hypobromite and isolated cellulose fibrils after blending, providing one of the first methods to produce a material that would later become microfibrillated cellulose in the 1980’s.⁵

Today, nanocellulose is defined as isolated cellulose particles with at least one dimension in the nanometer range (typically below 100 nm) whilst exhibiting novel properties associated with its nanostructure.⁶ Nanocellulose is a nascent material that has received increased attention over the past decade, presenting unique chemical, physical, and mechanical properties which lead to numerous potential applications in different fields, i.e.: food ingredients, cosmetic additives, packaging materials, hygiene products, pharmaceuticals, film and absorbance media, and nano-composite reinforcement agent.⁷ Nanocellulose can be prepared through either top-down approaches with the natural fiber resized to smaller particles (e.g.: homogenization, hydrolysis, combined chemical-mechanical processes) or bottom-up approaches (e.g.: electrospinning, bacterial biosynthesis) from multiple raw material sources (e.g.: wood pulp, cotton, bacterial, algae).^{7a, 8}

In this dissertation, a combined chemical-mechanical process (top-down) was employed, derived from the ground-breaking work of A. Isogai's group.⁹ A new type of microfibrillated cellulose that has an unusual thickness as low as 0.4 -0.8 nm, related to the thickness of cellulose mono- and bi-layer molecular sheets was isolated after ultrasonication. The new material was named "molecularly thin nanocellulose", or "MT nanocellulose". This unprecedented discovery largely shaped the framework of the dissertation, which revolved around the following points: understanding the mechanism of how MT nanocellulose is produced, characterizing MT nanocellulose from the supramolecular level, and leveraging the unique structure of MT nanocellulose to advance the understanding of plant cellulose microfibril structure. Additionally, this work also examined the fabrication process of nanocellulose from the life cycle assessment (LCA) perspective, providing quantified justification for nanocellulose's environmental-friendliness, as well as guiding its forthcoming large scale commercialization.

2. Scope and coverage

The dissertation research involved four major bodies of study: preparation of the MT nanocellulose, characterization of MT nanocellulose, modeling wood pulp-derived cellulose microfibril cross section structure, and a comparative LCA of different nanocellulose fabrication approaches.

2.1. Preparation (chapter 3)

MT nanocellulose was prepared through a combined chemical-mechanical approach, where cellulose raw material (kraft pulp in our case) was first chemically modified through the TEMPO-mediated oxidation, followed by intensive mechanical agitation-- sonication (Figure 1.1).^{7b, 10} The oxidized cellulose had the surface chains' C6 primary hydroxyl group selectively converted into carboxyl group, which introduced anionic charges onto the surface of cellulose microfibril, allowing separation even under mild mechanical agitation.^{7b, 9a, 11} Different from these past studies, a localized high-energy technique (sonication), known to exfoliate clay and graphite particles into single layer sheets of clay nanoparticles or graphene, respectively, was used to isolate MT nanocellulose.

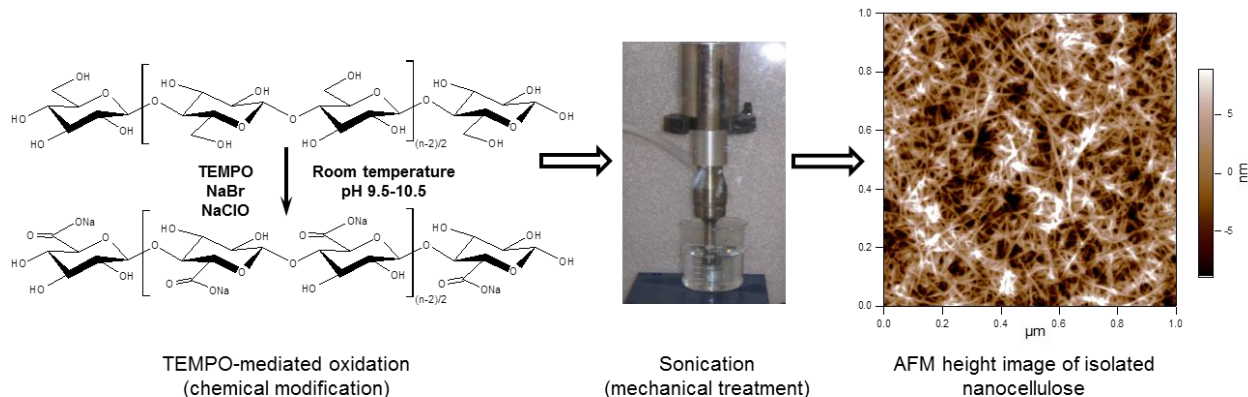


Figure 1.1. Nanocellulose was prepared by a combined chemical-mechanical approach.¹²

2.2. Characterization (chapter 3, 4, and 5)

The oxidized cellulose and isolated MT nanocellulose were thoroughly characterized through a series of microscopies and spectroscopies including: Atomic Force Microscopy (AFM), Transmission Electron Microscopy (TEM), X-ray Diffraction (XRD), Fourier Transform Infrared Spectroscopy (FTIR), Raman Spectroscopy (Raman), and Solid State ¹³C Nuclear Magnetic Resonance (NMR). The characterization revolved around their 3D dimensions and size distributions, crystallinity, hydrogen bonding system, C6 conformations (*gt*, *tg*, *gg*), glycosidic linkage torsion angles (Φ , Ψ , X), and the changes of these indexes under sonication treatment.

Dimensions and size distributions (chapter 3 and 5)

Statistical analyses of the length, thickness, and width distributions of the isolated nanocellulose were performed utilizing AFM and TEM. The results enabled the development of a model for the representative 3D structure of the isolated MT nanocellulose. While the length and width distributions were well aligned with the established understanding, the thickness profiles, however, indicated that a substantial portion of the MT nanocellulose presented a thickness around one tenth to one fifth of the common wood cellulose microfibril (2.3-4.8 nm) (Table 1.1.),¹³ which was related to the thickness of a cellulose monolayer or bilayer molecular sheet (0.4-0.8 nm) based on the C-axis of the unit cell for cellulose *I β* in the monoclinic arrangement (Figure 1.2).¹⁴

Table 1.1. Cross section dimensions of cellulose microfibrils from various sources^{13c, 15}

Cellulose sources	Dimensions	Determination methods
Ramie ^a	Cross section 7x3 nm	XRD, SEM
Flax fiber ^b	2.8--3.2 nm	SAXS
Spruce wood ^c	3.0 nm	SEM
Spruce wood ^d	2.3--2.7 nm	TEM, WAXS, SAXS
Pulp fiber ^e	4.5-- 4.8 nm	CP/MAS ¹³ C-NMR

Note: a. Frey-Wyssling 1954, b. Mueller et al. 1998, c. Fengel 1970, d. Jakob et al. 1995, e. Duchesne et al. 2001.

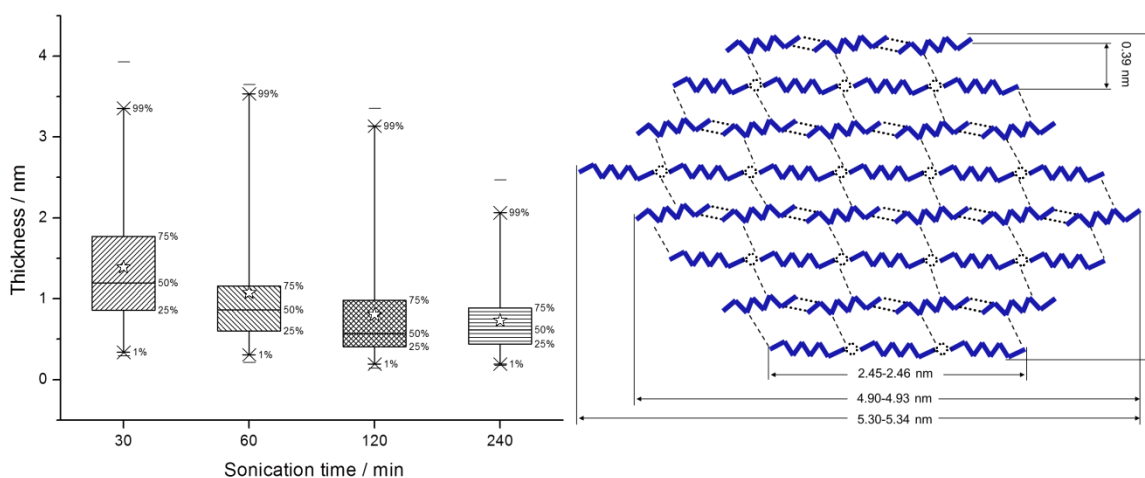


Figure 1.2. Left: thickness measurement statistics from AFM indicates that substantial portion of the MT nanocellulose presents a thickness value of 0.4-0.8 nm, related to cellulose monolayer or bilayer molecular sheet.^{13c} **Right:** schematic drawing of the cross section view of a 36-chain cellulose I β microfibril, indicating the thickness of a monolayer molecular sheet is 0.39 nm.^{13b} Reprinted with permissions from reference 13c and 13b, respectively. Copyrights (2009) Springer and (2011) American Chemical Society.

Crystallinity (chapter 4 and 5)

Crystallinity of the cellulose raw material, TEMPO-oxidized cellulose, and MT nanocellulose were investigated by XRD and NMR. Similar patterns of crystallinity variation under different treatment levels of sonication were observed with both instrumentations, although the crystallinity index varied with

different measuring techniques and calculation methods.¹⁶ Both techniques revealed that sonication time and cellulose crystallinity followed an inverse relationship, which indicated that sonication broke apart the cellulose crystalline structure. Further XRD analysis using the Scherrer equation revealed quantitative evidence that the crystalline structure was delaminated along the (200) plane in cellulose $I\beta$ crystal lattice. This delamination pattern was also corroborated by evidence on hydrogen bonds changes observed from FTIR and Raman spectra.^{13b, 16}

Hydrogen bonding (chapter 4)

The hydrogen bonding in crystalline cellulose and its changes under sonication treatments were examined by FTIR and Raman. Since hydrogen bonding is an indicator of the crystalline structure of cellulose,^{14a, 17} it was revealed that the crystalline structure changes only after sonication, but not after surface oxidation. It was also deduced from the XRD data that the intra-sheet hydrogen bonds were much stronger than the collective inter-sheet hydrogen bonds and van der Waals interaction,^{13b} which provided additional evidence to substantiate Qian and co-worker's computational research result (stating that intra-sheet interactions were approximately eight times greater than inter-sheet interactions, Figure 1.3).¹⁸

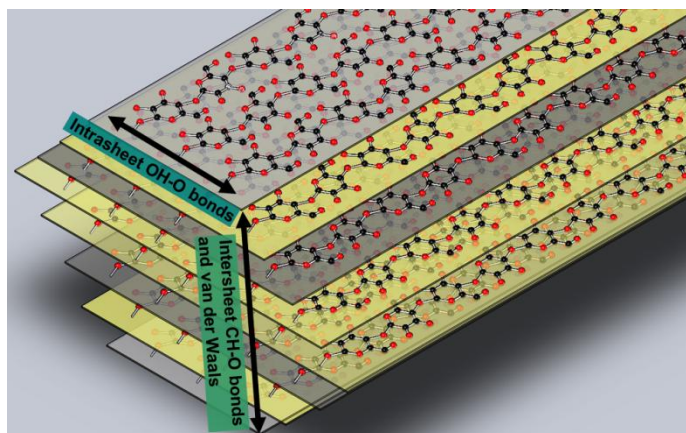


Figure 1.3. Schematic representation of intra-sheet hydrogen bonds, inter-sheet hydrogen bonds, and van der Waals interaction in cellulose $I\beta$ crystalline structure. Diffraction planes (200) are highlighted.^{13b} Reprinted with permission from reference 13b. Copyright (2011) American Chemical Society.

C6 conformations and glycosidic linkage torsion angles (Chapter 4 and 5)

C6 conformations (gt , tg , gg) and glycosidic linkage torsion angles (Φ , Ψ , X) are closely associated with cellulose crystalline structure and the degree of disorder (Figure 1.4),¹⁹ hence their variations were

tracked with FTIR, Raman, and NMR to advance the understanding on chain structure changes under sonication treatment. FTIR and Raman data revealed that more C6 adopted the *gg* conformation after sonication, because the delamination process released many cellulose chains from the interior crystalline structure to the microfibril surface. NMR results indicated that oxidation did not alter torsion angles Φ and Ψ , but sonication did have perceivable impact on them; also the changes on torsion angle X indicated that more *gg* conformation was presented after sonication; therefore, NMR results confirmed the findings from FTIR and Raman.

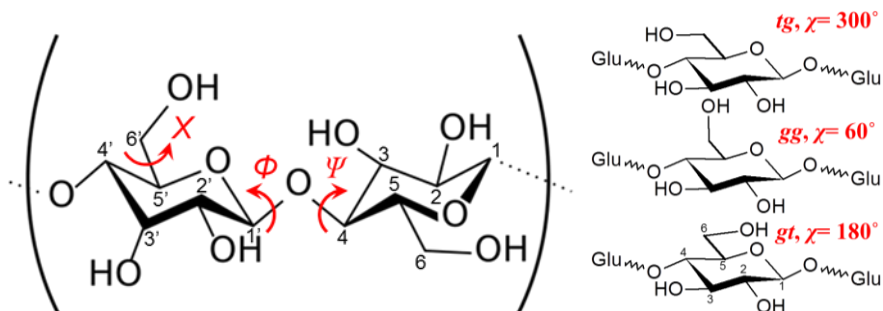


Figure 1.4. Schematic drawings represent cellulose torsion angles Φ , Ψ , and X (left) and three possible conformations at cellulose C6 position (right).

2.3. Supramolecular modeling (chapter 5)

In order to advance the understanding of plant cellulose supramolecular structure and refine the microfibril cross section model, the current models were critically reviewed with the most up-to-date knowledge on plant cellulose biosynthesis, cellulose crystal lattice structure, as well as the direct measurements/ observations from recent primary research efforts.

To put things into perspective and guide the modeling process, the primary information acquisition methodology, as well as the correlations among cross section dimensions, cross section shape, and chain packing numbers were constructed into a triangular scheme (Figure 1.5, left) to visualize these interdependent factors and their interrelationships, which collectively determined the cellulose $I\beta$ cross section structure. By integrating the evidence from direct experimental observations and all known constrains, a refined 24-chain hexagonal/elliptical hybrid cross section model (Figure 1.5, right) was found to be the most credible representation of the wood pulp cellulose microfibril.

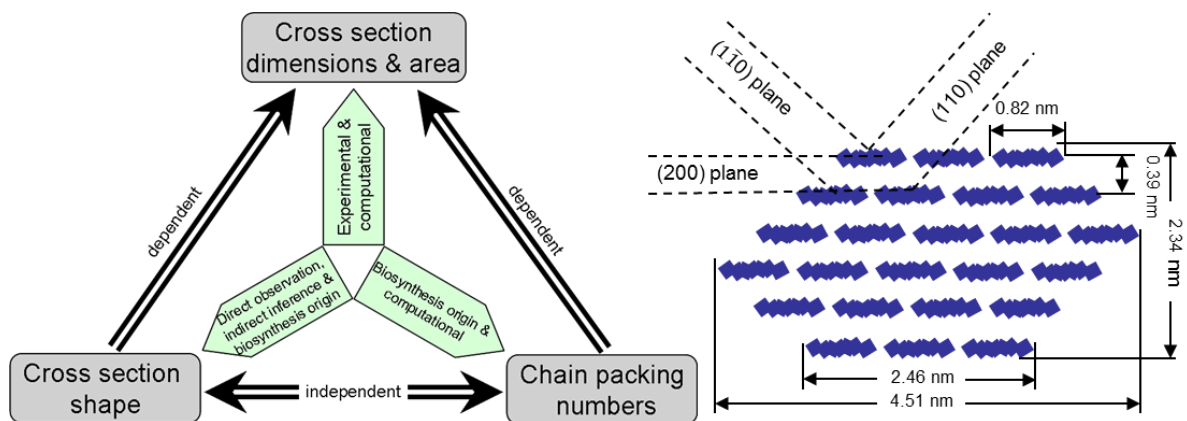


Figure 1.5. **Left:** the “cross section triangle” diagram highlights the primary data acquisition approaches and the interrelationships among cross section dimensions, cross section shape, and chain packing numbers, which collectively determine the microfibril cross section structure. **Right:** Schematic drawing of the refined 24-chain hexagonal/elliptical hybrid cross section model for cellulose $I\beta$ microfibril.

2.4. Life cycle assessment (LCA) (chapter 6)

A cradle-to-gate LCA was conducted to evaluate the cumulative environmental impact of the fabrication process of nanocellulose in a lab setting; the LCA results were compared with the pulping process and carbon nanotube fabrication process to reveal nanocellulose’s relative environmental burden.

The LCA results indicated that the fabrication approach of TEMPO-oxidation followed by homogenization (Figure 1.6, green route in figure) generated the least environmental impact; hence it was the most preferable lab practice from an environmental perspective. It was also revealed that the nanocellulose fabrication process presented a great environmental burden markup on the pulping process, which could raise concerns for the forthcoming large scale commercialization of nanocellulose. However, compared to other familiar nanoscale materials that share similar reinforcement applications like single-walled carbon nanotube (SWNT), nanocellulose presented major environmental advantages due to its relative low energy consumption (~1% of SWNT on unit mass).

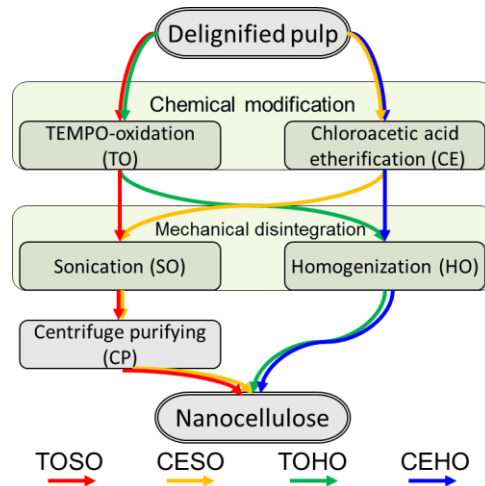


Figure 1.6. Nanocellulose fabrication process flow in lab setting for LCA, four comparable fabrication routes are indicated by arrows with designated colors.

3. Significance

The significance of this work is reflected through the following aspects: 1) the work developed a facile approach to produce a new type of nanocellulose, the MT nanocellulose, which enriched the nanocellulose family and further extended the potential application realm of nanocellulose; 2) the research thoroughly characterized the supramolecular structure of MT nanocellulose and unveiled its systematic changes under sonication treatment while advancing the understanding of wood cellulose supramolecular structure and refined the research methodology; and 3) this study performed the first quantification of the environmental-friendliness of nanocellulose, which raised concerns and provided guidance for its forthcoming commercialization efforts.

References

1. (a) Report on a memoir of Mr. Payen, regarding the composition of woody matter. *Comptes rendus* **1839**, *8*, 51-53; (b) Payen, A., Memoir on the composition of the tissue of plants and of woody [material]. *Comptes rendus* **1838**, *7*, 1052-1056.
2. Charles Frederick Cross, E. J. B. C. B., *Cellulose: An Outline of the Chemistry of the Structural Elements of Plants with Reference to Their Natural History and Industrial Uses*. Elibron Classics: 1895.
3. Nishikawa, S.; Ono, S., Transmission of X-rays through fibrous, lamellar and granular substances. *Proc. Tokyo Math.-Phys. Soc.* **1913**, *7*, 131-8.
4. Ranby, B. G., Aqueous colloidal solutions of cellulose micelles. *Acta Chem. Scand. (1947-1973)* **1949**, *3*, 649-650.
5. Patel, G. M., Optical investigations on oxycelluloses. *Die Makromolekulare Chemie* **1951**, *7* (1), 12-45.
6. (a) Klemm, D.; Kramer, F.; Moritz, S.; Lindström, T.; Ankerfors, M.; Gray, D.; Dorris, A., Nanocelluloses: A New Family of Nature-Based Materials. *Angewandte Chemie International Edition* **2011**, *50* (24), 5438-5466; (b) Klemm, D.; Schumann, D.; Kramer, F.; Hessler, N.; Hornung, M.; Schmauder, H. P.; Marsch, S., Nanocelluloses as innovative polymers in research and application. In *Polysaccharides II*, Springer-Verlag Berlin: Berlin, 2006; Vol. 205, pp 49-96.
7. (a) Moon, R. J.; Martini, A.; Nairn, J.; Simonsen, J.; Youngblood, J., Cellulose nanomaterials review: structure, properties and nanocomposites. *Chem. Soc. Rev.* **2011**, *40* (7), 3941-3994; (b) Isogai, A.; Saito, T.; Fukuzumi, H., TEMPO-oxidized cellulose nanofibers. *Nanoscale* **2011**, *3* (1), 71-85; (c) Eichhorn, S. J., Cellulose nanowhiskers: promising materials for advanced applications. *Soft Matter* **2011**, *7* (Copyright (C) 2011 American Chemical Society (ACS). All Rights Reserved.), 303-315; (d) Habibi, Y.; Lucia, L. A.; Rojas, O. J., Cellulose Nanocrystals: Chemistry, Self-Assembly, and Applications. *Chemical Reviews* **2010**, *110* (6), 3479-3500; (e) Eichhorn, S. J.; Dufresne, A.; Aranguren, M.; Marcovich, N. E.; Capadona, J. R.; Rowan, S. J.; Weder, C.; Thielemans, W.; Roman, M.; Renneckar, S.; Gindl, W.; Veigel, S.; Keckes, J.; Yano, H.; Abe, K.; Nogi, M.; Nakagaito, A. N.; Mangalam, A.; Simonsen, J.; Benight, A. S.; Bismarck, A.; Berglund, L. A.; Peijs, T., Review: current international research into cellulose nanofibres and nanocomposites. *J. Mater. Sci.* **2010**, *45* (1), 1-33; (f) Johnson, R. K.; Zink-Sharp, A.; Renneckar, S. H.; Glasser, W. G., A new bio-based nanocomposite: fibrillated TEMPO-oxidized celluloses in hydroxypropylcellulose matrix. *Cellulose (Dordrecht, Netherlands)* **2009**, *16* (2), 227-238; (g) Siqueira, G.; Bras, J.; Dufresne, A., Cellulosic Bionanocomposites: A Review of Preparation, Properties and Applications. *Polymers* **2010**, *2* (4), 728-765.
8. Hentze, H.-P. In *From Nanocellulose Science towards Applications*, Technical Research Center of Finland, Helsinki, June 2, 2010; Technical Research Center of Finland, Helsinki, 2010.
9. (a) Saito, T.; Nishiyama, Y.; Putaux, J. L.; Vignon, M.; Isogai, A., Homogeneous suspensions of individualized microfibrils from TEMPO-catalyzed oxidation of native cellulose. *Biomacromolecules* **2006**, *7* (6), 1687-1691; (b) Saito, T.; Isogai, A., TEMPO-Mediated Oxidation of Native Cellulose. The Effect of Oxidation Conditions on Chemical and Crystal Structures of the Water-Insoluble Fractions. *Biomacromolecules* **2004**, *5* (5), 1983-1989.

10. (a) Isogai, A.; Saito, T.; Fukuzumi, H.; Okita, Y., Preparation of cellulose single nanofibers by TEMPO-mediated oxidation of native celluloses: Fundamentals and applications. *Abstracts of Papers, 235th ACS National Meeting, New Orleans, LA, United States, April 6-10, 2008* **2008**, CELL-128; (b) Saito, T.; Kimura, S.; Nishiyama, Y.; Isogai, A., Cellulose nanofibers prepared by TEMPO-mediated oxidation of native cellulose. *Biomacromolecules* **2007**, *8* (8), 2485-2491.
11. Okita, Y.; Saito, T.; Isogai, A., Entire Surface Oxidation of Various Cellulose Microfibrils by TEMPO-Mediated Oxidation. *Biomacromolecules* **2010**, *11* (6), 1696-1700.
12. Tahiri, C.; Vignon, M. R., TEMPO-oxidation of cellulose: Synthesis and characterisation of polyglucuronans. *Cellulose* **2000**, *7*, 177-188.
13. (a) Beck-Candanedo, S.; Roman, M.; Gray, D. G., Effect of Reaction Conditions on the Properties and Behavior of Wood Cellulose Nanocrystal Suspensions. *Biomacromolecules* **2005**, *6* (2), 1048-1054; (b) Li, Q.; Renneckar, S., Supramolecular Structure Characterization of Molecularly Thin Cellulose I Nanoparticles. *Biomacromolecules* **2011**, *12* (3), 650-659; (c) Li, Q.; Renneckar, S., Molecularly thin nanoparticles from cellulose: isolation of sub-microfibrillar structures. *Cellulose (Dordrecht, Netherlands)* **2009**, *16* (6), 1025-1032.
14. (a) Nishiyama, Y.; Langan, P.; Chanzy, H., Crystal Structure and Hydrogen-Bonding System in Cellulose I β from Synchrotron X-ray and Neutron Fiber Diffraction. *Journal of the American Chemical Society* **2002**, *124* (31), 9074-9082; (b) Fernandes, A. N.; Thomas, L. H.; Altaner, C. M.; Callow, P.; Forsyth, V. T.; Apperley, D. C.; Kennedy, C. J.; Jarvis, M. C., Nanostructure of cellulose microfibrils in spruce wood. *Proceedings of the National Academy of Sciences* **2011**.
15. (a) Frey-Wyssling, A., The fine structure of cellulose microfibrils. *Science (Washington, DC, United States)* **1954**, *119*, 80-2; (b) Fengel, D., Ultrastructural Behavior of Cell Wall Polysaccharides. *Tappi* **1970**, *53* (3), 7; (c) Jakob, H. F.; Fengel, D.; Tschegg, S. E.; Fratzl, P., The Elementary Cellulose Fibril in *Picea abies*: Comparison of Transmission Electron Microscopy, Small-Angle X-ray Scattering, and Wide-Angle X-ray Scattering Results. *Macromolecules* **1995**, *28* (26), 8782-8787; (d) Mueller, M.; Czihak, C.; Vogl, G.; Fratzl, P.; Schober, H.; Riekkel, C., Direct Observation of Microfibril Arrangement in a Single Native Cellulose Fiber by Microbeam Small-Angle X-ray Scattering. *Macromolecules* **1998**, *31* (12), 3953-3957; (e) Duchesne, I.; Hult, E.-L.; Molin, U.; Daniel, G.; Iversen, T.; Lennholm, H., The influence of hemicellulose on fibril aggregation of kraft pulp fibres as revealed by FE-SEM and CP/MAS ¹³C-NMR. *Cellulose (Dordrecht, Netherlands)* **2001**, *8* (2), 103-111.
16. Park, S.; Baker, J.; Himmel, M.; Parilla, P.; Johnson, D., Cellulose crystallinity index: measurement techniques and their impact on interpreting cellulase performance. *Biotechnology for Biofuels* **2010**, *3* (1), 10.
17. Nishiyama, Y.; Sugiyama, J.; Chanzy, H.; Langan, P., Crystal Structure and Hydrogen Bonding System in Cellulose I α from Synchrotron X-ray and Neutron Fiber Diffraction. *Journal of the American Chemical Society* **2003**, *125* (47), 14300-14306.
18. Qian, X.; Ding, S.-Y.; Nimlos, M. R.; Johnson, D. K.; Himmel, M. E., Atomic and Electronic Structures of Molecular Crystalline Cellulose I β : A First-Principles Investigation. *Macromolecules* **2005**, *38* (25), 10580-10589.
19. (a) Kondo, T., Hydrogen bonds in cellulose and cellulose derivatives. In *Polysaccharides (2nd Edition)*, 2005; pp 69-98; (b) Atalla, R. H.; Isogai, A., Recent developments in spectroscopic and chemical characterization of

cellulose. *Polysaccharides (2nd Edition)* **2005**, 123-157; (c) Atalla, R. H.; VanderHart, D. L., The role of solid-state carbon-13 NMR spectroscopy in studies of the nature of native celluloses. *Solid State Nucl. Magn. Reson.* **1999**, *15* (Copyright (C) 2011 American Chemical Society (ACS). All Rights Reserved.), 1-19.

CHAPTER 2

Literature Review

1. Cellulose overview

Cellulose is the most abundant naturally-occurring biopolymer, and is considered an almost inexhaustible source of raw material for the increasing demand of environmentally friendly and biocompatible products.¹ Cellulose was first chemically identified by French chemist Anselme Payen in 1838² and the term was coined in 1839 through the French Academy.^{2d, 2f} "Cellulose" discovered by Payen was first obtained through purifying plant tissues with acid-ammonia treatment followed by water, alcohol, and ether extractions, to isolate a uniform carbohydrate (C(H₂O), Carbon 44.4%, Oxygen 49.4%, Hydrogen 6.2%).^{2a, 2d, 2f}

The chemical structure of cellulose is a linear homopolysaccharide composed of (1→4)-linked β-D-glucopyranose units; the repeating unit is cellobiose consisting of two glucose residues with every other glucose unit inverted because of the β-linkage (Figure 2.1). Cellulose molecules have strong tendency to form intra- and intermolecular hydrogen bonds due to its linear structure (Figure 2.1), which influences cellulose's physical and chemical properties.³

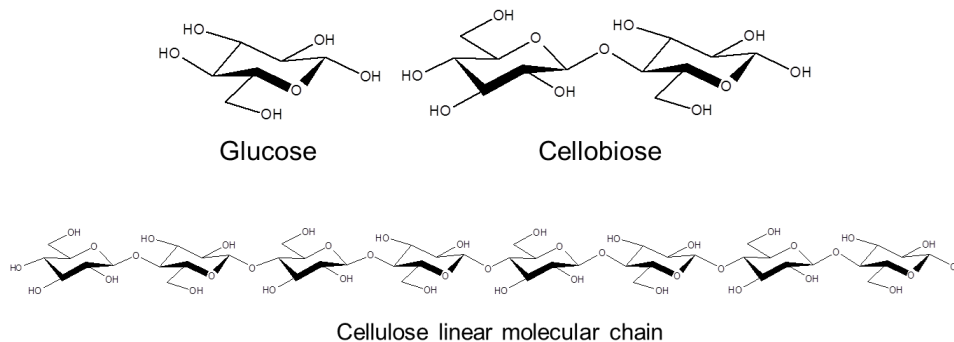


Figure 2.1. Glucose, cellobiose, and cellulose linear molecular chain.

1.1. Sources

In nature, most cellulose is produced by vascular plants; other natural sources include most groups of algae, the slime mold *Dictyostelium*, certain bacterial species, and tunicates (the only species that produces cellulose in the animal kingdom).⁴ From various biological sources, it is estimated that about 1.5 trillion tons of cellulose is produced each year from fixation of carbon dioxide during photosynthesis.^{2b}

1.2. Basic properties and applications of cellulose

In nature, cellulose is a structural polymer that serves the purpose of supporting the physical structures of vascular plants. This function is different from starch, an energy reserve polymer, although the two have the same monomer (glucose), but distinct physical and mechanical properties. As the result of the bonding pattern cellulose is tough and insoluble in water, while starch is amorphous and soluble.^{2c, 3a, 5} Cellulose is composed of β -D-glucopyranose units, linked together by (1 \rightarrow 4)-glycosidic bonds. Because each glucose residue has three hydroxyl groups (except for the terminal groups) with all the OH groups planar, cellulose molecules have a strong tendency to form intra- and inter-molecular hydrogen bonds.^{3b} Interacting through hydrogen bonds and van der Waals interactions, cellulose molecules are aggregated into microfibrils, and are insoluble in water and most common solvents.^{2b, 3-4, 6} This poor solubility is attributed

primarily to the strong intra- and inter-molecular hydrogen bonding between individual chains within its predominant crystalline structure.^{3b} Cellulose fibrils are in general strong, recyclable, and biocompatible,⁷ having extremely high aspect ratio and exhibit high stiffness (100-160 GPa), low thermal expansion (0.1 ppm/K), and yet low density (1.6g/cm³).^{1f, 8} Additionally, the inherent attributes of cellulose like its renewability and sustainability, as well as its abundance, facilitates its broad spectra of applications.^{1a, 2b}

Among different natural sources, wood pulp is by far the most important raw material for the processing of cellulose, most of which is used for the production of paper and cardboard, and a fraction (ca. 2% or 3.2 million tons in 2003) is used for the production of cellulose fibers, films, and synthesis of a large number of cellulose esters and ethers.^{2b} These derivatives are used as very important and well-known active components in coatings, optical films, sorption media and additives in building materials, drilling fluids, pharmaceuticals, foodstuffs, and cosmetics.^{3a, 5, 9}

Ever since the start of the “nano-era”, a major body of cellulose research has shifted into nanoscale too.^{1a, 1d, e, 2a, b, 6, 9a, 10} Cellulose nanoparticles (in fibril or crystal forms) exhibit unique properties in solid or solution states such as the following: solution thickening at low concentrations, thixotropy during processing, transparent or colored films dependent upon nanoparticle ordering, extensively expanded surface area, the ability to form highly porous foams and hydrogels, high specific strength and modulus, high sound attenuation, and relatively reactive surface.¹¹ These properties open great potential applications in fields like food products (non/low calorie food, food thickening agent, oxygen-barrier layers, emulsion stabilizer), cosmetics ingredients (thickener, dispenser, bodying agent), paint and coating additives/ fillers, oil field services, medical applications (binders, wound dressing), pharmaceutical area (excipient, filler, drug delivery agent), reinforcement in nanocomposites (flexible display panels), tissue engineering scaffolds, filtration media, value-added papermaking (filler retention aid, coating and dye carrier in paper tinting, gas-barrier and moisture-resistant paper laminate for packaging), and

major component in sanitary products (disposal diapers, napkins, incontinence pads).^{1a, 2b, 9b, 10b, 11}

2. Cellulose biosynthesis process

Abbreviations in this section: TC-- terminal complex, Cesa-- cellulose synthase catalytic subunit, CelS-- cellulose synthase complex, UDP-Glc-- uridine diphosphate glucose

2.1. Cellulose biosynthesis in bacteria

In addition to the most readily available source from plant cell walls, cellulose can also be synthesized by certain bacteria and animals.^{4b, c} Some strains of *Acetobacter* produce a gelatinous membrane called “pellicle” at the surface of the liquid culture.¹² Brown in 1886 chemically identified this material as composed of cellulose for the first time.¹³ Due to its high purity, bacterial cellulose has been extensively investigated on its microstructure and biosynthetic pathway, as a model of higher plant cellulose.¹²

2.1.1. Pathway for bacterial cellulose biosynthesis

In bacteria, cellulose is synthesized through cell metabolism.¹⁴ While no consensus has been reached on the exact mechanism so far due to lack of convincing evidence on either side, some argued that the polymerization of glucose residues into a β -1,4-linked cellulose chains was a multi-step process,^{12, 15} while others believed it was a direct one-step polymerization reaction.^{4a} The “multi-step” theory suggests that the whole process starts from glucose, goes through the pentose phosphate pathway to form glucose-1-phosphate, and then forms UDP-glucose (the direct precursor of cellulose) and finally polymerizes into long chains of cellulose. The newly formed cellulose is extruded into the extracellular culture by the cellulose synthase (a membrane protein).^{12, 15} The “direct one-step” theory proposes that the polymerization reaction is catalyzed

by the enzyme cellulose synthase, using UDP- α -glucose as the substrate; a single cellulose synthase molecule is capable of initiating, elongating and terminating a β -1,4-linked cellulose chain.^{4a}

2.1.2. From glucose polymerization to cellulose crystallization

While polymerization of glucose is the first and one of the most important steps in bacterial cellulose biosynthesis, the crystallization formation process draws significant research interest too.^{14b, 16} The crystallization and microfibril assembly process have been directly observed for *A. xylinum* in the space immediate exterior to the cell surface.^{14b} Cousins and Brown developed a two-step model to describe this crystallization process: 1) cellulose chains assemble into a monolayer molecular sheet via the van der Waals interaction, 2) the monolayer sheets assemble into type I cellulose crystalline structure via the inter-layer hydrogen bonding.¹⁷ For this process, cellulose chains assemble into sheets minimizing their hydrophobic surfaces. The cellulose chain structure with its planar hydrogen bonds forms a hydrophilic surface parallel the sheet surface,^{3b, 18} which could facilitate and help regulate the crystalline formation in the water environment. Because of the parallel arrangement of the cellulose sheets, the newly formed crystalline structure packs into the cellulose I unit cell structure to comply with this native configuration, otherwise the cellulose chains could have formed the more thermodynamically favored cellulose II or simply exist in amorphous state.^{4a} Although polymerization and crystallization are two separate events which happen in a sequential order, they are also coupled in certain manner that either one has an impact on the other-- it is observed that for *A. xylinum*, the rate of polymerization is influenced by crystallization.¹⁶

At the current understanding however, it is acknowledged that the paradigm of bacterial cellulose biosynthesis is not sufficient to account for the cellulose biosynthesis process observed in vascular plants, due to the significantly increased environmental complexity and very different conditions for biosynthesis process to take place.^{4a} However the simplified system serves as an

excellent model for cellulose fibril formation in an aqueous environment.

2.2. Cellulose biosynthesis in higher plants

2.2.1. Rosette, terminal complex, and cellulose synthase

In higher plants, cellulose microfibrils are extruded from a large membrane-localized apparatus, otherwise known as “rosette”; whereas hemicellulose are assembled and secreted from the Golgi vesicles.¹⁹ Similar structures to rosettes have been identified in almost all cellulose synthesizing organisms in higher plants.^{4a, 19b, 20} The rosette appears as an approximate hexagon with a six-fold symmetry and a diameter of 25-30 nm in vascular plants, which has been visualized through different microscopy studies.^{4a, 21} Each rosette is believed to consist of six “terminal complex”, or TCs; and each TC is further composed of six (three types of) cellulose synthases, or Cesa, together forming an array of 36 Cesa in one rosette with a six-fold symmetry (Figure 2.2).^{4a, 19b, 22} The number of Cesa can be deduced from the number of cellulose chains contained in an individualized cellulose microfibril. It was indicated that in order to assembly a cellulose microfibril from the TCs, all three different cellulose synthases (Cesa) have to be present otherwise the assembly cannot take place.^{19b, 23} Only a part of the rosette structure is exposed to the extracellular side of the plasma membrane, like the tip of an iceberg, whereas a significantly larger portion of this structure being present in the cytoplasm (Figure 2.3).^{22b, 24}

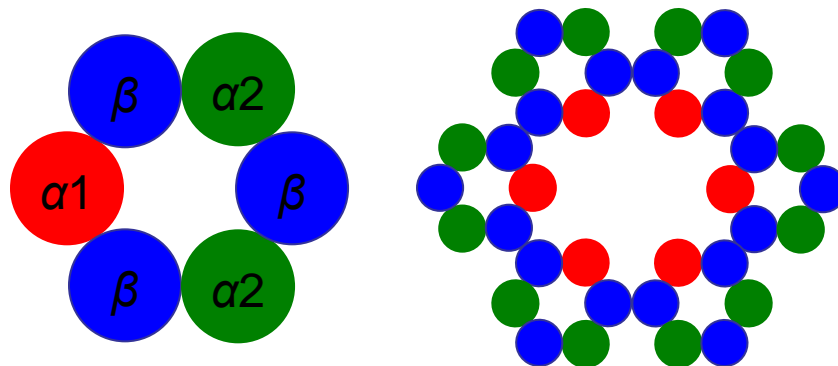


Figure 2.2. Left: one cellulose terminal complex (TC) is composed of six (three different kinds of) cellulose synthases (Cesa). Right: one “rosette” structure is composed of six such TCs.^{19b}

2.2.2. Understanding the rosette structure

The very first concept of the rosette structure in vascular plants was developed by Mueller and Brown in 1980, based on the observation of the freeze fracture image of a six-fold symmetry feature of “particle sub-unit” found on the P fracture face (i.e.: middle lamella viewed from outside the cell) of the plasma membrane.²¹ This understanding of the rosette morphology was not challenged until 1987 Kudlicka et al. discovered the cross-section view of a linear terminal complex and revealed that most of the rosette’s structure was actually deeply embedded in the cytoplasm of the cell, as depicted in Figure 2.3.^{1e, 24b} Later when more evidence accumulated, it was generally accepted that the “linear or rosette” morphology is just a small fraction of the structural unit.^{4a} The most up-to-date knowledge on rosette morphology concerns two levels of assembly of the cellulose synthases. Firstly, three different cellulose synthases assemble and form a linear arrays of six particles, deeply buried in the cytoplasm as the base of the rosette structure; and secondly, these linear arrays further assemble into a six-fold symmetry structure—the rosette (Figure 2.2).^{4a, 19b} The assembled rosette is then activated and transported to the plasma membrane for cellulose synthesis. The linear arrangement of rows within the rosette are believed to facilitate the formation of the layered structure of cellulose sheets.^{4a} This model has been justified by Cousins and Brown’s work on cellulose biosynthesis in *A. xylinum* in 1995 and 1997, respectively.^{17, 25}

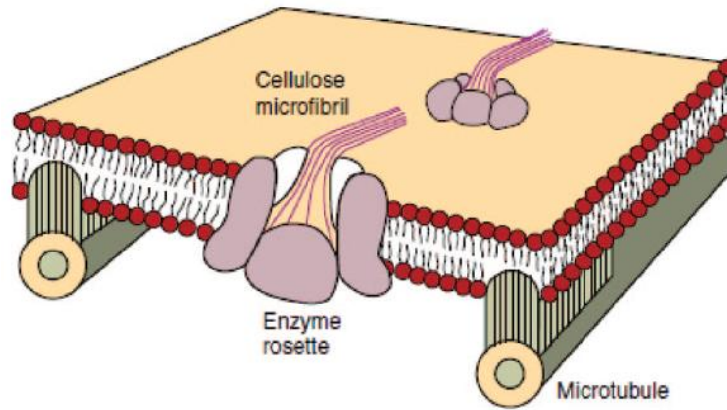


Figure 2.3. Schematic drawing of cellulose synthase rosette in plasma membrane: orientation of microtubules controlling the orientation of cellulose in the cell wall where the microtubules act as tracks to guide the cellulose enzymes floating in the cell membrane.^{1e} Reprinted with permission from reference 1e. Copyright (2010) American Chemical Society.

2.2.3. Cellulose microfibril deposition direction

Cellulose microfibrils are general deposited perpendicular to the axis of elongation, confining swelling in the lateral direction while allowing longitudinal growth. The general view of microfibril alignment is that microtubules serve as the channels, guiding the growth direction of the microfibrils.^{20, 26} However, there are studies investigating microtubule/microfibril interactions arguing a reversal in the role of orientation and that cellulose microfibrils may determine the orientation of the microtubules.²⁷

3. Supramolecular structure, crystallinity, hydrogen bonding, and existence in wood cell wall

3.1. Supramolecular structure of cellulose

3.1.1. Evolution of cellulose molecular chain models

The cellulose chain model was first proposed in publication by Sponsler and Dore in 1926 based on glucopyranose unit.^{2c, d} This model was later improved by Haworth and Freudenberg in two respects: (1) the new model defined cellobiose as the basic structural unit, and (2) the model proposed the β -1,4 glycosidic linkage for the anhydro glucose chains instead of the alternating 1-1 and 4-4 linkage in its previous version.^{2a} Even though this was a relatively accurate model representing cellulose chains, it was not widely accepted until much later after Meyer's efforts to re-introduce it. This resistance to accept the model was because of the once prevailing notion that the size and length of a molecule was limited by its unit cell of crystalline domains.^{2a, 28}

Hermanns and colleagues proposed the fringed micelle model in 1930, where a single molecule is conjectured to pass through several crystalline regions separated by amorphous area (Figure 2.4).^{2c, d, 29} Previously, the original concept of "micelles" was formed in 1850s, by Nageli and others to refer the anisotropic crystalline particles within the cellulose fibrils.^{2d} Based on both physical and chemical structural properties of cellulose, Frey-Wyssling (1943) and Kartky (1949) applied the established "fringe micellar" model to explain cellulose's complex properties, which was proved to be sufficient in explaining the mechanical deformation of regenerated cellulose and native cellulose as well.^{2d} However, the fringe-micellar model was strongly challenged by later developed cellulose aggregation models.^{2d} In early 1950s, Frey-Wyssling proposed the "micellar strand" model describing a microfibril with several aggregated elementary fibrils embedded in the paracrystalline cellulose.^{2c, 30} Ranby later in 1958 suggested the micelles are connected within the microfibrils by paracrystalline cellulose chains that composed of residues of glucose and other sugars.³¹ Preston (1974) further developed Ranby and Frey-Wyssling's model, proposed a microfibril model where one central crystalline core was surrounded by a paracrystalline cortex of molecular chains, which lies parallel to the microfibril longitudinal direction but are not packed in crystalline array.^{2d} In the early 1970s, Fengel developed a plant cell wall cellulose microfibril model where elementary fibrils were surrounded by hemicelluloses monolayers then four of such strands were enclosed together in the outer hemicelluloses and lignin layers.^{2d, 32}

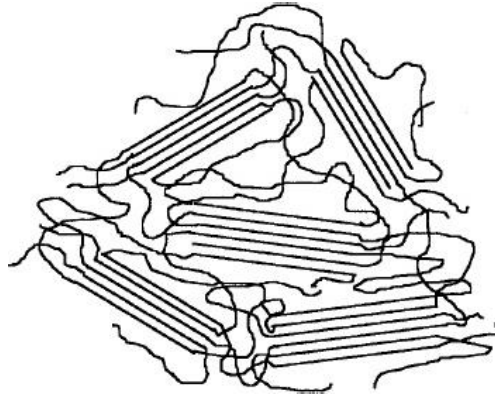


Figure 2.4. A schematic drawing showing fringed micelle structure.²⁹ Reprinted with permission from reference 29. Copyright (2002) Cambridge University Press.

3.1.2. From elementary fibrils to microfibrils

Frey-Wyssling and Muhlethaler (1963) demonstrated the presence of regular fibrils with a width of 3.5 nm consisting approximately 36 cellulose molecular chains in bacterial cellulose of *Acetobacter xylinum*, and named them “elementary fibrils”.³³ Since then, many have believed that “elementary fibrils” is the smallest and most fundamental structural unit of cellulose fibers and such structure is universally existed in all cellulose sources.³⁴ Manley (1964) proposed based on his results from ramie and *Valonia* cellulose, Muhlethaler’s earlier finding, together with Meyer and Misch’s unit cell model,^{28b} that all native celluloses have a basic structural element featured with an approximate 1 by 3.5 nm cross section dimension.³⁵ Also, Manley gave credits to the fringed micellar model to describe cellulose microfibrils behavior but at the same time challenged this model for being oversimplified.³⁵⁻³⁶ Later, Muhlethaler (1969) confirmed that the microfibrils are composed of isodiametric elementary fibrils having an average width of 3.5 nm and the fibrils seem to be crystalline along their entire length.^{2d}

Many literature sources has designated “elementary fibrils” as the basic cellulose fibril structure with fixed numbers of cellulose molecules and hence fixed lateral dimensions.³⁷ The existence and universality of such elementary fibrils within the cellulose microfibril was however questioned by many, and the smallest fibril was reported to be the microfibril that contained

single array of crystalline cellulose chains instead of multiple array.^{2c} This structure is conjectured to carry the features from the synthase arrangement to certain extent.³⁸ Moreover, hydrolysis and other studies have shown that there is a broad range for the lateral sizes of the “basic cellulose fibrils” from 3.5- 4.0 nm of wood cellulose, to 5.0- 7.0nm of flax and cotton, and to 14- 18 nm of *Valonia* cellulose. These variations in lateral dimensions both within and across cellulose species provide evidence against the universal elementary fibril concept.^{2c, d, 39} Therefore it appears that the size and basic structure of cellulose microfibrils at the supramolecular level should depend on the sample sources as well as their biosynthesis origins.

3.2. Cellulose crystalline nature

The crystalline nature of cellulose was first revealed by Nishikawa and Ono through the X-ray diffractions from various plant fiber bundles in 1913.⁴⁰ The molecular arrangements of these fibrillar bundles, consisting of aggregated cellulose molecular chains stabilized laterally by hydrogen bonding, have sufficient symmetry to generate X-ray diffraction patterns, and hence are regarded as having crystalline characteristics.^{2d, 41} However, many physical and chemical studies on cellulose microfibrils (fibrillar bundles) indicate that cellulose is not completely crystalline, but instead contain two distinct regions: one consists of highly ordered cellulose chains, or the crystalline region; the other is composed of less ordered cellulose chains, or paracrystalline region.^{2c, d}

3.2.1. Cellulose packing arrangements

Cellulose can be categorized based on their crystalline types, which essentially depends on the specific chain packing arrangements. The two major types are cellulose I (monoclinic arrangement for $I\beta$ and triclinic arrangement for $I\alpha$) and cellulose II (monoclinic arrangement). Almost all naturally occurred cellulose has type I arrangement, and cellulose II can be produced by mutants of *Acetobacter xylinum*, a bacterium that normally produces cellulose I.^{4a} Different crystalline sub-allomorphs of cellulose I, i.e.: $I\alpha$ and $I\beta$ have been identified by Attala and

VanderHart in 1984 via CP/MAS ^{13}C NMR spectroscopy.⁴² Cellulose from some algae and bacteria is found to be $I\alpha$ rich, while cellulose from cotton, wood, ramie and tunicates is $I\beta$ rich.⁴³ Also, the chain packing arrangements can be converted between one another in certain conditions, for example, cellulose $I\alpha$ is metastable and can be converted to $I\beta$ by annealing.^{4a}

Much work has gone into defining the molecular structure of cellulose I allomorphs using neutron scattering and X-ray scattering, providing information on the spacing of atoms in the unit cell. Now it is clear that cellulose $I\alpha$ has a one-chain triclinic unit cell, whereas cellulose $I\beta$ has a two parallel chains (reducing ends follow same direction) monoclinic unit cell (Figure 2.5).^{1d, 44} The major difference between the two allomorphs is how the consecutive hydrogen-bonded planes lie on top of each other: there is a unidirectional axial shift of each subsequent sheet of cellulose molecules in the $I\alpha$ structure, this results in some chains in one structure are shifted by half the repeating distance (along fiber axis) relative to those in the other.^{1d, 45}

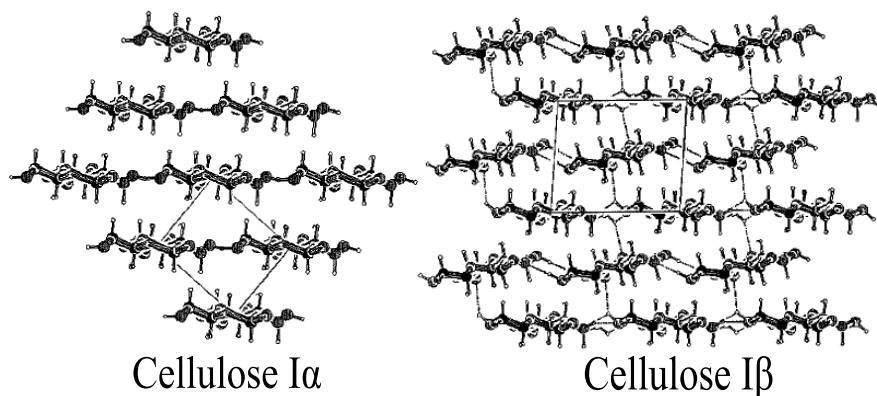


Figure 2.5. Unit cell structure of cellulose $I\alpha$ and $I\beta$ (viewed along the fiber direction).⁴⁴ Reprinted with permission from reference 44. Copyright (2000) John Wiley and Sons.

This layer stacking difference resulted in that the $I\beta$ form is more thermodynamically stable than the $I\alpha$ form.⁴⁶ Cellulose $I\beta$ crystalline structure differs from cellulose $I\alpha$ and the primitive cellulose I model in having two unique sheets that exhibiting distinct hydrogen-bonding patterns.⁴⁷ For the two-chain unit cell there are three possible packing modes for the two chains

(defined as corner chain and center chain), commonly referred to as “parallel up”, “parallel down” (collectively known as “parallel”), and “antiparallel”. “Parallel” and “antiparallel” refer to the two chains have the reducing ends pointing at the same direction and opposite directions, respectively.^{45, 48} A cellulose molecule is defined as being parallel “up” in the unit cell if the z-coordinate of O5 is greater than that of C5, otherwise it is oriented “down”.⁴⁵ The Meyer-Misch model (1937) presented an antiparallel orientation for cellulose I which was later disproved; Sarko et al (1976) proposed a parallel orientation for cellulose I and an antiparallel orientation for cellulose II based on the packing energy calculation; then Maurer and Fengel (1992) using end group labeling method experimentally suggested that both cellulose I and II were parallel oriented.⁴⁹

3.2.2. Crystallinity determination

The determination of crystallinity in cellulose has drawn a considerable body of research. Different types of crystallinity determination methods include: X-ray diffraction, density measurement, Fourier Transform infrared and Raman vibrational spectroscopies, nuclear magnetic resonance spectroscopy, and chemical methods (e.g.: deuterium exchange kinetics, hygroscopicity measurements, hydrolysis, periodate oxidation, substitution).^{2c, d, 50} The response of a cellulosic material to different measurement techniques varies and each technique has inherent variations in definitions and interpretations too.^{2d} Estimations of the proportions of crystalline part give a wide range of 50-90% (generally around 70%) crystallinity for native cellulose, and wood cellulose has somewhat lower values than cotton and ramie.^{2d, 50a}

3.3. Cellulose hydrogen bonding

In native cellulose microfibrils, there are three types of hydroxyl groups contributing to the formation of various kinds of intra- and intermolecular hydrogen bonds (in the order of the polarity or reactivity in water): secondary OH at C-2 position, primary OH at C-6 position, and secondary OH group at C-3 position.^{3b} In addition, all the OH groups are bonded to a

glucopyranose ring equatorially, while all the CH groups are bonded to a glucopyranose ring axially, resulting in the appearance of hydrophilic site parallel to the ring plane and the hydrophobic site perpendicular to the ring.^{3b, 10c} Reviewing these factors in the context of a cellulose crystalline structure, it is known that the OH--O (note: "--" indicates the hydrogen bonds occurs between the hydroxyl hydrogen atom and a neighboring oxygen atom) hydrogen bonding dominates the cellulose intra-sheet interactions (including both intra- and inter-chain bonding); and that CH--O hydrogen bonding and van der Waals interactions are responsible for the inter-sheet bonding (Figure 2.6).⁴⁷ It is inferred that the inter-sheet CH--O hydrogen bonding and van der Waals interactions are perhaps of equal magnitude,^{10c, 46} much less than intra-sheet hydrogen bonding. Also, computational research indicates that the inter-sheet interaction energy is approximately eight times weaker than the intra-sheet interaction.⁴⁶

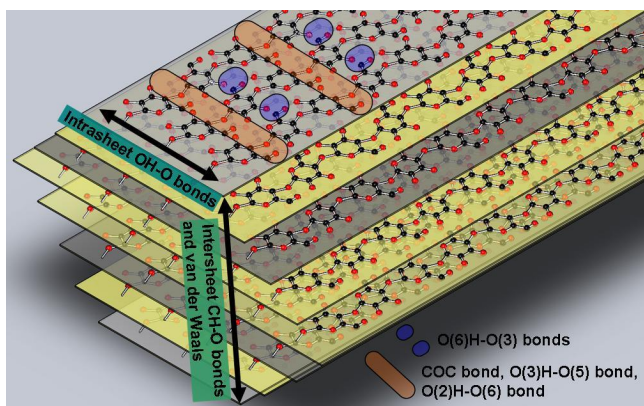


Figure 2.6. Hydrogen bonding system in native cellulose crystalline structure: OH—O bonds dominate the intra-sheet interaction, CH—O and van der Waals collectively are responsible for the inter-sheet interaction.⁵¹ Reprinted with permission from reference 51. Copyright (2011) American Chemical Society.

There are three possible conformations for the hydroxyl group at C6 position: *gt*, *tg* and *gg* (Figure 2.7). While *gt* is most thermodynamically favored conformation, representing 2/3 of the total conformations,^{3b} only *gg* conformation allows forming O(6)H--O(2) inter-sheet hydrogen bonding, because in this conformation the primary alcohol groups are essentially perpendicular to the average planes of the anhydroglucose rings so that they are pointing up toward the origin

chains of the layers above.⁵²

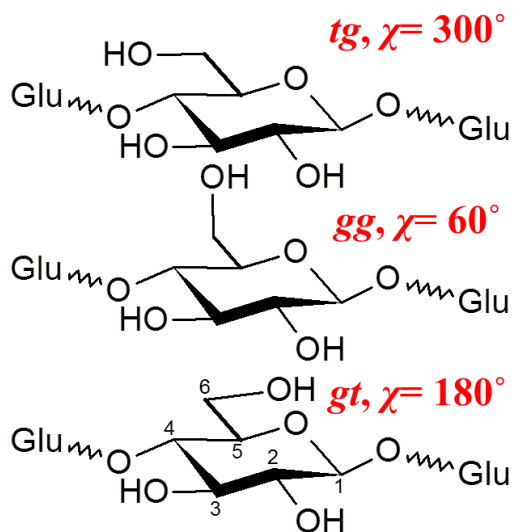


Figure 2.7. Three possible conformations at C6 primary hydroxyl group.

3.4. Existence of cellulose in wood cell wall

The wood cell wall is a complex composite essentially made of highly organized lamellae of polysaccharides and lignin (Figure 2.8).^{3a, 32, 53} The polysaccharides include: cellulose, glucomannan, xylan, xyloglucan, glucuronoxylan, and arabinoxylan (historically, the latter five are collectively known as hemicellulose). While the chemical compositions of the polysaccharides are already well understood, the chemical composition of lignin still cannot be precisely defined due to the lack of a selective procedure for quantitatively isolating this polymer in a pure and unaltered form.⁵³

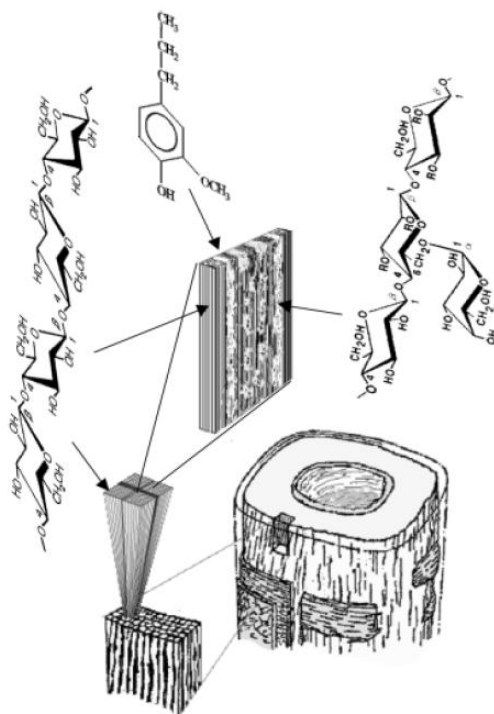


Figure 2.8. Schematic drawing of the hierarchical structure of wood polysaccharides and lignin in secondary cell wall of softwood tracheids.⁵⁴ Reprinted with permission from reference 54. Copyright (2003) De Gruyter (<http://www.degruyter.com/>).

There is evidence that the cellulose microfibrils are associated with glucomannan and xylan in different patterns, the interaction is primarily hydrogen bonding.⁵⁴⁻⁵⁵ During the pulping process however, the structures of xylan and mannan are altered and hence the interactions between hemicellulose and cellulose are different from those in native wood cell wall.^{53a} Other linkages contributing to the interactions between polysaccharides including glycosidic bonds and ester bonds (occur between carboxyl groups of uronic acid residues and hydroxyls on neighboring polysaccharides).^{53a} Lignins are deposited in a hetero-polysaccharides matrix, which is speculated to serve as a template for lignin formation since the hetero-polysaccharides and lignin are connected by both covalent and non-covalent bonds to form a lignin-polysaccharide complex (Figure 2.9).^{53a, 55b, 56} Different types of cross-linking and interactions between lignin and hetero-polysaccharides have been proposed as the following five types: 1) α or γ esters between uronic

acid and hydroxyl groups on lignin surfaces; 2) direct ether linkage between polysaccharides and lignin; 3) ester or ether linkage between hydroxycinnamoyl residues on polysaccharides and lignin; 4) possible hydrogen bonds; and 5) potential physical crosslinking (entanglement).^{53a}

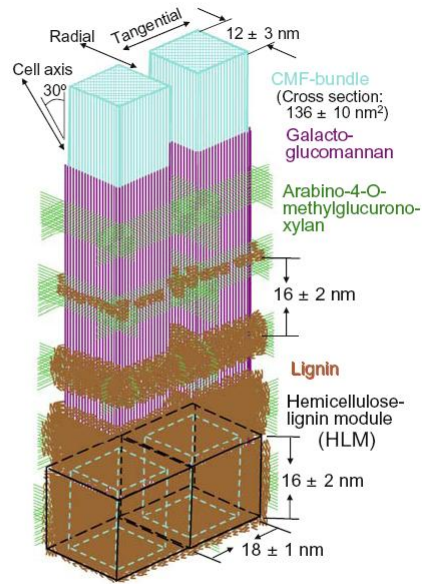


Figure 2.9. Simplified speculative schematic drawing of the assembly process (top down) of cellulose microfibril bundle, hemicelluloses, and lignin with their estimated dimension in wood cell wall S2 layer.^{55b} Reprinted with permission from reference 55b. Copyrights (2009) Springer.

4. Nanocellulose and its preparation

4.1. Nanocellulose

4.1.1. Definition and classification

As mentioned in the previous section, cellulose microfibrils are organized in lamellae within the cell wall. After delignification, it is possible to isolate cellulose fibrils and fiber bundles from this organized structure in its partially fibrillar form. Nanocellulose refers to isolated cellulose particles with at least one dimension in the nanometer range (below 100 nm), meanwhile

exhibiting novel properties associated with its nanostructure.^{1a, 57} Based on the preparation methods and raw material origin, nanocellulose are conventionally classified into three sub-categories (Figure 2.10): 1) Microfibrillated cellulose or MFC (a.k.a.: microfibril, nanofibril, nanofibrillated cellulose), an elongated fibril form of nanocellulose, is prepared from wood and other plant fibers via mechanical or combined chemical and mechanical treatments. 2) Nanocrystalline cellulose or NCC (a.k.a.: cellulose nanocrystals, crystallites, whiskers, rodlike cellulose microcrystals), a rodlike crystal form of nanocellulose, can be prepared from a broader range of raw materials including plant-originated cellulose, tunicin, algae and bacteria originated celluloses, as well as commercialized microcrystalline cellulose—Avicel, via acid or enzymatic hydrolysis. 3) Bacterial nanocellulose or BNC (a.k.a.: bacterial cellulose, microbial cellulose, biocellulose), a network form of nanocellulose, is a pure component of the biofilm produced by certain bacteria via their metabolic activities, consuming only low-molecular-weight sugars and alcohols.^{14b, 57}

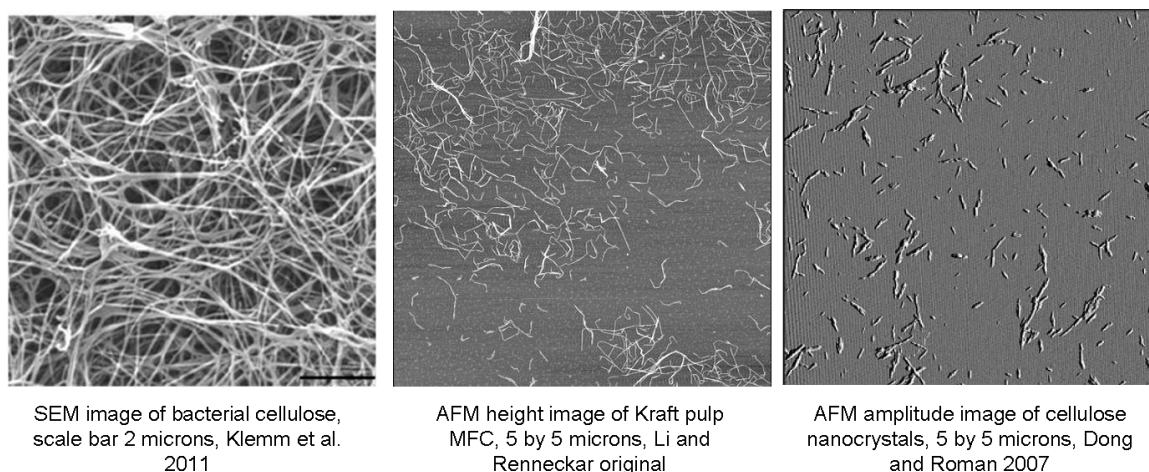


Figure 2.10. Images of different types of nanocelluloses.⁵⁷⁻⁵⁸ Reprinted with permissions from reference 57 and 58, respectively. Copyright (2011) John Wiley and Sons and (2007) American Chemical Society.

4.1.2. Properties and applications

Nanocelluloses possess important cellulose properties, like hydrophilicity, broad chemical-

modification potential, and formation of versatile semicrystalline fiber morphologies. Additionally the extensively expanded surface area may enhance specific properties related to filtration and sensor development.⁵⁷ Nanocelluloses have excellent mechanical properties especially the elastic modulus (ranging from around dozens to more than 200 GPa), which 200 GPa elastic modulus is comparable to bulk properties of carbon fibers, steel, and titanium alloy.^{1b, 57, 59} Nanocelluloses also have stable thermal properties with degradation temperature ranging between 200-300 °C depending on heating rate, particle type, and surface modification.^{1b} Rheological examination shows nanocelluloses suspensions exhibit a shear thinning property; this property depends on the surface charge and solution concentration, the shear thinning may be time dependent, i.e. thixotropy (for HCl derived crystals in high concentrations and MFC); MFC and CNC form stable gels in water when w/w concentration pass certain threshold level (e.g.: 0.5% for MFC)^{1b} Last but not least, nanocelluloses present amazing optical properties: they can form transparent films, exhibit liquid crystallinity as well as birefringence due to the anisotropic structure of individual particles.^{1b} Besides these properties, nanocelluloses also exhibit specific properties based on the different origins, processing methods, and end product conformations, and accordingly different applications may be developed to leverage these unique properties. For example, bacterial cellulose is shapeable during its biosynthesis process, and this property has been utilized to grow artificial blood vessels off the pre-designed cylindrical templates.^{1a, 2b, 60}

MFC finds its applications in paper making as reinforcement agents⁶¹ or functional coatings (e.g.: grease proofing or moisture absorbing),⁶² in food, cosmetic, pharmaceutical,⁶³ and hygiene products as the emulsion and/or dispersion additives; as well as in various nanocomposites⁶⁴ and films⁶⁵ as structural components.⁶⁶ All these applications are built upon MFC's unique combination of properties of bonding enhancing, water retention, aspect ratio, specific strength, rheology and optical characteristics, as well as its universal bio-friendliness.^{1a, b, 57}

As for **NCC**, even though the most interesting property is its self-ordering property, or the chiral

nematic phase nature, the most readily applications are based on its mechanical properties, used as the reinforcement agents in composite films to increase strength and dimension stability.⁶⁷ Owing to its biocompatibility and chemical modification capacity, NCC also finds novel applications in drug delivery.^{58, 68} NCC nanocomposites are typically produced through compression molding, extrusion, solution casting (followed by cross-linking or polymerization), and self-assembly (by spin coating or dip coatings). In terms of industrialization, conventional methods such as injection molding, extrusion and pressing are more likely routes, whereas solvent casting would have difficulties due to the involvement of volatile solvents, even though it produces better quality films.^{1b, c, 57}

BNC, due to its biosynthesis origin, has many unique properties which set it apart from MFC and NCC such as stable nanofiber network, shapability during biosynthesis, non-cytotoxic and non-genotoxic, excellent mechanical strength, while highly flexible in the wet state. These properties lend BNC into the novel application fields like artificial blood vessels,⁶⁰ wound dressing material,⁶⁹ fuel cell membranes,⁷⁰ and even films for electronic appliances.⁵⁷

4.2. Preparation methods

Nanocellulose can be prepared through many different approaches, which can be classified into two general categories: top-down and bottom-up.^{1b, 71} The top-down approaches, which obtain nanocelluloses by extracting cellulose particles from various sources at nanoscale,⁵² can be further divided into three subcategories: mechanical, chemical, and mechanical-chemical. The bottom-up approaches assemble cellulose nanostructures either from the solution state of cellulose molecules or from the biosynthesis process.^{57, 71} Through either “extraction” or “assembly”, nanocelluloses are relatively uniform particles with enormously expanded surface area, which brings in many of the favorable properties that lay the foundations of many potential applications.^{1a} Figure 2.11 exhibits the classification of nanocellulose fabrication approaches, the most representative approaches are highlighted below.

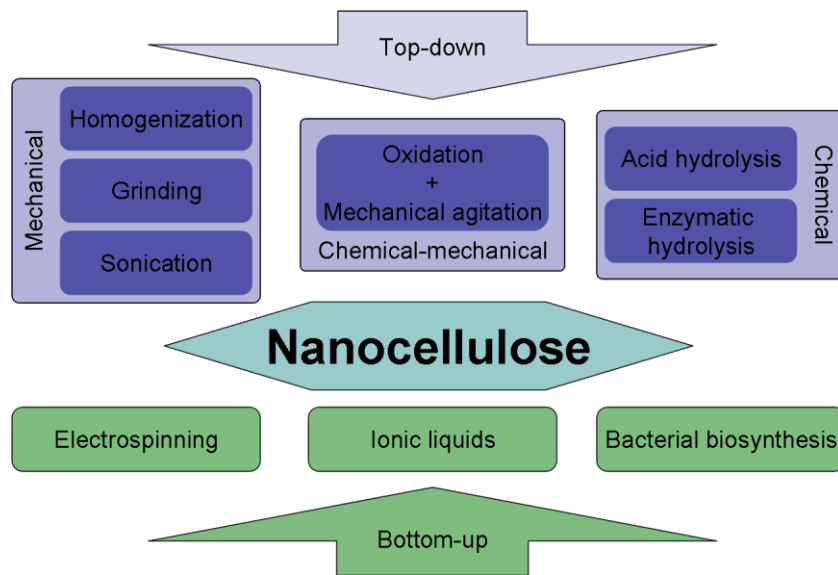


Figure 2.11. Classification of nanocellulose fabrication approaches.

4.2.1. Common top-down approaches

The top-down approaches, as the name suggests, typically start from raw materials like wood chips, pulps, cotton litters. From these sources mechanical, chemical, or combined chemical-mechanical methods are used to liberate cellulose microfibrils and nanocelluloses from their native recalcitrant structures (i.e.: cell wall or large fiber bundles). For high purity raw materials like cotton linter, this means to release individual microfibrils from the large fiber bundles. Whereas for the raw materials existed in the natural composite form like wood chips, the top-down approach means to separate cellulose from its lignin-hemicellulose matrix first then isolate individualized nanocellulose particles from large cellulose fiber bundles.

(1) Mechanical approaches

Homogenization: First described by Turbak et al in 1983, the homogenization method processes different types of pulps with intensive homogenization treatments with controlled pass numbers and high pressure through a small orifice (55 MPa or 8000 psi).^{9b} The predominant end product has a net-like structure, with a diameter ranging from 25-100 nm in dry state. Due to the large

increase in surface area, MFC has a dramatically increased water retention rate of more than 400% (compared to 50-90% of wood pulps).^{9b, 11i} Large energy consumption (25,000 kWh/t) is the major impediment of commercial success.^{57, 72}

Sonication: The first work to produce MFC with a mechanical agitation method was reported by Wuhrmann et al in 1946, where plant fibers from ramie, hemp, and cotton were subjected to intensive sonication treatment. From the process, fine fibrils (6-7 nm width) were yielded as a function of the mechanical agitation intensity.⁷³

Wet grinding: Abe and coworkers recently (2007) introduced the wet grinding method to process lignin containing plant fibers in order to yield uniform nanocellulose fibrils with dimension of 12-16 nm.^{11b} Prior to the grinding process, samples were pretreated to remove lignin and hemicellulose components from the cell wall matrix. The delignified samples were then passed through the grinder at 1500 rpm in slurry condition (1 wt%) to isolate the nanocellulose fibrils.^{11b}

Aqueous counter collision (a.k.a.: ultrahigh-pressure water jet treatment): Kondo and colleagues developed a novel method to prepare nanocellulose fibrils by subjecting cellulose water suspensions (≤ 0.4 wt%) under ultrahigh pressure (200 MPa) using a jet counter collision apparatus for multiple cycles (10-80) to produce “single-cellulose nanofibers” in water.^{34a, 74} The resulting nanocellulose has a width profile of several dozens of nanometers and a length profile of single to double digits microns.^{34a}

(2) Chemical approaches

Acid hydrolysis: Acid hydrolysis is a well-known process for removing accessible regions from native cellulose and produce nanocellulose crystals (NCC).^{52, 75} Different initial cellulosic materials (pulp, plant-based cellulose, bacterial cellulose, tunicate cellulose, etc.) are treated with concentrated mineral acid (most commonly sulfuric acid or hydrochloric acid) under elevated

temperatures (around 45 °C) with varied time periods.^{75b, 76} The end products are rod-like particles with lateral dimensions ranging from 3-30 nm and hundreds of nanometers in length, depending on the starting materials as well as the processing conditions. The NCC produced by acid hydrolysis can form birefringent gels and liquid crystalline structures, and exhibit helicoidal self-ordering (chiral nematic phase) properties in certain concentration range.^{1b, c, 76}

(3) Chemical-mechanical approaches

Different chemical pretreatments (e.g.: oxidation,⁷⁷ acid hydrolysis,^{75a} and enzymatic hydrolysis⁷⁸), mechanical agitations (e.g.: sonication, homogenization, blending, etc.), as well as the combinations have been extensively investigated. The most common chemical-mechanical approach is to first oxidize or hydrolyze the cellulose (e.g.: TEMPO oxidation,⁷⁹ chloroacetic acid etherification,⁸⁰ enzymatic hydrolysis,⁷⁸ and carboxymethylation⁸¹) followed by mild to intensive mechanical treatments to liberate carboxylated MFC from the raw materials.^{1f} The end product MFC is in long fibril forms, with lateral dimensions of single digit nanometers (or even sub-nanometers) and hundreds of nanometer to several microns in length.^{51, 82} This fabrication approach has been adopted by many research groups around the globe and the most up-to-date research progress has been summarized by Isogai and coworkers.⁸³

4.2.2. Common bottom-up approaches

Contrary to the top-down approaches, the bottom-up approaches produce nanocellulose through assembling from its molecular level building blocks. In the case of bacterial cellulose synthesis, nanocellulose is polymerized from UDP-glucose via the bacterial metabolic activity. For other cases like electrospinning, nanocellulose is regenerated into solid fibrous form from the solution state.

(1) Electrospinning: A typical electrospinning setup uses a polymer solution (or polymer melt) to spin continuous fibers under an electrical field. Under the high voltage, the solution or melt

deforms due to the repulsion of like charges at the surface of the drop. Once the charge repulsion overcomes the surface tension of the polymer, a fine jet is then ejected towards the collector to form the nanocellulose. Electrospinning can produce nanocellulose in non-woven fiber mat form or oriented fiber strands dependent on the configuration of the collector; fiber diameter ranges from single digit nanometers to microns.^{1b, c, 84}

(2) Bacterial biosynthesis: Bacterial nanocellulose (BNC) is produced by certain bacteria's biosynthesis process which converting low-molecular-weight sugars to cellulose molecules. The generated cellulose molecular chains were excreted into the aqueous culture medium in fiber form, and these fibers then combine to form ribbons and eventually a 3D nanofiber network. Simple purification process can remove all the impurities leave only pure cellulose fibers with nanometer diameters.⁵⁷

4.3 Additional information on the top-down approach TEMPO-mediated oxidation followed by sonication

Typical characterizations for nanocelluloses produced by different approaches include the 3D dimension distributions, crystallinity variations, supramolecular arrangement changes, fibril morphology, and degrees of modification (i.e.: oxidation, carboxylation, carboxymethylation). More focused and in-depth research would also expand the investigation into various other properties like total surface area,^{34a} surface charge,⁸⁵ viscosity,⁸⁶ optical properties,^{62, 87} film/foam forming ability,⁸⁸ and the related physical/mechanical properties.^{1f, 89} For the combined TEMPO-oxidation and sonication approach specifically, since it is still relative new, many of the key characteristics of the nanocellulose have not yet been fully carried out, such as the correlations between cellulose supramolecular arrangement variations and the sonication treatments. These extended characterizations would enhance insight to the fundamental understanding of the cellulose supramolecular structure and help explore new potential applications for nanocellulose.

References

- (a) Klemm, D.; Schumann, D.; Kramer, F.; Hessler, N.; Hornung, M.; Schmauder, H. P.; Marsch, S., Nanocelluloses as innovative polymers in research and application. In *Polysaccharides II*, Springer-Verlag Berlin: Berlin, 2006; Vol. 205, pp 49-96; (b) Moon, R. J.; Martini, A.; Nairn, J.; Simonsen, J.; Youngblood, J., Cellulose nanomaterials review: structure, properties and nanocomposites. *Chem. Soc. Rev.* **2011**, *40* (7), 3941-3994; (c) Eichhorn, S. J., Cellulose nanowhiskers: promising materials for advanced applications. *Soft Matter* **2011**, *7* (Copyright (C) 2011 American Chemical Society (ACS). All Rights Reserved.), 303-315; (d) Nishiyama, Y., Structure and properties of the cellulose microfibril. *Journal of Wood Science* **2009**, *55* (4), 241-249; (e) Habibi, Y.; Lucia, L. A.; Rojas, O. J., Cellulose Nanocrystals: Chemistry, Self-Assembly, and Applications. *Chemical Reviews* **2010**, *110* (6), 3479-3500; (f) Eichhorn, S. J.; Dufresne, A.; Aranguren, M.; Marcovich, N. E.; Capadona, J. R.; Rowan, S. J.; Weder, C.; Thielemans, W.; Roman, M.; Renneckar, S.; Gindl, W.; Veigel, S.; Keckes, J.; Yano, H.; Abe, K.; Nogi, M.; Nakagaito, A. N.; Mangalam, A.; Simonsen, J.; Benight, A. S.; Bismarck, A.; Berglund, L. A.; Peijs, T., Review: current international research into cellulose nanofibres and nanocomposites. *J. Mater. Sci.* **2010**, *45* (1), 1-33.
- (a) Zugenmaier, P., *Crystalline cellulose and derivatives: characterization and structures*. Springer: 2007; (b) Klemm, D.; Heublein, B.; Fink, H. P.; Bohn, A., Cellulose: Fascinating biopolymer and sustainable raw material. *Angew. Chem.-Int. Edit.* **2005**, *44* (22), 3358-3393; (c) Osullivan, A. C., Cellulose: the structure slowly unravels. *Cellulose* **1997**, *4* (3), 173-207; (d) Hon, D. N. S., Cellulose: a random walk along its historical path. *Cellulose* **1994**, *1* (1), 1-25; (e) Payen, A., Memoir on the composition of the tissue of plants and of woody [material]. *Comptes rendus* **1838**, *7*, 1052-1056; (f) Report on a memoir of Mr. Payen, regarding the composition of woody matter. *Comptes rendus* **1839**, *8*, 51-53.
- (a) Sjöström, E., *Wood Chemistry: Fundamentals and Applications, 2nd Edition*. 1993; p 293; (b) Kondo, T., Hydrogen bonds in cellulose and cellulose derivatives. In *Polysaccharides (2nd Edition)*, 2005; pp 69-98.
- (a) Saxena, I. M.; Brown, R. M., Cellulose Biosynthesis: Current Views and Evolving Concepts. *Annals of Botany* **2005**, *96* (1), 9-21; (b) Ranby, B. G., Physicochemical investigations on bacterial

- cellulose. *Ark. Kemi* **1952**, *4* (Copyright (C) 2011 American Chemical Society (ACS). All Rights Reserved.), 249-55; (c) Ranby, B. G., Physicochemical investigations on animal cellulose (Tunicin). *Ark. Kemi* **1952**, *4* (Copyright (C) 2011 American Chemical Society (ACS). All Rights Reserved.), 241-8.
5. *Polymer handbook*. 3rd ed.; Wiley: New York, 1989; Vol. 1 v. (various pagings)
 6. Siqueira, G.; Bras, J.; Dufresne, A., Cellulosic Bionanocomposites: A Review of Preparation, Properties and Applications. *Polymers* **2010**, *2* (4), 728-765.
 7. Kamel, S.; Ali, N.; Jahangir, K.; Shah, S. M.; El-Gendy, A. A., Pharmaceutical significance of cellulose: A review. *Express Polym. Lett.* **2008**, *2* (11), 758-778.
 8. Saito, T.; Hirota, M.; Tamura, N.; Kimura, S.; Fukuzumi, H.; Heux, L.; Isogai, A., Individualization of Nano-Sized Plant Cellulose Fibrils by Direct Surface Carboxylation Using TEMPO Catalyst under Neutral Conditions. *Biomacromolecules* **2009**, *10* (7), 1992-1996.
 9. (a) Samir, M.; Alloin, F.; Dufresne, A., Review of recent research into cellulosic whiskers, their properties and their application in nanocomposite field. *Biomacromolecules* **2005**, *6* (2), 612-626; (b) Turbak, A. F.; Snyder, F. W.; Sandberg, K. R., Microfibrillated cellulose, a new cellulose product: properties, uses, and commercial potential. *Journal of Applied Polymer Science: Applied Polymer Symposium* **1983**, *37* (Proc. Cellul. Conf., 9th, 1982, Part 2), 815-827; (c) *Cellulose Chemistry and Technology*. AMERICAN CHEMICAL SOCIETY: 1977; p 412.
 10. (a) Filson, P. B.; Dawson-Andoh, B. E., Sono-chemical preparation of cellulose nanocrystals from lignocellulose derived materials. *Bioresource Technology* **2009**, *100* (7), 2259-2264; (b) Azizi Samir, M. A. S.; Alloin, F.; Dufresne, A., Review of Recent Research into Cellulosic Whiskers, Their Properties and Their Application in Nanocomposite Field. *Biomacromolecules* **2005**, *6* (2), 612-626; (c) Jarvis, M., Chemistry - Cellulose stacks up. *Nature* **2003**, *426* (6967), 611-612.
 11. (a) Lasseguette, E.; Roux, D.; Nishiyama, Y., Rheological properties of microfibrillar suspension of TEMPO-oxidized pulp. *Cellulose* **2008**, *15* (3), 425-433; (b) Abe, K.; Iwamoto, S.; Yano, H., Obtaining Cellulose Nanofibers with a Uniform Width of 15 nm from Wood. *Biomacromolecules* **2007**, *8* (10), 3276-3278; (c) Nogi, M.; Handa, K.; Nakagaito, A. N.; Yano, H., Optically transparent bionanofiber composites with low sensitivity to refractive index of the polymer matrix. *Appl. Phys. Lett.* **2005**, *87* (Copyright (C)

- 2011 American Chemical Society (ACS). All Rights Reserved.), 243110/1-243110/3; (d) Iwamoto, S.; Nakagaito, A. N.; Yano, H.; Nogi, M., Optically transparent composites reinforced with plant fiber-based nanofibers. *Appl. Phys. A: Mater. Sci. Process.* **2005**, *81* (Copyright (C) 2011 American Chemical Society (ACS). All Rights Reserved.), 1109-1112; (e) Nakagaito, A. N.; Yano, H., The effect of morphological changes from pulp fiber towards nano-scale fibrillated cellulose on the mechanical properties of high-strength plant fiber based composites. *Appl. Phys. A: Mater. Sci. Process.* **2004**, *78* (Copyright (C) 2011 American Chemical Society (ACS). All Rights Reserved.), 547-552; (f) Nakagaito, A. N.; Yano, H., Novel high-strength biocomposites based on microfibrillated cellulose having nano-order-unit web-like network structure. *Appl. Phys. A: Mater. Sci. Process.* **2004**, *80* (Copyright (C) 2011 American Chemical Society (ACS). All Rights Reserved.), 155-159; (g) Hioki, S.; Hori, S.; Watanabe, K.; Morinaga, Y. Microbial cellulose dispersion for improving retention of paper making filler. 1995; (h) Hioki, S.; Hori, S.; Watanabe, K.; Morinaga, Y. Bacterial cellulose dispersion for improving retention of paper making filler. 1995; (i) Herrick, F. W.; Casebier, R. L.; Hamilton, J. K.; Sandberg, K. R., Microfibrillated cellulose: morphology and accessibility. *Journal of Applied Polymer Science: Applied Polymer Symposium* **1983**, *37* (Copyright (C) 2011 American Chemical Society (ACS). All Rights Reserved.), 797-813; (j) Herrick, F. W., Review of the treatment of cellulose with liquid ammonia. *Journal of Applied Polymer Science: Applied Polymer Symposium* **1983**, *37* (Copyright (C) 2011 American Chemical Society (ACS). All Rights Reserved.), 993-1023.
12. Yoshinaga, F.; Tonouchi, N.; Watanabe, K., Research progress in production of bacterial cellulose by aeration and agitation culture and its application as a new industrial material. *Biosci. Biotechnol. Biochem.* **1997**, *61* (2), 219-224.
13. Brown, A. J., The chemical action of pure cultivations of bacterium aceti. *J. Chem. Soc., Trans.* **1886**, *49* (Copyright (C) 2011 American Chemical Society (ACS). All Rights Reserved.), 172-187.
14. (a) Somerville, C., Cellulose synthesis in higher plants. *Annu. Rev. Cell Dev. Biol.* **2006**, *22*, 53-78; (b) Ross, P.; Mayer, R.; Benziman, M., Cellulose biosynthesis and function in bacteria. *Microbiol. Mol. Biol. Rev.* **1991**, *55* (1), 35-58.
15. Okuda, K.; Sekida, S.; Yoshinaga, S.; Suetomo, Y., Cellulose-synthesizing complexes in some

chromophyte algae. *Cellulose (Dordrecht, Netherlands)* **2004**, *11* (Copyright (C) 2011 American Chemical Society (ACS). All Rights Reserved.), 365-376.

16. Benziman, M.; Haigler, C. H.; Brown, R. M.; White, A. R.; Cooper, K. M., CELLULOSE BIOGENESIS - POLYMERIZATION AND CRYSTALLIZATION ARE COUPLED PROCESSES IN ACETOBACTER-XYLINUM. *Proceedings of the National Academy of Sciences of the United States of America-Biological Sciences* **1980**, *77* (11), 6678-6682.

17. (a) Cousins, S. K.; Brown, R. M., Jr., Photoisomerization of a dye-altered β -1,4 glucan sheet induces the crystallization of a cellulose-composite. *Polymer* **1997**, *38* (Copyright (C) 2011 American Chemical Society (ACS). All Rights Reserved.), 903-912; (b) Cousins, S. K.; Brown, R. M., Jr., X-ray diffraction and ultrastructural analyses of dye-altered celluloses support van der Waals forces as the initial step in cellulose crystallization. *Polymer* **1997**, *38* (Copyright (C) 2011 American Chemical Society (ACS). All Rights Reserved.), 897-902.

18. (a) Hishikawa, Y.; Inoue, S.-i.; Magoshi, J.; Kondo, T., Novel Tool for Characterization of Noncrystalline Regions in Cellulose: A FTIR Deuteration Monitoring and Generalized Two-Dimensional Correlation Spectroscopy. *Biomacromolecules* **2005**, *6* (5), 2468-2473; (b) Kondo, T., The assignment of IR absorption bands due to free hydroxyl groups in cellulose. *Cellulose* **1997**, *4* (4), 281-292.

19. (a) Urbanowicz, B. R.; Rayon, C.; Carpita, N. C., Topology of the maize mixed linkage (1 \rightarrow 3),(1 \rightarrow 4)-beta-D-glucan synthase at the Golgi membrane. *Plant Physiology* **2004**, *134* (2), 758-768; (b) Ding, S.; Himmel, M. E., The Maize Primary Cell Wall Microfibril: A New Model Derived from Direct Visualization. *J. Agric. Food Chem* **2006**, *54* (3), 597-606.

20. Somerville, C.; Bauer, S.; Brininstool, G.; Facette, M.; Hamann, T.; Milne, J.; Osborne, E.; Paredes, A.; Persson, S.; Raab, T.; Vorwerk, S.; Youngs, H., Toward a systems approach to understanding plant-cell walls. *Science* **2004**, *306* (5705), 2206-2211.

21. Mueller, S. C.; Brown, R. M., Jr., Evidence for an intramembrane component associated with a cellulose microfibril-synthesizing complex in higher plants. *J Cell Biol* **1980**, *84* (Copyright (C) 2011 U.S. National Library of Medicine.), 315-26.

22. (a) Himmel, M. E.; Ding, S.-Y.; Johnson, D. K.; Adney, W. S.; Nimlos, M. R.; Brady, J. W.; Foust, T.

- D., Biomass Recalcitrance: Engineering Plants and Enzymes for Biofuels Production. *Science* **2007**, *315* (5813), 804-807; (b) Bessueille, L., A survey of cellulose biosynthesis in higher plants. *Plant biotechnology (Tokyo, Japan)* **2008**, *25*, 315.
23. (a) Doblin, M. S.; Kurek, I.; Jacob-Wilk, D.; Delmer, D. P., Cellulose biosynthesis in plants: from genes to rosettes. *Plant Cell Physiol.* **2002**, *43* (12), 1407-1420; (b) Williamson, R. E.; Burn, J. E.; Hocart, C. H., Towards the mechanism of cellulose synthesis. *Trends Plant Sci.* **2002**, *7* (Copyright (C) 2011 American Chemical Society (ACS). All Rights Reserved.), 461-467.
24. (a) Kudlicka, K., Terminal complexes of cellulose synthesis. *Postepy Biol. Komorki* **1989**, *16* (Copyright (C) 2011 American Chemical Society (ACS). All Rights Reserved.), 197-212; (b) Kudlicka, K.; Wardrop, A.; Ito, T.; Brown, R. M., Jr., Further evidence from sectioned material in support of the existence of a linear terminal complex in cellulose synthesis. *Protoplasma* **1987**, *136* (Copyright (C) 2011 American Chemical Society (ACS). All Rights Reserved.), 96-103.
25. Cousins, S. K.; Brown, R. M., Cellulose I microfibril assembly: computational molecular mechanics energy analysis favours bonding by van der Waals forces as the initial step in crystallization. *Polymer* **1995**, *36* (20), 3885-3888.
26. (a) Mueller, S. C.; Brown, R. M., Jr., The control of cellulose microfibril deposition in the cell wall of higher plants. I. Can directed membrane flow orient cellulose microfibrils? Indirect evidence from freeze-fractured plasma membranes of maize and pine seedlings. *Planta* **1982**, *154* (Copyright (C) 2011 American Chemical Society (ACS). All Rights Reserved.), 489-500; (b) Mueller, S. C.; Brown, R. M., Jr., The control of cellulose microfibril deposition in the cell wall of higher plants. II. Freeze-fracture microfibril patterns in maize seedling tissues following experimental alteration with colchicine and ethylene. *Planta* **1982**, *154* (Copyright (C) 2011 American Chemical Society (ACS). All Rights Reserved.), 501-15.
27. Fisher, D. D.; Cyr, R. J., Extending the microtubule/microfibril paradigm. Cellulose synthesis is required for normal cortical microtubule alignment in elongating cells. *Plant Physiol.* **1998**, *116* (Copyright (C) 2011 American Chemical Society (ACS). All Rights Reserved.), 1043-1051.
28. (a) Meyer, K. H.; Misch, L., The structure of the crystalline part of cellulose. *V. Ber. Dtsch. Chem. Ges. B* **1937**, *70B* (Copyright (C) 2011 American Chemical Society (ACS). All Rights Reserved.), 266-74;

- (b) Meyer, K. H.; Misch, L., The constitution of the crystalline part of cellulose. VI. The positions of the atoms in the new space model of cellulose. *Helv. Chim. Acta* **1937**, *20* (Copyright (C) 2011 American Chemical Society (ACS). All Rights Reserved.), 232-244.
29. Bower, D. I., *An introduction to polymer physics*. Cambridge University Press: 2002.
30. Frey-Wyssling, A., The fine structure of cellulose microfibrils. *Science (Washington, DC, United States)* **1954**, *119*, 80-2.
31. (a) Ranby, B. G.; Katzmire, J. L., The formation of the native cellulose lattice. *Proc. Cellulose Conf., Ist, Syracuse* **1958**, (Copyright (C) 2011 American Chemical Society (ACS). All Rights Reserved.), 41-59; (b) Ranby, B. G., Fine structure of cellulose fibrils. *Fundamentals Paper-making Fibres, Trans. Symposium Cambridge (Francis Bolam, editor: Brit. Paper and Board Makers' Assoc.)* **1958**, (Copyright (C) 2011 American Chemical Society (ACS). All Rights Reserved.), 55-92.
32. Fengel, D., Ultrastructural Behavior of Cell Wall Polysaccharides. *Tappi* **1970**, *53* (3), 7.
33. Frey-Wyssling, A.; Muehlenthaler, K., The elementary fibrils of cellulose. *Makromol. Chem.* **1963**, *62* (Copyright (C) 2011 American Chemical Society (ACS). All Rights Reserved.), 25-30.
34. (a) Kose, R.; Mitani, I.; Kasai, W.; Kondo, T., "Nanocellulose" As a Single Nanofiber Prepared from Pellicle Secreted by *Gluconacetobacter xylinus* Using Aqueous Counter Collision. *Biomacromolecules* **2011**, *12* (3), 716-720; (b) Jakob, H. F.; Fengel, D.; Tschegg, S. E.; Fratzl, P., The elementary cellulose fibril in *Picea abies*: Comparison of transmission electron microscopy, small-angle X-ray scattering, and wide-angle X-ray scattering results. *Macromolecules* **1995**, *28* (26), 8782-8787; (c) Jakob, H. F.; Fratzl, P.; Tschegg, S. E., SIZE AND ARRANGEMENT OF ELEMENTARY CELLULOSE FIBRILS IN WOOD CELLS - A SMALL-ANGLE X-RAY-SCATTERING STUDY OF PICEA-ABIES. *Journal of Structural Biology* **1994**, *113* (1), 13-22; (d) Heyn, A. N. J., ULTRASTRUCTURE OF WOOD PULP WITH SPECIAL REFERENCE TO ELEMENTARY FIBRIL OF CELLULOSE. *Tappi* **1977**, *60* (11), 159-161; (e) Blackwell, J.; Kolpak, F. J., CELLULOSE MICROFIBRIL AS AN IMPERFECT ARRAY OF ELEMENTARY FIBRILS. *Macromolecules* **1975**, *8* (3), 322-326.
35. Manley, R. S. J., Fine Structure of Native Cellulose Microfibrils. *Nature* **1964**, *204* (4964), 1155-1157.

36. (a) McKeown, J. J.; Lyness, W. I., Evidence for the retention of the crystalline-amorphous ratio of cellulose during heterogeneous acid hydrolysis. *J. Polym. Sci.* **1960**, *47* (Copyright (C) 2011 American Chemical Society (ACS). All Rights Reserved.), 9-17; (b) Gjonnes, J.; Norman, N.; Viervoll, H., State of order in cellulose as revealed from x-ray diffractograms. *Acta Chem. Scand.* **1958**, *12* (Copyright (C) 2011 American Chemical Society (ACS). All Rights Reserved.), 489-94.
37. (a) Lenz, J.; Schurz, J., Fibrillar structure and deformation behavior of regenerated cellulose fibers. I. Methods of investigation and crystallite dimensions. *Cellul. Chem. Technol.* **1990**, *24* (Copyright (C) 2011 American Chemical Society (ACS). All Rights Reserved.), 3-21; (b) Lenz, J.; Schurz, J., Fibrillar structure and deformation behavior of regenerated cellulose fibers. Part II: elementary fibrils and deformation. *Cellul. Chem. Technol.* **1990**, *24* (Copyright (C) 2011 American Chemical Society (ACS). All Rights Reserved.), 679-92.
38. Brown, R. M., Cellulose structure and biosynthesis: What is in store for the 21st century? *Journal of Polymer Science Part A: Polymer Chemistry* **2004**, *42* (3), 487-495.
39. Dong, X. M.; Revol, J.-F.; Gray, D. G., Effect of microcrystallite preparation conditions on the formation of colloid crystals of cellulose. *Cellulose* **1998**, *5* (1), 19-32.
40. Nishikawa, S.; Ono, S., Transmission of X-rays through fibrous, lamellar and granular substances. *Proc. Tokyo Math.-Phys. Soc.* **1913**, *7*, 131-8.
41. (a) Langan, P.; Nishiyama, Y.; Chanzy, H., A Revised Structure and Hydrogen-Bonding System in Cellulose II from a Neutron Fiber Diffraction Analysis. *Journal of the American Chemical Society* **1999**, *121* (43), 9940-9946; (b) Balashov, V.; Preston, R. D., The fine structure of cellulose and other microfibrillar substances. *Nature (London, U. K.)* **1955**, *176* (Copyright (C) 2011 American Chemical Society (ACS). All Rights Reserved.), 64-5.
42. Atalla, R. H.; Vanderhart, D. L., NATIVE CELLULOSE - A COMPOSITE OF 2 DISTINCT CRYSTALLINE FORMS. *Science* **1984**, *223* (4633), 283-285.
43. Sugiyama, J.; Vuong, R.; Chanzy, H., Electron diffraction study on the two crystalline phases occurring in native cellulose from an algal cell wall. *Macromolecules* **1991**, *24* (14), 4168-4175.
44. Vietor, R. J.; Mazeau, K.; Lakin, M.; Perez, S., A priori crystal structure prediction of native

celluloses. *Biopolymers* **2000**, *54* (5), 342-354.

45. Finkenstadt, V. L.; Millane, R. P., Crystal structure of Valonia cellulose I beta. *Macromolecules* **1998**, *31* (22), 7776-7783.

46. Qian, X.; Ding, S.-Y.; Nimlos, M. R.; Johnson, D. K.; Himmel, M. E., Atomic and Electronic Structures of Molecular Crystalline Cellulose I β : A First-Principles Investigation. *Macromolecules* **2005**, *38* (25), 10580-10589.

47. Nishiyama, Y.; Langan, P.; Chanzy, H., Crystal Structure and Hydrogen-Bonding System in Cellulose I β from Synchrotron X-ray and Neutron Fiber Diffraction. *Journal of the American Chemical Society* **2002**, *124* (31), 9074-9082.

48. Gardner, K. H.; Blackwell, J., Structure of native cellulose. *Biopolymers* **1974**, *13* (10), 1975-2001.

49. Maurer, A.; Fengel, D., PARALLEL ORIENTATION OF THE MOLECULAR CHAINS IN CELLULOSE-I AND CELLULOSE-II DERIVING FROM HIGHER-PLANTS. *Holz Als Roh-Und Werkstoff* **1992**, *50* (12), 493-493.

50. (a) Park, S.; Baker, J.; Himmel, M.; Parilla, P.; Johnson, D., Cellulose crystallinity index: measurement techniques and their impact on interpreting cellulase performance. *Biotechnology for Biofuels* **2010**, *3* (1), 10; (b) Kim, U.-J.; Kuga, S.; Wada, M.; Okano, T.; Kondo, T., Periodate Oxidation of Crystalline Cellulose. *Biomacromolecules* **2000**, *1* (3), 488-492.

51. Li, Q.; Renneckar, S., Supramolecular Structure Characterization of Molecularly Thin Cellulose I Nanoparticles. *Biomacromolecules* **2011**, *12* (3), 650-659.

52. Atalla, R. H.; Brady, J. W.; Matthews, J. F.; Ding, S.-Y.; Himmel, M. E., Structures of Plant Cell Wall Celluloses. In *Biomass recalcitrance: deconstructing the plant cell wall for bioenergy*, Himmel, M. E., Ed. Blackwell Pub.: Oxford, 2008; Vol. xviii, 505 p.

53. (a) Rose, J. K. C., *The Plant Cell Wall*. [In: *Annu. Plant Rev.*, 2003; 8]. Blackwell Publishing Ltd.: 2003; p 381 pp; (b) Fengel, D., CHARACTERIZATION OF CELLULOSE BY DECONVOLUTING THE OH VALENCY RANGE IN FTIR SPECTRA. *Holzforschung* **1992**, *46* (4), 283-288.

54. Margaretha Åkerholm, L. S., The Oriented Structure of Lignin and its Viscoelastic Properties Studied by Static and Dynamic FT-IR Spectroscopy. **2003**.

55. (a) Salmen, L.; Olsson, A. M., Interaction Between Hemicelluloses, Lignin and Cellulose: Structure-Property Relationships. **1998**; (b) Terashima, N., Nanostructural assembly of cellulose, hemicellulose, and lignin in the middle layer of secondary wall of ginkgo tracheid. *Journal of Wood Science* **2009**, *55* (6), 409-416.
56. Salmen, L.; Olsson, A. M., Interaction between hemicelluloses, lignin and cellulose: structure-property relationships. *J. Pulp Pap. Sci.* **1998**, *24* (Copyright (C) 2011 American Chemical Society (ACS). All Rights Reserved.), 99-103.
57. Klemm, D.; Kramer, F.; Moritz, S.; Lindström, T.; Ankerfors, M.; Gray, D.; Dorris, A., Nanocelluloses: A New Family of Nature-Based Materials. *Angewandte Chemie International Edition* **2011**, *50* (24), 5438-5466.
58. Dong, S.; Roman, M., Fluorescently Labeled Cellulose Nanocrystals for Bioimaging Applications. *Journal of the American Chemical Society* **2007**, *129* (45), 13810-13811.
59. Nishino, T.; Takano, K.; Nakamae, K., Elastic modulus of the crystalline regions of cellulose polymorphs. *J. Polym. Sci., Part B: Polym. Phys.* **1995**, *33* (Copyright (C) 2012 American Chemical Society (ACS). All Rights Reserved.), 1647-51.
60. (a) Malm, C. J.; Risberg, B.; Bodin, A.; Backdahl, H.; Johansson, B. R.; Gatenholm, P.; Jeppsson, A., Small calibre biosynthetic bacterial cellulose blood vessels: 13-months patency in a sheep model. *Scandinavian Cardiovascular Journal* **2012**, *46* (1), 57-62; (b) Petersen, N.; Gatenholm, P., Bacterial cellulose-based materials and medical devices: current state and perspectives. *Applied Microbiology and Biotechnology* **2011**, *91* (5), 1277-1286.
61. Bulota, M.; Kreitsmann, K.; Hughes, M.; Paltakari, J., Acetylated microfibrillated cellulose as a toughening agent in poly(lactic acid). *Journal of Applied Polymer Science* **2012**, *126*, E448-E457.
62. Aulin, C.; Gallstedt, M.; Lindstrom, T., Oxygen and oil barrier properties of microfibrillated cellulose films and coatings. *Cellulose* **2010**, *17* (3), 559-574.
63. (a) Korhonen, J. T.; Hiekkataipale, P.; Malm, J.; Karppinen, M.; Ikkala, O.; Ras, R. H. A., Inorganic Hollow Nanotube Aerogels by Atomic Layer Deposition onto Native Nanocellulose Templates. *ACS Nano* **2011**, *5* (3), 1967-1974; (b) Evenou, F.; Couderc, S.; Kim, B.; Fujii, T.; Sakai, Y., Microfibrillated Cellulose

Sheets Coating Oxygen-Permeable PDMS Membranes Induce Rat Hepatocytes 3D Aggregation into Stably-Attached 3D Hemispheroids. *J. Biomater. Sci.-Polym. Ed.* **2011**, *22* (11), 1509-1522.

64. Johnson, R. K.; Zink-Sharp, A.; Renneckar, S. H.; Glasser, W. G., A new bio-based nanocomposite: fibrillated TEMPO-oxidized celluloses in hydroxypropylcellulose matrix. *Cellulose (Dordrecht, Netherlands)* **2009**, *16* (2), 227-238.

65. Svagan, A. J.; Samir, M.; Berglund, L. A., Biomimetic polysaccharide nanocomposites of high cellulose content and high toughness. *Biomacromolecules* **2007**, *8* (8), 2556-2563.

66. Siqueira, G.; Bras, J.; Dufresne, A., Cellulose Whiskers versus Microfibrils: Influence of the Nature of the Nanoparticle and its Surface Functionalization on the Thermal and Mechanical Properties of Nanocomposites. *Biomacromolecules* **2009**, *10* (2), 425-432.

67. Ma, H.; Zhou, B.; Li, H. S.; Li, Y. Q.; Ou, S. Y., Green composite films composed of nanocrystalline cellulose and a cellulose matrix regenerated from functionalized ionic liquid solution. *Carbohydrate Polymers* **2011**, *84* (1), 383-389.

68. Jackson, J. K.; Letchford, K.; Wasserman, B. Z.; Ye, L.; Hamad, W. Y.; Burt, H. M., The use of nanocrystalline cellulose for the binding and controlled release of drugs. *Int. J. Nanomed.* **2011**, *6*, 321-330.

69. (a) Maneerung, T.; Tokura, S.; Rujiravanit, R., Impregnation of silver nanoparticles into bacterial cellulose for antimicrobial wound dressing. *Carbohydrate Polymers* **2008**, *72* (1), 43-51; (b) Czaja, W.; Krystynowicz, A.; Bielecki, S.; Brown, R. M., Microbial cellulose - the natural power to heal wounds. *Biomaterials* **2006**, *27* (2), 145-151.

70. Evans, B. R.; O'Neill, H. M.; Malyvanh, V. P.; Lee, I.; Woodward, J., Palladium-bacterial cellulose membranes for fuel cells. *Biosens. Bioelectron.* **2003**, *18* (7), 917-923.

71. Hentze, H.-P. In *From Nanocellulose Science towards Applications*, Technical Research Center of Finland, Helsinki, June 2, 2010; Technical Research Center of Finland, Helsinki, 2010.

72. Spence, K. L.; Venditti, R. A.; Rojas, O. J.; Habibi, Y.; Pawlak, J. J., A comparative study of energy consumption and physical properties of microfibrillated cellulose produced by different processing methods. *Cellulose* **2011**, *18* (4), 1097-1111.

73. Wuhrmann, K.; Heuberger, A.; Muhlethaler, K., Electron-microscopic investigations of cellulose

fibers after supersonic treatment. *Experientia* **1946**, *2* (Copyright (C) 2012 American Chemical Society (ACS). All Rights Reserved.), 105-7.

74. Yoshioka, M.; Sakaguchi, K.; Ohno, T.; Nishio, Y.; Shiraishi, N., Fabrication of pulverized celluloses by ultra high-pressure water jet treatment and usage in polymer nanocomposites and graft copolymerization. *Journal of Wood Science* **2009**, *55* (5), 335-343.

75. (a) Bondeson, D.; Mathew, A.; Oksman, K., Optimization of the isolation of nanocrystals from microcrystalline cellulose by acid hydrolysis. *Cellulose* **2006**, *13* (2), 171-180; (b) Jiang, F.; Esker, A. R.; Roman, M., Acid-Catalyzed and Solvolytic Desulfation of H₂SO₄-Hydrolyzed Cellulose Nanocrystals. *Langmuir : the ACS journal of surfaces and colloids* **2010**, *26* (23), 17919-17925.

76. Revol, J. F.; Bradford, H.; Giasson, J.; Marchessault, R. H.; Gray, D. G., Helicoidal self-ordering of cellulose microfibrils in aqueous suspension. *International Journal of Biological Macromolecules* **1992**, *14* (3), 170-172.

77. Saito, T.; Nishiyama, Y.; Putaux, J. L.; Vignon, M.; Isogai, A., Homogeneous suspensions of individualized microfibrils from TEMPO-catalyzed oxidation of native cellulose. *Biomacromolecules* **2006**, *7* (6), 1687-1691.

78. Pääkkö, M.; Ankerfors, M.; Kosonen, H.; Nykänen, A.; Ahola, S.; Österberg, M.; Ruokolainen, J.; Laine, J.; Larsson, P. T.; Ikkala, O.; Lindström, T., Enzymatic Hydrolysis Combined with Mechanical Shearing and High-Pressure Homogenization for Nanoscale Cellulose Fibrils and Strong Gels. *Biomacromolecules* **2007**, *8* (6), 1934-1941.

79. Denooy, A. E. J.; Besemer, A. C.; Vanbekkum, H., SELECTIVE OXIDATION OF PRIMARY ALCOHOLS MEDIATED BY NITROXYL RADICAL IN AQUEOUS-SOLUTION - KINETICS AND MECHANISM. *Tetrahedron* **1995**, *51* (29), 8023-8032.

80. Eyholzer, C.; Bordeanu, N.; Lopez-Suevos, F.; Rentsch, D.; Zimmermann, T.; Oksman, K., Preparation and characterization of water-redispersible nanofibrillated cellulose in powder form. *Cellulose* **2010**, *17* (1), 19-30.

81. Wagberg, L.; Winter, L.; Odberg, L.; Lindstrom, T., ON THE CHARGE STOICHIOMETRY UPON ADSORPTION OF A CATIONIC POLYELECTROLYTE ON CELLULOSIC MATERIALS. *Colloids and*

Surfaces **1987**, 27 (1-3), 163-173.

82. Li, Q.; Rennekar, S., Molecularly thin nanoparticles from cellulose: isolation of sub-microfibrillar structures. *Cellulose (Dordrecht, Netherlands)* **2009**, 16 (6), 1025-1032.

83. Isogai, A.; Saito, T.; Fukuzumi, H., TEMPO-oxidized cellulose nanofibers. *Nanoscale* **2011**, 3 (1), 71-85.

84. Rodriguez, K.; Sundberg, J. F.; Rennekar, S.; Gatenholm, P., Design of microporous electrospun cellulose scaffolds for bone tissue engineering. *Abstr. Pap. Am. Chem. Soc.* **2011**, 241.

85. (a) Mihranyan, A.; Esmaeili, M.; Razaq, A.; Alexeichik, D.; Lindstrom, T., Influence of the nanocellulose raw material characteristics on the electrochemical and mechanical properties of conductive paper electrodes. *J. Mater. Sci.* **2012**, 47 (10), 4463-4472; (b) Razaq, A.; Nystrom, G.; Stromme, M.; Mihranyan, A.; Nyholm, L., High-Capacity Conductive Nanocellulose Paper Sheets for Electrochemically Controlled Extraction of DNA Oligomers. *Plos One* **2011**, 6 (12).

86. Mishra, S. P.; Manent, A. S.; Chabot, B.; Daneault, C., PRODUCTION OF NANOCELLULOSE FROM NATIVE CELLULOSE - VARIOUS OPTIONS UTILIZING ULTRASOUND. *BioResources* **2012**, 7 (1), 422-436.

87. Yang, J.; Ye, D. Y., Liquid crystal of nanocellulose whiskers' grafted with acrylamide. *Chinese Chemical Letters* **2012**, 23 (3), 367-370.

88. (a) Chun, S. J.; Lee, S. Y.; Jeong, G. Y.; Kim, J. H., Fabrication of hydrophobic self-assembled monolayers (SAM) on the surface of ultra-strength nanocellulose films. *Journal of Industrial and Engineering Chemistry* **2012**, 18 (3), 1122-1127; (b) Blaker, J. J.; Lee, K. Y.; Menner, A.; Bismarck, A., Renewable (greener) nanocomposite polymer foams synthesised from Pickering emulsion templates: using nanocellulose as a building tool. *Abstr. Pap. Am. Chem. Soc.* **2009**, 237.

89. Auad, M. L.; Contos, V. S.; Nutt, S.; Aranguren, M. I.; Marcovich, N. E., Characterization of nanocellulose-reinforced shape memory polyurethanes. *Polym. Int.* **2008**, 57 (4), 651-659.

CHAPTER 3

Molecularly Thin Nanoparticles from Cellulose: Isolation of Sub-microfibrillar Structures*

Abstract

We have succeeded in isolating nanostructures from never-dried cellulose wood pulp, in sheet-form that have sub-microfibril dimensions (single to double digit Å times 100's of nanometers in length). A recently developed oxidation procedure by Saito and co-workers (*Biomacromolecules* 2006, 7:1687-1691) combined with extensive ultrasonication was used to liberate nanoscale cellulose fibrils. We show structures, as determined with atomic force microscopy, that make up the well-known cellulose microfibril, which are 10 fold thinner than previous reports on nanoscale celluloses. This work provides indirect evidence in support of, and is consistent with, the hypothesis that the intersheet *van der Waals* bonding of the cellulose fibril is significantly weaker than the intrasheet *hydrogen* bonding of the cellulose microfibril. The structures are facile to isolate, contain enormous specific surface area with rich chemical functionality providing potential for numerous novel applications.

Key words: atomic force microscopy, microfibril, nanocellulose, cellulose nanocrystal, microfibrillated cellulose

*This chapter was reprinted with permission from Li, Q.; Renneckar, S., Molecularly thin nanoparticles from cellulose: isolation of sub-microfibrillar structures. *Cellulose (Dordrecht, Netherlands)* **2009**, 16 (6), 1025-1032. Copyright (2009) Springer.

1. Introduction

Cellulose is a water insoluble polysaccharide consisting of (1,4)-linked glucose units¹. In all native celluloses, the molecules are found in fibril form, with the microfibril highlighted as a primary constituent of the supramolecular structure. Within the microfibrils, the cellulose chains are organized as stacked sheets separated into molecular layers that have interchain hydrogen bonds connecting neighboring chains together in the X-Y direction². These positions of atoms of the unit cell of cellulose were determined using a combination of synchrotron X-ray and neutron diffraction³. Furthermore, computational studies⁴ have provided justification of the molecular spacing of the unit cell with dimensions of a 7.784 Å, b 8.201 Å, c 10.380 Å^{3a}, and give insight into the bonding differences within the cellulose superstructure; intersheet bonding is approximately 8 times weaker than in-plane intra-sheet bonding⁴.

A variety of experimental techniques have been used to characterize the size of the supramolecular structure of cellulose from a number of plant sources⁵. Based on plant source, there is variability amongst the dimension of microfibrils in their native state and after processing into pulp (Table 3.1.). A recent study investigated the cellulose structure within the developing maize primary plant cell wall with AFM, revealing microfibril dimensions that have a rectangular cross section of 3 x 5 nm⁶. Based on the cellulose synthase spatial pattern in the cell wall and the size of the cellulose microfibrils, a 36 chain sub-microfibril model was developed where the microfibril is a polygon with maximum width related to a ribbon of 6 adjacent chains and the depth proposed to be a stack of 8 layers⁶.

Another approach for understanding the microfibrillar structure is to isolate the cellulose microfibrils after chemical degradation. Cellulose microfibril fragments isolated after acid hydrolysis of plant cell walls have similar dimension in cross section to reported values, measured with either TEM or AFM, providing a thickness in the 4 to 5 nm range⁷. The length of the microfibrils of acid hydrolyzed fibrils have been related to the less ordered regions of cellulose; average lengths of ramie-based acid hydrolyzed fibrils match the periodic order seen in the meridional Bragg reflections as determined with small angle neutron scattering⁸. Saito and co-workers reported a facile isolation method for cellulose fibrils involving TEMPO mediated oxidation⁹ to achieve microfibrils 3-5 nm in cross section and lengths of microns. This material resembled microfibrillated cellulose, nanocellulose, isolated using either enzymatic or chemical modification followed by homogenization¹⁰. During the TEMPO oxidation process, primary hydroxyls were selectively oxidized to carboxylic salts¹¹ providing anionic functionality to the surface of the microfibrils. This technique follows a very similar method reported 50 years ago in

the investigation of cellulose microfibril structure. Ramie fibers were oxidized with hypobromite and then agitated with a Warring blender for 2 to 5 minutes to reveal cellulose fibrils 15 nm in width ¹².

Table 3.1. Dimensions of cellulose microfibrils from various sources

Cellulose sources	Dimensions	Determination methods
Ramie ¹	Cross section 7x3nm	XRD, SEM
Spruce wood ²	3.0nm	SEM
Spruce wood ³	2.3--2.7nm	TEM, WAXS, SAXS
Flax fiber ⁴	2.8--3.2nm	SAXS
Pulp fiber ⁵	4.5-- 4.8nm	CP/MAS ¹³ C-NMR

¹Frey-Wyssling (1954)

²Fengel (1970)

³Jakob et al. (1995)

⁴Mueller et al. (1998)

⁵Duchesne et al. (2001)

In this current communication we report on the dimensions of isolated oxidized cellulose microfibrils based on the hypothesis that ultrasonication can be used to decrease nanocellulose size as a function of time. This work was inspired by previous studies that reported sonication can be used to isolate fine fibril structures as a function of intensity ¹⁷. In the study, we have found the unexpected result that ultrasonication of oxidized cellulose can liberate mono- and bi- layer sheets of cellulose, based on size, that make up the recalcitrant cellulose microfibril, providing a method to prepare molecularly thin cellulose nanostructures.

2. Materials and methods

2.1. Materials

Never-dried kraft pulp, 88 brightness level, from the southeast United States was kindly provided by Weyerhaeuser Company. Sodium hypochlorite (NaClO), sodium bromide (NaBr), and 2,2,6,6-tetramethyl-1-piperidinyloxy (TEMPO), were obtained from Sigma Aldrich. Ultrapure water was used in the experiments with a resistivity of 18 m⁻¹cm and < 5 ppb (Millipore Direct Q3UV).

2.2. Methods

Oxidation Procedure

Pulp fibers, as received, were oxidized following previously reported techniques¹⁸ with the key parameter controlling oxidation of NaClO of 5 mmol/g of fiber. The oxidation experiments were performed in duplicate and the final acid content of the fiber, determined using conductometric titration was 1.12 mmol per gram of fiber.

Ultrasonication

Pulp fiber, 0.012 g (moisture content 75%, dry mass 0.003 g), suspended in 300 ml ultrapure water 10⁻³% (w/w) was placed in a temperature controlled bath at 4 °C. A 19mm diameter medium intensity horn was used to sonicate the solution at 20 kHz (VC700 Sonics and Materials) for intervals (30, 60, 120, and 240 min). After sonication, the clear solutions were centrifuged on a desktop centrifuge at 12,000 g for 15 min and the supernatant was decanted and stored in closed vials until further use. Previously it was shown that ultrasonication would yield as much as 98% nanocellulose after 20 minutes of sonication (Johnson et al. 2009), converting the bulk of the sample into nanoscale cellulose.

Atomic Force Microscopy

Dilute suspensions of cellulose 10⁻³ % (w/w) were spin-coated onto freshly cleaved mica. No pretreatment of mica was used after observation of nanocellulose on treated cleaved mica with a positively charged polymer, polyallylamine hydrochloride-- the pretreated surface contained similar images of nanocellulose to what is shown without pretreatment, but fibril overlap prevented statistical measurements of length. Samples were imaged on an Asylum Research MFP-3D AFM, using intermittent contact mode with silicon tips of two dimensions, nominal 10 nm radius, cantilever spring constant 42 N/m and 5 nm super sharp tips, cantilever spring constant 42 N/m. Typically, 10 high pixel resolution images, 5 by 5 μm scan size, were collected with 10 to 50 fibrils found per image. Digitally zoomed cellulose fibrils were then analyzed using IGOR pro software to measure height and length of the fibrils, averaging three thickness measurements for each cellulose particle. Because of tip broadening effects, width measurements contain convoluted data related to the tip width¹⁹ and are on average were found to be 10x greater than what is determined for TEM images (Johnson et al. 2009) and subsequently are not reported within the results. The number of fibrils measured per treatment was 200, providing a total of 800 measurements across all the treatments.

3. Results

Never-dried bleached kraft pulp fibers were selectively oxidized using TEMPO mediated oxidation of the accessible C6 groups^{9a} providing an acid content of 1.12 mmol/g. The clear supernatant of sonicated and centrifuged pulp fiber was deposited, via spin-coating, upon freshly cleaved mica surfaces (Figure 3.1). Dilution of the samples ($10^{-3}\%$ (w/w)) was required to achieve spatial spread of the fibrils in order to trace the end of the fibrils for length measurements. While great efforts were used to minimize noise in the system, it is clear the combination of the instrument parameters, sample dimension and type, and substrate approached the limits of the system. The number of samples imaged provides for random noise within the image to be averaged out.

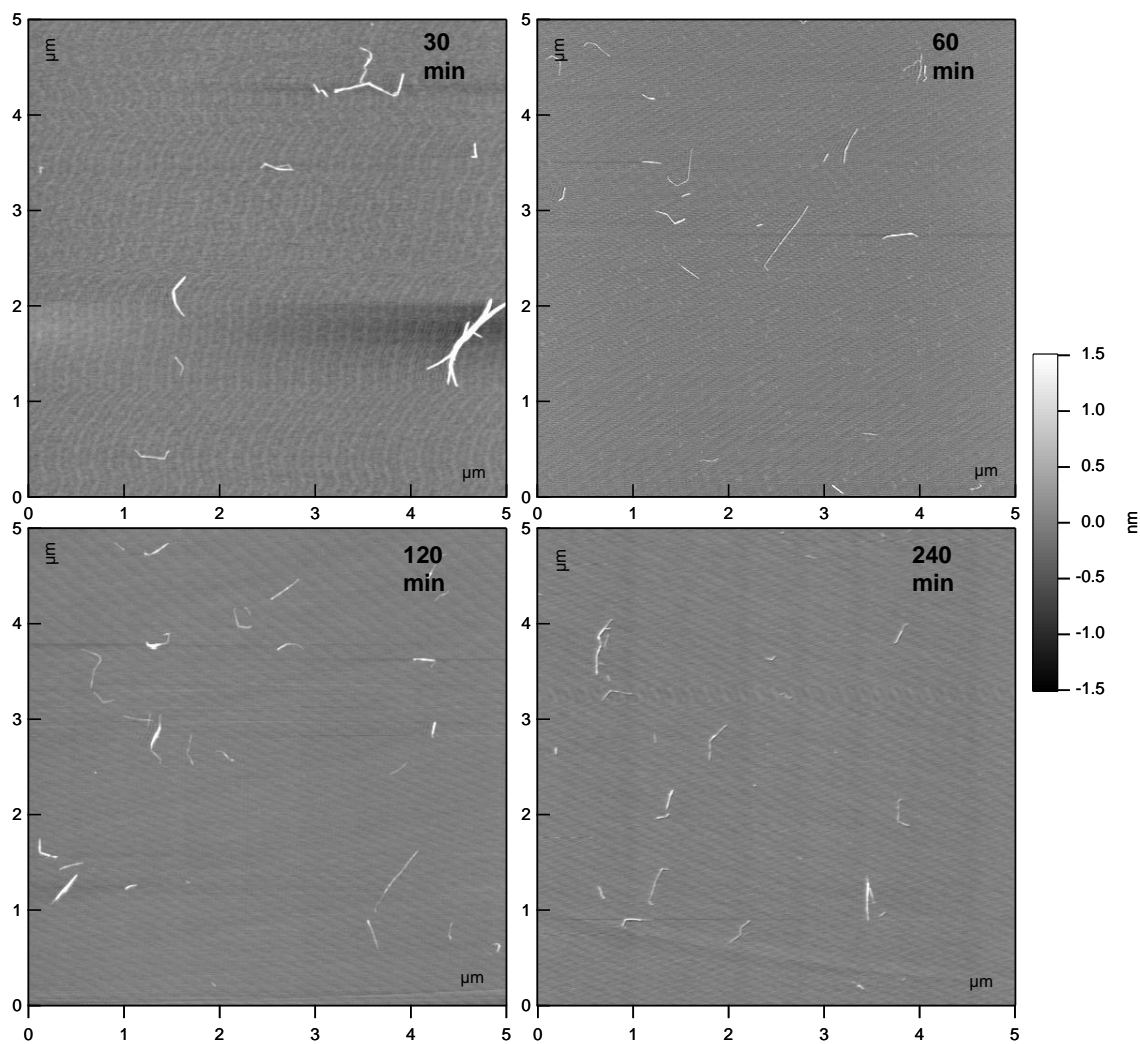


Figure 3.1. Typical AFM height images of nanocellulose on mica surface as a function of sonication time.

Thickness values changed as a function of sonication time for the oxidized nanoscale cellulose (Figure 3.2). For thickness measurements, 1% of the 800 total measurements are greater than the reported microfibril dimension of 3.11 nm⁶ that contain 8 sheets, 3.89 Å thickness per sheet^{3a}. These larger values between 3.11 and 3.9 nm occurred after sonication for the 30 min and 1 hr sonication times. For the lower limit of fibril size, accounting for the surface roughness of the mica (± 0.2 nm), there are no measurements outside the single layer of cellulose fibrils. Moreover, for the 30 min and 1 hr ultrasonication times, the mean is centered at a four sheet (1.4 nm) and three sheet depth (1.1 nm), respectively (Table 3.1.). Both 2 and 4 hr sonication times have two thirds of the fibrils under the two sheet depth (0.778nm), with means centered at (0.8 nm and 0.7 nm respectively). From inspection of Figure 3.2a, it is clear that there is a continuous range in size, instead of clusters around discrete sheet thicknesses. This continuous range is conjectured to be an artifact because the molecularly thin size of cellulose sheets is on the same order of roughness as the mica. When the thickness is greater than 2 nm (roughness of the mica is 10% of the value), there begins to be some differentiation between sheet sizes (Figure 3.2a). Detailed tests for statistical significance is available in appendix 1.

Length distributions changed as a function of sonication time, with the average fibril length declining from 580 nm to 260 nm for the 30 min and 4 hr samples, respectively (Figure 3.3). This data shows that there are micron sized fibrils present at low sonication times, confirming TEM observations based on blended oxidized cellulose^{9b}, and that these ribbons have minimum lengths similar to the lengths of cellulose nanocrystals derived from acid hydrolysis^{7a}. Evident in the histogram is how the overall distribution narrows for the extended sonication times (Figure 3.3a). Furthermore, the aspect ratios for the fibrils across sonication times remain at values above 500 (Table 3.2.).

Table 3.2. Statistical values for length, thickness, and aspect ratios of nanocellulose as a function of sonication time.

Sonication time (min)	Length (nm)		Thickness (nm)		Aspect ratio	
	mean	st. dev.	mean	st. dev.	mean	st. dev.
30	580	330	1.38	0.71	530	420
60	400	230	1.08	0.72	500	420
120	330	210	0.81	0.61	580	440
240	260	160	0.74	0.43	450	340

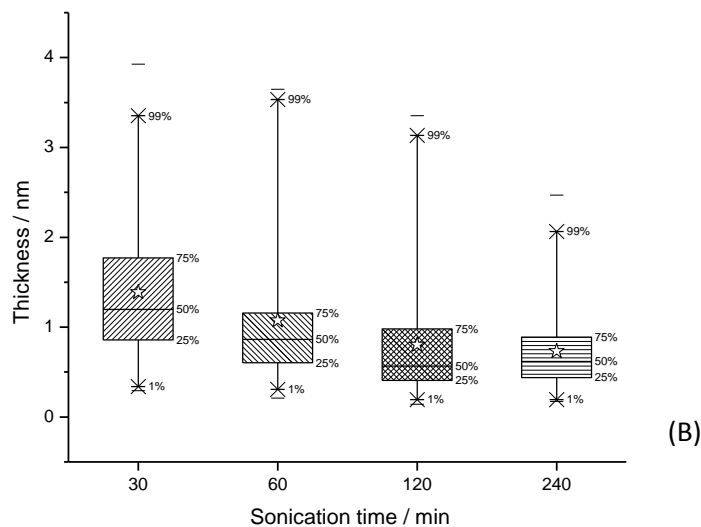
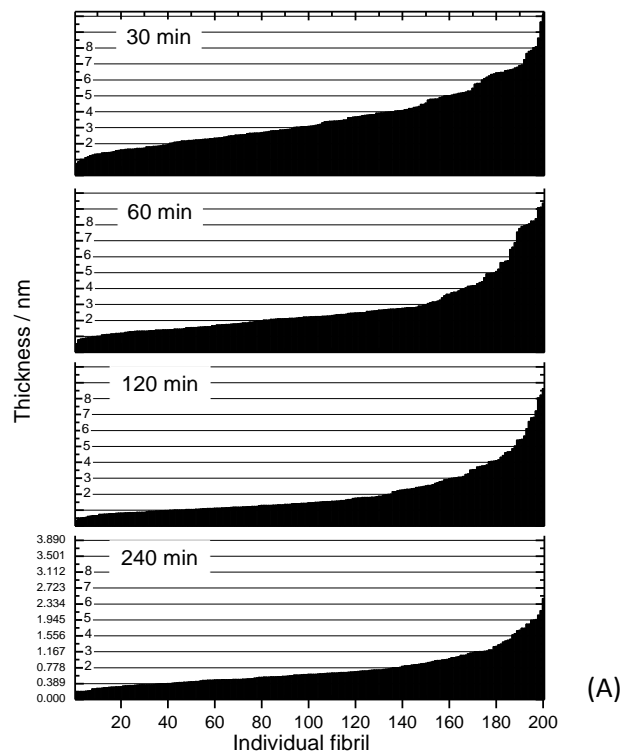


Figure 3.2. Measurements related to nanocellulose thickness. A) Thickness measurements arranged in ascending order for fibrils (each Y-value value corresponds to the average of three measurements on a single fibril). All Y-Axis values are plotted with the same scale and the number of layers related to proposed sub-microfibril sheets (2-8) is shown on inside of vertical axis. B) Box plot indicating the distribution of measurement values, line in center indicates median, while star in center indicates average.

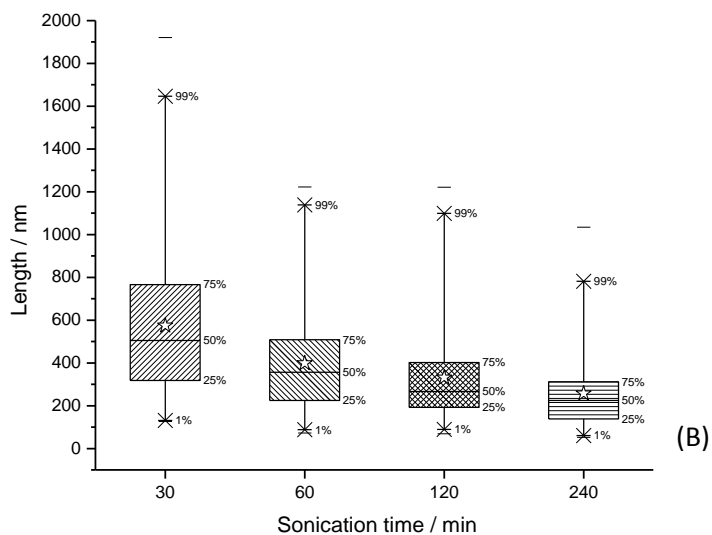
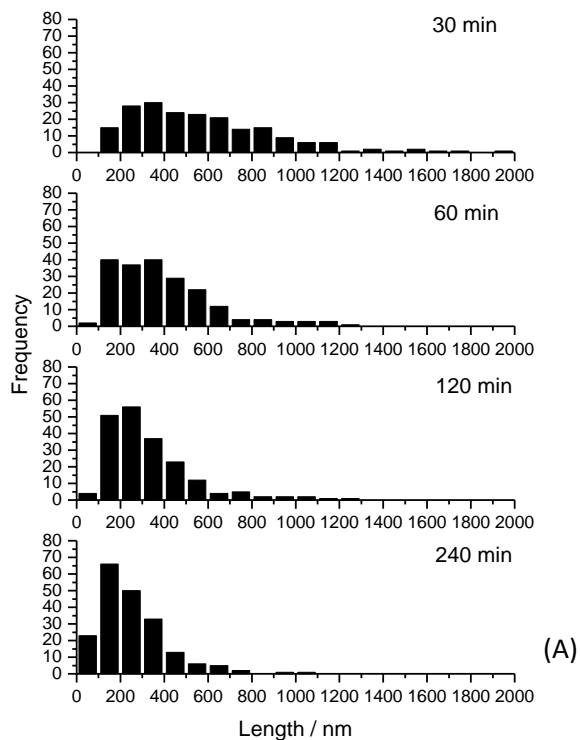


Figure 3.3. Measurements related to nanocellulose length. A) A histogram plot showing the frequency of measurement for each size. B) Box plot indicating the distribution of measurement values, line in center indicates median, while star in center indicates average.

4. Discussion

The mechanism for particle break-down during sonication involves cavitation and particle collisions. Sonication has been reported to cause defects within carbon nanotubes resulting in reduced length upon prolonged exposure²⁰. Defects within carbon nanoparticles were reported to be more sensitive to the ultrasonic cavitation providing justification for a weak-link hypothesis to the breakage of nanostructured materials. Investigation into the behavior of nickel catalyst microparticles during sonication found that the ultrasonic field gives rise to turbulent flow, providing interparticle collision at high velocities²¹. Furthermore it is known that at solid liquid surfaces, impinging microjets created during sonication results in erosions of surfaces²². Metal surfaces are most sensitive to erosion at the grain boundaries, giving rise to fragmentation and slippage (plastic deformation), between the grains²³. Cellulose intersheet spacing may be analogous to the grain boundaries in metals. In the present work, it is feasible that removal of surface layers is facilitated by the ultrasonic field. While a small fraction of the cellulose fibrils have a typical length of acid hydrolysis isolated cellulose particle, the mean length is twice the size, with only one quarter of the fibril thickness when compared to acid hydrolyzed cellulose. Hence, the weak links sensitive to acid hydrolysis of amorphous cellulose are not necessarily the weak links found for these cellulose ribbons. Differences must be contributed to variegations in mechanism between chemical attack and mechanical disruption. This fact may be related to how strain is dissipated from the fibril when exposed to the effects of microjet impingement and interparticle shear.

Cellulose microfibrils are connected through acetal linkages and intrachain hydrogen bonds between anhydroglucose units, hydrogen bonds between chains within a sheet, and weaker hydrogen and van der Waals bonds between sheets. Oxidation of the cellulose fibers by using the TEMPO-mediated procedure, reportedly converts every other hydroxyl on the surface of sub-microfibril to either a carboxylate salt or aldehyde^{11b}. The reason provided for the liberation (unwinding) of charged microfibrils from the fiber structure is based on like-charges repelling each other^{9a}, that overcome the myriad of hydrogen bonds holding the fibrils together (Figure 3.4a). Splitting of the fibril into sub-microfibril ribbons may also be facilitated by neighboring repulsive forces overcoming the van der Waals and weak hydrogen bonds. As seen in Figure 3.4b, partial sub-microfibrils are liberated from the microfibril, but presumably are still attached at one end. In other words, enough strain has moved the sheets out of their short ranged van der Waals bonds and weak hydrogen bonds (C-H***O)², but whole sections of the sub-microfibrils have not been dislocated. Interestingly, no correlation is found between the fibril length and thickness data based

on measurements upon the same fibril; i.e. the fibril does not need to break to smaller sizes before a fibril sheet is liberated. This fact provides insight that intersheet disruption could occur prior to intrachain destruction. However, it remains unclear why the minimum in fibril length approaches a prototypical level-off degree of polymerization (DP). As there is no folding in cellulose chains, the length measurements observed provides the range between the possible maximum intact chain length, DP of 4000 (or the maximum DP of cellulose derived from an industrial pulping process), and a minimum chain length DP, between 160 and 200, for each repeat unit having a length of 0.5nm (Nishiyama et al. 2003a). Likely, radicals generated during the ultrasonication process²² may lead to depolymerization of the cellulose (breakage of glycosidic bonds). However, the limit of attack is related to the small fraction that have approximately 200 anhydroglucose units, when at most, there is only inter-hydrogen bonding occurring between chains within a mono- or bi- layer sheet. Further investigation into this topic of the tenacity of intersheet bonding would need to involve statistical counting of width measurements using TEM.

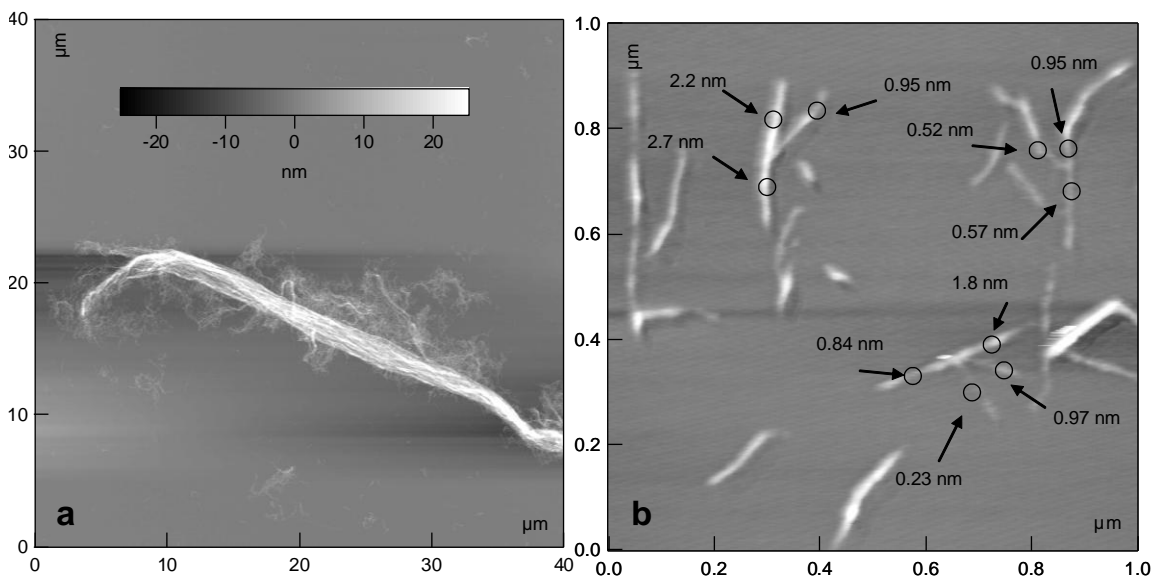


Figure 3.4. a) AFM height image of non-centrifuged and mechanically blended particle with microfibrils unwinding, and b) digitally zoomed AFM height image of sonicated sub-microfibrils shearing.

In the current study, the sonication time did not change width values, as measured by AFM, with the sonication treatment providing an average width of 40 nm for both 30 min and 4 hr. This data is known to be erroneous because of tip broadening and force delocalization effects^{19b}. In a previous study using TEM, Johnson and co-workers revealed TEMPO oxidized nanocellulose, sonicated for 20 min, had dimensions of 3-5 nm¹⁸. This measurement would correspond to 5 cellulose chains aligned side by side.

Future studies involving TEM measurements of longer sonication times will illuminate the influence of interchain hydrogen bonding on the recalcitrant nature of native cellulose. Finally, implicit within this work are questions that surround the nature of disordered regions of cellulose microfibrils as that we have observed that mono-molecular sheets remain, some with lengths over 900 nm, after sonication.

5. Conclusions

Atomic force microscopy was used to reveal that sonicating TEMPO mediated oxidized pulp will fibrillate fibers into sub-microfibril structures. As sonication time increased both fibril average length and thickness decreased. Our results provide insight into the molecular structure of native celluloses derived from woody plants, with a maximum thickness related to the proposed microfibril dimensions of primary cell wall of plants, and minimum thickness related to the molecularly thin single sheets of cellulose fibrils derived from X-ray diffraction data. This report provides evidence of a new molecularly thin nanoparticle.

Appendix

Appendix 1. Tests of statistical significance for AFM thickness distributions

One way ANOVA tests for logarithm transformed AFM thickness distributions indicate that only the difference between 120 min and 240 min levels is not significant, whereas the difference between all other levels are significant.

ANOVAOneWay (7/6/2010 14:12:11)

Notes

Input Data

Descriptive Statistics

	Sample Size	Mean	Standard Deviation	SE of Mean
LnT30m	200	0.19795	0.51833	0.03665
LnT60m	200	-0.09885	0.5612	0.03968
LnT120m	200	-0.43704	0.63578	0.04496
LnT240m	200	-0.46142	0.54012	0.03819

One Way ANOVA

Overall ANOVA

	DF	Sum of Squares	Mean Square	F Value	Prob>F
Model	3	58.6249	19.54163	61.08899	0
Error	796	254.63086	0.31989		
Total	799	313.25576			

Null Hypothesis: The means of all levels are equal.
 Alternative Hypothesis: The means of one or more levels are different.
 At the 0.05 level, the population means are significantly different.

Fit Statistics

	R-Square	Coeff Var	Root MSE	Data Mean
	0.18715	-2.83018	0.56559	-0.19984

Means Comparison

Tukey Te

		MeanDiff	SEM	q Value	Prob	Alpha	Sig	LCL	UCL
LnT60	LnT30	-0.29679	0.05656	7.42114	1.18079E-6	0.05	1	-0.4424	-0.15119
LnT120	LnT30	-0.63499	0.05656	15.87757	0	0.05	1	-0.7806	-0.48938
LnT120	LnT60	-0.3382	0.05656	8.45643	1.83099E-8	0.05	1	-0.48381	-0.19259
LnT240	LnT30	-0.65937	0.05656	16.48707	0	0.05	1	-0.80498	-0.51376
LnT240	LnT60	-0.36257	0.05656	9.06592	0	0.05	1	-0.50818	-0.21697
LnT240	LnT120	-0.02438	0.05656	0.60949	0.97315	0.05	0	-0.16998	0.12123

Sig equals 1 indicates that the means difference is significant at the 0.05 level.
 Sig equals 0 indicates that the means difference is not significant at the 0.05 level.

References

1. Klemm, D.; Heublein, B.; Fink, H.-P.; Bohn, A., Cellulose: Fascinating biopolymer and sustainable raw material. *Angew. Chem. Int. Edit.* **2005**, *44* (22), 3358-3393.
2. Nishiyama, Y.; Johnson, G. P.; French, A. D.; Forsyth, V. T.; Langan, P., Neutron Crystallography, Molecular Dynamics, and Quantum Mechanics Studies of the Nature of Hydrogen Bonding in Cellulose I β . *Biomacromolecules* **2008**, *9* (11), 3133-3140.
3. (a) Nishiyama, Y.; Langan, P.; Chanzy, H., Crystal structure and hydrogen-bonding system in cellulose I β from synchrotron x-ray and neutron fiber diffraction. *J. Am. Chem. Soc.* **2002**, *124* (31), 9074-9082; (b) Nishiyama, Y.; Sugiyama, J.; Chanzy, H.; Langan, P., Crystal Structure and Hydrogen Bonding System in Cellulose I α from Synchrotron X-ray and Neutron Fiber Diffraction. *J. Am. Chem. Soc.* **2003**, *125* (47), 14300-14306.
4. Qian, X. H.; Ding, S. Y.; Nimlos, M. R.; Johnson, D. K.; Himmel, M. E., Atomic and electronic structures of molecular crystalline cellulose I beta: A first-principles investigation. *Macromolecules* **2005**, *38* (25), 10580-10589.
5. Frey-Wyssling, A., The fine structure of cellulose microfibrils. *Science (Washington, DC, United States)* **1954**, *119*, 80-2.
6. Ding, S. Y.; Himmel, M. E., The maize primary cell wall microfibril: A new model derived from direct visualization. *J. Agr. Food Chem.* **2006**, *54* (3), 597-606.
7. (a) Beck-Candanedo, S.; Roman, M.; Gray, D. G., Effect of Reaction Conditions on the Properties and Behavior of Wood Cellulose Nanocrystal Suspensions. *Biomacromolecules* **2005**, *6* (2), 1048-1054; (b) Elazzouzi-Hafraoui, S.; Nishiyama, Y.; Putaux, J.-L.; Heux, L.; Dubreuil, F.; Rochas, C., The Shape and Size Distribution of Crystalline Nanoparticles Prepared by Acid Hydrolysis of Native Cellulose. *Biomacromolecules* **2008**, *9* (1), 57-65.
8. Nishiyama, Y.; Kim, U. J.; Kim, D. Y.; Katsumata, K. S.; May, R. P.; Langan, P., Periodic disorder along ramie cellulose microfibrils. *Biomacromolecules* **2003**, *4* (4), 1013-1017.
9. (a) Saito, T.; Kimura, S.; Nishiyama, Y.; Isogai, A., Cellulose Nanofibers Prepared by TEMPO-Mediated Oxidation of Native Cellulose. *Biomacromolecules* **2007**, *8* (8), 2485-2491; (b) Saito, T.; Nishiyama, Y.; Putaux, J.-L.; Vignon, M.; Isogai, A., Homogeneous Suspensions of Individualized Microfibrils from TEMPO-Catalyzed Oxidation of Native Cellulose. *Biomacromolecules* **2006**, *7* (6), 1687-1691.
10. (a) Wagberg, L.; Decher, G.; Norgren, M.; Lindstrom, T.; Ankerfors, M.; Axnas, K., The build-up of polyelectrolyte multilayers of microfibrillated cellulose and cationic polyelectrolytes. *Langmuir* **2008**, *24* (3), 784-795; (b) Paakko, M.; Ankerfors, M.; Kosonen, H.; Nykanen, A.; Ahola, S.; Osterberg, M.; Ruokolainen, J.; Laine, J.; Larsson, P. T.; Ikkala, O.; Lindstrom, T., Enzymatic hydrolysis combined with mechanical shearing and high-pressure homogenization for nanoscale cellulose fibrils and strong gels. *Biomacromolecules* *FIELD Full Journal Title: Biomacromolecules* **2007**, *8* (6), 1934-41.
11. (a) Saito, T.; Isogai, A., TEMPO-Mediated Oxidation of Native Cellulose. The Effect of Oxidation Conditions on Chemical and Crystal Structures of the Water-Insoluble Fractions. *Biomacromolecules* **2004**, *5* (5), 1983-1989; (b)

- Saito, T.; Shibata, I.; Isogai, A.; Suguri, N.; Sumikawa, N., Distribution of carboxylate groups introduced into cotton linters by the TEMPO-mediated oxidation. *Carbohydrate Polymers* **2005**, *61* (4), 414-419.
12. Patel, G. M., Optical investigations on oxycelluloses. *Makromolekulare Chemie* **1951**, *7*, 12-45.
 13. Fengel, D., Ultrastructural behavior of cell wall polysaccharides. *Tappi* **1970**, *53* (3), 497-503.
 14. Jakob, H. F.; Fengel, D.; Tschegg, S. E.; Fratzl, P., The Elementary Cellulose Fibril in Picea abies: Comparison of Transmission Electron Microscopy, Small-Angle X-ray Scattering, and Wide-Angle X-ray Scattering Results. *Macromolecules* **1995**, *28* (26), 8782-7.
 15. Mueller, M.; Czihak, C.; Vogl, G.; Fratzl, P.; Schober, H.; Riekkel, C., Direct Observation of Microfibril Arrangement in a Single Native Cellulose Fiber by Microbeam Small-Angle X-ray Scattering. *Macromolecules* **1998**, *31* (12), 3953-3957.
 16. Duchesne, I.; Hult, E.-L.; Molin, U.; Daniel, G.; Iversen, T.; Lennholm, H., The influence of hemicellulose on fibril aggregation of kraft pulp fibres as revealed by FE-SEM and CP/MAS ¹³C-NMR. *Cellulose (Dordrecht, Netherlands)* **2001**, *8* (2), 103-111.
 17. Wuhmann, K.; Heuberger, A.; Muhlethaler, K., Electron-microscopic investigations of cellulose fibers after supersonic treatment. *Experientia* **1946**, *2*, 105-7.
 18. Johnson, R.; Zink-Sharp, A.; Rennecker, S.; Glasser, W. G., A new bio-based nanocomposite: Fibrillated TEMPO-oxidized celluloses in hydroxypropylcellulose matrix. *Cellulose* **In press**.
 19. (a) VanCleaf, M.; Holt, S. A.; Watson, G. S.; Myhra, S., Polystyrene spheres on mica substrates: AFM calibration, tip parameters and scan artefacts. *J. Microsc.-Oxf.* **1996**, *181*, 2-9; (b) Wang, Y.; Chen, X. Y., Carbon nanotubes: A promising standard for quantitative evaluation of AFM tip apex geometry. *Ultramicroscopy* **2007**, *107* (4-5), 293-298.
 20. Lu, K. L.; Lago, R. M.; Chen, Y. K.; Green, M. L. H.; Harris, P. J. F.; Tsang, S. C., Mechanical damage of carbon nanotubes by ultrasound. *Carbon* **1996**, *34* (6), 814-816.
 21. Doktycz, S. J.; Suslick, K. S., Interparticle collisions driven by ultrasound. *Science* **1990**, *247* (4946), 1067-1069.
 22. Suslick, K. S., Sonochemistry. *Science* **1990**, *247* (4949), 1439-1445.
 23. Rao, B. C. S.; Buckley, D. H., Deformation and erosion of FCC metals and alloys under cavitation attack. *Materials Science and Engineering* **1984**, *67* (1), 55-67.

CHAPTER 4

Supramolecular Structure Characterization of Molecularly Thin Cellulose I Nanoparticles*

Abstract

Unusual fractions of cellulose microfibrils from woody material with dimensions of 100's of nanometers in length and single digit angstrom thickness were obtained by intensive sonication of TEMPO oxidized cellulose fibers. These cellulose microfibril fragments, composed of many mono- and bilayer molecular sheets, were analyzed with scattering and spectroscopy techniques to understand the structural changes at the supramolecular level. XRD data indicated that sonication breaks the cellulose microfibrils along its (200) planes, yet some form of the $I\beta$ crystalline structure is still retained with reduced crystallinity. The Raman and FTIR analysis indicated structural changes to the cellulose microfibrils do not occur until after sonication; furthermore, AFM observation indicates that the structural changes began to occur within 5 min of sonication. An altered supramolecular structure is evident after sonication: major features from cellulose I are preserved, although certain spectral features similar to mercerized and ball milled cellulose appeared in its FTIR and Raman spectra. These spectral differences are traced to changes in the methine environment, hydroxymethyl conformations, and skeletal vibrations. By integrating the present findings and previous research, a cellulose molecular sheet delamination scheme is proposed to describe this microfibril fragmentation along its 200 plane.

Keywords: microfibrils, nanocellulose, Raman spectroscopy, surface chains

*This chapter was reprinted with permission from Li, Q.; Rennekar, S., Supramolecular Structure Characterization of Molecularly Thin Cellulose I Nanoparticles. *Biomacromolecules* **2011**, *12* (3), 650-659. Copyright (2011) American Chemical Society.

1. Introduction

Cellulose is the main polymeric component in the majority of organisms occurring as the dominant structural polymer in all species within the kingdom *planta*.¹ To be the most ubiquitous structural polymer to support life, it must have intrinsic performance properties during exposure of the organism to a range of environmental factors. Performance is aided by the arrangement of the nascent cellulose macromolecules into supramolecular structures during cell wall formation.² These cellulose microfibril structural units within the plant cell wall are usually analogized to reinforcing elements within a fiber composite^{2b}, a high modulus component of stiffness value around 138 GPa³. The mechanical performance of cellulose microfibrils is traced to its extensive intra- and inter- chain hydrogen bonding network^{2a}.

Cellulose microfibrils, dependent upon the isolation method, have dimensions similar to that of carbon nanotubes; single digit nanometer in cross section dimension and 100's to 1000's of nanometers in length. Because of the combined performance and size attributes, isolating nanoscale celluloses have attracted considerable scientific attention in the past decade for materials research in clear films, foams, and additives for nanocomposites^{1b, c, 3-4}. Almost all isolation procedures for nanoscale cellulose can be traced back to methods in understanding cellulose supramolecular structures involving acid hydrolysis⁵, homogenization and sonication⁶, or oxidation with mechanical treatment⁷. Recent studies have shown that grinding freshly prepared pulp⁸ or homogenizing enzymatically treated pulp⁹ can also facilitate isolation of nanoscale cellulose, originating from initial studies by Turbak^{6b}. Different isolation procedures are used to either chemically degrade the accessible surfaces amongst adjacent microfibrils by controlled exposure to mineral acids (acid hydrolysis) or mechanically disrupt the hydrogen bonding on the surface of the microfibrils by a combination of impact and frictional shear forces (fibrillation). For the latter case, oxidation or enzymatic treatment on the material remediates or prevents inter-microfibril aggregation and crystallization⁹⁻¹⁰. The end product contains the highly ordered structure of native cellulose with a monoclinic or triclinic unit cell, dependent upon starting materials¹¹.

The size of the isolated microfibrils was reported to be equivalent to crystallite size determined from peak broadening in WAXS¹²; however microfibril fractions with angstrom thickness were recently reported in the literature¹³, Figure 4.1. Cellulose structures were

identified that had a thickness corresponding to half the size of the “a” axis of the cellulose $I\beta$ unit cell. The study suggested that, remarkably, the microfibril structure is capable of delaminating, breaking the intersheet bonds, while maintaining interchain hydrogen bonds within a sheet¹³.

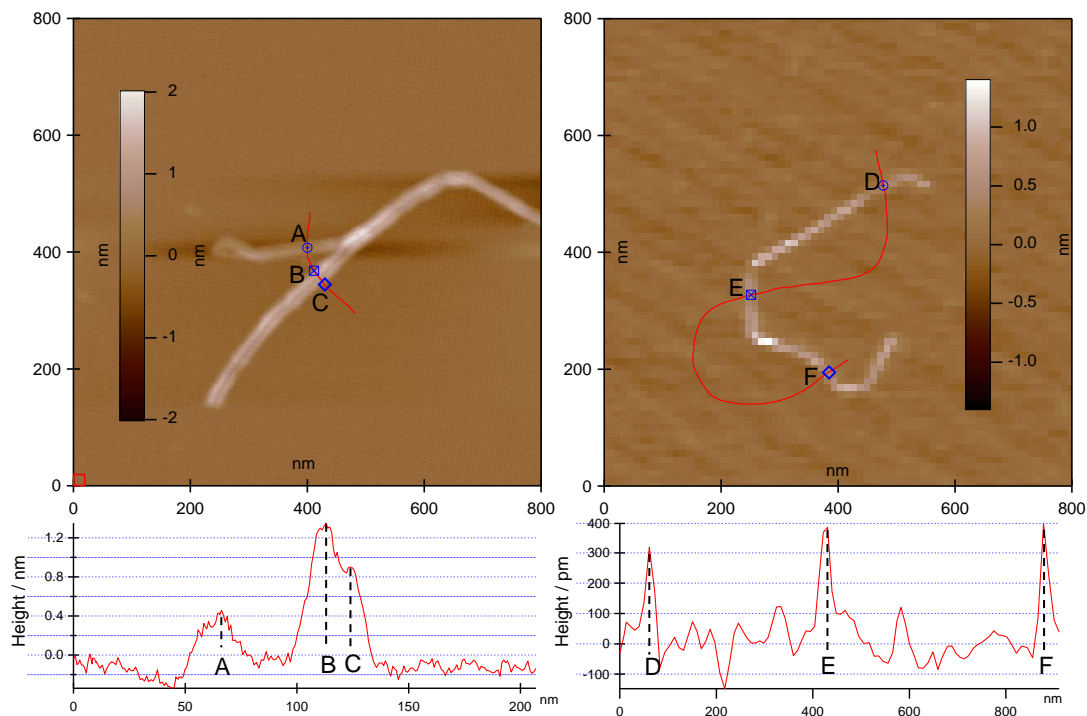


Figure 4.1. AFM height images of cellulose microfibril with height profiles below. Points A, D, E and F are related to cellulose mono-layer sheet thickness, whereas point B is related to a three-layer sheet thickness, point C is related to a bi-layer sheet thickness.

This hypothesis was suggested based on the native microfibril structure. Within the microfibril all the hydroxyl (OH) groups are equatorial, with the methine (CH) groups oriented to the ring axially; arrangement of these groups results in the appearance of hydrophilic site parallel to the ring plane and the hydrophobic site perpendicular to the ring^{2a, 14} (Figure 4.2). These factors in the context of a cellulose crystalline structure determine how the OH--O hydrogen bonding dominates the cellulose intrasheet interactions (referring to both intra- and interchain bonding) within the unit cell; and that weaker CH--O hydrogen bonding and van der Waals interactions are responsible for the intersheet bonding¹⁵. Moreover, the spacing within the intersheet layer was shown to be sensitive to both moisture and temperature, as the (200) plane shifts as a function of these variables¹⁶.

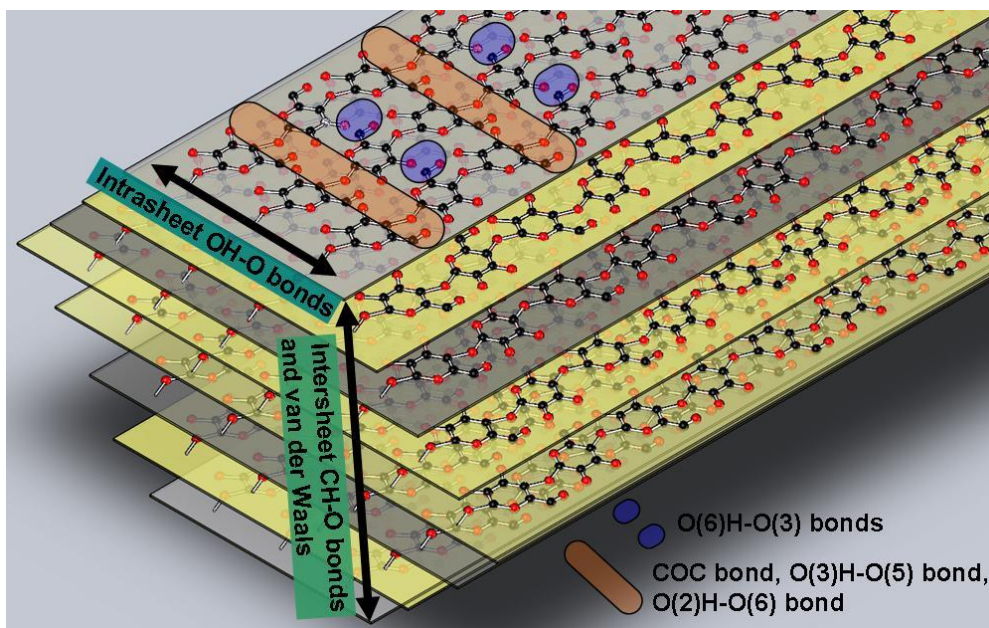


Figure 4.2. Schematic drawing of hydrogen bonding directions and the layered structure in cellulose $I\beta$, diffraction planes (200) are highlighted.

In this presented work, the unique cellulose sub-microfibrillar structures, generated after oxidation and sonication, are investigated by scattering and spectroscopy techniques to identify the global changes. The results have important implications in 1) furthering the understanding of the fine structure of cellulose microfibrils and the supramolecular changes during the isolation process, and 2) providing a facile approach to prepare cellulose nanoparticles with dramatically increased surface area and profoundly extended application potentials. Fragmenting the tenacious cellulose fibril and identifying the resulting spectroscopic changes provide a unique insight into the destruction of the crystalline structure.

2. Materials and methods

Materials. Never-dried kraft pulp (88% brightness with a degree of polymerization ranging from 1,600-1,694, as indicated by supplier), from the southeast United States, was kindly provided by Weyerhaeuser Company. Sodium hypochlorite (NaClO), sodium bromide (NaBr), and 2,2,6,6-Tetramethylpiperidine-1-oxyl (TEMPO), were obtained from Sigma Aldrich. Ultrapure water was used in the experiments with conductivity of 0.30 $\mu\text{s}/\text{cm}$ and <5 ppb (Millipore Direct-Q 3UV).

TEMPO-mediated Oxidation. Kraft pulp fibers, as received, were oxidized following previously reported techniques^{4a} with the key parameter controlling oxidation of NaClO of 5 mmol/g of fiber. The oxidation experiments were performed in duplication and the final acid content of the fiber, determined using conductometric titration method was 1.12 mmol/g of fiber. Details about the conductometric titration method was described elsewhere¹⁷.

Ultrasonication. The isolated nanocellulose fibrils were obtained by sonicating the oxidized pulp fibers at different time intervals, in aqueous condition, with a temperature controlled bath at 4 °C. The nanocellulose fibrils for yield calculation and AFM imaging were prepared at concentration $5 \times 10^{-3}\%$ (w/w), sonicated for 5 time levels (5, 30, 60, 120, 240min). For XRD, Raman and FTIR analysis, nanocellulose fibrils were prepared at higher concentration of 0.2% (w/w), due to the relative large quantity needed for sample preparation, sonicated for 3 time levels (30, 60, 120min). A 19 mm diameter medium intensity horn was used to sonicate the fibril suspension at 20 kHz (VC700, Sonics & Materials). The sonicated suspension was centrifuged at 4500 rcf for 15min and the decanted transparent supernatant was lyophilized and stored in a desiccator for future characterizations. The samples are noted as wood pulp (WP); TEMPO-mediated oxidized wood pulp (WT); and TEMPO-mediated oxidized wood pulp that underwent sonication treatment for 30min (WTS30), 60min (WTS60), and 120min (WTS120).

Yield calculation. The yields of the nanocellulose fibrils from the sonication treatment were calculated by taking the weight ratio of the lyophilized supernatant portion and the initial (before sonication) dry fibers, for 5 sonication time intervals (5, 30, 60, 120, 240min), according to equation (1).

$$Yield = \frac{\text{lyophilized weight}}{\text{initial dry fiber weight}} \times 100\% \quad (1)$$

AFM. Dilute nanocellulose suspension $5 \times 10^{-3}\%$ (w/w) was sonicated for 5 min, centrifuged at 4500 rcf for 15min, and then the transparent supernatant was spin-coated onto freshly cleaved mica to examine the nanocellulose. Images were obtained using an Asylum Research MFP-3D AFM, in intermittent contact mode, with Olympus AC 240 tips. AFM images were processed in IGOR pro software.

XRD. XRD measurements were performed using a Bruker D8 Discover XRD system, CuK α ($\lambda=0.154\text{nm}$) radiation operating at 40 kV/ 40 mA. The diffraction profile was detected using a locked couple 2 theta scan from 10-40°. XRD samples were prepared by flattening the lyophilized samples into pellet form between two glass slides. Peak fitting process of the diffraction profile for the Scherrer Equation calculation was done in Origin Pro 8.1 SR3 version, using Lorentz distribution with major diffraction peak positions fixed.

The crystallinity index was calculated with equation (2), according to the conventional peak intensity method, details are described elsewhere,¹⁸

$$I_{CR} = \frac{I_{200} - I_{AM}}{I_{200}} \quad (2)$$

where I_{CR} is crystallinity index, I_{200} is the peak intensity at plane (200) in the XRD profile, I_{AM} is the minimum intensity at the valley between plane (200) and (110).

Lateral dimensions of the crystalline portions were evaluated according to the Scherrer Equation below,

$$D_{hkl} = \frac{0.9\lambda}{\beta_{1/2} \cos \theta} \quad (3)$$

where D_{hkl} is the dimension of the crystal perpendicular to the diffracting planes with hkl Miller indices, θ is the diffraction angle, λ is the wavelength of the X-ray radiation, $\beta_{1/2}$ is the full width at half maximum (FWHM) of the diffraction peaks.

FTIR. FTIR spectra were obtained from a Thermo Nicolet 8700 spectrometer. Cellulose microfibril samples were analyzed as KBr pellets (3:200, w/w). The spectra were obtained within a dry-air purged environment, at resolution of 1 cm^{-1} , averaging 128 scans, over the region of 4000-500 cm^{-1} . Apodization was applied to the higher range of the spectra (3700-2700 cm^{-1}) to deconvolute the broad OH peak centered at 3400 cm^{-1} and CH₂ peak centered at 2900 cm^{-1} , with Happ-Genzel function applied (key parameters: bandwidth 30 cm^{-1} , enhancement 2.0) in OMNIC soft v7.3.

Raman. Raman spectra of samples were obtained from a Bruker Senterra spectrometer. Laser light was excited from a Neon emission lamp at $\lambda=785$ nm with an output power of 100 mW. The charge-coupled device (CCD) detector was thermoelectrically cooled down to -64 °C before each scan started. The spectra were recorded from 3400-50 cm^{-1} , with a resolution of 2 cm^{-1} . Because Raman spectroscopy does not require very sophisticated sample preparation, the cellulose pellet samples from XRD experiments were used for the subsequent Raman scans. The 100x objectives lens was applied to focus near the surface of the sample mats. The scans were conducted with integration time of 100 s and co-additions number of 2, without shape correction and automatic fluorescent rejection (each scan took ca. 7min). Each spectrum is obtained by averaging 3 individual scans of different areas within the same sample.

3. Results

3.1. Yield

The yields of cellulose nanofibrils from different sonication time intervals are shown under Supporting Information in SI Figure 4.1. Sonication starts to produce nanofibrils as soon as 5 min (12 wt%); as sonication time extended, the yield increases and finally reaches 87 wt% at 240 min. This result indicates a proportional relationship between the nanofibril yield and the sonication time, or the total energy input. It is important to note that the yield is also related to the input power density, which involves cellulose suspension concentration, sonicator tip size, output power, as well as the constrained volume (container size). The importance of these variables is illustrated by the fact of an earlier study that showed higher yields at lower sonication times when the power input density was greater^{4a}. Whereas in this current study the relationship between sonication time and yield are discussed with all other factors related to input power density fixed.

3.2. AFM

The effects of short time (5 min) intensive sonication on cellulose disintegration with AFM were contrasted with the long time (30--240 min) sonication results from previous study¹³. The results indicate that cellulose microfibrils start to disintegrate as soon as 5 min sonication (Figure 4.3 left) and many fibrils with thickness around 1 nm are observed. Less

than 2% portion of the fibrils had a thickness related to mono- or bi-layer cellulose sheets (~0.4 to 0.8 nm, Figure 4.3 right). This observation is not surprising, considering the yield for 5 min sonication is only 12%. At longer sonication times, 75% of the material sampled had a thickness of less than 1 nm¹³, which would be proportionally representative of the population based on the total yield.

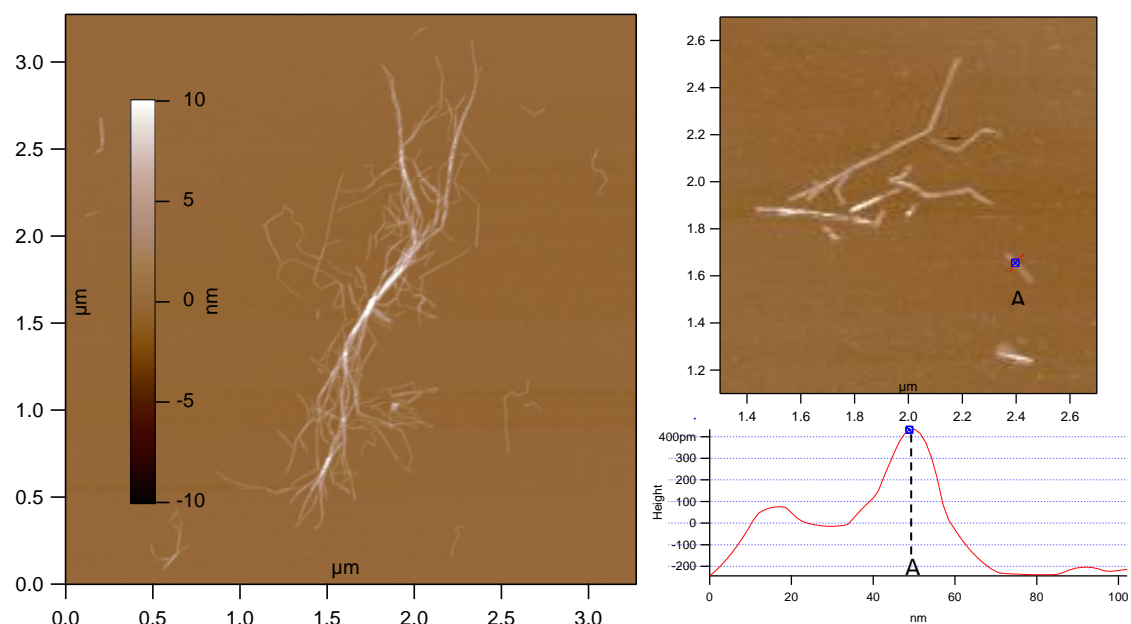


Figure 4.3. Left: AFM height image shows one large cellulose bundle being disintegrated into individual nanofibrils upon 5 min sonication. Right: 5 min sonication sample, only fractional portion of the nanofibrils shows thickness related to cellulose mono- or bi-layer, as indicated in the height profile, units of picometers.

3.3. XRD

XRD diffractogram of all cellulose samples is shown in Figure 4.4 and calculated crystallinity index displayed in Table 4.1. Both the WP and WT samples have similar diffraction profiles. The crystallinity index of WP is 73.5%, highest among all levels. The WT has a very similar crystallinity index compared with wood pulp of 72.0%, which agreed with the previous observation that the TEMPO-mediated oxidation process does not change the cellulose crystallinity¹⁹. The WTS samples have broadened diffraction peaks at corresponding diffraction planes, indicating that certain portion of the microfibril fragments still show supramolecular ordering upon sonication and lyophilizing. The three sonication

treatment levels reduced the cellulose crystallinity to 54.5% for WTS30, 52.4% for WTS60, and 52.0% for WTS120, respectively. Prolonged sonication time did not have a significant effect on further reducing the crystallinity. These observations suggest that overall sonication does not change the unit cell crystal structure of the remaining population of diffracting crystals; however, the broadening of the peaks indicates that the crystal size distribution is affected by sonication. Also, the minor peak shifts at (200) plane towards the lower degree are observed, this may due to the increasing of amorphous peak around 19° and affected the major diffraction peak at (200).

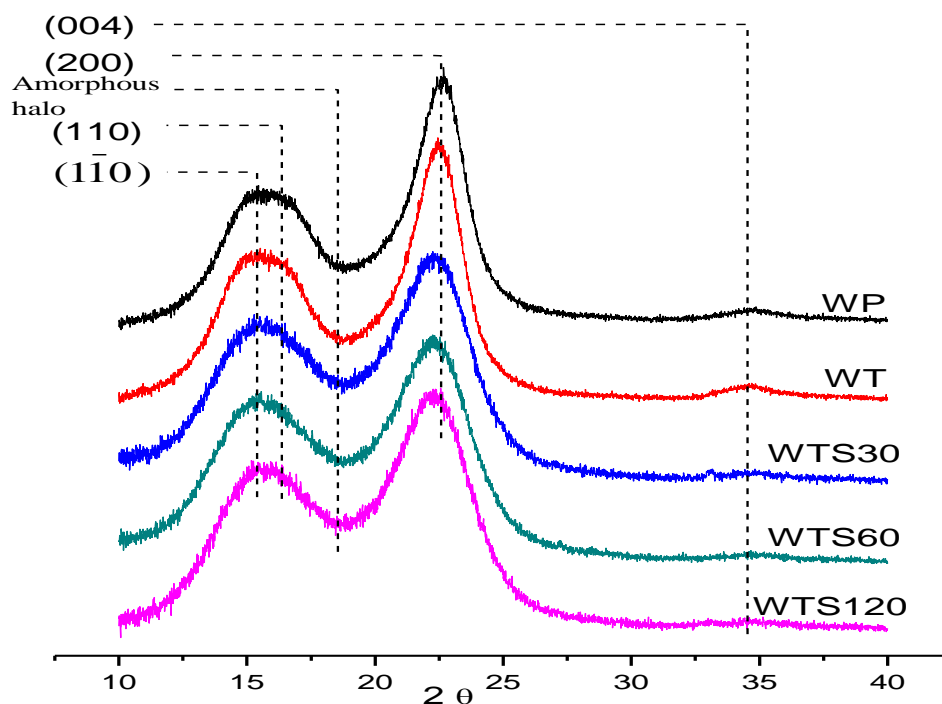


Figure 4.4. XRD diffractogram of cellulose samples with reflection planes labeled. WP-- wood pulp; WT-- TEMPO-mediated oxidized cellulose; WTS30, 60, 120-- oxidized cellulose sonication for 30 min, 60 min, and 120 min respectively.

Normally for materials such as ceramics and metals, the average crystal size can be readily quantified by the Scherrer equation^{12, 20}. While there is precedent in describing the cellulose crystallite size using this methodology, issues surround the subjective determination of curve fitting ranges as well as the size and placement of the “amorphous-halo” of the cellulose; this halo dramatically impacts the curve fitted peak parameters. With the caveat for possible artifacts, the average thicknesses of cellulose crystalline regions were calculated

according to Scherrer equation (Table 4.1.). In cellulose $I\beta$, diffraction from plane (200) is related to the thickness of the molecular sheets in the stacking direction (a-axis of the $I\beta$ unit cell). From Table 4.1., significant drops of this thickness were observed for WTS. This reduction in thickness provides direct evidence that sonication has disrupted the microfibril along the (200) plane. Not surprisingly, the majority of the fibrils that were analyzed with AFM did have thickness values¹³ smaller than the Scherrer equation derived value.

Table 4.1. Crystallinity index and crystalline region thickness evaluated by XRD diffraction peaks on plane (200) according to Scherrer equation.

Treatment levels	Crystallinity index (%)	Thickness by plane (200) (nm)
WP	73.5	4.05
WT	72.0	4.25
WTS30	54.5	2.73
WTS60	52.4	2.66
WTS120	52.0	2.79

3.4. Raman Spectroscopy

Raman spectra, known to be sensitive for detecting polymorphic changes of the cellulose samples²¹, are shown under Supporting Information in SI Figure 4.2, with particular regions highlighted in Figures 4.5-4.7. All the major Raman bands observed in the spectra are listed under Supporting Information in Table 4.S-1, with vibrational modes assigned based on past literature.²² The spectra of the samples can be grouped into two categories: with wood pulp (WP) and oxidized pulp (WT) showing similarities, while differences noted for the spectra of the three sonicated oxidized wood pulp samples (WTS30, WTS60, WTS120). This distinction indicates that sonication exerts more influence on the Raman spectra than the oxidization process, also agreeing with the XRD data. Additionally, the similarities between

the WP and WT indicate that a significant portion of the cellulose chains remained unmodified by the oxidation process.

CH₂ and CH related changes, OH related changes

Figure 4.5 displays Raman peaks that are related to possible CH--O hydrogen bonding (i.e. CH₂ and CH groups), underlined by “ ”, and the Raman peaks that related to OH--O hydrogen bonding (OH groups), underlined by “ ”, as assigned in references from Supporting Information in Table 4.S-1.²² Peaks at 1289, 990, and 961 cm⁻¹ are related to the molecular environment of CH₂ and CH, and their relative intensities all reduce with extended sonication time. This result suggests coherent evidence that CH and CH₂, groups involved in CH--O intersheet hydrogen bonding, were significantly affected by sonication (Figure 4.5, Figure 4.7a).

Peaks at 1241, 1057, and 1036 cm⁻¹ are related to OH--O hydrogen bonding. The bands at 1057 and 1036 cm⁻¹ are broadened while their relative intensities only show minimal change. For the peak at 1241 cm⁻¹ and its vicinity region 1180-1270 cm⁻¹ both relative intensity and peak shape are dramatically changed after sonication (Figure 4.5). This region is assigned to a number of delocalized modes involving skeletal stretching, methine bending²³ and C-OH out of plane deformation²⁴. Given that the methine axial orientation and the OH equatorial orientation¹⁴, the increase in intensity around the band at 1241 cm⁻¹ provides evidence that sonication significantly impacts intersheet interactions.

At 1458 cm⁻¹, a new peak is evident for the WTS groups, which is assigned to bending deformations from CH₂, and primary OH at C6. It is interesting to note that other methods that disrupt the native crystal structure, like ball milling and mercerization, cause similar changes at the 1458 peak cm⁻¹.²⁵

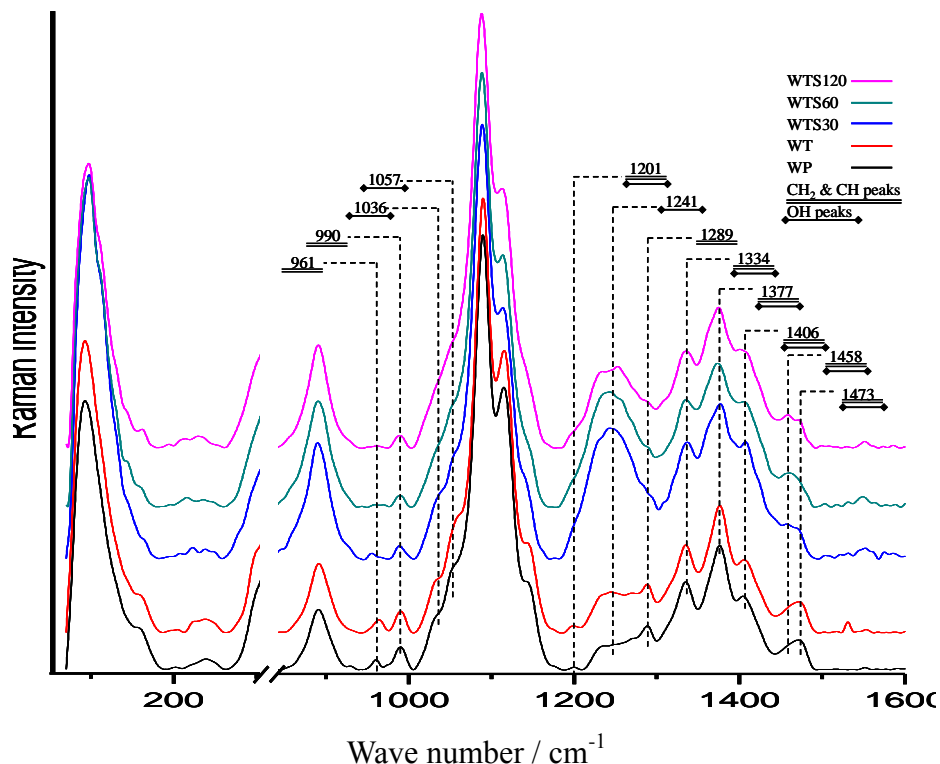


Figure 4.5. Raman spectra for CH₂ and CH related peaks (underlined by —) and OH related peaks (underlined by ◀—▶).

COC related changes, ring breathing and deformation related changes

Figure 4.6 displays all the Raman peaks related to COC glycosidic linkage deformations, underlined by “—”, and to ring deformations, underlined by “◀—▶”.

Peaks 560, 510 and 491 cm⁻¹ are related to the C-O-C glycosidic linkage deformation and delocalized skeletal deformations. A general trend observed is that sonication reduces the peak intensities, especially at peak 510 cm⁻¹, and this reduction is proportional to the sonication time (except for peak 491 cm⁻¹). The observation agrees with previous AFM results¹³ that sonication reduces the cellulose chain length by breaking the C-O-C glycosidic linkage. At peak 560 cm⁻¹, the intensity reduction is also accompanied with peak broadening and shifts towards the higher wavenumber.

Peaks 1145, 450, 428, 370, 344 and 322 cm⁻¹ are related to different combination modes of the ring deformations (CCC, CCO, CC, CO symmetric or asymmetric deformation, ring

breathing). From overlaid images (Figure 4.7b and 4.7c), it can be seen that after sonication, the intensity is reduced; significant drops occurred at band ca. 370 and 428 cm^{-1} . Previously, it was noted that the ca. 380 cm^{-1} band (which relates to the 370 cm^{-1} band in our spectra) is sensitive to the state of cellulose crystallinity²⁶.

Also observed are peak shifts at bands 450, 370 and 322 cm^{-1} . All the shifts are towards the lower wavenumber and the shifts increase with the extended sonication time-- WPS120 has the greatest shift among all levels. The peaks at 1115 and 1090 cm^{-1} are combination vibration modes from C-O-C glycosidic linkage deformation, and ring breathing and stretching. Peak intensities at 1115 cm^{-1} decrease as sonication increases, and both 1115 and 1090 cm^{-1} peaks show a peak shift towards lower wavenumbers upon sonication (Supporting Information in Table 4.S-1, Figure 4.7d). Kong and co-workers²⁷, have related Raman peak shifts at ca. 1090 cm^{-1} to the deformation of C-O-C glycosidic carbon backbone, arising from an increased bond distance as the cellulose is strained. Qualitatively, the Raman shift is proportional to the sonication time, indicating that the packing of the cellulose chains is altered with sonication.

Peak 891 cm^{-1} variations

The sonication treatment significantly increased the intensity at peak 891 cm^{-1} (Figure 4.6), which is assigned to the methine group at C1.²⁸ Also, it was suggested that the intensity of this peak is proportional to the amount of disorder in cellulose C6 positions and OH groups.²⁹ Either disorder of C6 groups or changes to the methine environment would be impacted by the fragmentation of the microfibril. This significant change in intensity supports the hypothesis that sonication had liberated sheets from microfibrils. It should be noted that the intensity difference between WP and WT is minimal, indicating that this 891 cm^{-1} peak may not be sensitive to C6 on the surface chains, as those are the only ones oxidized by the TEMPO treatment.

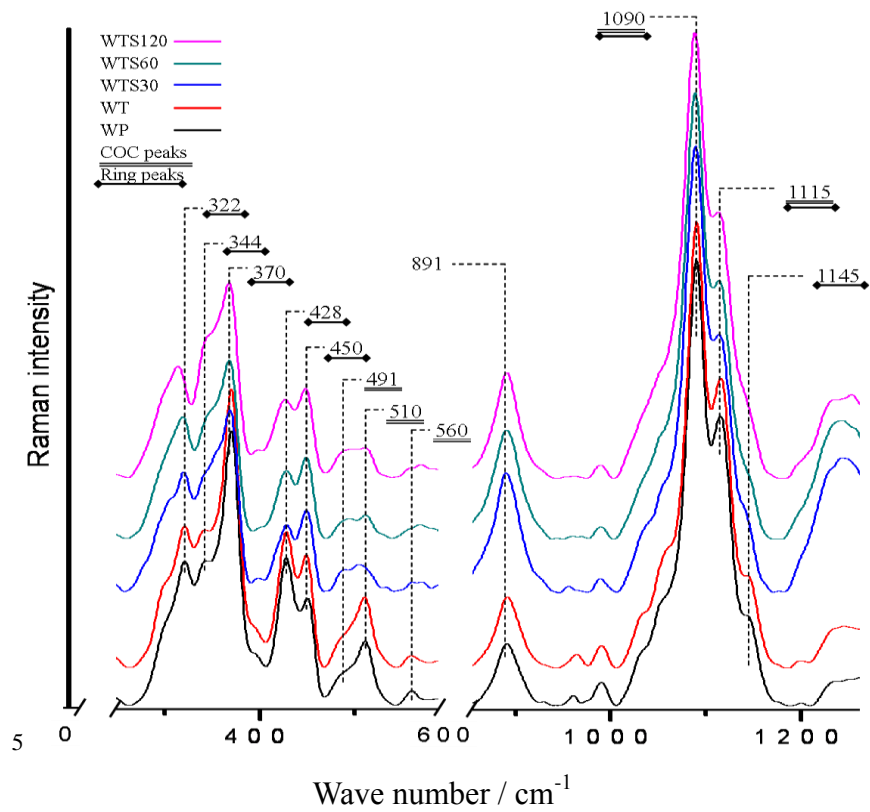


Figure 4.6. Raman spectra for COC deformation related peaks (underlined by —) and ring deformation related peaks (underlined by ↔)

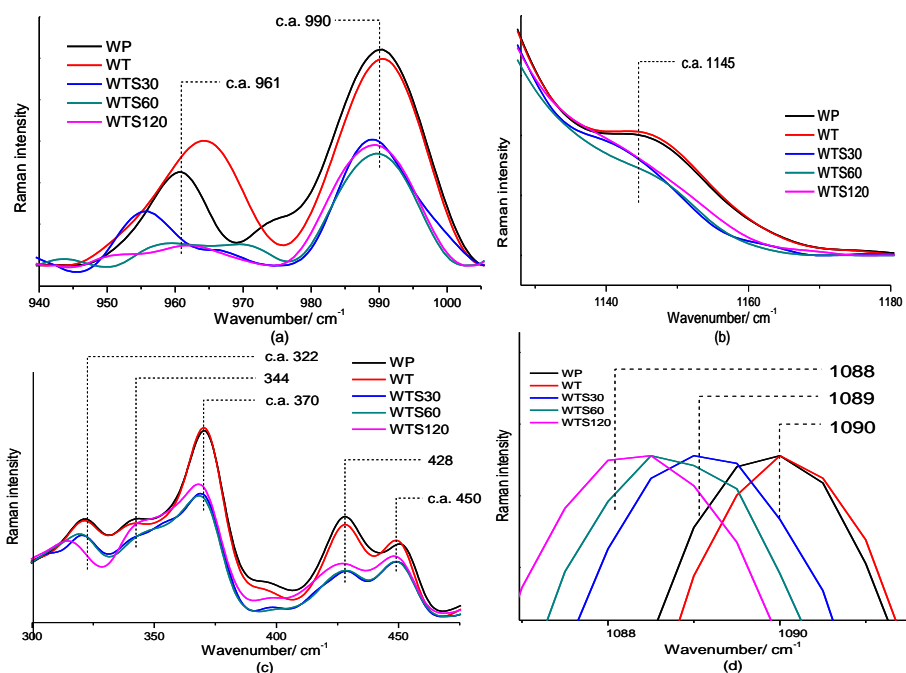


Figure 4.7. Overlaid Raman spectra at different band regions, all spectra are normalized at band ca. 1090 cm^{-1} .

3.5. FTIR

SI Figure 4.3 under Supporting Information displays the full FTIR spectra of the lyophilized samples collected in the solid state, embedded in KBr pellets. The spectra reveal similarities in absorbance in the main regions highlighted in Figures 4.8 and 4.9. One striking, but expected difference is the new absorbance peak at ca. 1610 cm^{-1} related to the oxidation of the cellulose in the TEMPO modification process (Fig. 9). Otherwise, the wood pulp and the TEMPO oxidized wood pulp have very similar spectra.

Region 3700-2700 cm^{-1}

The higher range of cellulose IR spectra, i.e.: above 2700 cm^{-1} , are known to have a poor resolution due to the broad convoluted OH peaks³⁰. Different efforts, including deconvolution, second derivation, and 2D FTIR, have been made to unravel this region to better interpret the IR spectra³⁰⁻³¹. In this study, the Happ-Genzel apodization function³² was

applied to the higher range (3700-2700 cm^{-1}) to deconvolute the broad OH and CH_2 peaks and revealed moderate changes that otherwise would be overlooked.

The broad region 3700-3200 cm^{-1} is related to OH vibrations (Supporting Information Table 4.S-2).^{31a, 33} Previous literature had resolved this wide peak and assigned the representative bands to three types of hydrogen bonding in cellulose: O(2)H--O(6) intramolecular, O(3)H--O(5) intramolecular, O(6)H--O(3) intermolecular^{31d}. Inspection of the three major hydrogen bonding bands of the apodization processed spectra in Figure 4.8 indicate sonicated groups (WTS) exhibit smoother spectra compared with WP and WT groups; otherwise the main difference noted is the decreased band intensity in the intramolecular bonding region around 3350 cm^{-1} (see inset in Figure 4.8). Intramolecular OH--O hydrogen bonding at the O(3)H-O(5) positions should be affected together with COC linkage in the chain cleavage process during the sonication. Also noted is a slight decrease at ca. 3310 cm^{-1} ; Marechal and Chanzy indicated this region was sensitive to one of the conformations of the C6 position^{31a}.

Region 2980-2835 cm^{-1} is assigned to CH_2 and CH_2OH stretching mode (Supporting Information Table 4.S-2). From Figure 4.8, WP and WT show relative well-defined peaks, while the sonicated WTS groups show less defined peaks, or wider absorption ranges. CH_2 at C6 is associated with intrachain and intersheet CH--O hydrogen bonding¹⁴, and the conformation of C6(OH) is related to the crystal structure too. As mentioned in the discussion section below, Raman data also supports a change in conformation of the C6, as peak broadening indicates multiple conformations.

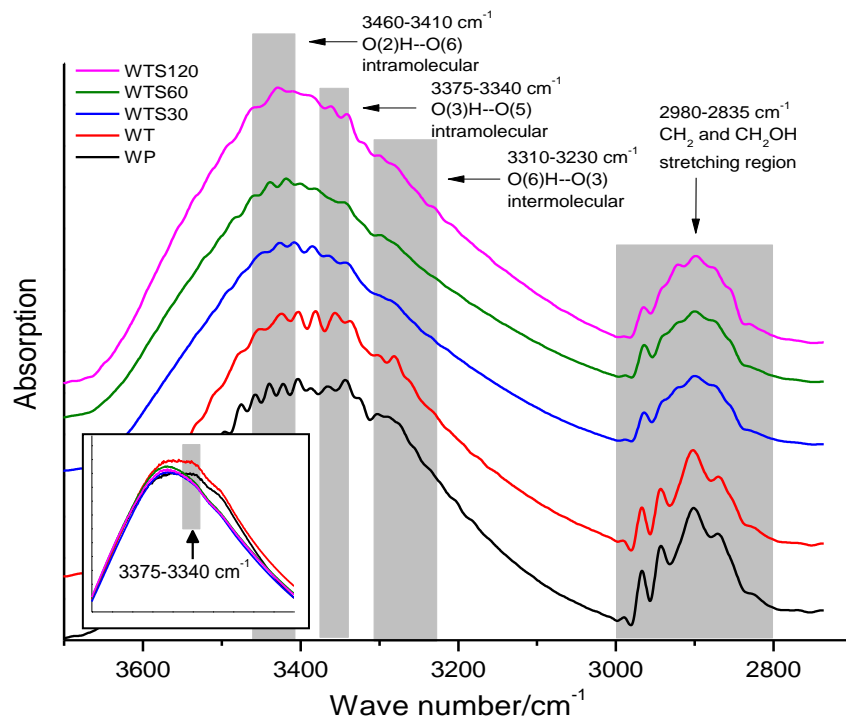


Figure 4.8. FTIR spectra in 3700-2700 cm^{-1} range, Happ-Genzel apodization function applied to deconvolute the peaks; inset shows the intensity decrease at band 3375-3340 cm^{-1} .

Region 1800-500 cm^{-1}

The lower range of cellulose IR spectra, from 1800-500 cm^{-1} , has relatively well defined peaks-- hence apodization deconvolution was not applied. In Figure 4.9, WP shows a small absorption peak at band 1635 cm^{-1} which is assigned to bound water and carboxylates from the bleaching process.^{31d} In the four treatments (WT, WTS30, 60, 120) this band is merged into the much stronger carboxyl salt peak at 1610 cm^{-1} resulted from the TEMPO-mediated oxidation treatment.

The valleys at 1110-1090 cm^{-1} and 1050-1035 cm^{-1} are flattened on the WTS groups. The relative intensity measurements indicate that no absorption bands of 1110 or 1035 cm^{-1} change much across the five levels, rather it is the broadening of band 1058 cm^{-1} that caused the flattened valley. Absorption band 1058 cm^{-1} , the strongest band across the cellulose spectra, is assigned to CO stretching at C3 position^{31a}, suggesting that the CO stretching range is broadened upon sonication. Disrupting the internal structure of the native microfibril may bring this change. Very similar changes for the WTS are observed for the valleys at 1429-1372 cm^{-1} and 670-626

cm^{-1} , which are related to CH deformation and OH out-of-plane bending respectively. In both cases, it is the broadening of the neighboring peaks causing the flattened valley, confirming that sonication treatments introduced a degree of disorder within the microfibril.

The absorption band, 1161 cm^{-1} , is assigned to COC stretching motion. The band intensities relative to band 1058 cm^{-1} (CO stretching at C3) drop significantly for the WTS group compared with the WT and WP group, indicating the chain cleavage effect of the sonication treatments similar to what is found with the Raman analysis and previous AFM data¹³. Also noticeable is that CO absorption band at ca. 1058 cm^{-1} shifts towards lower wavenumbers as sonication time is extended (Supporting Information in Table 4.S-2, Figure 4.9). This data reveals the same trend as what is observed in Raman spectra at band ca. 1090 cm^{-1} , which is related to COC vibration (Figure 4.7d). Other changes observed include the intensity change at 1282 cm^{-1} and the development of the band at 1262 cm^{-1} for the sonicated samples.

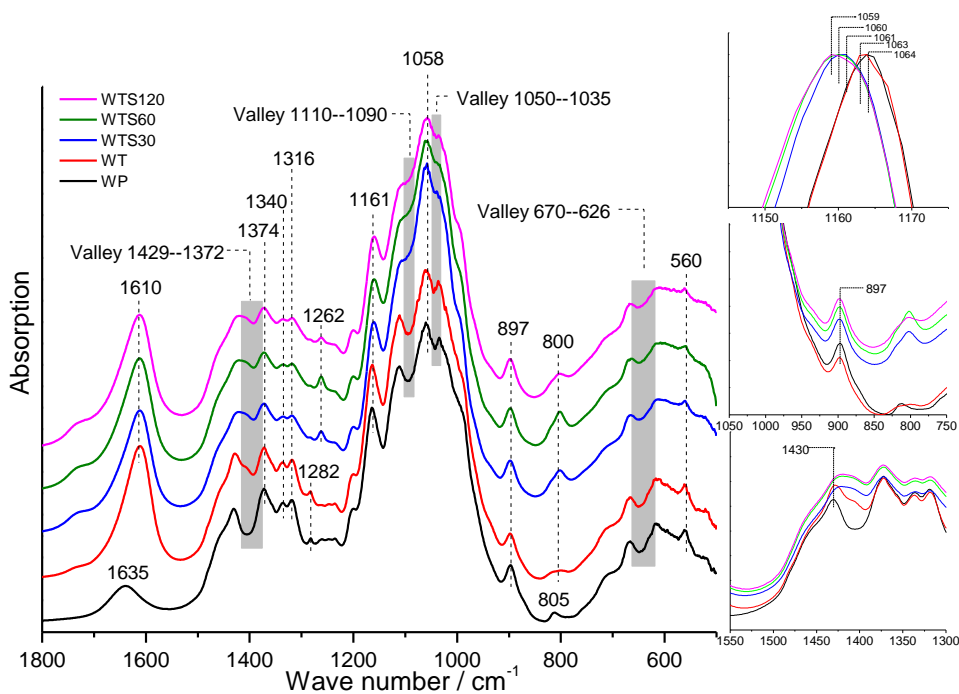


Figure 4.9. FTIR spectra in range of $1800\text{-}500 \text{ cm}^{-1}$. Insets contain overlaid spectra.

4. Discussion

4.1. Fibril surface oxidation vs sonication

The two major treatments introduced to the wood pulp are reexamined: TEMPO-mediated oxidation and sonication. For the oxidation treatment, the apparent change is the introduction of the carboxyl groups on the C6 position of the surface chains on the microfibrils. This change does not impact the supramolecular structure since the crystallinity index, as shown in Table 4.1., as well as in other previous reports^{19, 34}, is not changed by the surface oxidation. For the TEMPO oxidized pulp fibers that were not sonicated, very little change is observed in the results from the three analytical methods. The most outstanding feature is in the FTIR spectrum that confirmed the oxidation. However, little else is seen in the spectrum even though considerable amount of primary hydroxyl on microfibril surface had been oxidized^{10b, 35}. This data strongly suggests that there is a lack of frequencies that are resolved in the spectroscopy techniques that directly relate to the chains restricted to the surface of the microfibrils; this fact is especially pertinent to the current samples, as wood derived celluloses contain the most fibril surface chains^{10b, 19}. Once the TEMPO oxidized nanocellulose was sonicated, the changes that are reported in Raman and FTIR are clearly evident. Significantly, the XRD data for the sonicated samples still retain the cellulose I diffraction pattern, albeit broadened.

4.2. Destruction of the microfibril structure

XRD, Raman, and FTIR have been utilized to follow the impact of varying treatments on the crystallinity of cellulose^{22a, 25-26, 36}. These studies indicate scattering and spectral changes as a function of ball milling time and mercerization. As fragmentation of the microfibrils occurs given the sonication treatment, the observed changes in the present study are related to the previous work on the modification of native cellulose structure. XRD data of the sonicated samples indicated that microfibril lateral dimensions, as well as the crystallinity index were all impacted, but maintained the characteristic cellulose I diffraction pattern. In contrast, when cellulose is ball milled for extensive periods of time, native diffraction patterns are merged into a single amorphous peak²⁶. For wood cellulose treated with 12% NaOH, diffraction patterns have the 110 and 200 peaks merge in overlapping peaks near 20 and 22°, respectively^{16c}.

For sonicated samples, changes in Raman and FTIR spectra have similar characteristics as the ball milling and mercerization treatments. The most significant changes in Raman spectra for

sonicated samples indicated in the current study are related to the methylene group bending frequencies around 1450 to 1480 cm^{-1} ; a new peak at 1275 cm^{-1} related to HCC and HCO bending; and either the methylene or C1 conformation at 891 cm^{-1} . FTIR spectra of sonicated samples showed complementary changes at the 1430, 1262, and 897 cm^{-1} absorption bands. It has been previously noted that the relative intensity around 1430 cm^{-1} decreases, while absorption bands at 897 cm^{-1} increases upon the conversion of cellulose I to cellulose II or after extensive ball milling³⁷. In the current data, there is a significant increase in absorption at 897 cm^{-1} combined with a slight increase at 1430 cm^{-1} (Figure 4.9). While 897 cm^{-1} has been placed as importance for “amorphous” cellulose band, 1430 cm^{-1} has been indicative of a crystalline band from the methylene bending. For FTIR both groups are impacted together in the same direction; this unusual result gives insight that sonication has produced an altered structure that has more surface chains while retaining the cellulose I structure.

It was observed that Raman peak at 1090 cm^{-1} shifted with sonication time. In this current study, the peak shifts two wavenumbers with sonication, indicating strain of approximately 0.75% to 1%³⁸. Correspondingly, the (004) plane of the TEMPO oxidized and sonicated samples were greatly reduced (Figure 4.4). As well, changes in the skeletal stretching occurred below 600 cm^{-1} , indicated that the sonicated samples had a different environment for the skeletal groups. This data strongly suggests that the cellulose chains are no longer in their native crystal environment.

The Raman 891 cm^{-1} peak is confounding as it has not been absolutely assigned to a group frequency and is expected to be strongly delocalized²³. It was previously correlated with the number of surface chains on the fibril; moreover, it does change significantly with ball milling and conversion into cellulose II^{22a, 39}. Both of these treatments are related to native crystal destruction and disorder. Blackwell and co-workers reported this peak was very sensitive to conformation of the C1 methine⁴⁰. The local environment of the C1 methine would be impacted by a change in association of the cellulose chains from sonication.

4.3. Hydrogen bonding and C6 conformation alternations

Much effort has been applied to determining the absolute structure of cellulose, capped with two high-resolution scattering studies^{15, 41}. Confounding data within these studies revealed two co-existing hydrogen bonding schemes that were further analyzed as a function of temperature demonstrating that they most likely co-exist⁴². The data was related to a bifurcated interchain

hydrogen bond in one scheme (proton from O6 interacts with both O2 and O3) relative to a second scheme (proton from O2 interacting with O6). Changes in hydrogen bonding at the surface or near crystalline grain boundaries indicated that aspects of the second scheme could be developed. In contrast, cellulose II has a single hydrogen bonding scheme, with an alternate hydroxymethyl position (*gt* instead of *tg*) that contain some hydroxymethyl disorder⁴³. Ball milling would no doubt disrupt the hydrogen bonding scheme, allowing multiple positions of the hydroxymethyl groups including *gg*. Previously researchers hinted at not being able to distinguish the hydroxymethyl conformation using Raman bands based on polarization and orientation²³. However, cellulose *Iβ* contains predominately *tg* conformation of the C6 and the corresponding Raman band at 1480 cm⁻¹ is related to the methylene positions. Cellulose II contains a large amount of *gt* for the C6 position, and there is a shift in its absorbance to 1450 cm⁻¹. The data strongly suggests assignment of these bands to their corresponding conformations. The TEMPO oxidized nanocellulose has a slightly increased intensity at 1450 cm⁻¹, while still retaining significant intensity at 1480 cm⁻¹. Molecular dynamics studies have shown alternate positions of the surface chain of hydroxymethyl groups⁴². Hence, fragmentation of microfibrils would impact the number of surface chains, giving rise to alternate positions of the hydroxymethyl groups. This result is qualitatively shown in the WTS groups by the broadening of the methylene stretching region of the FTIR spectra.

4.4. Cellulose *Iβ* crystalline model and microfibrils delamination mechanism

Based on these observations, we suggest that the sonication treatment following oxidation breaks the CH--O intersheet hydrogen bonding and the van der Waals interactions, so as to liberate the cellulose sheets that retained lateral intrasheet bonding of multiple cellulose chains (Figure 4.2). From this delamination of sheets, the amount of “disorder” in the microfibril increased, increasing the total surface area of the microfibrils. The delamination process also involves cellulose chain cleavage from the glycosidic bonds, which breaks O(2)H--O(6) and O(3)H--O(5) intramolecular hydrogen bonding. Meanwhile, by creating more surface chains, the delamination process converts some of the C6(OH) from more preferred *tg* conformation in the crystalline state to either a *gt* or *gg* conformation in a more disordered state^{2a}.

AFM data has provided evidence that structures related to the thickness of mono- or bi-layer cellulose sheets had been disintegrated from cellulose microfibrils by TEMPO-mediated oxidation followed by sonication. In the light of the earlier computational research on cellulose

$I\beta$ unit cell dimensions^{15, 44}, and a previous cellulose microfibril model derived from plant biosynthesis process⁴⁵, we combine the body of work (Figure 4.10, Figure 4.11) to describe how the cellulose $I\beta$ microfibrils can be delaminated preferentially between cellulose sheets contained in the microfibril.

As Figure 4.10 shows, a model cellulose $I\beta$ crystallite has a thickness of 3.12-3.15 nm, width of 5.30-5.34 nm, with 8 layer sheets. Note that the 8-layer sheet model is derived from Ding and Himmel's model for primary maize cell walls⁴⁵, but the terminal complex that synthesizes cellulose microfibrils within the maize cell wall is similar to that in other angiosperms.⁴⁶ Additionally, this model is only one of several that provide a speculative view of the microfibril structure. Each monolayer has a defined thickness of 0.39 nm based on unit cell dimensions; width is varied and depends upon the side-by-side cellulose chain numbers, from 2.45 nm of 3 chains to 4.93 nm of 6 chains. According to Qian and co-workers⁴⁷, the intrasheet hydrogen interaction (dotted lines) is 8 times greater than the intersheet hydrogen and van der Waals interactions (broken lines). Therefore when the surface oxidized cellulose microfibrils (the oxidized fibers) undergo intensive external mechanical disturbance, like the case of sonication, the intersheet bonding, which is very sensitive to intermolecular distance, will be cleaved, while the intrasheet bonding is still intact. This preferential bond breakage would result in mono- or bi-layer sheets of cellulose liberated from the microfibril crystallites, as depicted in Figure 4.11.

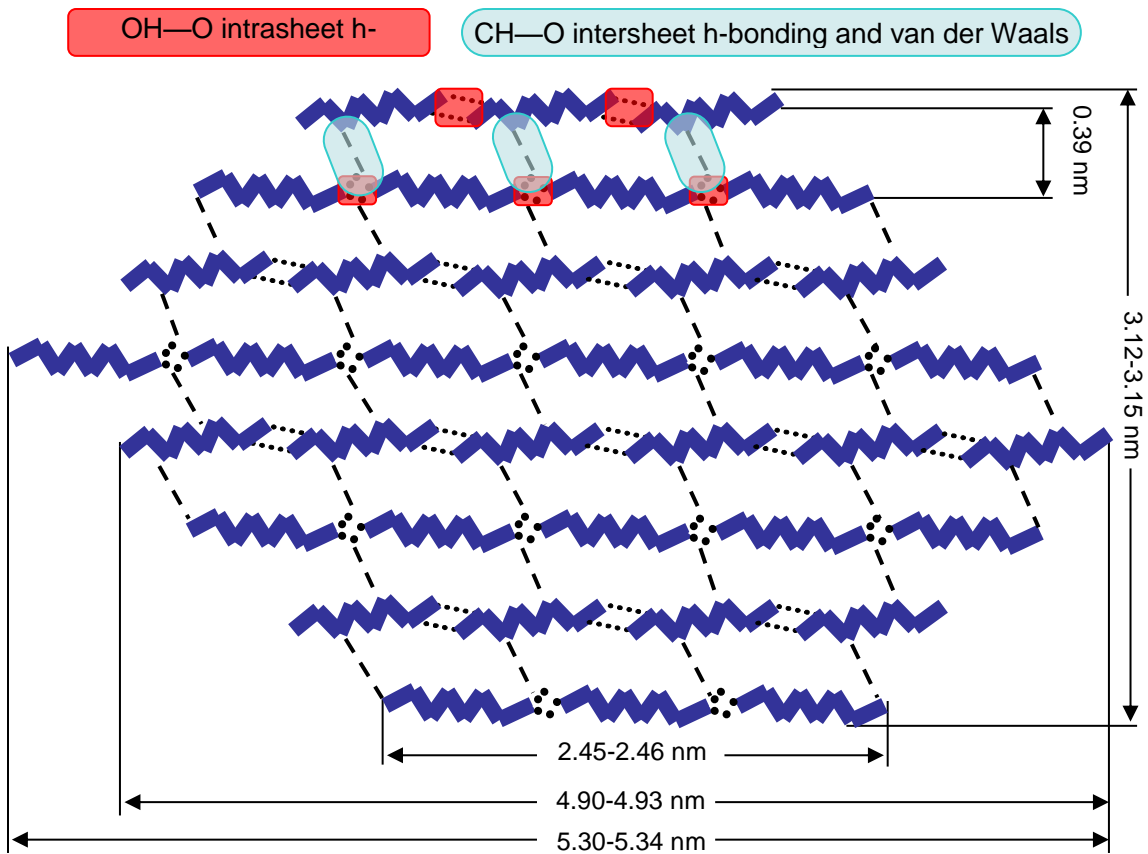


Figure 4.10. Schematic drawing of cellulose $I\beta$ microfibril 36-chain model, cross section view (chain direction perpendicular to paper plain). The thick dotted lines represent the intermolecular (intra sheet) hydrogen bonding; the thin broken lines represent the intersheet hydrogen bonding. This model is modified and combined based on previous models and calculations by Ding et al.⁴⁵, Finkenstadt et al.^{44c}, Vietor et al.⁴⁸, and Nishiyama¹¹.

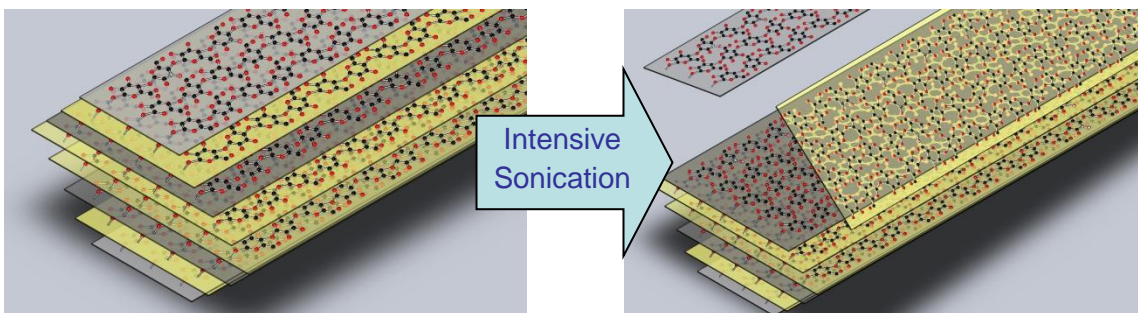


Figure 4.11. Schematic detailing molecularly thick sheets fragmenting along the (200) plane: Intact cellulose microfibril (left) has the intersheet CH--O bonds and van der Waals bonds broken (right) after intensive sonication.

5. Conclusions

Wood pulp, with high levels of cellulose $I\beta$ structure was oxidized and subsequently sonicated to isolate the sub-microfibril structure. A series of global characterizations identified that intensive sonication has a major impact on the chain bonding within the cellulose supramolecular structure. XRD analysis indicated that sonication breaks the cellulose microfibrils along its (200) planes, yet the $I\beta$ crystalline structure is still retained with reduced crystallinity. The Raman and FTIR analysis indicated that structural changes to the cellulose microfibrils do not occur until after sonication; furthermore, AFM observation indicated that the structural changes occur within 5min of sonication. The sonicated samples have certain features similar to mercerized and ball milled cellulose identified within IR and Raman spectra. These differences are traced to changes in the methine frequencies, hydroxymethyl conformations, and skeletal vibrations. By integrating the present findings and previous works, a cellulose molecular sheet delamination scheme is proposed to describe this microfibril disintegration process. Overall, this work provides global evidence to substantiate the hypothesis that monolayer molecular sheets of cellulose, fragmented at the (200) plane, can be obtained by the combination treatment of surface oxidation and intensive sonication.

Appendix-- Supporting Information

Table 4.S-1. Assignments for vibrational Raman bands of allomorphs cellulose $I\beta^{22a, 22c, 23-24, 29}$

Wavenumbers (cm ⁻¹)					Assignments	Observations/comments
WP	WT	WTS30	WTS60	WTS120		
1473w	1473w	1473sh	1473sh	1473sh	Deformation of CH ₂ , COH, and primary alcohol C6OH ²⁴	WTS peaks broadened
1458sh	1458sh	1458w	1458w	1458w	CH ₂ , COH, and primary alcohol C(6)OH bending ^{22a, 22c, 23-24}	WTS show new peaks
1406w	1406w	1406w	1406sh	1406sh	CH ₂ , HCC, HCO, and COH bending ²³⁻²⁴	WTS peaks broadened
1377m	1377m	1377m	1373m	1375m	HCC, HCO, COH, and CH ₂ deformation ²³⁻²⁴	Peak shifts, relative intensity increased for WTS
1334m	1334m	1334m	1334m	1334m	HCC, HCO bending ²³ CH ₂ deformation, COH wagging ²⁴	Relative intensity increased for WTS
1289w	1289w	1289sh	1289sh	1289sh	HCC, HCO bending ²³ CH ₂ twisting ²⁴	Peaks disappeared in WTS
1241sh	1241sh	1241m	1241m	1241m	COH out of plane deformation ²⁴	Peaks showed up for WTS
1201w	1201w	N/A	N/A	N/A	Deformation of COH and CCH ²⁴	WTS peaks broadened
1145sh	1145sh	N/A	N/A	N/A	CC deformation, CO asymmetric ring breathing ^{22c}	Shoulders disappeared
1115m	1115m	1114w	1114w	1113w	COC glycosidic link symmetric deformation, COC ring breathing ^{22c, 24}	Peaks shift to the lower wavenumbers
1090vs	1090vs	1089vs	1088vs	1088vs	COC glycosidic link deformation, ring breathing symmetric stretching ^{22c, 24}	Peaks shift to the lower wavenumbers
1057sh	1057sh	N/A	N/A	N/A	CO 2° alcohol stretching ²⁴	Shoulders disappear
1036sh	1036sh	N/A	N/A	N/A	CO 1° alcohol stretching ^{22c, 24}	Shoulders disappear
990w	990w	990w	990w	990w	CH ₂ deformation ^{22c, 23-24}	Relative intensities reduce
961w	965w	956sh	N/A	N/A	CH ₂ deformation ^{22c, 24}	WT peak shifted, WTS peak disappeared
891vs	891vs	890vs	890vs	890vs	Intensity related to cellulose crystallites lateral size ²³ ; intensity is proportional to the amount of disorder in cellulose ²⁹ ;	Relative intensities increase
560w	560w	560sh	560sh	560sh	COC deformation glycosidic link, in plane ^{22c, 24}	Peaks disappeared for the WTS
510m	510m	505sh	511sh	511sh	COC deformation glycosidic link ^{22c, 24}	Peaks disappeared for WTS

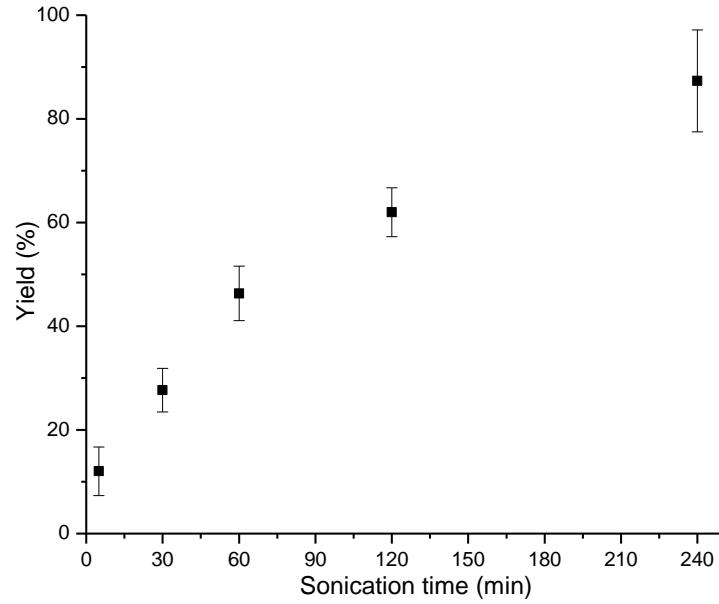
491sh	491sh	491w	491w	491w	COC deformation glycosidic link ²⁴	Peaks showed up for WTS
450w	450w	449w	449w	448w	CCC, CCO ring deformation ^{22c, 24}	Intensity ratios changes relative to 428cm ⁻¹
428w	428w	428w	428w	428w	CCC, CCO ring deformation ²⁴	Intensity ratios changes relative to 450cm ⁻¹
370m	370m	369m	368m	368m	CCC, CCO, CO ring deformation ^{22c, 24}	Peaks shift for WTS, relative intensities change
344sh	344sh	344sh	344sh	344sh	CCC, CCO, CO ring deformation ^{22c, 24}	Shoulders weaker
322w	322w	320w	319w	315w	CCC, CCO, CO ring deformation ^{22c, 24}	WTS peaks shift towards lower wavenumbers region
93vs	93vs	97vs	97vs	97vs		WTS peaks shift towards higher wavenumber region

Note: 1. WP-- wood pulp, WT-- oxidized pulp, WTS30-- oxidized pulp sonication 30min, WTS60-- oxidized pulp sonication 60min, WTS120-- oxidized pulp sonication 120min.

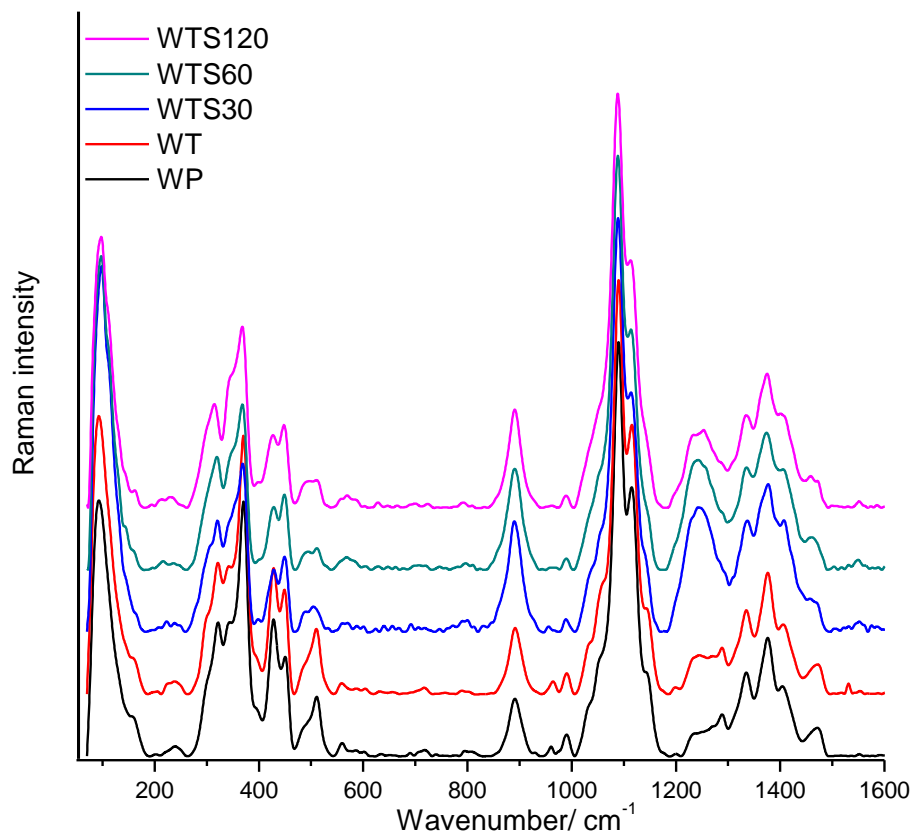
2. vs-- very strong peak, m-- medium strong peak, w-- weak peak, sh-- shoulder peak^{22a, 22c, 23}

Table 4.S-2. Assignments for FTIR bands for cellulose^{2a, 22b, 31a, 31d, 33a, 33c}

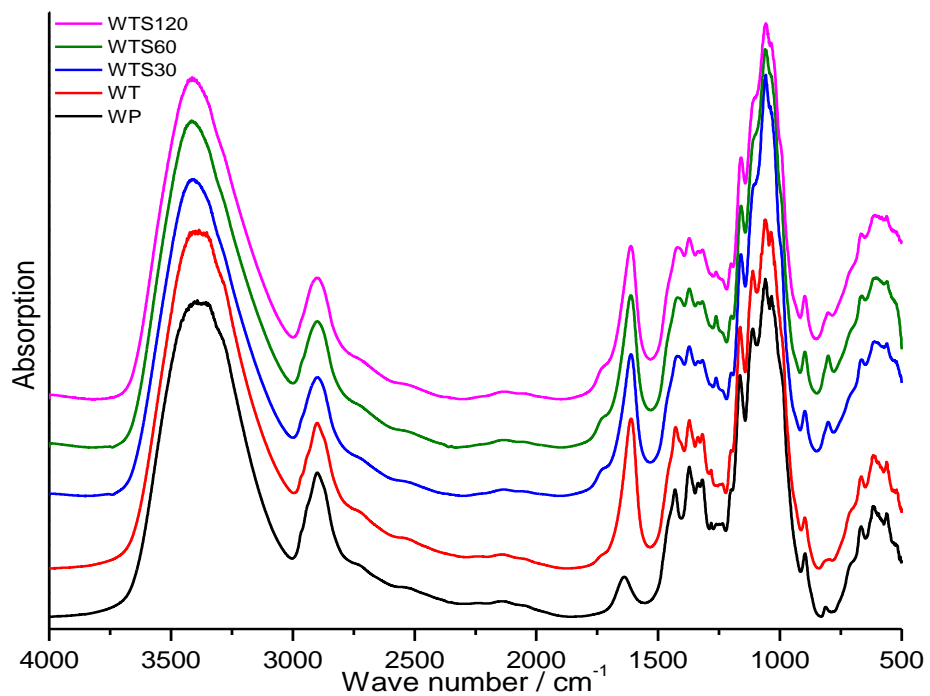
Wavenumbers/ ranges (cm ⁻¹)					Assignments	Observations/comments
WP	WT	WTS30	WTS60	WTS120		
		3460-3410			O(2)H--O(6) intramolecular H-bond ^{31d}	By apodization: WP and WT show less smooth spectra compared with WTS
		3375-3340			O(3)H--O(5) intramolecular H-bond ^{31d}	
		3310-3230			O(6)H--O(3) intermolecular H-bond ^{31d}	
		2980-2835			CH ₂ and CH ₂ OH stretching ^{33a}	By apodization: WP and WT show defined peaks, WTS show broadened peaks
1635	-	-	-	-	Absorbed water ^{31d}	-
-	1610	1610	1610	1610	Sodium carboxylate ^{33b}	-
		Valley 1429-1372				Valley bottom shifted from 1403 of WP to 1393 of WT and WTS
1374	1374	1374	1374	1374	CH deformation vibration ^{33a}	WTS peaks less intense
1282	1282	-	-	-	CH bending ^{33c}	WTS peaks flattened
-	-	1262	1262	1262	COH bending at C2 or C3 ^{22b}	WTS peaks show up
1161	1161	1161	1161	1161	COC stretching ^{2a, 31a}	WTS peaks less intense
		Valley 1110-1090				WTS valleys flattened
1061	1062	1058	1062	1058	CO stretching at C3, CC stretching ^{22b, 31a, 33a, 33c}	Normalized to this peak
		Valley 1050-1035			C-O stretching at C6 ^{2a, 33a}	WTS valleys flattened
897	897	897	897	897	COC stretching, CCO and CCH stretching at C5 and C6 ^{22b}	-
805	-	-	-	-	Due to glucomannan ^{33a}	Only in WP
-	-	800	800	800	Ring breathing ^{33c}	Only in WTS
		Valley 670-626			OH out-of-plane bending ^{33c}	WTS valleys flattened
560	560	560	560	560	-	WTS peaks flattened



SI Figure 4.1. Cellulose nanofibrils yield as a function of sonication time. Sonication started to produce nanofibrils as soon as 5min (yield 12%), and the yield finally reached 87% at 240 min sonication. The yield was calculated based on averages of three replications for each level.



SI Figure 4.2. Raman spectra in 1600-50 cm^{-1} range, peaks normalized on ca. 1090 cm^{-1} . WP-- wood pulp, WT-- oxidized pulp, WTS30-- oxidized pulp sonication 30 min, WTS60-- oxidized pulp sonication 60 min, WTS120-- oxidized pulp sonication 120 min



SI Figure 4.3. FTIR spectra in 4000-500 cm^{-1} range, peaks normalized on ca. 1161 cm^{-1} .

References

1. (a) Klemm, D.; Heublein, B.; Fink, H. P.; Bohn, A., Cellulose: Fascinating biopolymer and sustainable raw material. *Angew. Chem.-Int. Edit.* **2005**, *44* (22), 3358-3393; (b) Habibi, Y.; Lucia, L. A.; Rojas, O. J., Cellulose Nanocrystals: Chemistry, Self-Assembly, and Applications. *Chemical Reviews* **2010**, *110* (6), 3479-3500; (c) Siqueira, G.; Bras, J.; Dufresne, A., Cellulosic Bionanocomposites: A Review of Preparation, Properties and Applications. *Polymers* **2010**, *2* (4), 728-765.
2. (a) Kondo, T., Hydrogen bonds in cellulose and cellulose derivatives. In *Polysaccharides (2nd Edition)*, 2005; pp 69-98; (b) Sjöström, E., *Wood Chemistry: Fundamentals and Applications, 2nd Edition*. 1993; p 293.
3. Eichhorn, S. J.; Dufresne, A.; Aranguren, M.; Marcovich, N. E.; Capadona, J. R.; Rowan, S. J.; Weder, C.; Thielemans, W.; Roman, M.; Renneckar, S.; Gindl, W.; Veigel, S.; Keckes, J.; Yano, H.; Abe, K.; Nogi, M.; Nakagaito, A. N.; Mangalam, A.; Simonsen, J.; Benight, A. S.; Bismarck, A.; Berglund, L. A.; Peijs, T., Review: current international research into cellulose nanofibres and nanocomposites. *J. Mater. Sci.* **2010**, *45* (1), 1-33.
4. (a) Johnson, R. K.; Zink-Sharp, A.; Renneckar, S. H.; Glasser, W. G., A new bio-based nanocomposite: fibrillated TEMPO-oxidized celluloses in hydroxypropylcellulose matrix. *Cellulose (Dordrecht, Netherlands)* **2009**, *16* (2), 227-238; (b) Klemm, D.; Schumann, D.; Kramer, F.; Hessler, N.; Hornung, M.; Schmauder, H. P.; Marsch, S., Nanocelluloses as innovative polymers in research and application. In *Polysaccharides II*, Springer-Verlag Berlin: Berlin, 2006; Vol. 205, pp 49-96; (c) Li, Z.; Renneckar, S.; Barone, J., Nanocomposites prepared by in situ enzymatic polymerization of phenol with TEMPO-oxidized nanocellulose. *Cellulose* **2010**, *17* (1), 57-68; (d) Azizi Samir, M. A. S.; Alloin, F.; Dufresne, A., Review of Recent Research into Cellulosic Whiskers, Their Properties and Their Application in Nanocomposite Field. *Biomacromolecules* **2005**, *6* (2), 612-626.
5. (a) Ranby, B. G., The colloidal properties of cellulose micelles. *Discuss. Faraday Soc.* **1951**, No. 11, 158-164, discussion 208-213; (b) Ranby, B. G., Aqueous colloidal solutions of cellulose micelles. *Acta Chem. Scand. (1947-1973)* **1949**, *3*, 649-650.
6. (a) Manley, R. S. J., Fine Structure of Native Cellulose Microfibrils. *Nature* **1964**, *204* (4964), 1155-1157; (b) Turbak, A. F.; Snyder, F. W.; Sandberg, K. R., Microfibrillated cellulose, a new cellulose product: properties, uses, and commercial potential. *Journal of Applied Polymer Science: Applied Polymer Symposium* **1983**, *37* (Proc. Cellul. Conf., 9th, 1982, Part 2), 815-827.
7. Patel, G. M., Optical investigations on oxycelluloses. *Die Makromolekulare Chemie* **1951**, *7* (1), 12-45.
8. Nakagaito, A.; Yano, H., The effect of fiber content on the mechanical and thermal expansion properties of biocomposites based on microfibrillated cellulose. *Cellulose* **2008**, *15* (4), 555-559.

9. Pääkkö, M.; Ankerfors, M.; Kosonen, H.; Nykänen, A.; Ahola, S.; Österberg, M.; Ruokolainen, J.; Laine, J.; Larsson, P. T.; Ikkala, O.; Lindström, T., Enzymatic Hydrolysis Combined with Mechanical Shearing and High-Pressure Homogenization for Nanoscale Cellulose Fibrils and Strong Gels. *Biomacromolecules* **2007**, *8* (6), 1934-1941.
10. (a) Abe, K.; Iwamoto, S.; Yano, H., Obtaining Cellulose Nanofibers with a Uniform Width of 15 nm from Wood. *Biomacromolecules* **2007**, *8* (10), 3276-3278; (b) Saito, T.; Nishiyama, Y.; Putaux, J. L.; Vignon, M.; Isogai, A., Homogeneous suspensions of individualized microfibrils from TEMPO-catalyzed oxidation of native cellulose. *Biomacromolecules* **2006**, *7* (6), 1687-1691; (c) Abe, K.; Yano, H., Comparison of the characteristics of cellulose microfibril aggregates of wood, rice straw and potato tuber. *Cellulose (Dordrecht, Netherlands)* **2009**, *16* (6), 1017-1023.
11. Nishiyama, Y., Structure and properties of the cellulose microfibril. *Journal of Wood Science* **2009**, *55* (4), 241-249.
12. Elazzouzi-Hafraoui, S.; Nishiyama, Y.; Putaux, J. L.; Heux, L.; Dubreuil, F.; Rochas, C., The shape and size distribution of crystalline nanoparticles prepared by acid hydrolysis of native cellulose. *Biomacromolecules* **2008**, *9* (1), 57-65.
13. Li, Q.; Renneckar, S., Molecularly thin nanoparticles from cellulose: isolation of sub-microfibrillar structures. *Cellulose (Dordrecht, Netherlands)* **2009**, *16* (6), 1025-1032.
14. Jarvis, M., Chemistry - Cellulose stacks up. *Nature* **2003**, *426* (6967), 611-612.
15. Nishiyama, Y.; Langan, P.; Chanzy, H., Crystal Structure and Hydrogen-Bonding System in Cellulose I β from Synchrotron X-ray and Neutron Fiber Diffraction. *Journal of the American Chemical Society* **2002**, *124* (31), 9074-9082.
16. (a) Hori, R.; Wada, M., The Thermal Expansion of Wood Cellulose Crystals. *Cellulose* **2005**, *12* (5), 479-484; (b) Abe, K.; Yamamoto, H., Mechanical interaction between cellulose microfibril and matrix substance in wood cell wall determined by X-ray diffraction. *Journal of Wood Science* **2005**, *51* (4), 334-338; (c) Fink, H. P.; Hofmann, D.; Philipp, B., Some aspects of lateral chain order in cellulose from X-ray scattering. *Cellulose* **1995**, *2* (1), 51-70.
17. Katz, S.; Beatson, R. P.; Scallan, A. M., The determination of strong and weak acidic groups in sulfite pulps. *Svensk Papperstidning* **1984**, *87* (6), R48-R53.
18. Zhang, Y.-H. P.; Lee, R. L., Toward an aggregated understanding of enzymatic hydrolysis of cellulose: Noncomplexed cellulase systems. *Biotechnology and Bioengineering* **2004**, *88* (7), 797-824.
19. Saito, T.; Kimura, S.; Nishiyama, Y.; Isogai, A., Cellulose nanofibers prepared by TEMPO-mediated oxidation of native cellulose. *Biomacromolecules* **2007**, *8* (8), 2485-2491.
20. Murdock, C. C., The Form of the X-Ray Diffraction Bands for Regular Crystals of Colloidal Size. *Physical Review* **1930**, *35* (1), 8-23.
21. Atalla, R. H., Raman spectral studies of polymorphy in cellulose. Part I: Celluloses I and II. *Applied Polymer Symposia* **1976**, *28* (Proc. Cellul. Conf., 8th, 1975, Vol. 2), 659-669.

22. (a) Eronen, P.; Österberg, M.; Jääskeläinen, A. S., Effect of alkaline treatment on cellulose supramolecular structure studied with combined confocal Raman spectroscopy and atomic force microscopy. *Cellulose* **2009**, *16* (2), 167-178; (b) Oh, S. Y.; Yoo, D. I.; Shin, Y.; Kim, H. C.; Kim, H. Y.; Chung, Y. S.; Park, W. H.; Youk, J. H., Crystalline structure analysis of cellulose treated with sodium hydroxide and carbon dioxide by means of X-ray diffraction and FTIR spectroscopy. *Carbohydr. Res.* **2005**, *340* (15), 2376-2391; (c) Schenzel, K.; Fischer, S., NIR FT Raman spectroscopy - a rapid analytical tool for detecting the transformation of cellulose polymorphs. *Cellulose* **2001**, *8* (1), 49-57.
23. Wiley, J. H.; Atalla, R. H., Band assignments in the raman spectra of celluloses. *Carbohydr. Res.* **1987**, *160*, 113-129.
24. Adebajo, M. O.; Frost, R. L.; Klopogge, J. T.; Kokot, S., Raman spectroscopic investigation of acetylation of raw cotton. *Spectrochimica Acta Part a-Molecular and Biomolecular Spectroscopy* **2006**, *64* (2), 448-453.
25. Fischer, S.; Schenzel, K.; Fischer, K.; Diepenbrock, W., Applications of FT Raman spectroscopy and micro spectroscopy characterizing cellulose and cellulosic biomaterials. *Macromol. Symp.* **2005**, *223*, 41-56.
26. Agarwal, U.; Reiner, R.; Ralph, S., Cellulose I crystallinity determination using FT-Raman spectroscopy: univariate and multivariate methods. *Cellulose* **2010**, *17* (4), 721-733.
27. (a) Kong, K.; Wilding, M. A.; Ibbett, R. N.; Eichhorn, S. J., Molecular and crystal deformation of cellulose: uniform strain or uniform stress? *Faraday Discuss.* **2008**, *139*, 283-298; (b) Kong, K.; Eichhorn, S. J., The influence of hydrogen bonding on the deformation micromechanics of cellulose fibers. *Journal of Macromolecular Science-Physics* **2005**, *B44* (6), 1123-1136.
28. (a) Cael, J. J.; Gardner, K. H.; Koenig, J. L.; Blackwell, J., Infrared and Raman spectroscopy of carbohydrates. V. Normal coordinate analysis of cellulose I. *Journal of Chemical Physics* **1975**, *62* (3), 1145-1153; (b) Blackwell, J.; Vasko, P. D.; Koenig, J. L., Infrared and Raman Spectra of the Cellulose from the Cell Wall of *Valonia ventricosa*. *Journal of Applied Physics* **1970**, *41* (11), 4375-4379.
29. Hamad, W. Y., Studies of deformation processes in celluloses using Raman microscopy. *Characterization of Lignocellulosic Materials* **2008**, 121-137.
30. Fengel, D., CHARACTERIZATION OF CELLULOSE BY DECONVOLUTING THE OH VALENCY RANGE IN FTIR SPECTRA. *Holzforschung* **1992**, *46* (4), 283-288.
31. (a) Maréchal, Y.; Chanzy, H., The hydrogen bond network in I[beta] cellulose as observed by infrared spectrometry. *Journal of Molecular Structure* **2000**, *523* (1-3), 183-196; (b) Hishikawa, Y.; Inoue, S.-i.; Magoshi, J.; Kondo, T., Novel Tool for Characterization of Noncrystalline Regions in Cellulose: A FTIR Deuteration Monitoring and Generalized Two-Dimensional Correlation Spectroscopy. *Biomacromolecules* **2005**, *6* (5), 2468-2473; (c) Hinterstoisser, B.; Salmén, L., Two - dimensional step - scan FTIR: a tool to unravel the OH - valency - range of the spectrum of Cellulose I. *Cellulose* **1999**, *6* (3), 251-263; (d) Fengel, D., INFLUENCE OF WATER ON THE OH VALENCY RANGE IN DECONVOLUTED FTIR SPECTRA OF CELLULOSE. *Holzforschung* **1993**, *47* (2), 103-108; (e) Michell, A. J., Second derivative F.t.-i.r. spectra of celluloses I and II and related mono- and oligo-saccharides. *Carbohydr. Res.* **1988**, *173*

- (2), 185-195; (f) Kondo, T., The assignment of IR absorption bands due to free hydroxyl groups in cellulose. *Cellulose* **1997**, *4* (4), 281-292.
32. (a) Bretzlaff, R. S.; Bahder, T. B., Apodization effects in Fourier transform infrared difference spectra. *Rev. Phys. Appl. (Paris)* **1986**, *21* (12), 833-844; (b) Rabolt, J. F.; Bellar, R., The Nature of Apodization in Fourier Transform Spectroscopy. *Applied Spectroscopy* **1981**, *35*, 132-135.
33. (a) Schwanninger, M.; Rodrigues, J. C.; Pereira, H.; Hinterstoisser, B., Effects of short-time vibratory ball milling on the shape of FT-IR spectra of wood and cellulose. *Vibrational Spectroscopy* **2004**, *36* (1), 23-40; (b) Silverstein, R. M.; Webster, F. X., *Spectrometric Identification of Organic Compounds*, 6th Edition. Wiley: 1997; p 496; (c) *Polymer handbook*. 3rd ed.; Wiley: New York, 1989; Vol. 1 v. (various pagings)
34. Saito, T.; Isogai, A., TEMPO-Mediated Oxidation of Native Cellulose. The Effect of Oxidation Conditions on Chemical and Crystal Structures of the Water-Insoluble Fractions. *Biomacromolecules* **2004**, *5* (5), 1983-1989.
35. Okita, Y.; Saito, T.; Isogai, A., Entire Surface Oxidation of Various Cellulose Microfibrils by TEMPO-Mediated Oxidation. *Biomacromolecules* **2010**, *11* (6), 1696-1700.
36. Atalla, R. H.; Brady, J. W.; Matthews, J. F.; Ding, S.-Y.; Himmel, M. E., Structures of Plant Cell Wall Celluloses. In *Biomass recalcitrance: deconstructing the plant cell wall for bioenergy*, Himmel, M. E., Ed. Blackwell Pub.: Oxford, 2008; Vol. xviii, 505 p.
37. (a) Hurtubise, F.; Krassig, H., Classification of fine structural characteristics in cellulose by infrared spectroscopy. . . use of KBr pellet technique. *Anal. Chem.* **1960**, *32*, 177-181; (b) O'Connor, R. T.; DuPre, E. F.; Mitcham, D., Application of infrared absorption spectroscopy to investigations of cotton and modified cottons. I. Physical and crystalline modifications and oxidation. *Textile Research Journal* **1958**, *28*, 382-392.
38. Rusli, R.; Shanmuganathan, K.; Rowan, S. J.; Weder, C.; Eichhorn, S. J., Stress-Transfer in Anisotropic and Environmentally Adaptive Cellulose Whisker Nanocomposites. *Biomacromolecules* **2010**, *11* (3), 762-768.
39. Schenzel, K.; Fischer, S.; Brendler, E., New method for determining the degree of cellulose I crystallinity by means of FT Raman spectroscopy. *Cellulose* **2005**, *12* (3), 223-231.
40. Blackwell, J., Infrared and raman spectroscopy of polysaccharides. *ACS Symposium Series* **1977**, *45* (Extracell. Microb. Polysaccharides, Symp.), 103-113.
41. Nishiyama, Y.; Sugiyama, J.; Chanzy, H.; Langan, P., Crystal Structure and Hydrogen Bonding System in Cellulose I α from Synchrotron X-ray and Neutron Fiber Diffraction. *Journal of the American Chemical Society* **2003**, *125* (47), 14300-14306.
42. Nishiyama, Y.; Johnson, G. P.; French, A. D.; Forsyth, V. T.; Langan, P., Neutron Crystallography, Molecular Dynamics, and Quantum Mechanics Studies of the Nature of Hydrogen Bonding in Cellulose I β . *Biomacromolecules* **2008**, *9* (11), 3133-3140.

43. Langan, P.; Nishiyama, Y.; Chanzy, H., A Revised Structure and Hydrogen-Bonding System in Cellulose II from a Neutron Fiber Diffraction Analysis. *Journal of the American Chemical Society* **1999**, *121* (43), 9940-9946.
44. (a) Gardner, K. H.; Blackwell, J., Structure of native cellulose. *Biopolymers* **1974**, *13* (10), 1975-2001; (b) Sarko, A.; Muggli, R., Packing Analysis of Carbohydrates and Polysaccharides. III. Valonia Cellulose and Cellulose II. *Macromolecules* **1974**, *7* (4), 486-494; (c) Finkenstadt, V. L.; Millane, R. P., Crystal structure of Valonia cellulose I beta. *Macromolecules* **1998**, *31* (22), 7776-7783.
45. Ding, S.; Himmel, M. E., The Maize Primary Cell Wall Microfibril: A New Model Derived from Direct Visualization. *J. Agric. Food Chem* **2006**, *54* (3), 597-606.
46. Buchanan, B. B.; Grisse, W.; Jones, R. L., *Biochemistry & Molecular Biology of Plants*. 2000; p 1367.
47. Qian, X.; Ding, S.-Y.; Nimlos, M. R.; Johnson, D. K.; Himmel, M. E., Atomic and Electronic Structures of Molecular Crystalline Cellulose I β : A First-Principles Investigation. *Macromolecules* **2005**, *38* (25), 10580-10589.
48. Vietor, R. J.; Mazeau, K.; Lakin, M.; Perez, S., A priori crystal structure prediction of native celluloses. *Biopolymers* **2000**, *54* (5), 342-354.

CHAPTER 5

Understanding the Supramolecular Structure of Cellulose Microfibrils via Molecularly Thin Nanocellulose— Perspectives from TEM and NMR Investigations

Abstract

Unique structure of molecularly thin nanocellulose (MT nanocellulose) –obtained by TEMPO-oxidation and sonication– was examined by TEM and solid-state ^{13}C NMR to advance the current understanding on the supramolecular structure of cellulose I microfibrils. The width distribution of the microfibril was determined from TEM images, and a holistic view of the microfibril cross section was developed by integrating the height distribution result from previous work.¹ Systematic changes of NMR spectra upon oxidation and sonication treatments were observed and attributed to the corresponding changes on crystallinity, glycosidic linkage torsion angles, as well as C6 primary hydroxyl conformations. Lastly, current microfibril cross section models were collectively reviewed, and a revised 24-chain hexagonal/elliptical hybrid model was identified as the most credible representation for the experimental data and the known constraints.

1. Introduction

Nanocellulose has become an emerging field of research interests not only because the extensive availability and sustainability of its precursor cellulose,² but also due to its broad chemical modification range, excellent physical and mechanical properties, as well as the enormous potential applications related to nanotechnology.³

Isogai and coworkers have developed a facile way of producing nanocellulose via TEMPO-oxidation and mechanical agitations.⁴ Many efforts since then have been devoted into the isolation, characterization, and application of the fine structure of the oxidized cellulose microfibrils derived from native cellulose sources.⁴ Li and Rennekar have successfully isolated cellulose mono- and bi-layer molecular sheets (i.e.: molecularly thin nanocellulose, or MT nanocellulose) that constitute the microfibrils through extended sonication of TEMPO-oxidized kraft pulp fibers. The thickness profile of the sheets has been determined by atomic force microscopy (AFM).¹ Further investigation with X-ray diffraction, Raman, and FTIR indicates that this delamination occurs along the (200) plane in the cellulose $I\beta$ crystalline structure (Figure 5.1).

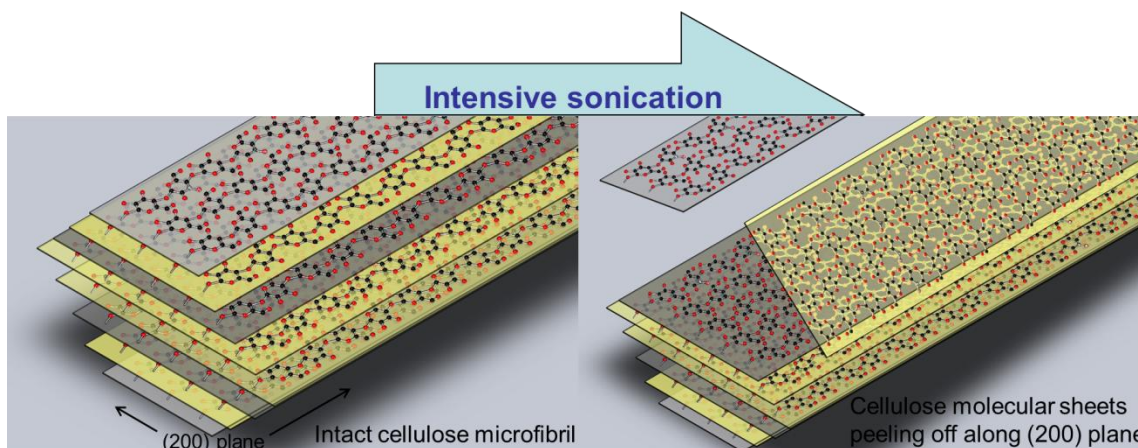


Figure 5.1. Cellulose microfibril delaminates along the (200) plane under intensive sonication, reproduced from Li and Rennekar 2011.⁵ Reproduced with permission from reference 5.

Copyright (2011) American Chemical Society.

TEM helps complete the MT nanocellulose 3D view

So far only height (thickness) and length profiles of the MT nanocellulose were examined whereas the width profile was not, due to the inherent tip convolution effect of AFM (certain technique has been developed to cope with this limitation and improve the accuracy though),^{1, 6} hence a holistic (3D) view of cellulose molecular sheets has not been available. Due to its advantageous horizontal resolution,⁷ transmission electron microscopy (TEM) has been applied in many past research to characterize the nanocellulose width and length profiles that prepared through different methods (hydrolysis,^{7a} TEMPO-oxidation combined with sonication^{7b, 7g}) and from different raw material sources (wood pulp,^{7b, 7e, 7g} cotton, tunicin, Avicel^{7a}); negative staining techniques are often applied to enhance the contrast.^{7a, 7g} With the assistance from TEM analysis, the knowledge gap for MT nanocellulose can be bridged and the understanding on the supramolecular structure of cellulose microfibril, which is essentially the assembly of several cellulose molecular sheets (i.e.: the MT nanocellulose), will also be advanced.

NMR obtains insight on supramolecular changes in oxidation and sonication treatments

Cross polarized magic angle spinning solid-state ¹³C nuclear magnetic resonance (NMR) spectroscopy is regarded as an invaluable approach to elucidate the supramolecular structure, morphology, domain sizes, as well as the crystallinity of cellulose.⁸ The NMR chemical shifts of cellulose material are readily obtained by conventional solid state ¹³C NMR and are very important parameters to evaluate conformations, hydrogen bonding, and molecular packing.⁹ There has been research indicating that clear dependence of chemical shift on cellulose C6 conformations (Figure 5.2, right), hydrogen bonding, and chain packing.¹⁰ It has also been indicated that the glycosidic linkage conformation, which defined by two glycosidic linkage torsion angles¹¹ Φ (O5'-C1'-O4-C4) and Ψ (C1'-O4-C4-C5) (Figure 5.2, left), affects the cellulose supramolecular structure significantly and is related to C1 and C4 chemical shifts.¹²

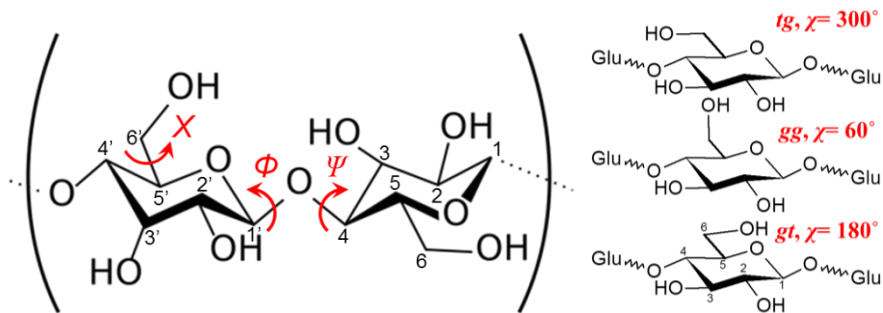


Figure 5.2. Schematic drawings represent cellulose torsion angles Φ , Ψ , and X ($O6'-C6'-C5'-C4'$) (left) and three possible conformations at cellulose C6 position (right).

During the delamination of cellulose microfibrils, although we have identified that the fragmentation occurs along the (200) plane, an elucidation on how the change in structure impacts the torsion angles of the cellulose chains on the surface microfibril is still missing.⁵ Insights from NMR investigation on the minute changes of torsion angles and crystallinity will advance the understanding on the delamination effects of sonication.

Modeling the cellulose microfibril cross section structure

The models of supramolecular structure of microfibrils are approximations and predictions of the true molecular assembly states (i.e.: chain packing numbers, cross section shape, and cross section dimensions) derived from the available theoretical/experimental knowledge, and are used as a tool to guide future research. As microscopy and spectroscopy technologies progress overtime, more credible primary research evidence has cumulated, which unfortunately does not always agree with what has been suggested from past models, hence constant refining the models based on new fact is necessary.

Back in 1954, Frey-Wyssling suggested a near rectangular cross section arrangement to describe the plant derived cellulose microfibrils, based on microscopy and XRD evidence.¹³ Today, wood-based cellulose microfibrils have been proposed having a cross section shape approximate to either a hexagon,¹⁴ a rectangle,^{4, 14} or an ellipse,¹⁵ based on direct microscopy

observation or indirect evidence from its biosynthesis process.¹⁶ Since the terminal complex of a cellulose microfibril has a six-fold symmetry,¹⁷ the hexagonal and elliptical cross section arrangements can better reflect this feature. The cellulose chain numbers contained in the microfibril is believed to be constant based on the assumption that one terminal complex extrude one microfibril.¹⁴ Many has suggested a 36-chain packing scheme,¹⁸ while others have raised doubt over whether this packing scheme is too larger to fit the experimental observations and suggested 24-chain packing scheme instead.¹⁴ The current understanding on cellulose microfibril cross section structures were deduced from plant cellulose biosynthesis origin, crystal lattice dimension, microfibril dimension, as well as the premises on cross section shapes.^{14, 18b, 19} However, due to the uncertainties in microfibril dimension, crystalline structure, as well as the ambiguity of the cross section shape described above, many agreements on microfibril cross section arrangement have yet to be reached. By integrating the cellulose 3D dimensions from TEM and AFM, we can further eliminate these uncertainties and derive a more credible cross section model.

In the present study, TEMPO-oxidized kraft pulp was sonicated under different time intervals to produce MT nanocellulose. TEM and NMR were utilized to examine the MT nanocellulose in order to obtain additional information on its unique structure, including: width profile distribution, crystallinity, glycosidic linkage torsion angles, C6 primary hydroxyl group conformations, as well as the changes of these indexes under sonication. The structure features of MT nanocellulose were integrated with previous knowledge to develop new insights on the microfibril cross section models, and a refined 24-chain hexagonal/elliptical hybrid model was proposed.

2. Experimental

Materials

Never-dried kraft pulp (88% brightness with a DP ranging from 1600- 1694, as indicated by supplier), from southeastern US was the starting material, courtesy of Weyerhaeuser Co., Ltd. NaClO, NaBr, and 2,2,6,6-tetramethylpiperidine-1-oxyl (TEMPO) were obtained from Sigma Aldrich. Ultrapure water used in the experiments were generated by Millipore System (Direct-Q 3UV), with a conductivity of 0.30 $\mu\text{s}/\text{cm}$ and purity < 5 ppb.^{1, 5}

TEMPO-mediated oxidation

Kraft pulp fibers, as received, were oxidized following previously reported techniques with the key parameter controlling oxidation of NaClO at 5 mmol per gram of dry fiber.¹ The final degree of oxidation, determined by conductometric titration,²⁰ was 1.43 mmol/g of fiber, equivalent to a DS of 0.23 (23% of the total AGUs have their C6 primary hydroxyl group converted to carboxyl group).

Sonication

Both kraft pulp and oxidized pulp underwent sonication treatment to generate nanocellulose fibrils. Sonication was conducted at five time intervals (5, 30, 60, 120, and 240 min), at 0.1% (w/w) concentration of fiber slurry, with a temperature controlled bath at 4°C. A 19 mm diameter medium intensity horn was used to sonicate the fibril suspension at 20 kHz (VC700, Sonics and Materials). The sonicated suspension was centrifuged at 4500 rcf for 15 min and the decanted transparent supernatant was stored for later processing into TEM and NMR samples. All samples for TEM and NMR were noted as follows: kraft wood pulp (WP), 120 min sonicated kraft wood pulp (WP120), TEMPO-oxidized wood pulp (WT), TEMPO-oxidized wood pulp that undergone 5, 30, 60, 120, and 240 min sonication (WT 5, WT30, WT60, WT120, and WT240).

TEM experiment

Cellulose suspensions with ca. $5 \times 10^{-3}\%$ (w/w) concentration were first deposited onto Formvar TEM grids (400-mesh), sitting for 5 min before the suspensions were blotted with filter paper. Then 2% uranyl acetate solution was deposited onto the cellulose samples for negative staining. Staining solution was allowed to sit for 2 min before being blotted with filter paper. The stained samples were then immediately observed under a ZEISS 10CA TEM, operating at 60 kV. The TEM images were then analyzed with NIS-Elements BR software for fibril width measurements and statistical analysis. 400 measurements were made from 10-15 images for each sonication time level, and the images were magnified with the assistance of “zoom” tool within the software package to ensure the accurate measurements to the nearest resolved pixel. In order to avoid the errors induced from the incidental twisting (abrupt narrow parts with color changes, Figure 5.3, right) on the fibrils, all the measurements were taken from the most representative parts on the fibrils.

(CP/MAS) solid-state ^{13}C NMR experiment

Cellulose lyophilized samples were ground with Wiley® Mini Mill into fine powders (mesh number 60, 250 μm) and were packed into rotors for NMR scanning. NMR spectra were obtained on a Bruker AVAMCE DPX 300 instrument, operating at 75 MHz carbon frequency, with sample spinning at 6.5 kHz, total contact time 1ms, 3 s relaxation delay, and at ambient temperature. The chemical shift scale is calibrated in relative to tetramethylsilane (TMS), with CH high-field peak set at 29.5 ppm.

NMR crystallinity index evaluation

Crystalline and non-crystalline contributions are determined by peak integration method, which was to calculate the peak areas that represent crystalline region and non-crystalline region respectively. For crystalline part, the designated integration limits are 86.5-- 80.6 ppm, for non-crystalline region the limits are 93-- 86.5 ppm.^{8a} The Crystalline Index (CI) is then calculated

follow equation (1)

$$CI_{NMR} = \frac{A_{cr}}{A_{cr} + A_{non-cr}} \times 100\% \quad (1)$$

3. Results and discussion

3.1. TEM results-- MT nanocellulose width profile

The MT nanocellulose in the TEM exists in long flat fibril form; the width is mostly uniform throughout individual fibrils with incidental narrowed sections, indicating possible twisting structures (Figure 5.3 right). The MT nanocellulose width distribution was obtained by plotting 400 width data points for each sonication time level (Figure 5.3 left).

Tests of statistical significance indicate that the width difference between 5 min and 30min levels, and 30 min and 60 min levels are significant; whereas the difference between 60 min and 120 min levels, and 120 min and 240 min levels are insignificant (Appendix 1). The overall average width for extended sonication groups “60MinPlus” (60, 120, and 240 min combined) is 3.93 nm. Distribution narrows down as sonication time was extended, which is an indication that greater portions of the fiber bundles being disintegrated into individual microfibrils, or even delaminated into layers of cellulose sheets according to previous AFM results from the samples undergone same treatments.¹ The average width decreases and levels off to approximately 4 nm after 60 min sonication, which suggests that 60 min sonication would be sufficient in isolating majority of the individual microfibrils, this result also reconfirms and extends the depth of Johnson’s and Saito’s investigations related to sonication.^{7g, 21} More importantly, the thickness characterization from AFM indicated that the smallest thickness was related to a monolayer sheet; whereas the width characterization from TEM indicated that the smallest width is related to a three-chain across sheet. This suggested that the intra-sheet hydrogen bonds were strong enough

to resist degradation to the lowest segment (one-chain) while the inter-sheet kept breaking down to the lowest possible thickness. Therefore it seems that the intra-sheet bonding is what makes cellulose recalcitrant.

Even though shorter sonication time exhibit longer distribution tails at higher ends, the minimum widths all have a cutoff value around 2 nm regardless, indicating that an approximate 3-chain sheet (one chain is 0.82 nm across) could be the smallest MT nanocellulose structure, which is consistent with the microfibril cross section model suggested in our previous study.⁵ On the higher end, as sonication time increases, the “shoulders” around 5 nm become more distinguished. This result suggests the maximum width of individual sheet is around 5 nm, corresponding to approximate 6 cellulose chains connecting each other side-by-side (4.92 nm). While the larger width values (5 nm and above) could be the manifestation of the “non-individualized” fiber bundles and/ or sheets connected side-by-side via inter-chain hydrogen bonds.^{18b, 22}

For extended sonication levels (60, 120, 240 min, collectively noted as “60MinPlus” group in Figure 5.3, left), the majority (75% percentile) of the width measurements are below 5 nm. Integrating with the previous AFM results on microfibril thickness,¹ the isolated cellulose molecular sheets can be visualized as a long flat ribbon with thickness approximate to or below 1 nm (depending only the layer number, AFM data),¹ width ranges from 2-5 nm (TEM data), and length ranges from hundreds of nanometers to several micrometers (AFM data and other group’s work).^{1, 7b} Also, as many indicated the helix structure of cellulose microfibrils,^{7a, 14, 23} was well observed as the twisting feature within the TEM images (Figure 5.3, right). The structure appears as width variations along individual microfibrils,²³ and is similar with what had been observed from other cellulose species too.^{7a}

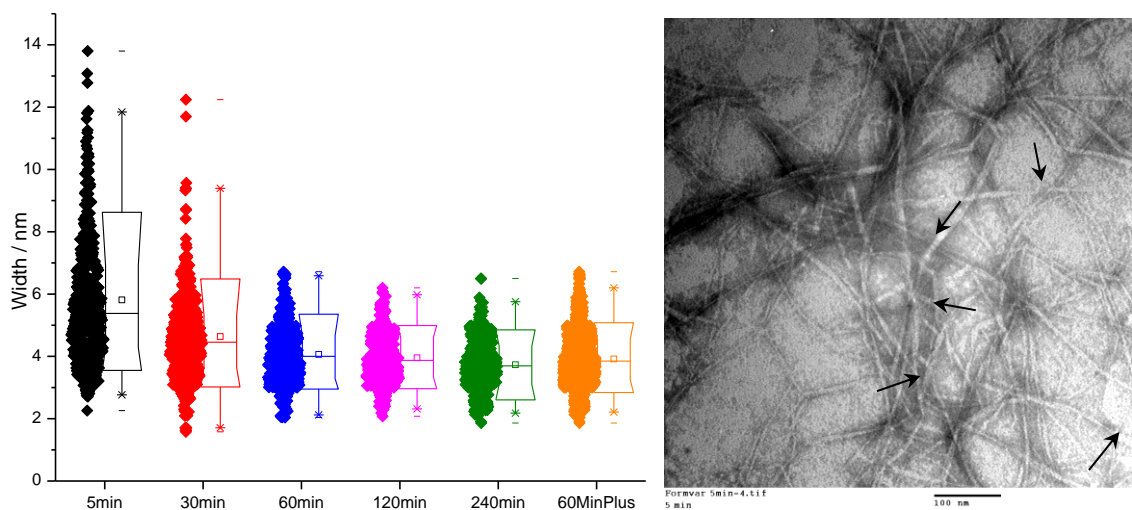


Figure 5.3. **Left:** Nanocellulose width distribution from TEM indicates average fibril width leveled off after 60 min sonication and the width cut-off value is ca. 2 nm across all levels regardless of the sonication time. **Right:** TEMPO-Oxidized cellulose undergone 5 min of sonication, ribbon shape fibrils and twisting features are revealed (representative twisting features were indicated with arrows).

Note: 1) 400 data points were collected for each time level, “60MinPlus” level is the collective statistics for 60 min, 120 min, and 240 min, with 1200 total data points; 2) 25%, 50%, and 75% percentiles are denoted as the long horizontal bars, 1% and 99% percentiles are denoted as “*”, the mean is denoted as “□”, and the full range of the distribution is in between the short horizontal bars at both ends of the box-whisker plot.

3.2. NMR results-- crystallinity, molecular conformation, chain conformation

3.2.1. NMR confirmation of successful oxidation

Figure 5.4 contains the (CP/MAS) ^{13}C NMR spectra across all treatment levels, showing the variations between the plain kraft pulp, oxidized pulp, and oxidized and sonicated pulp. A carboxylate peak emerges at ca. 175 ppm for the oxidized samples.⁴

For ^{13}C NMR spectra of cellulose, the relative intensities of the peaks are supposed to correspond to the proportion of the specific carbons giving rise to them,^{8c} hence the carboxylate peak intensity seems to agree with the degree of oxidation. Since oxidation only occurs on the

fiber surface and ~23% of the C6 are converted to carboxylate group under our experimental conditions (see experimental part for details), the peak intensity ratio between carboxylate and C6 should be around 23%. From the spectra, ratios of ($I_{\text{Carboxylate}} : I_{\text{C6}}$) are: 19%, 22%, 19%, and 23% for WT, WT30, WT60, and WT120, respectively, which agree with the degree of oxidation determined by conductometric titration method.

We speculate that the carboxylate peak upfield displacement relates to the increased *gg* conformation at C6 position as shown by the ~1 ppm upfield shift at the carboxylate peak region upon the sonication treatment and suspect this might due to the much increased *gg* conformation at C6 position. Since after sonication, surface chain proportion should increase from 40-50% to 80% (see 3.2.3 for rationale); accordingly more C6 is exposed to the surface and converted to (possibly more preferred) *gg* conformation (see 3.2.3. C6 torsion angle section for detailed rationale).

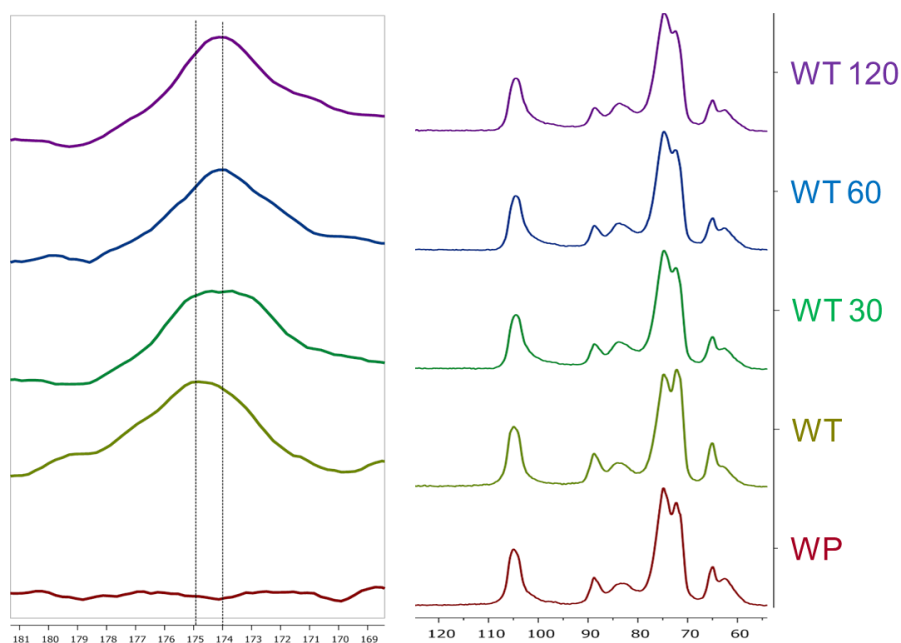


Figure 5.4. Right: (CP/MAS) ^{13}C NMR spectra of WP, WT, WT30, WT60, and WT120 in 55-125 ppm region; **Left:** expansion of the carboxylate group chemical shift region, indicating that i) carboxylate group peak emerges after oxidation, and ii) the carboxylate peak shifts ca. 1 ppm towards upfield upon sonication.

3.2.2. NMR crystallinity determination

Different methods have been developed to evaluate the crystallinity index of cellulose with (CP/MAS) ^{13}C NMR: curve fitting²⁴, peak area separation²⁵, and chemometric analysis (a.k.a.: principle component analysis)²⁶. All these methods seem to have their own limitations: curve fitting methods are not very precise in terms of chemical shifts assignments associated with the disordered regions, plus the results are operator dependent and difficult to reproduce even by same operator;²⁶ the peak area separation tends to overestimate the narrower crystalline peak;^{8a} and the chemometrical analysis is model-independent and supposedly providing more consistent results²⁶, but requires large scan numbers and extended data collecting time. The peak area separation method was applied in this study to compare the differences introduced by different treatment levels.

The NMR CI calculation results for all levels are presented in Table 5.1., and Figure 5.5 demonstrates the calculation for WP level. The general trend for CI variation across all levels is similar to the results derived from XRD previously, and the major cause for a significant CI drop upon sonication is that the delamination effect has destructed some of the crystalline structure.⁵ This data was supported by the crystal size measurement using Scherrer equation, where the (200) plane thickness was reduced by ~30%.⁵ With regard to the difference between the CI absolute value determined by “XRD height” and “NMR peak integration” (noticed that NMR CI values are overall much smaller than XRD CI), Park et al has provided a comprehensive account, essentially stating that the XRD height method is a “time-saving empirical measure of relative crystallinity” and is likely to overestimate the crystalline portion.²⁵

One striking result though is the increase in crystallinity after the oxidation. A plausible explanation is that part of the amorphous hemicellulose in the kraft pulp (up to 25%²⁷) has been removed during the oxidation and the follow-up purifying process, leading to the increase in

relative proportion of the crystalline cellulose, and hence the CI. Similar CI increase of cellulose I also was observed by XRD analysis.²⁸

Table 5.1. Crystallinity index (CI) value calculated by peak integration method.

	WP	WT	WT30	WT60	WT120
Crystallinity Index	39.67%	43.50%	31.33%	30.33%	30.00%

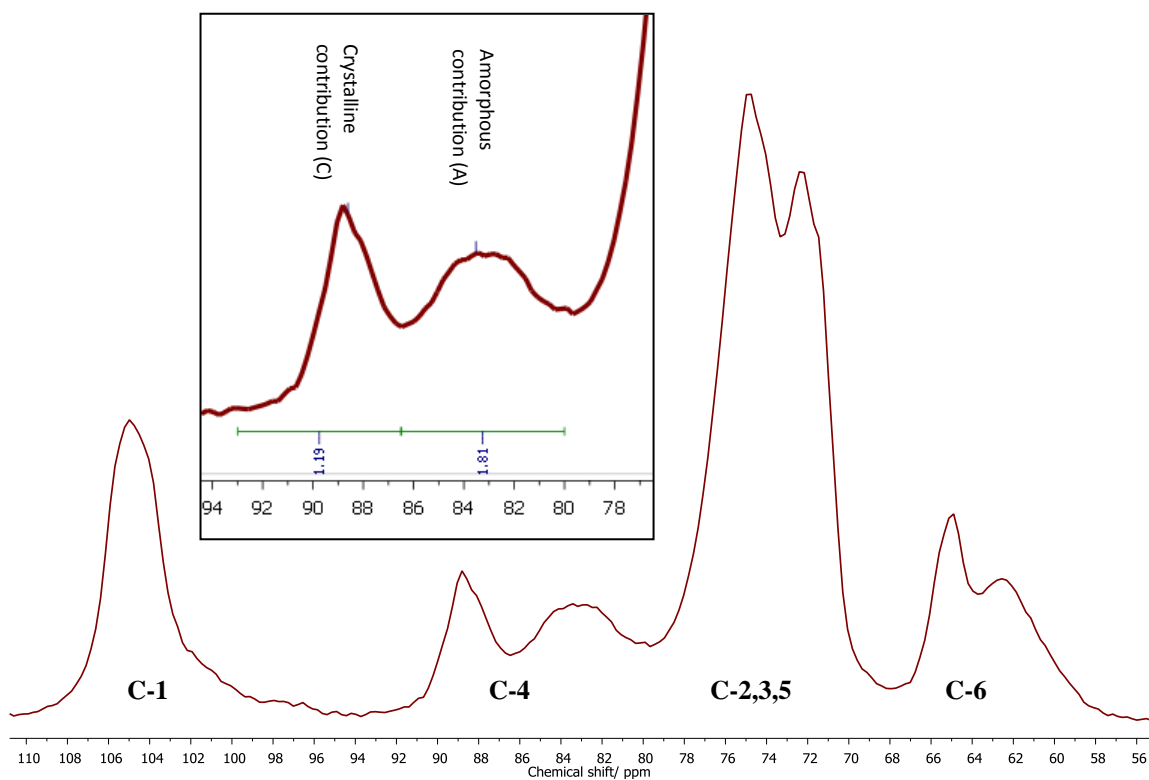


Figure 5.5. (CP/MAS) ¹³C NMR spectrum of kraft wood pulp. Inset demonstrates the area based crystallinity index (CI) calculation: $CI=C/(C+A)$.²⁵

3.2.3. NMR implication on molecular and chain conformation changes under sonication

C1 and C4 chemical shift and torsion angles Φ and Ψ

Figure 5.6 shows the peak shifts for C1 and C4 under oxidation and different sonication treatment levels. C1 peak positions do not show any displacement after oxidation, but exhibit 0.5

ppm displacement towards upfield upon sonication. Similarly, C4 downfield peaks do not show any displacement after oxidation, but exhibit a perceivable shift of ~ 0.2 ppm towards upfield upon sonication. C4 upfield broad peaks are sharpened, and their relative intensities to the downfield sharp peaks increase upon sonication. The following four implications can be derived from the changes seen in the spectra:

i) **Surface chains are to have an elevated impact on NMR spectra upon sonication, due to increased surface chain proportion.** Both oxidation and sonication treatments affect only the surface chains.^{5, 7e, 29} According to the relationship between crystallite width and surface chain proportion indicated by Vietor et al,¹² cellulose from kraft pulp should have approximately 40~50% chains on the surface. Sonication has a major delamination effect on microfibrils, 60 min sonication on oxidized fiber will reduce the average fiber thickness to around 1 nm,⁵ which results in an overall proportion of surface chain increasing to $\sim 80\%$. Since NMR spectra reflects the mean conformation of surface and core chains,¹² the spectra of the sonicated samples are likely to be more of a representation of the surface chains instead of the core chains.

ii) **Oxidation does not change torsion angles at glycosidic linkage but sonication does.** C1 and C4 chemical shifts are dependent on Φ and Ψ ,³⁰ although not in a linear fashion like in the case of X .¹⁰ From Figure 5.6, both WP and WT have C1 chemical shifts at 105 ppm while the three sonication groups WT30, 60, and 120 all have their C1 chemical shifts displaced 0.5 ppm towards upfield to 104.5 ppm, which indicates that oxidation does not significantly affect the torsion angle Φ but sonication apparently does. Unlike C1, the C4 chemical shifts do not reveal very explicit displacements across the five levels. The three sonication levels do have their downfield peaks blunted, indicating a tendency of upfield displacement, or change in Ψ . Therefore, both spectra changes at C1 and C4 position indicate that oxidation does not change the glycosidic linkage conformation but sonication does cause a change in bond angles. This means the addition of carboxylate group on the surface has little impact on glycosidic linkage torsion

angles, as long as the microfibril is intact; and once the microfibril is delaminated, glycosidic linkage will gain more freedom and exhibit more arrangements.

iii) Glycosidic linkage changes reflect more pronounced on C1 chemical shift than C4.

Since sonication has changed torsion angles at glycosidic bond, assuming the rotation of each linkage is shared almost equally between Φ and Ψ ,¹² this unbalanced response from C1 and C4 chemical shifts displacements may well support Vietor's theory that the glycosidic conformation affect C1 chemical shift more than C4, either through association with torsion angle or through hydrogen bonds at O3.¹²

iv) Oxidation increases crystallinity, while sonication reduces crystallinity but increases surface chain proportion. Three features are identified contrasting the C4 downfield sharp peaks with upfield broad peaks: 1) relative intensity of the upfield peaks versus downfield peaks significantly increased after sonication, indicating the decreased crystallinity of the sonicated groups; 2) the C4 upfield broad peaks sharpened at ca. 84 ppm upon sonication, according to Newman's assignment,³¹ this suggests an increased surface chain proportion, which corroborates previous published results^{1,5}; and 3) the C4 upfield broad peaks exhibit a downfield displacement from 83 ppm to 83.75 ppm while WT C1 peak exhibits a receding slope from 100-102 ppm after oxidation. These two pieces of evidence indicate the removal of residual hemicellulose during the oxidation which causes the diminishing of the contributions from the corresponding hemicellulose peaks at ca. 81.9, 81.2 ppm and 101-102 ppm, according to previously published peak assignments.^{14,32}

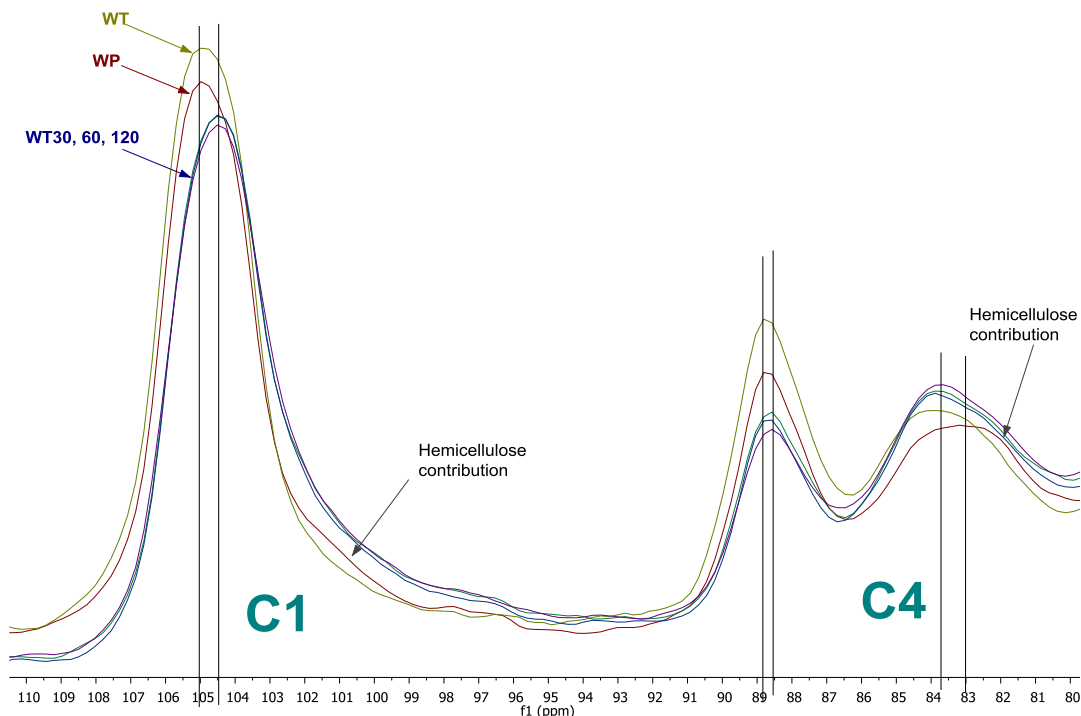


Figure 5.6. (CP/MAS) ^{13}C NMR spectra of the peak shifts for C1 and C4 under oxidation and different sonication treatment levels

C6 chemical shift and torsion angle X

The peak shifts for C6 under oxidation and different sonication treatment levels are presented in Figure 5.7. The relative intensities of the C6 downfield peak were reduced upon sonication and the upfield peak revealed the tendency of peak shifted lower ppm ($63 \rightarrow 62.5$ ppm). These observations lead to the following three implications: i) **gg conformation proportion rises with elevated surface chain percentage.** C6 chemical shift is confirmed to have a linear relationship with torsion angle X 's three energy minimal positions (tg $X=300^\circ$, gt $X=180^\circ$, gg $X=60^\circ$).^{10, 33} The reduction in downfield peak intensity (65 ppm, related to tg conformation) and the upfield peak shift towards 62 ppm (related to gg conformation)^{30b, 33-34} both indicate more $\text{CH}_2(\text{OH})$ side groups have been converted to gg conformation from the dominant tg and gt conformation³⁵ upon more surface chains being exposed by sonication. ii) **Surface chains favor gg conformation.** After sonication, cellulose microfibrils are delaminated and the total surface area is expected to

increase drastically,^{1, 5} therefore the much enriched *gg* conformation may suggest the regioselectivity of the C6 primary hydroxyl group on crystal and fibril surface. This result means either surface chains are more energy favorable towards *gg* conformation than inner chains or their spatial arrangements raise greater probability for *gg* conformation, or both. While Newman et al have confirmed *gg* conformation for cellulose I at the cellulose-water interface,³⁴ our result suggests that in the solid state too, the *gg* conformation might be more favorable on the fibril surface, if not dominant. iii) **Carboxylate side group may contribute in adopting *gg* conformation.** Since TEMPO-oxidation converts ~23% C6 primary hydroxyl groups to carboxyl groups, the larger size of carboxyl group may also be a contributing factor, resulting in *gg* a more stereochemical preferred conformation than either *gt* or *tg* conformations at the cellulose-air interface. Interestingly, this trend does not appear when contrasting WP and WT spectra. This is because the contribution from residual hemicellulose and lignin in WP to the upfield broad peak may large enough to disturb the trend.

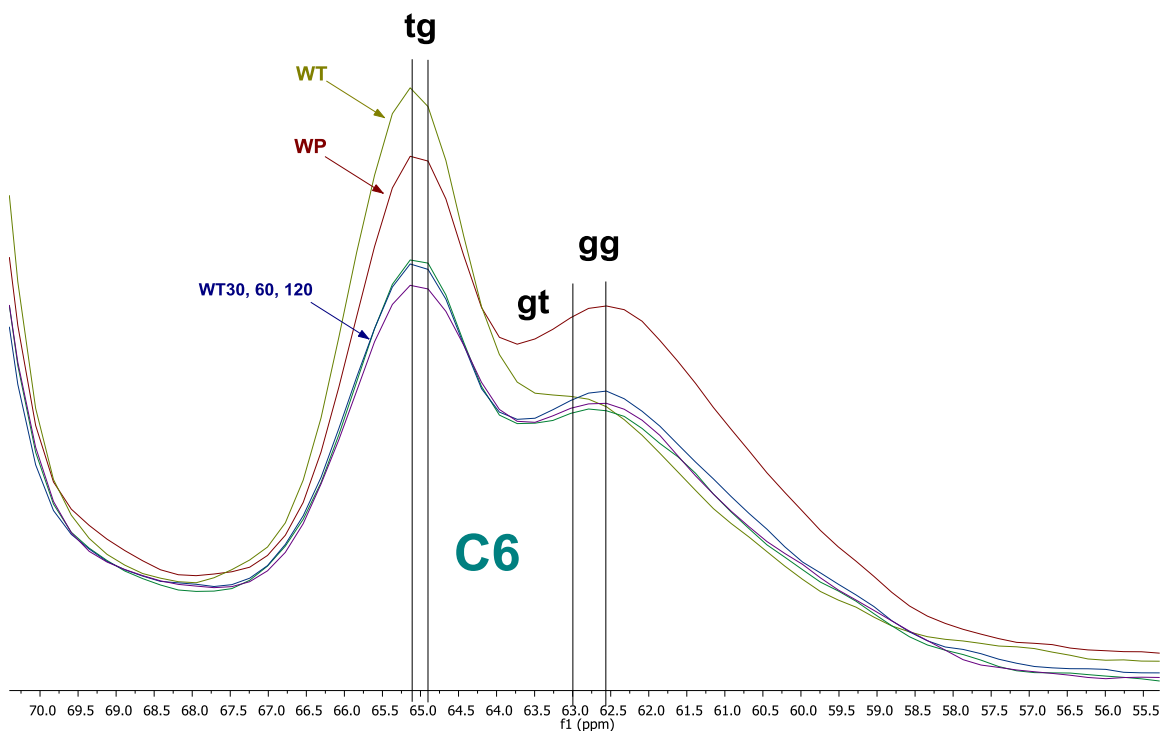


Figure 5.7. (CP/MAS) ^{13}C NMR spectra of the peak shifts for C6 under oxidation and different

sonication treatment levels

C2, C3, and C5 chemical shifts

Figure 5.8 indicates that the relative peak intensities at ca. 72 ppm increase upon oxidation and decrease upon sonication. Also, peaks at ca. 72 ppm exhibit tendency of downfield displacement upon sonication. Based on previous assignments for C2, C3, and C5,^{12, 14, 36} the peak at ca. 75 ppm relates to C5 and the peak at ca. 72 ppm relates to C2 and C3 for kraft pulp. Since oxidation converted ~23% primary hydroxyl group at C6 to carboxylate group and oxidation itself does not alter the crystal structure,^{4-5, 28} carboxylation at C6 becomes the only reason that responsible for the rise of C2,3 peak. For sonication, the major changes it introduced to the system include: increased surface chain proportion (40-50% to ~80%) and decreased crystallinity. Interestingly, it was noticed that the crystallinity index calculated based on C4 peak also follow the same pattern across five groups (refer to earlier text, WT>WP>WTS30, 60, and 120); it appears that there might be a correlation between crystallinity index and the C2,3 peak intensity, although deeper understanding and further study are needed to validate this hypothesis.

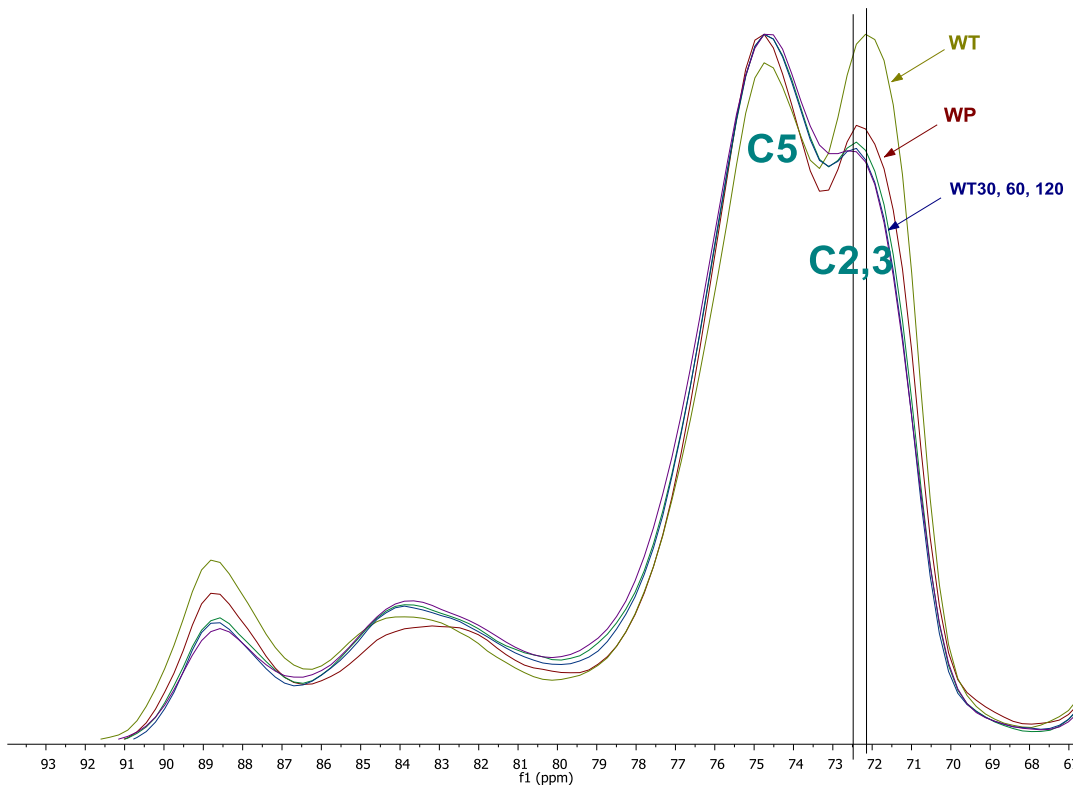


Figure 5.8. (CP/MAS) ^{13}C NMR spectra of the peak shifts for C2, C3, and C5 under oxidation and different sonication treatment levels

3.3. Reflections on cellulose microfibril supramolecular structure

3.3.1. Current understanding

Many research efforts revolving around cellulose $I\beta$ microfibril structure of wood has been devoted into the understanding of its internal chain structure and size.^{14, 17, 24, 37} Nevertheless, some important agreements have yet to be reached in three key areas before a well-defined microfibril structure is clearly identified: lateral dimensions, cross section shape, and chain packing numbers within individual microfibrils.^{14, 18b, 23, 38}

The microfibril lateral dimensions have been characterized with many techniques (SEM, TEM, AFM, XRD, SAXS, NMR) for a variety of plant sources, and it is understood that the lateral dimensions are source dependent, in a wide range of approximately 2-7 nm.^{1, 15} The cross

section shape of plant cellulose microfibrils has been suggested as either hexagonal,^{18b} rectangular,³⁹ or approximate elliptical,^{15, 40} but recent crystallography data indicates that the rectangular shape is more likely to be the case.¹⁴ The chain packing numbers are determined by the cellulose synthase numbers presented within a rosette terminal complex (TC) in wood.^{17b} The microfibril cross-sectional area and the chain packing patterns are combined to derive the chain packing numbers.^{19a} The numbers of chains extruded from TC are supposed to be constant in normal conditions (although exception has also been reported),¹⁴ hence the microfibril diameter (lateral dimensions) should also be consistent at least within same plant species. A 36-chain model was frequently suggested after Herth's initial proposal based on estimation from electron microscopy,^{17b, 18a, 19a, b, 41} which was deduced from the diameter of the rosette TC and the fact that each rosette is composed of 6 subunits.⁴² However, a recent study has challenged this model, arguing that the actual cross-sectional area (assuming circular shape) of a microfibril can only fit in 22 chains sufficiently, and proposed a 24-chain model instead.¹⁴

3.3.2. Dimension-shape-packing numbers triangle scheme

To put things into perspective, the primary data acquisition methods as well as the correlations among cross section dimensions, cross section shape, and chain packing numbers are plotted into a triangular scheme (Figure 5.9) to visualize these interdependent factors and their interrelationships that collectively determine the cellulose $I\beta$ cross section structure. The cross section dimensions (height, width, diameter, etc.), which can be determined by direct experimental measurements (microscopy, crystallography, and spectroscopy)^{8a, 15, 18b, 43} and indirect model-based computational estimation,⁵ is dependent on both cross section shapes and chain packing numbers. The cross section shape, which can be detected by direct microscopy observation,^{19a} indirect crystallography inference,¹⁴ or derived from cellulose biosynthesis process,^{18b} is independent from the chain packing numbers but determines cross section dimensions. Finally the chain packing numbers, which can be derived either from the biosynthesis process^{37b} or by taking the cross-sectional area ratio of single microfibril and single

chain,¹⁴ is independent from the cross section shape and determines the cross-sectional area and hence the cross-section dimensions.

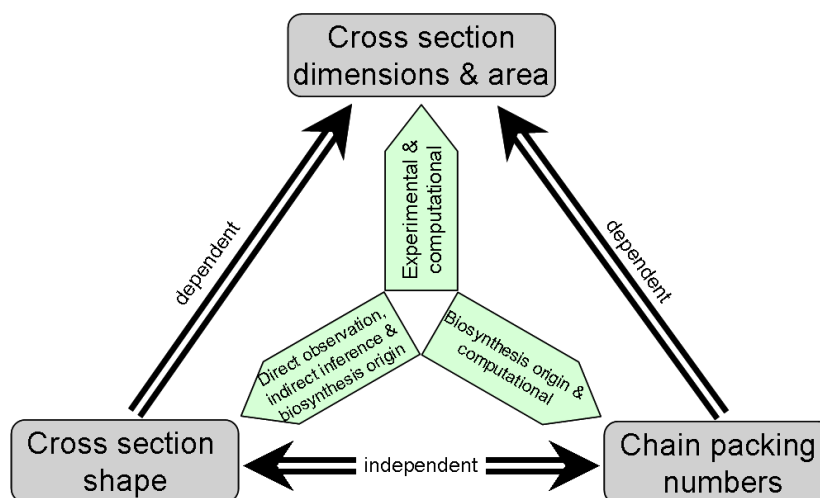


Figure 5.9. The “Dimension-shape-packing numbers” triangle scheme indicates primary information acquisition approaches and the interrelationships among cross section dimensions, cross section shape, and chain packing numbers, which collectively determine the microfibril cross section structure.

Even though there are multiple techniques to characterize the “triangle”, especially the “dimensions” vertex, it seems that we have yet to find the a silver bullet for this purpose—AFM is good for height information with serious convolution effect on width measurements at single-digit or sub- nanometer scale;⁴⁴ TEM is good for width measurements, although the staining process brings in non-negligible errors and electron radiation damages biomaterial samples too;^{44a} X-ray diffraction methods are global techniques and only good for crystalline portions of the material, plus instrumental broadenings and operator-dependent peak deconvolution process all factor into the errors;^{15, 25} NMR method is based on a series of assumptions (on peak assignments) and approximations (on cross section shape), and are as well heavily operator dependent.^{8a, 25} However, by combining information from different techniques, we are able to characterize the “triangle” with minimal uncertainty.

3.3.3. Refining the microfibril cross section model: 24-chain hexagonal/elliptical hybrid model

Among the three vertexes of the “triangle”, there are more directive and diversified approaches to obtain information regarding to the “dimensions” vertex than the other two. Since dimensions are dependent on cross section shape and chain packing numbers (collectively defined as packing arrangement), microfibril lateral dimensions can be estimated through $I\beta$ unit cell dimensions and the presumed chain packing arrangements. This model-based data and experimental data are compared to identify the most likely microfibril cross section configuration.

Table 5.2. below shows the microfibril cross section dimensions that were determined experimentally from multiple research groups and with diversified techniques. Table 5.3. contains the calculated microfibril cross section dimensions under different packing arrangements. Based on the unit cell structure derived by Nishiyama et al,⁴⁵ single cellulose $I\beta$ chain in crystalline state has a cross-sectional area of 0.317 nm^2 , assuming independent from microfibril cross section shapes. Then cross-sectional areas of microfibrils are determined by the chain packing numbers, in perfect crystalline regions. With predetermined areas and packing arrangements, the corresponding microfibril cross section dimensions can be deduced for each scenario, i.e.: different cross section shapes and packing numbers. These combinations of shape and dimension are compared with the experimental data shown in Table 5.2. to identify the best matches. In the comparison, experimental data is used as the reference upper boundary, meaning a combination in Table 5.3. will be rejected if one or more dimensions are greater than the corresponding experimental data. This is because the calculated dimensions are based on perfect crystalline regions, which should have the smallest dimensions given other conditions equivalent.

Table 5.2. Experimentally determined wood cellulose microfibril lateral dimensions from different techniques (unit nm).

NMR lateral dimensions ^{24, 32}	TEM width*	AFM height ⁴⁰	XRD crystal average thickness ^{**5}		
			(200) plane	(1 $\bar{1}$ 0) plane	(110) plane
3.9- 4.8	2.8-5.1 (average 3.93)	4.2-5.3	4.05 ± 1.01	2.89 ± 0.72	2.55 ± 0.64

Notes: *Result from this study, TEM part 60MinPlus group ranging of 25-75% percentile. **Results have taken into consideration of 25% instrumental error,⁴⁶ (1 $\bar{1}$ 0) and (110) results are the unpublished data from the same work.


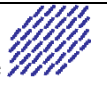

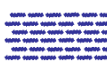

As a result, all 36-chain combinations in Table 5.3. are rejected: NMR lateral dimensions (Table 5.2.) fail 36-chain hexagonal (200), 36-chain rectangular, and 36-chain elliptical; XRD (1 $\bar{1}$ 0) and (110) thickness (Table 5.2.) fail 36-chain hexagonal (1 $\bar{1}$ 0) and (110). The same XRD data also fails 30-chain hexagonal (1 $\bar{1}$ 0) and (110). All the combinations directly failed by experimental data are indicated as a red block in Table 5.3.

Additionally, even though the 30-chain hexagonal (200) and 30-chain elliptical combinations have all their dimensions within the experimental boundary, they are not likely to be representative of the microfibril packing model. This suggestion is due to the microfibrils helix structure along their longitudinal direction,²³ which means the hexagonal model should allow the microfibrils to lay on any of its six sides, and hence all three 30-chain hexagonal arrangements should be accepted or rejected together. Since two of the 30-chain hexagonal arrangements are directly rejected by experimental data, the last one is automatically rejected too. Similarly, the 30-chain elliptical arrangement is also rejected, because it is regarded as the paracrystalline to non-crystalline region on the same microfibril where the crystalline region is the hexagonal shape. Another, the 30-chain and 24-chain rectangular arrangements are less likely to be the appropriate model. Because the TEM data indicates a broad distribution of microfibril width (Table 5.2., Figure 5.3.), which is in accord with the different sheet widths from both hexagonal and elliptical arrangements, yet the uniformed sheet structure of the rectangular model cannot be

used to explain this width distribution profile. The combinations failed by indirect experimental evidence and rationales are marked as yellow blocks in Table 5.3.

The three 24-chain hexagonal and elliptical arrangements are the remaining combinations that fit the experimental data (marked as green blocks). The hexagonal and elliptical cross sections are essentially very close in nature. If the outside layer could be non-crystalline as suggested in earlier research,^{18b} the two models are essentially interchangeable, with hexagonal shape representing the perfect crystalline region and the elliptical representing paracrystalline to non-crystalline region. Another reason to favor the hexagonal/elliptical hybrid model is due to its biosynthesis process: cellulose synthase rosette TC in wood has a 6-fold symmetry, so it is logical that the microfibrils also carry this feature to certain extent.

Table 5.3. Calculated cellulose I β microfibril cross sectional dimensions under different combinations of chain packing numbers and cross section shapes

Chain packing numbers ^a		36-chain	30-chain ^c	24-chain ^c	
Cross-sectional areas (0.317 nm ² / chain) ^b		11.41 nm ²	9.51 nm ²	7.61 nm ²	
Cross section shape	Hexagonal	Height on (200) plane 	H= 3.09 nm W= 4.92 nm	H= 2.82 nm W= 4.49 nm	H= 2.52 nm W= 4.02 nm
		Height on (1 $\bar{1}$ 0) plane 	H= 3.57 nm W= 3.72 nm	H= 3.26 nm W= 3.40 nm	H= 2.91 nm W= 3.04 nm
		Height on (110) plane 	H= 3.72 nm W= 3.57 nm	H= 3.40 nm W= 3.26 nm	H= 3.04 nm W= 2.91 nm
	Rectangular 	H= 2.32 nm W= 4.92 nm	H= 2.12 nm W= 4.49 nm	H= 1.89 nm W= 4.02 nm	
	Elliptical ^d 	H= 2.95 nm W= 4.92 nm	H= 2.69 nm W= 4.49 nm	H= 2.41 nm W= 4.02 nm	

Annotation: red blocks are rejected by experimental data because at least one dimension exceeded experimental upper boundary; yellow blocks are rejected indirectly by experimental evidence and rationales; green blocks are the final chosen cross section arrangements

Notes:

- a) The chain numbers have to be divisible by 6 due to the 6-fold symmetry of the rosette TC.^{19a}
- b) Cellulose I β individual chain cross-sectional area is calculated based on the monoclinic (P2₁) crystal lattice parameters: a=0.778, b=0.820, c=1.038nm, and $\gamma=96.5^\circ$.⁴⁵ One single chain's area is half of this 2-chain unit cell: $(a*b*\sin\gamma)/2 = 0.317 \text{ nm}^2$. Detailed calculation is available in appendix 2.
- c) Dimensions for 30-chain and 24-chain models are estimated by proportionally scaling the 36-chain dimensions.
- d) Elliptical cross section is envisaged as consisting of a crystalline core (blue) and a paracrystalline to non-crystalline sheath (green).^{18b}

Based on the above discussion, we suggest a “24-chain hexagonal/elliptical” packing arrangement as the refined cellulose I β microfibril cross section model, with alternative cross section shapes of hexagonal (in crystalline phase) and elliptical (in non-crystalline phase), as shown in Figure 5.10. This hybrid model have its dimensions fit in all the observed experimental

data to date; the hexagonal structure also accounts for the broad width distribution from our TEM investigation; last but not least, its hexagonal/elliptical cross section shape also inherits the six-fold symmetry feature from the biosynthesis process of plant cellulose. One assumption to note is that the model is constructed under the assumption that all chains being crystalline to simplify the calculation, and the real microfibril size with non-crystalline portion presented should have slightly larger lateral dimension. Overall this new model agrees with the 24-chain packing scheme recently proposed by Fernandes et al,¹⁴ and introduces the hybrid hexagonal/elliptical cross section shape to account for the crystalline and non-crystalline regions as well as to better explain the broad experimental width distribution.

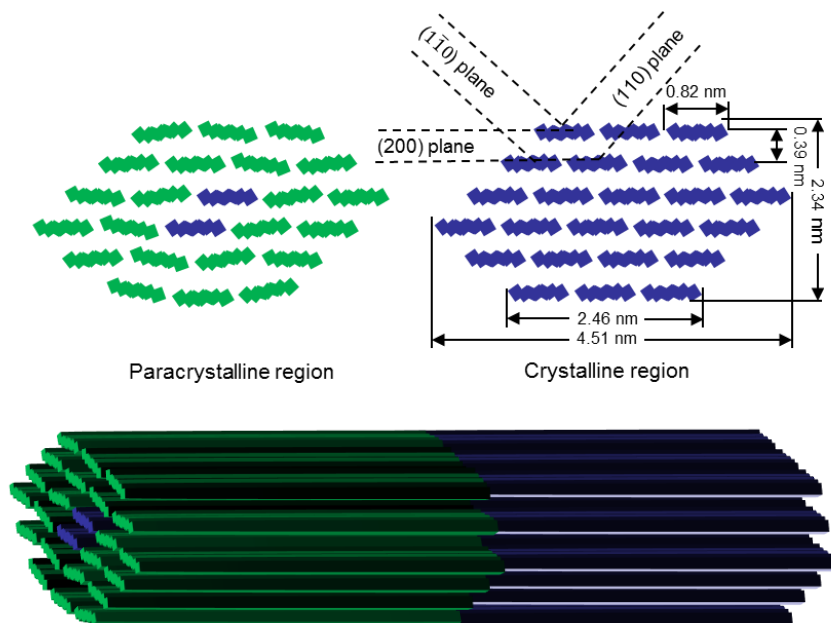


Figure 5.10. Schematic drawing of the refined 24-chain hexagonal-elliptical hybrid model for cellulose I β microfibril. Top left figure represents the cross section view of the paracrystalline region where the two core chains are in crystalline state (blue) and the outer layers are in non-crystalline state (green); top right figure represents cross section view of the crystalline region where all the chains are in crystalline state; bottom figure is the corresponding 3D view along the microfibril longitudinal direction, where the left half is in paracrystalline state and the right half is in crystalline state.

4. Conclusions

MT nanocellulose prepared through TEMPO-oxidation and sonication was examined by TEM and Solid State ^{13}C NMR for its width distribution profile, crystallinity, glycosidic linkage torsion angles, C6 primary hydroxyl conformations, as well as the changes of these indexes under different sonication time intervals. New findings from these characterizations were integrated with previous knowledge to refine the current models for cellulose microfibril cross section structure. The major conclusions are as follows:

MT nanocellulose width profile obtained from TEM indicates that sufficiently separated MT nanocellulose has a defined width range of approximate 2-5 nm, corresponding to the 3-6 chain structures in a specific sheet. Integrated with previous knowledge on thickness and length profiles, individual MT nanocellulose 3D structure is envisaged as an extended long flat ribbon with thickness nearly or below 1 nm (depending on layer number), width ranges from 2-5 nm (depending on chain number), and length varies from hundreds of nanometers to several microns. 60 min sonication is proved to be sufficient in isolating majority (ca. 75%) of the individual microfibrils from TEMPO-oxidized pulp.

Supramolecular structure changes of cellulose upon TEMPO-oxidation and sonication were monitored by solid state ^{13}C NMR. Oxidation of C6 primary hydroxyl group is confirmed by the emerging carboxylate peak at 175 ppm and its relative peak intensity agrees with the degree of oxidation. Peak separation method reveals that MT nanocellulose has lower crystallinity index than kraft pulp and TEMPO-oxidized cellulose; extended sonication time does not have further impact on reducing MT nanocellulose crystallinity. Glycosidic linkage torsion angles Φ and Ψ are not altered by TEMPO-oxidation but are impacted by sonication, appearing in NMR spectra

as the systematic upfield peak shifts. C6 hydroxyl group favors *gg* conformation when exposed to surface and/or oxidized, stereochemical preference and energy minimization are believed to be the major contributing factors.

Lastly, the cellulose microfibril “cross section triangle scheme” -visualizing the interdependent relationships among “cross section dimension”, “cross section shape”, and “chain packing numbers”- was developed to guide the cross section model refining process. A 24-chain hexagonal/elliptical hybrid model is believed to be the most credible representation of the microfibril configuration, with hexagonal portion representing the crystalline segments and elliptical representing the less ordered paracrystalline to non-crystalline region.

Appendix

Appendix 1. Tests of statistical significance for TEM width distributions

1. Nonparametric Mann-Whitney Test indicates that the average width of 5 min sonication samples is significantly greater than the average width of 30 min sonication.

Mann-Whitney Test (8/12/2012 09:26:06)

Notes

X-Function	Mann-Whitney Test
User Name	LQQ
Time	8/12/2012 09:26:06

Input Data

	Data	Range
1st Data Range	[RawData]Significance Test!5min	[1*:400*]
2nd Data Range	[RawData]Significance Test!30min	[1*:400*]

Descriptive Statistics

	N	Min	Q1	Median	Q3	Max
5min	400	2.26	4.2775	5.38	6.9225	13.8
30min	400	1.58	3.6325	4.455	5.3275	12.24

Ranks

	N	Mean Rank	Sum Rank
5min	400	471.585	188634
30min	400	329.415	131766

Test Statistics

	U	Z	Asymp. Prob>U
	108434	8.70056	0

Null Hypothesis: $F(x) \leq G(y)$
 Alternative Hypothesis: $F(x) > G(y)$
 At the 0.05 level, the x's do significantly tends to be greater than the y's

2. Nonparametric Mann-Whitney Test indicates that the average width of 30 min sonication samples is significantly greater than the average width of 60 min sonication.

Mann-Whitney Test (8/12/2012 09:28:38)

Notes

X-Function	Mann-Whitney Test
User Name	LQQ
Time	8/12/2012 09:28:38

Input Data

	Data	Range
1st Data Range	[RawData]Significance Test!30 min	[1*:400*]
2nd Data Range	[RawData]Significance Test!60 min	[1*:400*]

Descriptive Statistics

	N	Min	Q1	Median	Q3	Max
30min	400	1.58	3.6325	4.455	5.3275	12.24
60min	400	2.04	3.2825	4	4.6675	6.72

Ranks

	N	Mean Rank	Sum Rank
30min	400	448.54375	179417.5
60min	400	352.45625	140982.5

Test Statistics

	U	Z	Asymp. Prob>U
	99217.5	5.88036	2.0469E-9

Null Hypothesis: $F(x) \leq G(y)$
 Alternative Hypothesis: $F(x) > G(y)$
 At the 0.05 level, the x's do significantly tends to be greater than the y's

3. Nonparametric Mann-Whitney Test indicates that the average width of 60 min sonication samples is NOT significantly greater than the average width of 120 min sonication.

Mann-Whitney Test (8/12/2012 09:29:37)

Notes

X-Function	Mann-Whitney Test
User Name	LQQ
Time	8/12/2012 09:29:37

Input Data

	Data	Range
1st Data Range	[RawData]Significance Test!60 min	[1*:400*]
2nd Data Range	[RawData]Significance Test!120 min	[1*:400*]

Descriptive Statistics

	N	Min	Q1	Median	Q3	Max
60min	400	2.04	3.2825	4	4.6675	6.72
120min	400	2.08	3.3325	3.87	4.6175	6.2

Ranks

	N	Mean Rank	Sum Rank
60min	400	409.47125	163788.5
120min	400	391.52875	156611.5

Test Statistics

	U	Z	Asymp. Prob>U
	83588.5	1.09792	0.13612

Null Hypothesis: $F(x) \leq G(y)$
 Alternative Hypothesis: $F(x) > G(y)$
 At the 0.05 level, the x's do NOT significantly tends to be greater than the y's

4. Nonparametric Mann-Whitney Test indicates that the average width of 120 min sonication samples is NOT significantly greater than the average width of 240 min sonication.

Mann-Whitney Test (8/12/2012 09:31:12)

Notes

X-Function	Mann-Whitney Test
User Name	LQQ
Time	8/12/2012 09:31:12

Input Data

	Data	Range
1st Data Range	[RawData]Significance Test!12 0min	[1*:400*]
2nd Data Range	[RawData]Significance Test!24 0min	[1*:400*]

Descriptive Statistics

	N	Min	Q1	Median	Q3	Max
120min	400	2.08	3.3325	3.87	4.6175	6.2
240min	400	1.86	3.1	3.695	4.33	6.5

Ranks

	N	Mean Rank	Sum Rank
120min	400	430.49875	172199.5
240min	400	370.50125	148200.5

Test Statistics

	U	Z	Asymp. Prob>U
	91999.5	3.67168	1.2048E-4

Null Hypothesis: $F(x) \leq G(y)$
 Alternative Hypothesis: $F(x) > G(y)$
 At the 0.05 level, the x's do significantly tends to be greater than the y's

Appendix 2. Calculation of the dimensions of different chain packing arrangements

1. Determine unit cell area (UCA): $UCA = (a \cdot b \cdot \sin \gamma) / 2 = (0.778 \cdot 0.820 \cdot \sin 96.5^\circ) = 0.317$

2. Calculating cross-sectional area (CSA) for each arrangements: $CSA = UCA \cdot \text{Chain no.}$

a. 36 Chain $CSA = 0.317 \cdot 36 = 11.41$

b. 30 Chain $CSA = 0.317 \cdot 30 = 9.51$

c. 24 Chain $CSA = 0.317 \cdot 24 = 7.61$

3. Calculating dimensions for 36-chain cross section shapes

a. 36-Chain Hexagonal--sitting on (200) plane:

i. height = $CSA / (3\text{-chain length} + 6\text{-chain length}) \cdot 2 = [11.41 / (3 \cdot 0.82 + 6 \cdot 0.82)] \cdot 2 = 3.09$

ii. width = $6 \text{ chain} \cdot b/\text{chain} = 6 \cdot 0.820 = 4.92$

b. 36-Chain Hexagonal—sitting on (1 $\bar{1}$ 0) plane (see SI Figure 5.1 below for geometry):

i. height = $6\text{-layer} \cdot 0.595/\text{layer} = 3.57$

ii. width = $7\text{-layer} \cdot 0.532/\text{layer} = 3.72$

c. 36-Chain Hexagonal—sitting on (110) plane:

i. height = $7\text{-layer} \cdot 0.532/\text{layer} = 3.72$

ii. width = $6\text{-layer} \cdot 0.595/\text{layer} = 3.57$

d. 36-Chain Rectangular:

i. height = $CSA/\text{width} = 11.41/4.92 = 2.32$

ii. width = $6 \text{ chain} \cdot b/\text{chain} = 6 \cdot 0.820 = 4.92$

e. 36-Chain Elliptical:

i. height = 2.95 (Using "[Ellipse Calculator](#)")

ii. width = 4.92 (Assuming 6-chain length)

4. Calculating dimensions for 30-chain cross section shapes by scaling down from the

36-chain parameters—times a factor of $\sqrt{30/36}$ on width and height, respectively:

a. 30-Chain Hexagonal—sitting on (200) plane:

i. height=3.09 * $\sqrt{30/36}$ = 2.82

ii. width= 4.92 * $\sqrt{30/36}$ =4.49

b. 30-Chain Hexagonal—sitting on (1 $\bar{1}$ 0) plane:

i. height= 3.57 * $\sqrt{30/36}$ = 3.26

ii. width= 3.72 * $\sqrt{30/36}$ = 3.40

c. 30-Chain Hexagonal—sitting on (110) plane:

i. height= 3.72 * $\sqrt{30/36}$ = 3.40

ii. width= 3.57 * $\sqrt{30/36}$ = 3.26

d. 30-Chain Rectangular:

i. height= 2.32 * $\sqrt{30/36}$ = 2.12

ii. width= 4.92 * $\sqrt{30/36}$ = 4.49

e. 30-Chain Elliptical:

i. height = 2.95 * $\sqrt{30/36}$ = 2.69

ii. width = 4.92 * $\sqrt{30/36}$ = 4.49

5. Calculating dimensions for 24-chain cross section shapes by scaling down from the

36-chain parameters—times a factor of $\sqrt{24/36}$ on width and height, respectively:

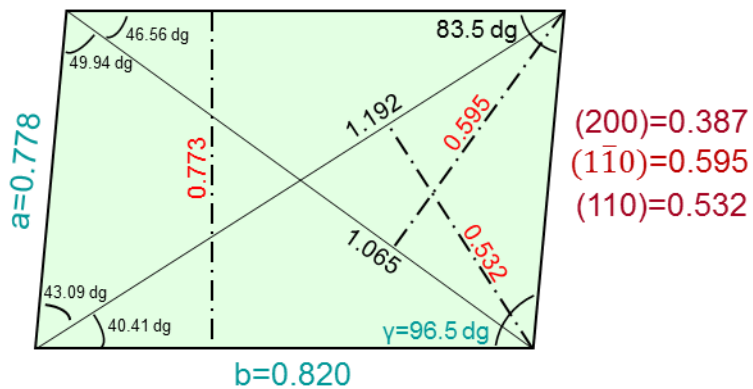
a. 24-Chain Hexagonal—sitting on (200) plane:

i. height=3.09 * $\sqrt{24/36}$ = 2.52

ii. width= 4.92 * $\sqrt{24/36}$ =4.02

b. 24-Chain Hexagonal—sitting on (1 $\bar{1}$ 0) plane:

- i. height= $3.57 * \sqrt{24/36} = 2.91$
 - ii. width= $3.72 * \sqrt{24/36} = 3.04$
- c. 24-Chain Hexagonal—sitting on (110) plane:
- i. height= $3.72 * \sqrt{24/36} = 3.04$
 - ii. width= $3.57 * \sqrt{24/36} = 2.91$
- d. 24-Chain Rectangular:
- i. height= $2.32 * \sqrt{24/36} = 1.89$
 - ii. width= $4.92 * \sqrt{24/36} = 4.02$
- e. 24-Chain Elliptical:
- i. height = $2.95 * \sqrt{24/36} = 2.41$
 - ii. width = $4.92 * \sqrt{24/36} = 4.02$



SI Figure 5.1. Cellulose I β unit cell geometry

Reference

1. Li, Q.; Renneckar, S., Molecularly thin nanoparticles from cellulose: isolation of sub-microfibrillar structures. *Cellulose (Dordrecht, Netherlands)* **2009**, *16* (6), 1025-1032.
2. Klemm, D.; Heublein, B.; Fink, H. P.; Bohn, A., Cellulose: Fascinating biopolymer and sustainable raw material. *Angew. Chem.-Int. Edit.* **2005**, *44* (22), 3358-3393.
3. Klemm, D.; Kramer, F.; Moritz, S.; Lindström, T.; Ankerfors, M.; Gray, D.; Dorris, A., Nanocelluloses: A New Family of Nature-Based Materials. *Angewandte Chemie International Edition* **2011**, *50* (24), 5438-5466.
4. Isogai, A.; Saito, T.; Fukuzumi, H., TEMPO-oxidized cellulose nanofibers. *Nanoscale* **2011**, *3* (1), 71-85.
5. Li, Q.; Renneckar, S., Supramolecular Structure Characterization of Molecularly Thin Cellulose I Nanoparticles. *Biomacromolecules* **2011**, *12* (3), 650-659.
6. Navarro, F. Cellulose Nanocrystals: Size Characterization and Controlled Deposition by Inkjet Printing. Virginia Tech, 2010.
7. (a) Elazzouzi-Hafraoui, S.; Nishiyama, Y.; Putaux, J. L.; Heux, L.; Dubreuil, F.; Rochas, C., The shape and size distribution of crystalline nanoparticles prepared by acid hydrolysis of native cellulose. *Biomacromolecules* **2008**, *9* (1), 57-65; (b) Shinoda, R.; Saito, T.; Okita, Y.; Isogai, A., Relationship between Length and Degree of Polymerization of TEMPO-Oxidized Cellulose Nanofibrils. *Biomacromolecules* **2012**; (c) Eichhorn, S. J., Cellulose nanowhiskers: promising materials for advanced applications. *Soft Matter* **2011**, *7* (Copyright (C) 2011 American Chemical Society (ACS). All Rights Reserved.), 303-315; (d) Eichhorn, S. J.; Dufresne, A.; Aranguren, M.; Marcovich, N. E.; Capadona, J. R.; Rowan, S. J.; Weder, C.; Thielemans, W.; Roman, M.; Renneckar, S.; Gindl, W.; Veigel, S.; Keckes, J.; Yano, H.; Abe, K.; Nogi, M.; Nakagaito, A. N.; Mangalam, A.; Simonsen, J.; Benight, A. S.; Bismarck, A.; Berglund, L. A.; Peijs, T., Review: current international research into cellulose nanofibres and nanocomposites. *J. Mater. Sci.* **2010**, *45* (1), 1-33; (e) Saito, T.; Hirota, M.; Tamura, N.; Kimura, S.; Fukuzumi, H.; Heux, L.; Isogai, A., Individualization of Nano-Sized Plant Cellulose Fibrils by Direct Surface Carboxylation Using TEMPO Catalyst under Neutral Conditions. *Biomacromolecules* **2009**, *10* (7),

- 1992-1996; (f) Saito, N.; Usui, Y.; Aoki, K.; Narita, N.; Shimizu, M.; Hara, K.; Ogiwara, N.; Nakamura, K.; Ishigaki, N.; Kato, H.; Taruta, S.; Endo, M., Carbon nanotubes: biomaterial applications. *Chem. Soc. Rev.* **2009**, *38* (7), 1897-1903; (g) Johnson, R. K.; Zink-Sharp, A.; Renneckar, S. H.; Glasser, W. G., A new bio-based nanocomposite: fibrillated TEMPO-oxidized celluloses in hydroxypropylcellulose matrix. *Cellulose (Dordrecht, Netherlands)* **2009**, *16* (2), 227-238; (h) Samir, M.; Alloin, F.; Dufresne, A., Review of recent research into cellulosic whiskers, their properties and their application in nanocomposite field. *Biomacromolecules* **2005**, *6* (2), 612-626.
8. (a) Zuckerstaetter, G., The elucidation of cellulose supramolecular structure by ¹³C CP-MAS NMR. *Lenzinger Berichte* **2009**, *87*, 38; (b) Ibbett, R. N.; Domvoglu, D.; Fasching, M., Characterisation of the supramolecular structure of chemically and physically modified regenerated cellulosic fibres by means of high-resolution Carbon-13 solid-state NMR. *Polymer* **2007**, *48* (5), 1287-1296; (c) Atalla, R. H.; VanderHart, D. L., The role of solid-state carbon-13 NMR spectroscopy in studies of the nature of native celluloses. *Solid State Nucl. Magn. Reson.* **1999**, *15* (Copyright (C) 2011 American Chemical Society (ACS). All Rights Reserved.), 1-19.
9. Atalla, R. H.; Isogai, A., Recent developments in spectroscopic and chemical characterization of cellulose. *Polysaccharides (2nd Edition)* **2005**, 123-157.
10. Suzuki, S.; Horii, F.; Kurosu, H., Theoretical investigations of ¹³C chemical shifts in glucose, cellobiose, and native cellulose by quantum chemistry calculations. *J. Mol. Struct.* **2009**, *921* (Copyright (C) 2011 American Chemical Society (ACS). All Rights Reserved.), 219-226.
11. French, A.; Johnson, G., What crystals of small analogs are trying to tell us about cellulose structure. *Cellulose* **2004**, *11* (1), 5-22.
12. Vietor, R. J.; Newman, R. H.; Ha, M.-A.; Apperley, D. C.; Jarvis, M. C., Conformational features of crystal-surface cellulose from higher plants. *Plant J.* **2002**, *30* (Copyright (C) 2011 American Chemical Society (ACS). All Rights Reserved.), 721-731.
13. Frey-Wyssling, A., The fine structure of cellulose microfibrils. *Science (Washington, DC, United States)* **1954**, *119*, 80-2.

14. Fernandes, A. N.; Thomas, L. H.; Altaner, C. M.; Callow, P.; Forsyth, V. T.; Apperley, D. C.; Kennedy, C. J.; Jarvis, M. C., Nanostructure of cellulose microfibrils in spruce wood. *Proceedings of the National Academy of Sciences* **2011**.
15. Leppänen, K.; Andersson, S.; Torkkeli, M.; Knaapila, M.; Kotelnikova, N.; Serimaa, R., Structure of cellulose and microcrystalline cellulose from various wood species, cotton and flax studied by X-ray scattering. *Cellulose* **2009**, *16* (6), 999-1015.
16. Mueller, S. C.; Brown, R. M., Jr., Evidence for an intramembrane component associated with a cellulose microfibril-synthesizing complex in higher plants. *J Cell Biol* **1980**, *84* (Copyright (C) 2011 U.S. National Library of Medicine.), 315-26.
17. (a) Doblin, M. S.; Kurek, I.; Jacob-Wilk, D.; Delmer, D. P., Cellulose biosynthesis in plants: from genes to rosettes. *Plant Cell Physiol.* **2002**, *43* (12), 1407-1420; (b) Brown, R. M.; Saxena, I. M., Cellulose biosynthesis: A model for understanding the assembly of biopolymers. *Plant Physiology and Biochemistry* **2000**, *38* (1-2), 57-67.
18. (a) Endler, A.; Persson, S., Cellulose Synthases and Synthesis in Arabidopsis. *Mol. Plant.* **2011**, *4* (2), 199-211; (b) Ding, S.; Himmel, M. E., The Maize Primary Cell Wall Microfibril: A New Model Derived from Direct Visualization. *J. Agric. Food Chem* **2006**, *54* (3), 597-606.
19. (a) Saxena, I. M.; Brown, R. M., Cellulose Biosynthesis: Current Views and Evolving Concepts. *Annals of Botany* **2005**, *96* (1), 9-21; (b) Somerville, C.; Bauer, S.; Brininstool, G.; Facette, M.; Hamann, T.; Milne, J.; Osborne, E.; Paredez, A.; Persson, S.; Raab, T.; Vorwerk, S.; Youngs, H., Toward a systems approach to understanding plant-cell walls. *Science* **2004**, *306* (5705), 2206-2211; (c) Bessueille, L., A survey of cellulose biosynthesis in higher plants. *Plant biotechnology (Tokyo, Japan)* **2008**, *25*, 315.
20. Katz, S.; Beatson, R. P.; Scallan, A. M., The determination of strong and weak acidic groups in sulfite pulps. *Svensk Papperstidning* **1984**, *87* (6), R48-R53.
21. Saito, T.; Okita, Y.; Nge, T. T.; Sugiyama, J.; Isogai, A., TEMPO-mediated oxidation of native cellulose: Microscopic analysis of fibrous fractions in the oxidized products. *Carbohydrate Polymers* **2006**, *65* (4), 435-440.

22. Emons, A. M. C., METHODS FOR VISUALIZING CELL-WALL TEXTURE. *Acta Botanica Neerlandica* **1988**, 37 (1), 31-38.
23. Atalla, R. H.; Brady, J. W.; Matthews, J. F.; Ding, S.-Y.; Himmel, M. E., Structures of Plant Cell Wall Celluloses. In *Biomass recalcitrance: deconstructing the plant cell wall for bioenergy*, Himmel, M. E., Ed. Blackwell Pub.: Oxford, 2008; Vol. xviii, 505 p.
24. Hult, E. L.; Larsson, P. T.; Iversen, T., A comparative CP/MAS C-13-NMR study of the supermolecular structure of polysaccharides in sulphite and kraft pulps. *Holzforschung* **2002**, 56 (2), 179-184.
25. Park, S.; Baker, J.; Himmel, M.; Parilla, P.; Johnson, D., Cellulose crystallinity index: measurement techniques and their impact on interpreting cellulase performance. *Biotechnology for Biofuels* **2010**, 3 (1), 10.
26. Rondeau-Mouro, C.; Bizot, H.; Bertrand, D., Chemometric analyses of the 1H-13C cross-polarization build-up of celluloses NMR spectra: A novel approach for characterizing the cellulose crystallites. *Carbohydrate Polymers* **2011**, 84 (Copyright (C) 2011 American Chemical Society (ACS). All Rights Reserved.), 539-549.
27. Sjöström, E., *Wood Chemistry: Fundamentals and Applications, 2nd Edition*. 1993; p 293.
28. Saito, T.; Isogai, A., TEMPO-Mediated Oxidation of Native Cellulose. The Effect of Oxidation Conditions on Chemical and Crystal Structures of the Water-Insoluble Fractions. *Biomacromolecules* **2004**, 5 (5), 1983-1989.
29. Okita, Y.; Saito, T.; Isogai, A., Entire Surface Oxidation of Various Cellulose Microfibrils by TEMPO-Mediated Oxidation. *Biomacromolecules* **2010**, 11 (6), 1696-1700.
30. (a) Jarvis, M. C., Relationship of chemical shift to glycosidic conformation in the solid-state 13C NMR spectra of (1→4)-linked glucose polymers and oligomers: anomeric and related effects. *Carbohydr. Res.* **1994**, 259 (Copyright (C) 2011 American Chemical Society (ACS). All Rights Reserved.), 311-18; (b) Horii, F.; Hirai, A.; Kitamaru, R., Cross-Polarization-Magic Angle Spinning Carbon-13 NMR Approach to the Structural Analysis of Cellulose. In *The Structures of Cellulose*, American Chemical Society: 1987; Vol. 340, pp 119-134.

31. Newman, R. H., Evidence for assignment of C-13 NMR signals to cellulose crystallite surfaces in wood, pulp and isolated celluloses. *Holzforschung* **1998**, *52* (2), 157-159.
32. Hult, E. L.; Larsson, P. T.; Iversen, T., A comparative CP/MAS C-13-NMR study of cellulose structure in spruce wood and kraft pulp. *Cellulose* **2000**, *7* (1), 35-55.
33. Horii, F.; Hirai, A.; Kitamaru, R., Solid-state ¹³C-NMR study of conformations of oligosaccharides and cellulose. *Polymer Bulletin* **1983**, *10* (7), 357-361.
34. Newman, R.; Davidson, T., Molecular conformations at the cellulose–water interface. *Cellulose* **2004**, *11* (1), 23-32.
35. (a) Maréchal, Y.; Chanzy, H., The hydrogen bond network in I[beta] cellulose as observed by infrared spectrometry. *Journal of Molecular Structure* **2000**, *523* (1-3), 183-196; (b) Kondo, T., Hydrogen bonds in cellulose and cellulose derivatives. In *Polysaccharides (2nd Edition)*, 2005; pp 69-98.
36. Horii, F.; Hirai, A.; Kitamaru, R., Solid-State High-Resolution ¹³C-NMR Studies of Regenerated Cellulose Samples with Different Crystallinities. *Polymer Bulletin* **1982**, *8* (2), 163-170.
37. (a) Fengel, D., Ultrastructural Behavior of Cell Wall Polysaccharides. *Tappi* **1970**, *53* (3), 7; (b) Brown, R. M., Cellulose structure and biosynthesis: What is in store for the 21st century? *Journal of Polymer Science Part A: Polymer Chemistry* **2004**, *42* (3), 487-495; (c) Osullivan, A. C., Cellulose: the structure slowly unravels. *Cellulose* **1997**, *4* (3), 173-207; (d) Hult, E. L.; Iversen, T.; Sugiyama, J., Characterization of the supermolecular structure of cellulose in wood pulp fibres. *Cellulose* **2003**, *10* (2), 103-110; (e) Jakob, H. F.; Fengel, D.; Tschegg, S. E.; Fratzl, P., The Elementary Cellulose Fibril in Picea abies: Comparison of Transmission Electron Microscopy, Small-Angle X-ray Scattering, and Wide-Angle X-ray Scattering Results. *Macromolecules* **1995**, *28* (26), 8782-8787.
38. Nishiyama, Y., Structure and properties of the cellulose microfibril. *Journal of Wood Science* **2009**, *55* (4), 241-249.
39. Frey-Wyssling, A.; Muehlenthaler, K., The elementary fibrils of cellulose. *Makromol. Chem.* **1963**, *62* (Copyright (C) 2011 American Chemical Society (ACS). All Rights Reserved.), 25-30.
40. Beck-Candanedo, S.; Roman, M.; Gray, D. G., Effect of Reaction Conditions on the Properties and Behavior of Wood Cellulose Nanocrystal Suspensions. *Biomacromolecules* **2005**, *6* (2), 1048-1054.

41. Somerville, C., Cellulose synthesis in higher plants. *Annu. Rev. Cell Dev. Biol.* **2006**, *22*, 53-78.
42. Herth, W., Arrays of plasma-membrane "rosettes" involved in cellulose microfibril formation of Spirogyra. *Planta* **1983**, *159* (4), 347-356.
43. Kennedy, C. J.; Cameron, G. J.; Sturcova, A.; Apperley, D. C.; Altaner, C.; Wess, T. J.; Jarvis, M. C., Microfibril diameter in celery collenchyma cellulose: X-ray scattering and NMR evidence. *Cellulose (Dordrecht, Netherlands)* **2007**, *14* (Copyright (C) 2011 American Chemical Society (ACS). All Rights Reserved.), 235-246.
44. (a) Hanley, S. J.; Giasson, J.; Revol, J. F.; Gray, D. G., ATOMIC FORCE MICROSCOPY OF CELLULOSE MICROFIBRILS - COMPARISON WITH TRANSMISSION ELECTRON-MICROSCOPY. *Polymer* **1992**, *33* (21), 4639-4642; (b) Knoll, A.; Magerle, R.; Krausch, G., Tapping Mode Atomic Force Microscopy on Polymers: Where Is the True Sample Surface? *Macromolecules* **2001**, *34* (12), 4159-4165.
45. Nishiyama, Y.; Langan, P.; Chanzy, H., Crystal Structure and Hydrogen-Bonding System in Cellulose I β from Synchrotron X-ray and Neutron Fiber Diffraction. *Journal of the American Chemical Society* **2002**, *124* (31), 9074-9082.
46. Klug, H. P.; Alexander, L. E., *X-Ray Diffraction Procedures for Polycrystalline and Amorphous Materials*. 2nd ed. Wiley-Interscience: 1974; p 966 pp.

CHAPTER 6

Nanocellulose Life Cycle Assessment

Abstract

Nanocellulose is a nascent and promising material with many exceptional properties and a broad spectrum of potential applications. Because of the unique and functional materials that can be created using nanocellulose, pilot-scale development for commercialization has begun. Thus a thorough understanding of its environmental impact, covering every aspect of the whole life cycle of nanocellulose, becomes the foundation for its long-term sustainable success. In this current study, four comparable lab scale nanocellulose fabrication routes were evaluated through a cradle-to-gate life cycle assessment (LCA) adopting the Eco-Indicator 99 method. The results indicated that for the chemical-mechanical fabrication routes the majority of the environmental impact of nanocellulose fabrication is attributed to the mechanical treatments and the difference overshadows that from the chemical modifications. Adapting the best practice based on unit mass production was 2,2,6,6-tetramethylpiperidine-1-oxyl (TEMPO) oxidation followed by homogenization; whereas when based on batch production, the best practice is TEMPO-oxidation followed by sonication. Even though the fabrication process of nanocellulose presents a large environmental footprint markup relative to its raw material extraction process (kraft pulping), it still exhibits prominent environmental advantages over other popular nanomaterials like carbon nanotubes.

1. Introduction

The commercialization of nanocellulose is forthcoming with the projected GPD of \$600 billion worldwide by 2020,¹ hence it is critical that we understand how much environmental impact the fabrication process will generate and design the best manufacturing system accordingly. Life cycle assessment (also known as life cycle analysis, LCA) can be used for evaluating the cumulative environmental impact associated with all stages of fabrication of materials from the initial extraction of raw materials (cradle) through the end-of-life disposal of final products (grave).² LCA enables the selection of best fabrication methods with quantified indexes (LCA scores) related to environmental impact.^{2b-d,3} LCA requires careful goal and scope definition in order to define the objectives, the functional unit, and the system boundaries. Based on the systems boundaries a life cycle inventory analysis (LCI) is performed that documents and quantifies inputs related to the material and energy flows. The power of life cycle impact assessment (LCIA) is the transformation of the inventory data into comparable values in standardized categories. Based on the data analysis, meaningful insights and conclusions can be determined to estimate environment impact of products.^{2c}

Cellulose is a naturally occurring biopolymer and has been recognized for its many environmentally friendly characteristics, such as biodegradability and biocompatibility.⁴ Cellulose exists in a supramolecular structure in its native state, with the individual polymer chains assembled together in fibrils of a few nanometers in cross-section, with dimensions dependent on plant type. Isolated cellulose with at least one dimension in the nanometer range (usually below 100 nm) exhibits novel properties associated with its size is referred to as nanocellulose.^{4b, 5} Nanocellulose is used in many material applications such as polymer reinforcement⁶ and transparent films.⁷ Nanocellulose can be prepared through many different approaches, which can be classified into two general categories: top-down and bottom-up.^{4a, 8} The top-down approaches, which obtain nanocelluloses by extracting cellulose particles from various sources⁹ typically involve intensive mechanical and/or chemical treatments to deconstruct the intrinsic native structures from the plant cell wall. Top down approaches can be further divided into three subcategories: mechanical, chemical, and chemical-mechanical. The bottom-up approaches assemble cellulose nanostructures either from the solution state of cellulose molecules or utilize the biosynthesis process.^{4b, 8} Based on the preparation methods and raw material origin, nanocelluloses are conventionally classified into three sub-categories (Figure 6.1): i) microfibrillated cellulose or MFC, an elongated fibril form of nanocellulose, is prepared

from wood and other plant fibers via chemical, mechanical, or combined treatments; ii) nanocrystalline cellulose or NCC (cellulose nanocrystals, crystallites, whiskers), is a rodlike highly crystalline form of nanocellulose, prepared from a broader range of raw materials including plant, animal, or bacteria originated cellulose via acid hydrolysis; iii) bacterial nanocellulose or BNC (a.k.a.: bacterial cellulose, microbial cellulose, biocellulose), is a network form of nanocellulose, arising from the biofilm produced by certain bacteria, consuming only low-molecular-weight sugars and alcohols.^{4b, 10}

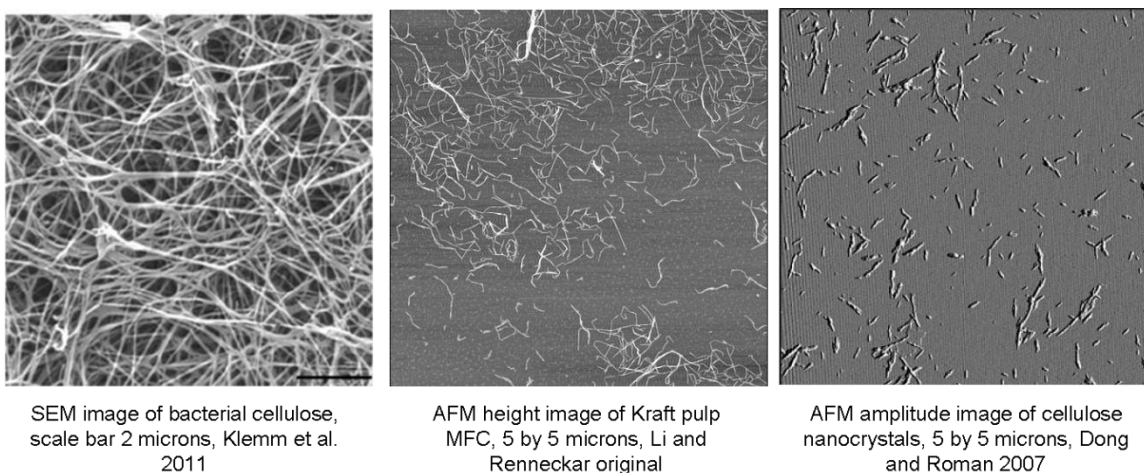


Figure 6.1. Images of different types of nanocelluloses^{4b, 11} Reprinted with permissions from reference 4b and 11, respectively. Copyright (2011) John Wiley and Sons and (2007) American Chemical Society.

Nanocelluloses have developed applications across a number of markets and thus will have an increasing impact on consumer, health, food, and industrial goods. MFC finds its applications in paper making as reinforcement agents or functional coatings (e.g.: grease proofing or moisture absorbing), and in food, cosmetic, pharmaceutical, and hygiene products as the emulsion and/or dispersion additives, as well as in various nanocomposites and films as structural components. All these applications are built on MFC's unique combination of properties: surface chemistry, water retention, large aspect ratio, large specific strength, rheology and optical characteristics, as well as its universal compatibility with natural and biological environment.^{4a, b, 5, 10b} As for NCC, the most intriguing property is its self-ordering into chiral nematic phases. The most readily implementable applications are based on mechanical properties which allow use as a reinforcement agent in composite films to increase strength.^{4a, b, 4e, 11} This form of nanocellulose also shows potential applications in nano-medicines.¹¹⁻¹² BNC has many properties that set it

apart from MFC and NCC such as it forms a stable nanofiber network, has shapability during biosynthesis, exhibits excellent mechanical strength while maintaining high flexibility, and has been proved to be non-cytotoxic and non-genotoxic.^{4b} These properties lend BNC into the novel application fields like food gels, artificial blood vessels, wound dressing material, fuel cell membranes, and even films for electronic appliances.^{4b} An example for the successful commercialization of BNC in food industry is the Nata de coco-- a jelly-like food product produced via *Acetobacter xylinus* fermenting in coconut milk.¹³

MFC is one of the most widely studied nanocelluloses prepared from different approaches including: pure mechanical treatment or combined chemical-mechanical treatment (chemical pretreatment followed by mechanical agitation). First described by Turbak et al in 1983, homogenization processes different types of pulps with intensive shear treatments with controlled pass numbers through a small orifice at high pressure.^{10b, 14} The predominant end product has a net-like structure, with a diameter ranging from 25-100 nm in dry state. Because releasing nanocellulose from native cellulose fibers requires the disruption of the hydrogen bonding system, the energy consumption is relatively large (25,000 kWh/t), which becomes the major impediment of its commercial success.^{4b, 10b} Sonication is another technique to overcome the inter-fibril bonds within pulp fibers. The first work to produce MFC with mechanical agitation method was reported by Wuhrmann et al in 1946, where plant fibers from ramie, hemp, and cotton were subjected to intensive sonication treatment and fine fibrils (6-7 nm width) were yielded solely as a function of the mechanical agitation intensity.¹⁵ Inspired by Wuhrmann's work, many groups have employed sonication as a major avenue to isolate nanocellulose.^{6b, 7a, 16} Different chemical pretreatments (e.g.: oxidation,^{16d} carboxymethylation,^{7a, 17} acid hydrolysis,¹⁸ and enzymatic hydrolysis¹⁹), mechanical agitations (e.g.: sonication, homogenization, blending, etc.), as well as their different combinations have been extensively investigated to generate MFC.^{4e, 20} The most common chemical-mechanical approach is to modify the cellulose fiber surface via carboxylation or carboxymethylation reactions (e.g.: TEMPO oxidation,²¹ chloroacetic acid etherification¹⁷) to introduce negative charges onto the microfibril surface allowing easy separation; the modified fibers are subjected to mild to intensive mechanical treatments to liberate MFC from the raw materials.²⁰ The end product, MFC, is in long fibril forms with lateral dimensions of single digit nanometers (or even sub-nanometers) and hundreds of nanometer to several microns in length.^{16b, 22}

Given all the promising applications, however, the commercialization of the MFC

nanocellulose is still in its early stage.^{1, 4a, 4e} The primary reason, except for the on-going efforts of identifying the best marketplace beyond the conventional stereotype of “stronger and stiffer” reinforcement agent for structural materials^{4a} is actually the high energy consumption and capital cost for industrial scale production,^{4b} which neutralizes the intrinsic eco-friendly characteristics of nanocelluloses if not properly addressed. Therefore comprehensive LCA for nanocelluloses (especially the energy consumption analysis during production) are an essential step in their commercialization efforts as well as enhancing this emerging industry’s responsible and sustainable development.

Besides the energy consumption concern, there is also the tendency to assume that nanocellulose should share the same favorable environmental impact as its precursor such as wood pulp, since the nanoscale particles are isolated directly from cellulose.^{4b, 5, 8} However, the processes of isolating nanocellulose via chemical modifications and mechanical disintegrations can involve polluting or toxic chemicals and energy intensive steps,¹⁴ which may produce significant environmental burdens, and may neutralize or even overshadow the inherent environmental benefits using cellulose. LCA can be utilized to gauge the cumulative environmental impact associated with the nanocellulose fabrication process, reveal the relative environmental footprint markup to its precursor raw material, and provide an impartial reference to assess the environmental attributes of different nanomaterials that serve similar applications (i.e. polymer reinforcement). To the best of our knowledge, no LCA work has been done on nanocellulose, so very little is known in regarding to the environmental impact associated with its fabrication process. Although many fabrication methods/ routes have been suggested and practiced in lab setting, there are no quantitative justifications available yet from the environmental perspective on the best practice, which makes further improvement ineffective. Therefore, LCA can guide the emerging fabrication technologies towards reducing environmental footprints through early identification of leverage points,²³ and the data collected at laboratory scale have important implications for the large scale industrial production.

In this LCA, four comparable chemical-mechanical approaches for lab scale nanocellulose fabrication (TEMPO-oxidation followed by sonication or homogenization, chloroacetic etherification followed by sonication or homogenization) were examined with the Eco-Indicator 99 method. The overall environmental impacts cumulated across these fabrication routes were quantified. The best practice, which yielded the least environmental footprint, was identified under two different scenarios. The most environmental demanding step across the fabrication

process flow was determined based on the impact scores. The LCA results were also compared with the kraft pulping process, where nanocellulose’s precursor was produced, to indicate the relative environmental impact markup attributed to nanocellulose. Lastly, the nanocellulose LCA results were compared against another familiar nanomaterial, single-walled carbon nanotubes, which serve similar applications in polymer composite reinforcement, to gain additional insights.

2. Materials and methods

2.1. Scope definition

The system boundary of this LCA (Figure 6.2) is defined as “cradle-to-gate”. This boundary includes the steps associated with the nanocellulose fabrication, starting from delignified kraft pulp, followed by chemical modification, mechanical disintegration, and purifying, until the final product nanocellulose is ready to deliver at the “factory gate” in the wet state. The system inputs taken into considerations are wood pulp, energy (in the form of electricity), chemicals, and water; the corresponding outputs were final product nanocellulose, and all emissions in gas, liquid and solid phases. The system boundary however excludes all upstream processes for producing raw material (delignified kraft pulp) related to chemicals, electricity, and water, since these are independent from the nanocellulose fabrication process. The LCA functional unit is defined as 10 g equivalent dry mass of the end product nanocellulose.

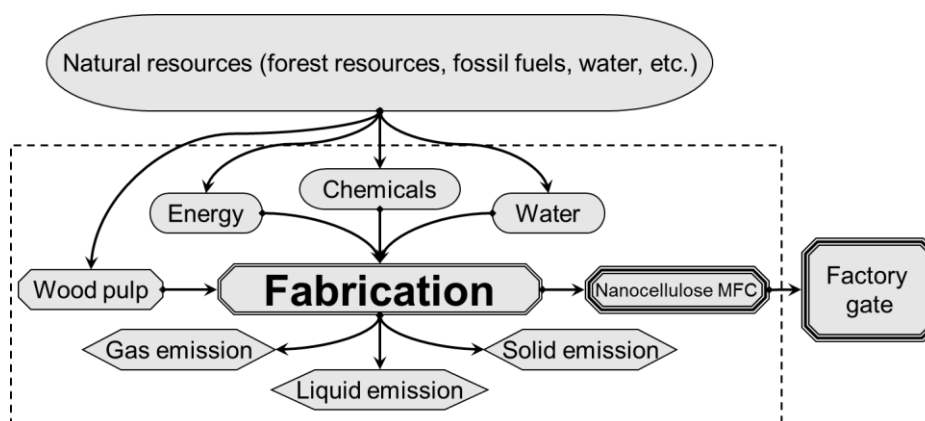


Figure 6.2. Cradle-to-gate LCA system boundary (indicated by the dashed line box) of lab-scale nanocellulose fabrication

2.2. Nanocellulose (MFC) fabrication process description

The nanocellulose fabrication routes evaluated in this LCA are presented in Figure 6.3. Fabrication comprised a chemical modification process, a mechanical disintegration process, and a centrifuge purifying process (only for sonication treated samples). Two comparable methods for both chemical modification and mechanical disintegration processes were selected. The starting material, delignified kraft pulp (kindly donated by Weyerhaeuser Company), was converted to nanocellulose. As a result, four different fabrication routes were designed, indicated with four colors (Figure 6.3): the red route is TOSO (TEMPO-oxidation for chemical modification, sonication for mechanical disintegration), the green route is TOHO (TEMPO-oxidation for chemical modification, homogenization for mechanical disintegration), the yellow route is CESO (chloroacetic acid etherification for chemical modification, sonication for mechanical disintegration), and the blue route is CEHO (chloroacetic acid etherification for chemical modification, homogenization for mechanical disintegration). Primary data for TEMPO oxidation was collected for this study, while the chloroacetic acid modification relied on previously reported inputs.¹⁷

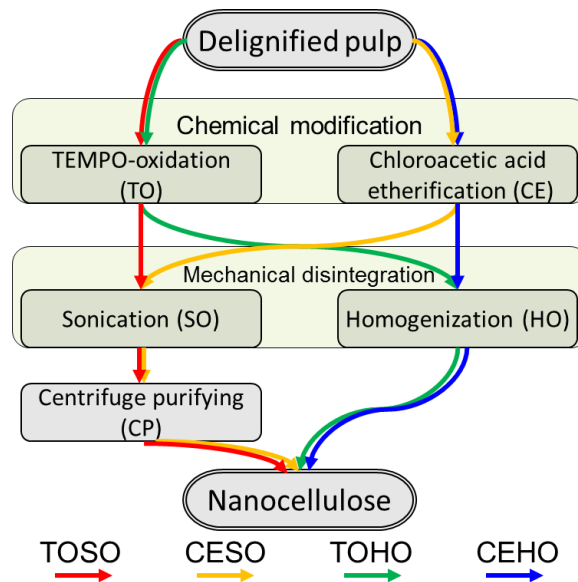


Figure 6.3. Cellulose MFC fabrication process flow, with colored arrows indicating 4 distinct path ways: red—TOSO, yellow—CESO, green—TOHO, and blue—CEHO.

Chemical and mechanical processes descriptions

Chemical modification process, TEMPO oxidation (TO): delignified kraft pulp was oxidized following previously reported techniques with the key parameter controlling oxidation of NaClO

at 5 mmol per gram of dry fiber.^{16b} System inputs included: 10 g equivalent dry mass of kraft pulp, 0.06 g of 2,2,6,6-tetramethylpiperidine-1-oxyl (TEMPO), 2.4 g of sodium bromide (NaBr) powder, 21.4 mL of sodium hypochlorite solution (13% w/w concentration), 50 ml of 0.5 N sodium hydroxide (NaOH) solution (for controlling the pH environment), 5.5 L of deionized water (0.5 L for reaction and 5 L for washing), 200 mL of ethanol (for quenching the reaction), and electricity to power the experiment equipment (over-head blender, syringe pump, and pH meter). System outputs were surface modified pulp (oxidized cellulose, intermediate product) and liquid emissions.

Chemical modification process of chloroacetic acid etherification (CE): delignified kraft pulp was dispersed in aqueous suspension, and then aqueous NaOH and chloroacetic acid were added into the system in sequence to activate the reaction at 60 °C. The reaction was stopped by cooling down to room temperature and adjusting the pH to neutral range after 2 h.¹⁷ System inputs included: 10 g equivalent dry mass of delignified kraft pulp, 1.41 g of NaOH powder, 2.12 g of chloroacetic acid powder, 5.12 L of deionized water (0.12 L for reaction and 5 L for washing), 435 g of isopropanol, and 262 g of ethanol. System outputs were surface modified pulp (carboxymethylated cellulose, intermediate product) and liquid emissions.

Mechanical disintegration process by homogenization (HO): chemically modified pulp was processed with high-pressure homogenizer (Mini DeBEE) under certain pressure range (10-15 MPa) and for designated pass numbers (2 passes for this LCA) to produce nanocellulose. System inputs were chemically modified pulp and electricity; output was end product nanocellulose. Batch size is defined as 1 g/ batch, equivalent to a concentration of 0.2 g wt% in 500 mL DI water.

Mechanical disintegration process by sonication (SO): chemically modified pulp was subjected to intensive sonication treatment (a 19 mm diameter horn was used to sonicate the modified pulp at 20 kHz, VC700, Sonics & Materials) for designated time intervals (30 min for this LCA) to produce nanocellulose. System inputs were chemically modified pulp and electricity; output was unpurified nanocellulose (with titanium impurities from the sonication process). Batch size is defined as 0.3 g/ batch, equivalent to a concentration of 0.1 g wt% in 300 mL DI water.

Centrifuge purification (CP): nanocellulose after sonication needed to be purified through

centrifugation (15 min @ 5000 rpm, Eppendorf centrifuge 5804) to remove the titanium particle impurities introduced during the sonication. System inputs were unpurified sonicated nanocellulose suspensions and electricity; outputs are end product nanocellulose, solid and liquid emissions.

2.3. Key assumptions

The following assumptions are made to facilitate the LCA of nanocellulose from the above laboratory practices.

1. Kraft pulp (starting material) loss during the fabrication process is negligible. The material mass balance indicated that although weight loss may occur during the washing, transferring, and purifying steps, the total weight loss is below 3%. For simplicity consideration, we assume this weight loss exerts no significant influence to the LCA result.
2. The two chemical modification processes (TO and CE) produce comparable surface charged cellulose fibers. The TO modified pulp is carboxylated cellulose (with C6 converted to carboxyl group, DS~ 0.23) while CE modified pulp is carboxymethylated cellulose (with primary hydroxyl groups converted to carboxymethyl group, DS~ 0.13), so the chemical structures are slightly different and degrees of substitution are also different.^{4c, 7a} But both modified pulp are similar in the sense that the modification processes introduce anionic surface charges onto the pulp while maintaining the primary physical and mechanical properties of the isolated nanocellulose.
3. The two mechanical disintegration processes (SO and HO) produce comparable nanocellulose, and are independent from the previous chemical modifications. Both processes deconstruct surface modified pulp into disintegrated nanocellulose. However, due to the different mechanisms as well as the starting materials (carboxylated cellulose vs carboxymethylated cellulose), the products could be different in dimension distributions, surfaces charges, and the associated bulk properties. We assume these differences are insignificant for most of the downstream applications.
4. Batch processing capacities of homogenization (HO) is assumed to be three times of that of sonication (SO). The batch processing capacities for both HO and SO can vary in certain ranges, dependent on the target concentration of the nanocellulose and the batch volume limits of the equipment. In our lab practice, the most common batch capacity for HO is 3.3 times of that of SO. Therefore for 10 g (the functional unit) of dry

- nanocellulose, it takes 10 batches if processed via HO (1 g/batch or 0.2 wt% in 500 mL DI water) and 33 batches via SO (0.3 g/batch or 0.1 wt% in 300 mL DI water). Also, since SO processed nanocellulose has to go through the centrifuge purifying (CP) to remove the titanium impurity, it actually requires 33 batches of SO plus an additional 33 batches of centrifugation to process 10 g nanocellulose.
5. All the common procedures do not influence the comparison among four fabrication routes, hence is negligible for simplicity consideration.
 6. The heat generated during the mechanical disintegration processes is negligible.

2.4. Life cycle inventory analysis (LCI)

All the data used in this LCA comes from the following four sources: original data, literature data,¹⁷ SimaPro database, and estimations. Inventory details are provided in the Appendix.

Original data

- 1) For chemical processes, all the inputs and outputs (emissions) data were scaled to the equivalent amount for producing 10 g dry nanocellulose (the functional unit) in the wet state. The energy input (in the form of electricity) during the chemical processes (i.e.: overhead stirring system, heating plat, pH meter, centrifuge washer, cooling system, etc.) was monitored with an electricity usage monitor (P4400 Kill A Watt[®], P3 International); three readings were taken to get the average value.
- 2) For mechanical processing, electricity was the only input taken into account beyond the intermediate product (kraft pulp). The electricity consumption was calculated based on the operation time and the equipment power specifications.

SimaPro database

The upstream manufacturing data for kraft pulping, chemicals, water, and electricity are directly cited from the SimaPro database (ecoinvent v.2, US LCI), version 7.3.

Estimations

For some apparent insignificant data (e.g.: exact volume for the tap water used in washing the intermediate product), we estimated for the most reasonable value within 10%. Additionally, there are two key reactants in the TEMPO oxidation process that were not available. TEMPO

was not included in the impact estimation, because very limited information about its environmental impact (or immediate precursor chemicals). NaBr, not listed in any of the SimaPro databases, was replaced with NaCl for impact estimation, because the two chemicals share many similarities in the industrial manufacturing processes and environmental pollutions²⁴. Both TEMPO and NaBr could be modeled more accurately in the future if evidence suggests the associated impacts are significant.

3. Results

3.1. Eco-Indicator 99 assessment method

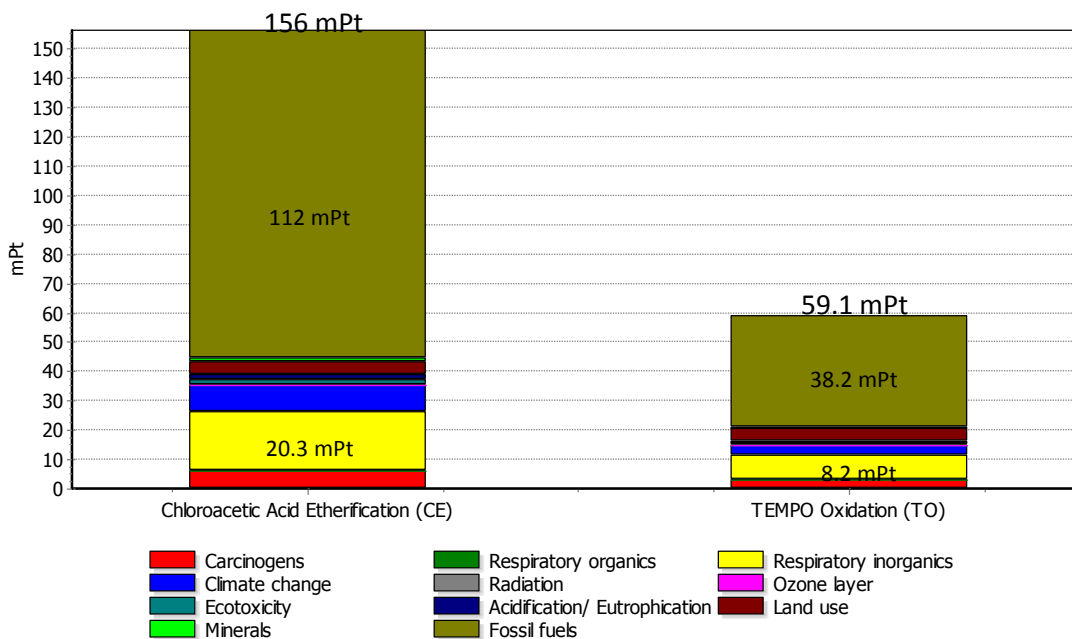
The impact assessment method applied in this LCIA is Eco-Indicator 99 (EI99).²⁵ EI99 is a damage (or endpoints in ISO terminology) oriented method, allowing to measure various environmental impacts.²⁵ The environmental impact categories considered in this method are shown in table 6.1. below. EI99 translates environmental damage into impacting points under three major “endpoint” categories: human health, ecosystem quality, and resources; these points are then normalized, weighted, and reported collectively as one single score.²⁵⁻²⁶ The EI99 method is “easy to understand but there is the risk of losing transparency”.^{26a} The single score reported from EI99 is a dimensionless value, defined in such a way that one point is equivalent to 1/1000 of the overall annual environmental load per capita, in continental Europe.²⁵ There are three weighting sets in EI99 reflecting different perspectives in gauging the damage, i.e.: egalitarian perspective, hierarchist perspective, and individualist perspective.²⁵ After running our model in all three perspectives, we found out that the impact score for individual item could vary as much as 50%, but the orders of damage magnitude across all comparisons stayed the same. Since the egalitarian perspective generally returned the highest impact score for our model, we chose to use this perspective (EI99 E/E) to interpret the result.

Table 6.1. The environmental impact categories considered in Eco-Indicator 99²⁵

Environmental Impacts	Endpoint Categories
Carcinogens	Human Health
Respiratory organics	
Respiratory inorganics	
Climate change	
Radiation	
Ozone layer	
Ecotoxicity	Ecosystem Quality
Acidification/ Eutrophication	
Land use	
Minerals	Resources
Fossil fuels	

3.2. Comparison between the chemical processes

The EI99 single score comparison between two chemical modification processes of pulp fiber, CE and TO, is presented in Figure 6.4. The overall impact from CE is approximately 2.6 times of that from TO. For both processes, the major impact contribution categories are fossil fuels depletion (72% for CE and 65% for TO) and respiratory inorganics pollution (13% and 14% total score, respectively), Table 6.2. A further examination of these two categories indicates that the use of alcohols (isopropanol and ethanol) in both processes is responsible for the majority of the fossil fuel depletion (90% for CE and 68% for TO, respectively) as well as the respiratory inorganics pollution (81% and 85%, respectively), Table 6.2.



Comparing 1 p 'Chloroacetic Acid Etherification (CE)' with 1 p 'TEMPO Oxidation (TO)';
Method: Eco-indicator 99 (E) V2.08 / Europe EI 99 E/E / Single score

Figure 6.4. EI99 single score results for the chemical processes: CE and TO.

Table 6.2. Impact categories (fossil fuel depletion and respiratory inorganics pollution) involved in the chemical modification processes

	Chloroacetic Acid Etherification	TEMPO-mediated Oxidation
Fossil fuel	112 out of 156 mPt, 72%	38.2 out of 59.1 mPt, 65%
	90% from isopropanol & ethanol	68% from ethanol
Respiratory inorganics	20.3 out of 156 mPt, 13%	8.2 out of 59.1 mPt, 14%
	81% from isopropanol & ethanol	85% from ethanol

Note: CE process consumes both isopropanol and ethanol, while TO process only consumes ethanol.

In order to understand the cause of the significant impact difference between CE and TO, EI99 scores of the two chemical processes was broken down into their major components (i.e.: kraft pulp, isopropanol, ethanol, NaClO, and electricity) to compare individual components side-by-side (Figure 6.5). Apparently, the use of isopropanol in the CE process is responsible for the overall difference in EI99 scores, since the scores from all other components are either on par or only present insignificant differences.

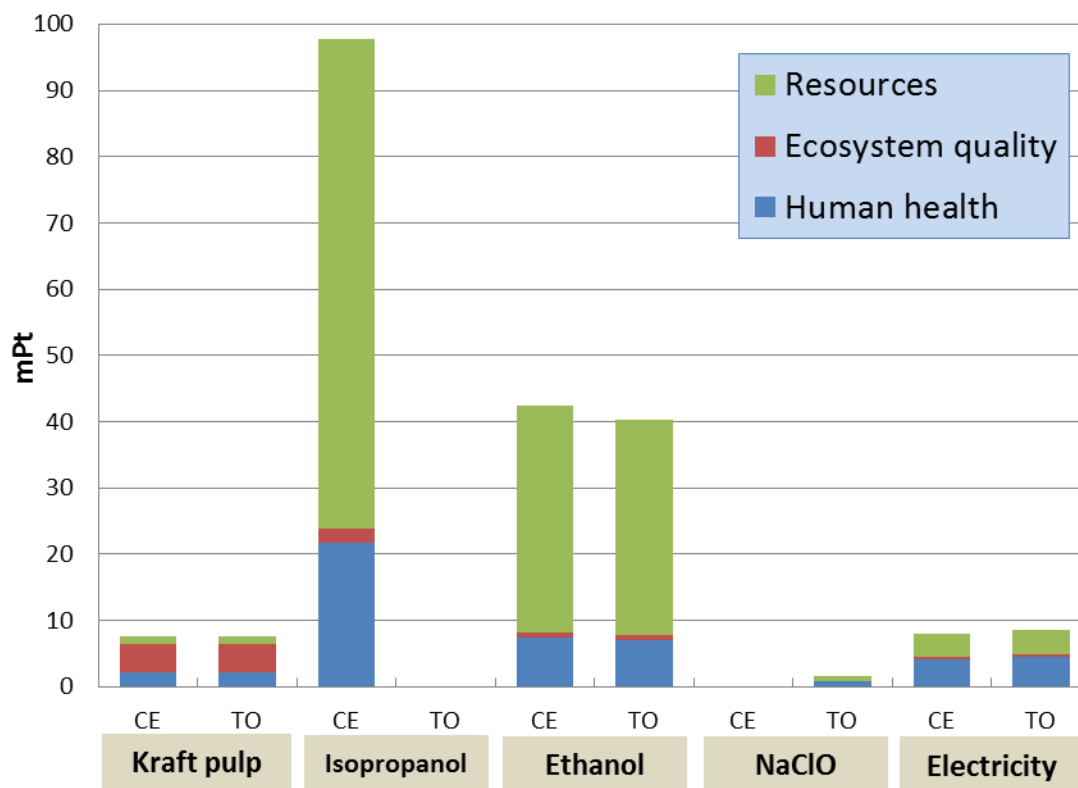


Figure 6.5. EI99 single score break down for chloroacetic acid etherification and TEMPO mediated oxidation processes based on major contributing sources, indicating the difference in overall impact is from the use of isopropanol of the CE process. Note, chloroacetic acid did not have measurable impact (<1 mPt) based on the functional unit of 10g of pulp.

3.3. Comparison between the mechanical processes

The EI99 single score result for the two mechanical processes (homogenization and sonication) and centrifuge purification is presented in Figure 6.6. Since electricity is the only input taken into account, all three processes share exactly the same impact score proportions from different categories. The impact scores generated from 10 g of nanocellulose are 241, 209, and 497 mPt for homogenization, sonication, and centrifuge purification, respectively. The score from sonication is 87.5% of that from homogenization when comparing the two methods; therefore sonication appeared to have reduced environmental impact over homogenization. However, since each sonication process has to go with a purification process (as discussed in the system description part), the difference is overshadowed by the relatively large score of

purification. The collective score for sonication and centrifugation is 706 mPt, nearly three times of that of homogenization; therefore, homogenization is a better method, solely from an environmental impact perspective. Moreover, since homogenization has a greater capacity and does not require a follow-up centrifuge step, it also has an advantage on production efficiency over sonication.

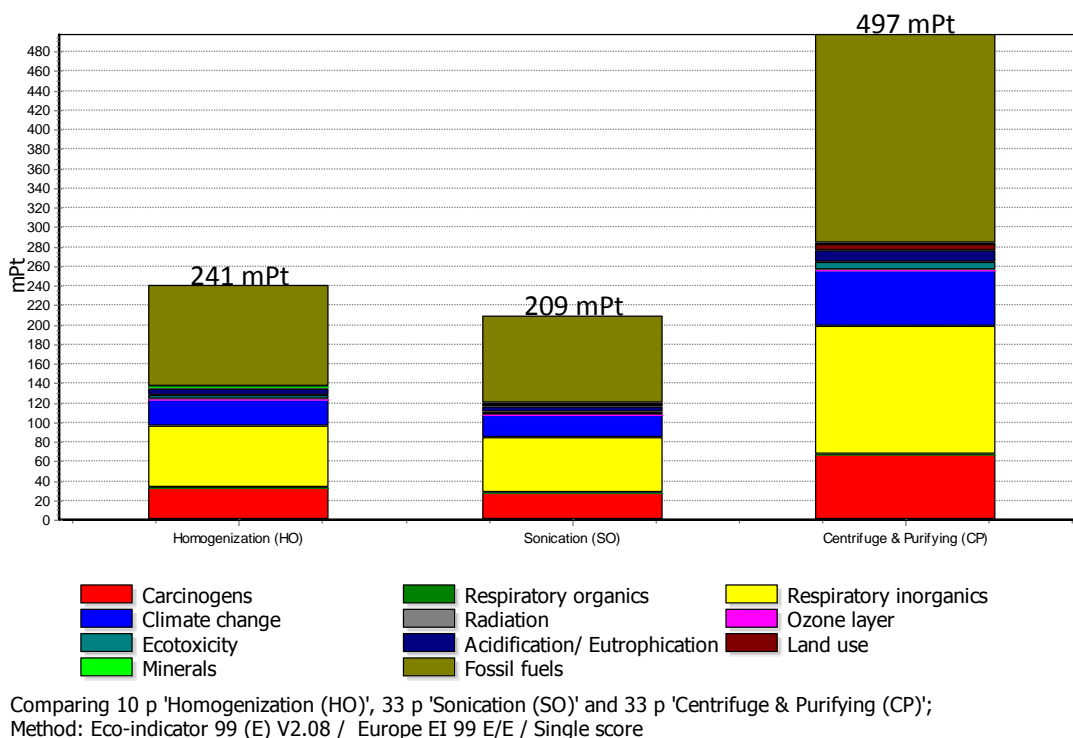


Figure 6.6. EI99 single score results for the mechanical and purifying processes.

3.4. Overall comparison based on functional unit (scenario I)

The EI99 single scores for the four nanocellulose fabrication routes are presented in Figure 6.7; total scores are broken down into individual contributions from chemical, mechanical, and purifying processes. TEMPO oxidation with homogenization presents the lowest impact score of 300 mPt, followed by carboxymethylation with homogenization (397 mPt), TEMPO oxidation with sonication and purification (765 mPt), and carboxymethylation followed by sonication and purification (863 mPt). The overall scores were impacted more by the differences from the mechanical processes (155% and 117%) than by that from the chemical modifications (32% and 13%): the total scores are more than doubled upon switching mechanical process from homogenization to sonication and centrifugation, while only 32% and 13% are increased,

respectively, if switching the chemical process from TEMPO oxidation to carboxymethylation. The implications are the following dependent upon level of fabrication: 1) for lab scale fabrication, TEMPO oxidation with homogenization is the best practice and carboxymethylation with sonication and centrifugation is the least preferred based on the current inventory data, from a pure environmental footprint perspective; 2) for industrial scale fabrication, the difference in environmental impact between the two chemical processes will be overshadowed by the follow-up mechanical processes; and 3) for industrial scale fabrication, homogenization is the more viable option for time efficiency, not accounting for clogs that may occur during processing.

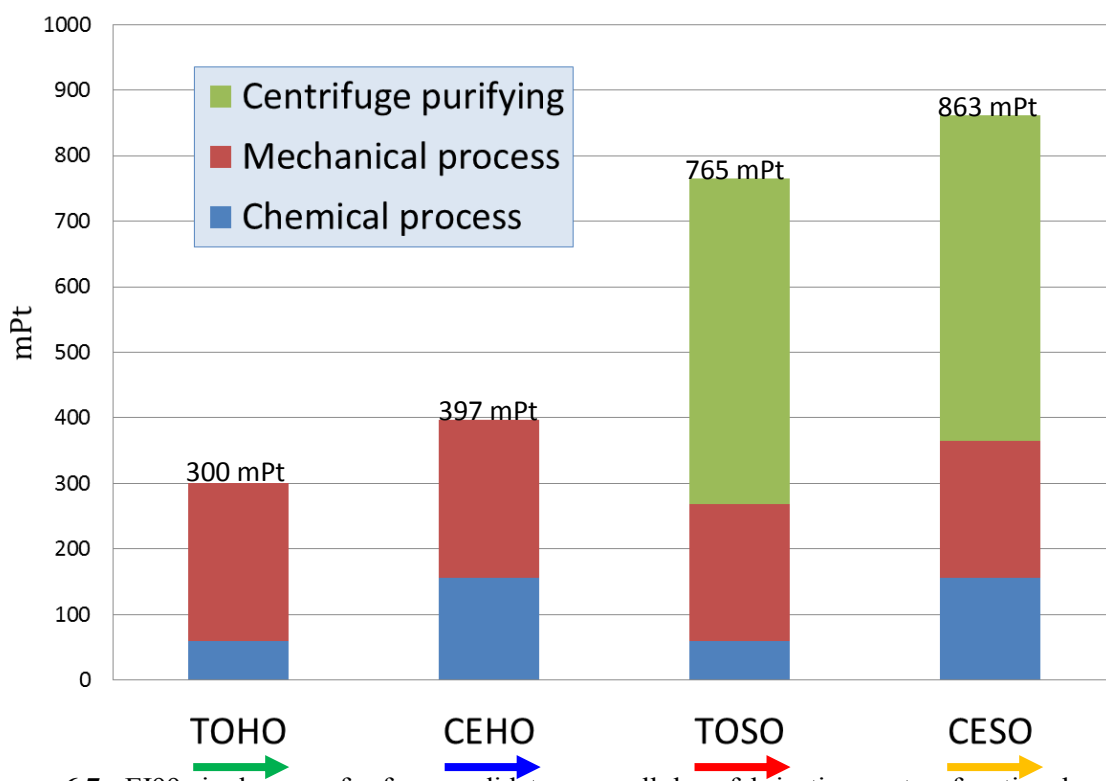


Figure 6.7. EI99 single score for four candidate nanocellulose fabrication routes, functional unit of 10 g equivalent dry nanocellulose. The colored arrows are corresponding to the fabrication routes defined in Figure 6.3.

3.5. Overall comparison based on single batch (scenario II)

For the lab practice, the functional unit of 10 g is a relatively large quantity, equivalent to a total yield of 10 batches HO and 33 batches SO. It makes sense to also examine the impact score from a “per batch” perspective (Figure 6.8). From Figure 6.8, on single batch basis, TEMPO oxidation with sonication and centrifugation now presents the smallest impact score of 23.2 mPt,

followed by CESO (26.1 mPt), TOHO (30.0 mPt), and CEHO (39.7 mPt). Also notice, the chemical process TEMPO oxidation presents smaller impact than carboxymethylation, same as in “functional unit based” analysis; however, homogenization generates greater impact than sonication (and sonication plus centrifugation) when the impact is a single batch, reversing the ranking in the “functional unit based” analysis. The most environmental burdensome route, carboxymethylation with homogenization (per batch), imposes 40% more impact than the least burdensome route TEMPO oxidation with sonication and centrifugation (per batch). Note that the absolute EI99 scores of single batches are fairly insignificant regardless of the fabrication routes.

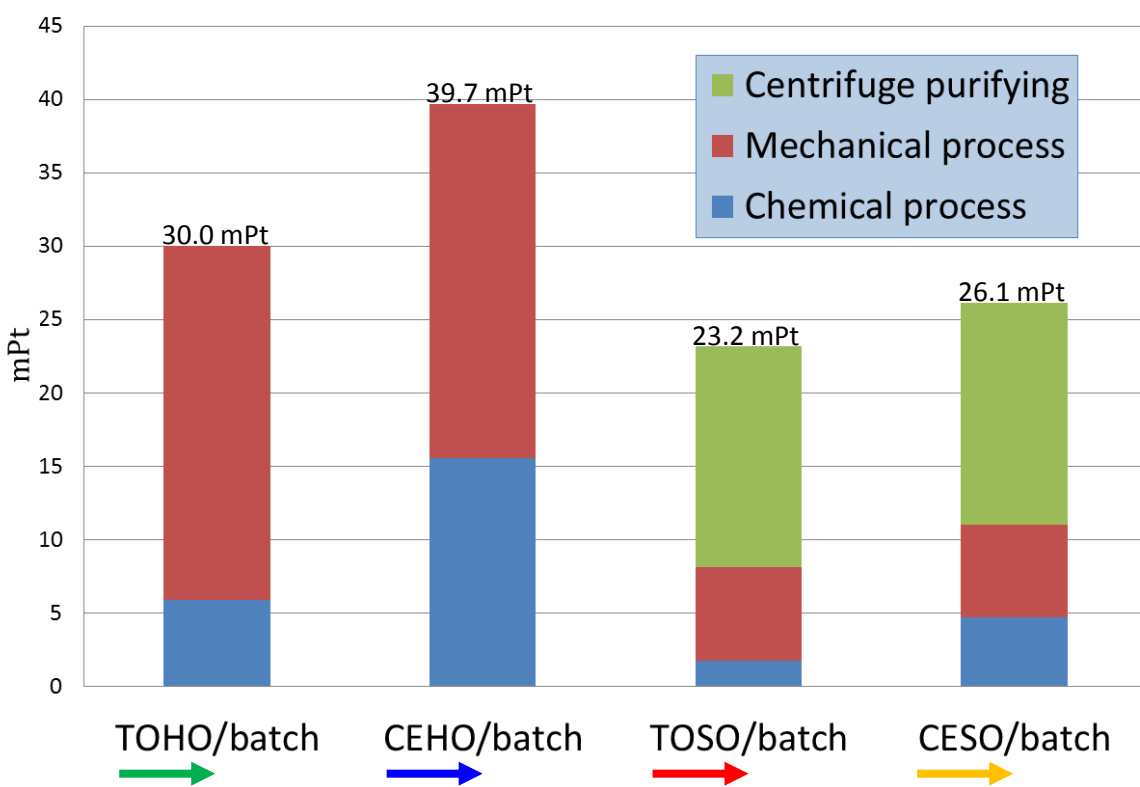


Figure 6.8. EI99 single score for four candidate nanocellulose fabrication routes, per batch basis. The colored arrows are corresponding to the fabrication routes defined in Figure 6.3.

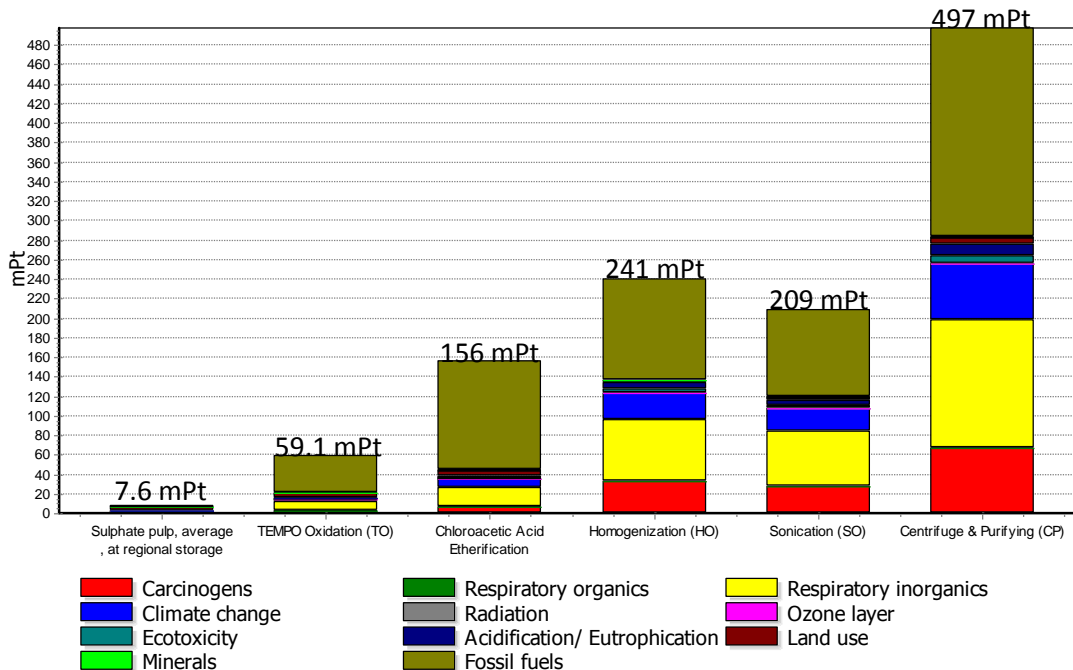
The impact from nanocellulose fabrication is also evaluated in a larger context by comparing with kraft pulp and carbon nanotubes.

3.6. Nanocellulose vs kraft pulp

The impact of nanocellulose production relative to the kraft pulping process was compared to

understand how much environmental impact markup the nanocellulose fabrication added to its precursor kraft pulp. The kraft pulping process used in this comparison is assumed under such a situation in SimaPro where the pulp is produced from an average technology European pulping facility, and the product kraft pulp is transported from the production site to a central distribution site within a European country. As the exponential growth of nanocellulose production is expected,¹ it is crucial to understand the potential environmental risk associated with this new material so that environmentally burdensome steps can be addressed proactively and guide the emerging nanocellulose fabrication technologies towards the minimization of overall environmental impact.

Figure 6.9 shows the EI99 scores for kraft pulping process and the nanocellulose fabrication processes. It is striking that even the lowest impacting process TO presents a score nearly eight times of the kraft pulping process, while the highest impacting process CP is 65 times. This markup from nanocellulose fabrication is somewhat surprising since nanocellulose is assumed to be an environmentally friendly nanomaterial. To make sense of this fact from the pulping perspective: i) modern pulping technology is largely self-sustained energy wise,²⁷ hence the overall environmental burden is brought down substantially; and ii) the already minimal environmental burden becomes trivial when spread out onto 10 g of dry pulp (as the functional unit in this LCA). Additionally from the nanocellulose fabrication perspective isolation of nanocellulose from native wood fiber's hierarchical structure is intrinsically an energy-intensive process.⁹



Analyzing 1 p 'Pulp vs Nanocellulose (all steps);
 Method: Eco-indicator 99 (E) V2.08 / Europe EI 99 E/E / Single score

Figure 6.9. EI99 impact score comparison between kraft pulping process and nanocellulose fabrication processes

3.7. Nanocellulose vs carbon nanotubes

It has been established that energy consumption accounts for the majority environmental impact of nanocellulose fabrication, and it is even more so for another popular nanomaterial—the single walled carbon nanotubes (SWNT).^{23, 28} Hence the fabrication energy demand of nanocellulose was compared with SWNT, to learn where nanocellulose stands in the field of nanotechnology from a pure energy consumption perspective.

Figure 6.10 indicates the sharp contrast of the energy consumption for producing 1 kg of nanocellulose (via TEMPO oxidation and homogenization or sonication and purification) and SWNT (via laser vaporization) in lab setting^{28b}. Laser vaporization was reported having comparable energy consumption as other SWNT synthesis methods, but it is a promising approach to scale up and achieve substantial energy saving.^{28b} According to Figure 6.10, although nanocellulose fabrication process presented an increased environmental impact relative to the kraft pulping process, it is only marginal (less than 1%) to the laser vaporization process for producing SWNT on a unit mass basis. This relative low energy consumption will provide

nanocellulose an advantage over SWNT in the applications where the properties of both materials are acceptable. To make these two equivalent, SWNT must undergo additional processing (oxidation with acid mixtures) to achieve aqueous dispersible nanoparticles. A caveat about this general comparison is that when considering a specific application, the relative amount of materials desired to achieve certain property enhancement also counts, i.e.: if SWNT takes much less amount to achieve the same result, then the energy consumption advantage of nanocellulose might be neutralized.

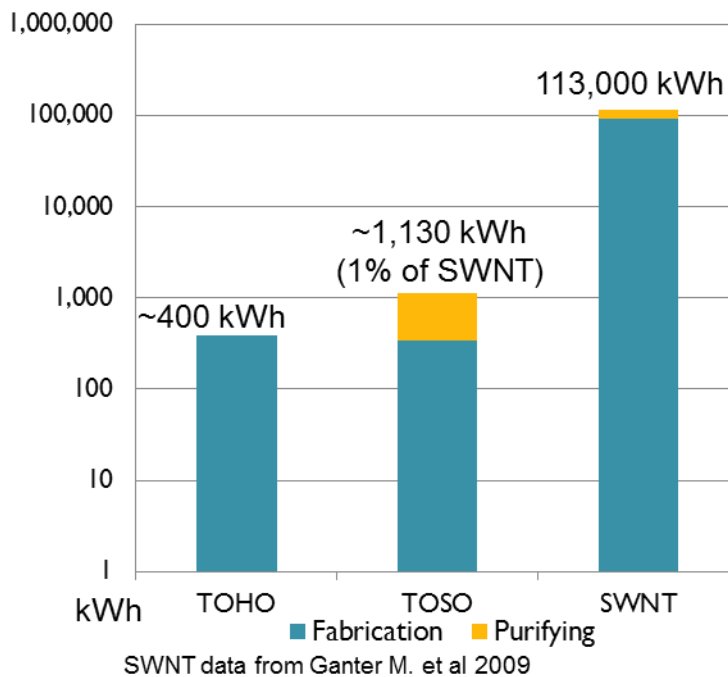


Figure 6.10. Energy consumption for producing 1 kg of material of nanocellulose and SWNT in lab setting, TOHO and TOSO refers to two fabrication routes for nanocellulose.

4. Conclusions

The present work discussed a cradle-to-gate LCA for lab scale nanocellulose fabrication. Four fabrication routes (composed of two interchangeable chemical and mechanical processes) were evaluated with Eco-Indicator 99 single score method. The best practice and the environmental burdensome spots were identified in the LCA model. The LCA results were also

compared with kraft pulping process and single-walled carbon nanotubes (SWNT) fabrication.

The primary conclusions are:

- 1) When evaluating the environmental impact based on unit mass of the nanocellulose product, the majority of the impact comes from the energy consumption attributed to the mechanical disintegration process (in the form of electricity). Raw material inputs, chemicals, and waste emissions, were a fraction of the impact, which suggests that reducing the energy consumption should be the top concern for the overall environmental impact control.
- 2) Eco-Indicator 99 single score results indicated that: i) of the two chemical modification processes, TEMPO-mediated oxidation presented less environmental impact than chloroacetic acid etherification, due to its zero consumption of isopropanol; ii) of the two candidate mechanical disintegration approaches, homogenization overall presented lower impact than sonication, due to the fact that it does not require an energy-intensive centrifugation step to purify the final product.
- 3) For nanocellulose MFC fabrication: scenario (I)— the best practice was TEMPO-mediated oxidation followed by homogenization based on unit mass analysis; scenario (II)— in the lab setting, TEMPO-mediated oxidation followed by sonication and centrifugation turned out to be the least environmental demanding approach based on single batch production (instead of unit mass), albeit all four routes present the minimal impact on a single batch basis.
- 4) Lab scale fabrication of nanocellulose has a substantial environmental burden markup on the kraft pulping process, which indicated the urgent needs for developing the environmental impact control measures to accommodate the forthcoming large scale commercialization of nanocellulose.
- 5) When comparing nanocellulose fabrication with SWNT, the energy consumption to produce nanocellulose was only marginal (less than 1%) of that of SWNT. This highlighted its prominent environmental advantage over other promising nanomaterials.

Appendix

Appendix 1. Life cycle inventory raw data

SI Table 6.1. LCI TEMPO-oxidation and sonication data

PROCESS NAME:	Nanocellulose Life Cycle Inventory					
PROCESS ID:	Chemical modification--TEMPO-oxidation + Sonication					
REFERENCE FLOW:	10	Units:	gram	of:	nanocellulose	
PROCESS DESCRIPTION:	Summary of LCI to produce 10 grams of nanocellulose from wood pulp to be used in nanocomposite in lab scale					
BASICS OF CALCULATIONS						
Process Inputs						
	Chemicals	Quantity			Units	
Material	Pulp	40			gram	never dried pulp, MC ~25%
	TEMPO	0.06			gram	
	NaClO	21.4 (or 19.28 g)			ml	
	NaBr	2.4			gram	
	NaOH	100 (or 4g)			ml	
	Ethanol	200 (or 250 g)			ml	
	Phase	Quantity			Units	
Water	Reaction	0.5			leter	
	Washing	5			leter	
	Equipment	Quantity			Units	
Electricity	Cable blender	0.055			kW h	
	pH meter	0 negligible				
	Synringe pump	0.01			kW h	
	Centrifuge Washer	0.07			kW h	
	TEMPO-Oxidation sum	0.135			kW h	
	Desktop Centrifuge	0.2375	950w (j/s) for 15min		kW h	
	Wailey Mill	0.04			kW h	
	Ultrasonication	0.1			kW h	
Process Outputs						
	Chemicals	Quantity			Units	
Product	Nanocellulose	10			gram	
By-product	NaCl	50			mmol	
Air Emissions						
	N/A					
Water Emissions						
		Reaction	Washing	Total	Units	CAS Number
	Water	0.5	5	5.5	leter	
	Ethanol	0	0.2	0.2	leter	
	TEMPO	0.6	0	0.6	gram	
	Na+	2.4	0	2.4	gram	
	Br-	1.86	0	1.86	gram	
	Cl-	1.06	0	1.1	gram	
	Hemicellulose	2	0	2	gram	8024-50-8
Solid Waste N/A						
Raw Materials Extracted						
	Pulp					
	Chemicals					
Water Consumption						
Land Use	N/A					

SI Table 6.2. LCI chloroacetic acid etherification data

PROCESS NAME:		Nanocellulose Life Cycle Inventory							
PROCESS ID:		Chemical modification-- Chloroacetic acid etherification							
REFERENCE FLOW:		10	Units:	gram	of:	esterified cellulose			
PROCESS DESCRIPTION:		Summary of LCI to produce 10 grams of nanocellulose from wood pulp							
BASICS OF CALCULATIONS									
Process Inputs									
	Chemicals	Quantity		Units					
Material	Kraft wood pulp	40		gram		equivalent dry mass			
	Chloroacetic acid	2.12		gram					
	Isopropanol	434.66		gram					
	Ethanol	261.95		gram					
	NaOH	1.41		gram					
	Phase	Quantity		Units					
Water	Reaction	0.12		leter		Solvent from pulp suspension and NaOH solution			
	Washing	5		leter		Total waste water round up to 5.5 L to be consistent with TEMPO process			
	Equipment	Quantity		Units					
Electricity	Heating & stirring plate	0.12	estimation based on 70	kW h		keeping 60 °C for 2h			
	Centrifuge Washer	0.07		kW h					
	pH meter	0	negligible	kW h					
	Esterification sum	0.127	Heating, stirring, Centrifuge	kW h					
	Desktop Centrifuge	0.2375	950w (j/s) for 15min	kW h					
Process Outputs		Name	Quantity		Units				
		Carboxylated cellulose	10		gram				
Product		glycolic acid	1.71		gram				
By-product									
		Quantity		Units					
Water Emissions	Water	5.5		leter					
	Isopropanol	435		gram					
	Ethanol	262		gram					
	Cl-	0.8		gram					
	Na+	0.81		gram					
Solid & Air Emmissions	N/A								
Raw Materials Extracted									
	Pulp								
	Chemicals								
Water Consumption									
	N/A								
Land Use									

SI Table 6.3. LCI homogenization data

Mini DeBEE Homogenizaer Specifications			
Max Operation pression	30,000		Psi
Max Flow Rate	200		mL/min
Motor Power	4		kW
Electric Supply	380	12	Units: V, A
Working Power	4.56		kW
Homogenization processes			
Energy consumption per batch	0.38		kWh
Quantity per batch	1		g
Number of batches	10		batch
Functional unit	10		g nanocellulose
Unit energy consumption of homogenization			
	0.38		kWh
Batch quantity	0.2% (w/w) @500 mL==> 1g / 500 mL		
Batch processing time	500 mL * 2/ (200 mL/min)= 5 min/batch		

References

1. (a) Crotagino, R. *The Economic Impact of Nanocellulose*; Arbora Nano: Washington D.C., March 27-28, 2012, 2012; (b) TAPPI *International Nanocellulose Standards-- The Need and Purpose of Standards for Nanocellulosic Materials*; TAPPI: June 9, 2011, 2011.
2. (a) Wikipedia.org Life-cycle assessment. http://en.wikipedia.org/wiki/Life_cycle (accessed January 10th); (b) US Environmental Protection Agency, E. Defining Life Cycle Assessment. <http://www.gdrc.org/uem/lca/lca-define.html> (accessed January 10); (c) ISO, Environmental management -- Life cycle assessment -- Principles and framework. 2006; Vol. 14040:2006; (d) Curran, M. A. *Life Cycle Assessment: Principles and Practice*; U.S. ENVIRONMENTAL PROTECTION AGENCY: Cincinnati, 2006; p 88; (e) Guinee, J. B.; Heijungs, R. In *Life cycle assessment*, John Wiley & Sons, Inc.: 2005; pp 805-831; (f) Righi, S.; Morfino, A.; Galletti, P.; Samori, C.; Tugnoli, A.; Stramigioli, C., Comparative cradle-to-gate life cycle assessments of cellulose dissolution with 1-butyl-3-methylimidazolium chloride and N-methyl-morpholine-N-oxide. *Green Chemistry* **2011**, *13* (2).
3. ISO, Environmental management -- Life cycle assessment -- Requirements and guidelines. 2006; Vol. 14044.
4. (a) Moon, R. J.; Martini, A.; Nairn, J.; Simonsen, J.; Youngblood, J., Cellulose nanomaterials review: structure, properties and nanocomposites. *Chem. Soc. Rev.* **2011**, *40* (7), 3941-3994; (b) Klemm, D.; Kramer, F.; Moritz, S.; Lindström, T.; Ankerfors, M.; Gray, D.; Dorris, A., Nanocelluloses: A New Family of Nature-Based Materials. *Angewandte Chemie International Edition* **2011**, *50* (24), 5438-5466; (c) Isogai, A.; Saito, T.; Fukuzumi, H., TEMPO-oxidized cellulose nanofibers. *Nanoscale* **2011**, *3* (1), 71-85; (d) Fernandes, A. N.; Thomas, L. H.; Altaner, C. M.; Callow, P.; Forsyth, V. T.; Apperley, D. C.; Kennedy, C. J.; Jarvis, M. C., Nanostructure of cellulose microfibrils in spruce wood. *Proceedings of the National Academy of Sciences* **2011**; (e) Eichhorn, S. J., Cellulose nanowhiskers: promising materials for advanced applications. *Soft Matter* **2011**, *7* (Copyright (C) 2011 American Chemical Society (ACS). All Rights Reserved.), 303-315.
5. Klemm, D.; Schumann, D.; Kramer, F.; Hessler, N.; Hornung, M.; Schmauder, H. P.; Marsch, S., Nanocelluloses as innovative polymers in research and application. In *Polysaccharides II*, Springer-Verlag Berlin: Berlin, 2006; Vol. 205, pp 49-96.
6. (a) Li, Z.; Renneckar, S.; Barone, J., Nanocomposites prepared by in situ enzymatic polymerization of phenol with TEMPO-oxidized nanocellulose. *Cellulose* **2010**, *17* (1), 57-68; (b) Johnson, R. K.; Zink-Sharp, A.; Renneckar, S. H.; Glasser, W. G., A new bio-based nanocomposite: fibrillated TEMPO-oxidized celluloses in hydroxypropylcellulose matrix. *Cellulose (Dordrecht, Netherlands)* **2009**, *16* (2), 227-238.
7. (a) Wagberg, L.; Decher, G.; Norgren, M.; Lindstrom, T.; Ankerfors, M.; Axnas, K., The build-up of polyelectrolyte multilayers of microfibrillated cellulose and cationic polyelectrolytes. *Langmuir : the ACS journal of surfaces and colloids* **2008**, *24* (3), 784-95; (b) Iwamoto, S.; Nakagaito, A. N.; Yano, H.; Nogi, M., Optically transparent composites reinforced with plant fiber-based nanofibers. *Appl. Phys. A: Mater.*

- Sci. Process.* **2005**, *81* (Copyright (C) 2011 American Chemical Society (ACS). All Rights Reserved.), 1109-1112; (c) Nakagaito, A. N.; Yano, H., Novel high-strength biocomposites based on microfibrillated cellulose having nano-order-unit web-like network structure. *Appl. Phys. A: Mater. Sci. Process.* **2004**, *80* (Copyright (C) 2011 American Chemical Society (ACS). All Rights Reserved.), 155-159; (d) Fukuzumi, H.; Saito, T.; Iwata, T.; Kumamoto, Y.; Isogai, A., Transparent and High Gas Barrier Films of Cellulose Nanofibers Prepared by TEMPO-Mediated Oxidation. *Biomacromolecules* **2008**, *10* (1), 162-165.
8. Hentze, H.-P. In *From Nanocellulose Science towards Applications*, Technical Research Center of Finland, Helsinki, June 2, 2010; Technical Research Center of Finland, Helsinki, 2010.
 9. Atalla, R. H.; Brady, J. W.; Matthews, J. F.; Ding, S.-Y.; Himmel, M. E., Structures of Plant Cell Wall Celluloses. In *Biomass recalcitrance: deconstructing the plant cell wall for bioenergy*, Himmel, M. E., Ed. Blackwell Pub.: Oxford, 2008; Vol. xviii, 505 p.
 10. (a) Ross, P.; Mayer, R.; Benziman, M., Cellulose biosynthesis and function in bacteria. *Microbiol. Mol. Biol. Rev.* **1991**, *55* (1), 35-58; (b) Spence, K. L.; Venditti, R. A.; Rojas, O. J.; Habibi, Y.; Pawlak, J. J., A comparative study of energy consumption and physical properties of microfibrillated cellulose produced by different processing methods. *Cellulose* **2011**, *18* (4), 1097-1111.
 11. Dong, S.; Roman, M., Fluorescently Labeled Cellulose Nanocrystals for Bioimaging Applications. *Journal of the American Chemical Society* **2007**, *129* (45), 13810-13811.
 12. Beck-Candanedo, S.; Roman, M.; Gray, D. G., Effect of Reaction Conditions on the Properties and Behavior of Wood Cellulose Nanocrystal Suspensions. *Biomacromolecules* **2005**, *6* (2), 1048-1054.
 13. Wikipedia.org Nata de coco. http://en.wikipedia.org/wiki/Nata_de_coco (accessed July 25).
 14. Turbak, A. F.; Snyder, F. W.; Sandberg, K. R., Microfibrillated cellulose, a new cellulose product: properties, uses, and commercial potential. *Journal of Applied Polymer Science: Applied Polymer Symposium* **1983**, *37* (Proc. Cellul. Conf., 9th, 1982, Part 2), 815-827.
 15. Wuhrmann, K.; Heuberger, A.; Muhlethaler, K., Electron-microscopic investigations of cellulose fibers after supersonic treatment. *Experientia* **1946**, *2* (Copyright (C) 2012 American Chemical Society (ACS). All Rights Reserved.), 105-7.
 16. (a) Faria Tischer, P. C. S.; Sierakowski, M. R.; Westfahl, H., Jr.; Tischer, C. A., Nanostructural Reorganization of Bacterial Cellulose by Ultrasonic Treatment. *Biomacromolecules* **2010**, *11* (5), 1217-1224; (b) Li, Q.; Renneckar, S., Molecularly thin nanoparticles from cellulose: isolation of sub-microfibrillar structures. *Cellulose (Dordrecht, Netherlands)* **2009**, *16* (6), 1025-1032; (c) Elazzouzi-Hafraoui, S.; Nishiyama, Y.; Putaux, J. L.; Heux, L.; Dubreuil, F.; Rochas, C., The shape and size distribution of crystalline nanoparticles prepared by acid hydrolysis of native cellulose. *Biomacromolecules* **2008**, *9* (1), 57-65; (d) Saito, T.; Nishiyama, Y.; Putaux, J. L.; Vignon, M.; Isogai, A., Homogeneous suspensions of individualized microfibrils from TEMPO-catalyzed oxidation of native cellulose. *Biomacromolecules* **2006**, *7* (6), 1687-1691; (e) Cheng, Q.; Wang, S.; Han, Q., Novel process for isolating fibrils from cellulose fibers by high-intensity ultrasonication. II. Fibril characterization. *Journal of Applied Polymer Science* **2009**, *115* (5), 2756-2762.

17. Eyholzer, C.; Bordeanu, N.; Lopez-Suevos, F.; Rentsch, D.; Zimmermann, T.; Oksman, K., Preparation and characterization of water-redispersible nanofibrillated cellulose in powder form. *Cellulose* **2010**, *17* (1), 19-30.
18. Bondeson, D.; Mathew, A.; Oksman, K., Optimization of the isolation of nanocrystals from microcrystalline cellulose by acid hydrolysis. *Cellulose* **2006**, *13* (2), 171-180.
19. Pääkkö, M.; Ankerfors, M.; Kosonen, H.; Nykänen, A.; Ahola, S.; Österberg, M.; Ruokolainen, J.; Laine, J.; Larsson, P. T.; Ikkala, O.; Lindström, T., Enzymatic Hydrolysis Combined with Mechanical Shearing and High-Pressure Homogenization for Nanoscale Cellulose Fibrils and Strong Gels. *Biomacromolecules* **2007**, *8* (6), 1934-1941.
20. Eichhorn, S. J.; Dufresne, A.; Aranguren, M.; Marcovich, N. E.; Capadona, J. R.; Rowan, S. J.; Weder, C.; Thielemans, W.; Roman, M.; Renneckar, S.; Gindl, W.; Veigel, S.; Keckes, J.; Yano, H.; Abe, K.; Nogi, M.; Nakagaito, A. N.; Mangalam, A.; Simonsen, J.; Benight, A. S.; Bismarck, A.; Berglund, L. A.; Peijs, T., Review: current international research into cellulose nanofibres and nanocomposites. *J. Mater. Sci.* **2010**, *45* (1), 1-33.
21. Denooy, A. E. J.; Besemer, A. C.; Vanbekkum, H., SELECTIVE OXIDATION OF PRIMARY ALCOHOLS MEDIATED BY NITROXYL RADICAL IN AQUEOUS-SOLUTION - KINETICS AND MECHANISM. *Tetrahedron* **1995**, *51* (29), 8023-8032.
22. Li, Q.; Renneckar, S., Supramolecular Structure Characterization of Molecularly Thin Cellulose I Nanoparticles. *Biomacromolecules* **2011**, *12* (3), 650-659.
23. Wender, B. A.; Seager, T. P. In *Towards prospective life cycle assessment: Single wall carbon nanotubes for lithium-ion batteries*, Sustainable Systems and Technology (ISSST), 2011 IEEE International Symposium on, 16-18 May 2011; 2011; pp 1-4.
24. (a) Wikipedia.org Sodium Chloride. http://en.wikipedia.org/wiki/Sodium_chloride (accessed July 25); (b) Wikipedia.org Sodium Bromide. http://en.wikipedia.org/wiki/Sodium_bromide (accessed July 25).
25. Goedkoop, M.; Spriensma, R. *The Eco-indicator 99 A Damage Oriented Method for Life Cycle Impact Assessment*; PRé Consultants: June 22, 2001, 2001.
26. (a) Audenaert, A.; De Cleyn, S. H.; Buyle, M., LCA of low-energy flats using the Eco-indicator 99 method: Impact of insulation materials. *Energy and Buildings* **2012**, *47* (0), 68-73; (b) Dreyer, L.; Niemann, A.; Hauschild, M., Comparison of Three Different LCIA Methods: EDIP97, CML2001 and Eco-indicator 99. *The International Journal of Life Cycle Assessment* **2003**, *8* (4), 191-200.
27. Zhi Fu, G.; Chan, A.; Minns, D., Preliminary Assessment of the Environmental Benefits of Enzyme Bleaching for Pulp and Paper Making (7 pp). *The International Journal of Life Cycle Assessment* **2005**, *10* (2), 136-142.
28. (a) Peralta-Videa, J. R.; Zhao, L.; Lopez-Moreno, M. L.; de la Rosa, G.; Hong, J.; Gardea-Torresdey, J. L., Nanomaterials and the environment: a review for the biennium 2008-2010. *J Hazard Mater* **2011**, *186* (1), 1-15; (b) Ganter, M. J.; Seager, T. P.; Schauerman, C. M.; Landi, B. J.; Raffaele, R. P. In *A life-cycle*

energy analysis of single wall carbon nanotubes produced through laser vaporization, Sustainable Systems and Technology, 2009. ISSST '09. IEEE International Symposium on, 18-20 May 2009; 2009; pp 1-4.

CHAPTER 7

Summary and Conclusions

A new type of nanocellulose –molecularly thin nanocellulose (MT nanocellulose)—was synthesized through a combined chemical-mechanical approach. A series of characterization and modeling work were conducted to investigate the mechanism of the formation of MT nanocellulose. The unique molecular sheet structure of MT nanocellulose was utilized to advance the understanding of wood cellulose microfibril configuration. Lastly, life cycle assessment (LCA) was applied to quantify the environmental impact from the fabrication process of nanocellulose. The major conclusions of the dissertation were summarized from the following four aspects: MT nanocellulose preparation, characterization, supramolecular modeling, and LCA.

MT nanocellulose preparation

1. MT nanocellulose was prepared through a combined chemical-mechanical approach: TEMPO-mediated oxidation followed by intensive sonication from 5-240 min.
2. Oxidized pulp fiber had a carboxylate content ranging from 1.12-1.43 mmol/g under designated reaction condition, corresponding to the degree of oxidation of 0.18-0.23.
3. Oxidation of hydroxyl groups were confirmed by the emerging carboxylate peak at $\sim 1610\text{ cm}^{-1}$ in FTIR spectra and 175 ppm in NMR spectra with a change to the 63 ppm C6 group. The relative peak intensity of carboxylate in NMR spectra agreed with the degree of oxidation.
4. The thinnest MT nanocellulose, according to the AFM measurements, has a thickness $\sim 0.4\text{ nm}$ which was related to a cellulose mono-layer molecular sheet from the unit cell dimensions.
5. AFM investigation revealed that delamination of MT nanocellulose occurred at 5 min of sonication; TEM results suggested that 60 min sonication was sufficient to isolate majority ($\sim 75\%$) of the individual microfibrils; AFM indicated that 120 min sonication converted more than 75% of the microfibrils into mono- and bi-layers MT nanocellulose sheets.
6. By integrating the present findings and theoretical work on bond strength within a fibril, a cellulose molecular sheet delamination scheme was proposed to describe this MT nanocellulose formation process.

Characterization

1. *Dimensions and size distributions*

- a. MT nanocellulose was envisaged as an extended long flat ribbon with thickness ~ 1 nm or below (corresponding to 1-2 layers), width from 2-5 nm (corresponding to 3-6 chains), and length from hundreds of nanometers to several microns.
- b. The thickness, width, and length profiles (means of the distributions) all decreased with extended sonication time, and followed a similar pattern leveling off after 1-2 h sonication.
- c. The level-off dimension for the thickness distribution was ~ 0.4 nm, relating to a cellulose monolayer sheet; the level-off for width distribution was ~ 2 nm, relating to a three-chain sheet; whereas the length distribution did not present a very clear level-off value. This indicated that the smallest MT nanocellulose obtained from sonication was a monolayer molecular sheet with three chains connected side-by-side through intra-sheet hydrogen bonds with an indefinite length; it also implied that intra-sheet hydrogen bonding was much stronger than the inter-sheet hydrogen bonding.

2. *Crystallinity*

- a. Crystallinity of the cellulose raw material, TEMPO-oxidized cellulose, and MT nanocellulose of different sonication time levels determined by XRD and NMR revealed the same trend across all levels: TEMPO-oxidized cellulose showed a slight increase in crystallinity compared with cellulose raw material; MT nanocellulose presented a moderate decline in crystallinity and it did not show strong correlations with extended sonication time.
- b. Crystal size decreased upon sonication, along its (200) diffraction plane, but the cellulose $I\beta$ nature was maintained. Direct evidence was from XRD investigation, where (200) plane peaks were broadened and reduced upon sonication.
- c. Indirect evidence of supramolecular structure disruption from Raman, FTIR, and NMR indicated an increased degree of disorder, and C6 *gg* conformation provided additional support for this argument.

3. *Hydrogen bonding*

- a. A series of global characterizations (i.e.: FTIR, Raman, XRD, and NMR) identified that intensive sonication had a major impact on the hydrogen bonding within the cellulose

supramolecular structure, but TEMPO-oxidation did not alter the hydrogen bonding significantly.

- b. Experimental evidence from AFM, TEM, XRD, Raman, and FTIR showing the contrast before and after sonication treatments indicated that the inter-layer hydrogen bonding was significantly impacted while intra-layer was not. This result corroborated the theoretical calculation that intra-layer hydrogen bonding was much stronger than inter-layer hydrogen bonding.
4. *C6 conformations and glycosidic linkage torsion angles*
- a. C6 hydroxyl group exhibited greater degree of disorder upon sonication, evidence were seen from heightened 891 cm^{-1} peaks in Raman spectra and less defined ca. 2900 cm^{-1} CH_2 peaks in FTIR spectra.
 - b. C6 hydroxyl group favored *gg* conformation when exposed to surface and/or oxidized, stereochemical preference and energy minimization were believed to be the major contributing factors.
 - c. Glycosidic linkage torsion angles Φ and Ψ were not altered by TEMPO-oxidation but were impacted by sonication, appearing in NMR spectra as the systematic upfield peak shifts.

Supramolecular modeling

1. The microfibril “cross section triangle scheme” – that illustrated the interdependent relationships among “cross section dimension”, “cross section shape”, and “chain packing numbers”- was developed to guide the cross section modeling process.
2. A 24-chain hexagonal/elliptical hybrid model, which fit well with the experimental observations as well as all known constraints, was proposed to be the most credible representation of wood cellulose microfibril configuration with hexagonal portion representing the crystalline segments and elliptical representing the less ordered paracrystalline region.

Life cycle assessment of nanocellulose

Cradle-to-gate LCA for lab scale nanocellulose fabrication was conducted with Eco-indicator 99 single score method on four chemical-mechanical fabrication routes with each route consisted of a chemical treatment step and a follow-up mechanical disintegration step.

1. For the whole fabrication process, the majority of impact was from the energy consumption of the mechanical disintegration step rather than from the raw material inputs, chemicals, and waste emissions. Implications of this result suggested that reducing the energy consumption during fibrillation should be the top concern for the environmental impact management.
2. For the two chemical and mechanical processes employed: i) TEMPO-mediated oxidation presented less impact than chloroacetic acid etherification, due to its zero isopropanol consumption; and ii) homogenization overall presented lower impact than sonication, because it did not require an energy-intensive centrifuge step to purify the final product.
3. Based on unit mass, the best practice for nanocellulose fabrication was TEMPO-mediated oxidation followed by homogenization. Based on lab scale single batch production, the best practice was TEMPO-mediated oxidation followed by sonication (plus centrifuge), albeit all four routes presented minimal impact in this case.
4. Lab scale fabrication of nanocellulose presented a substantial environmental impact markup on the kraft pulping process, which indicated the urgent need for developing the environmental impact control measures to accommodate the forthcoming large-scale commercialization of nanocellulose.
5. When comparing nanocellulose with single-walled carbon nanotubes (SWNT)—another familiar nanomaterial sharing similar reinforcement applications—the energy consumption to produce nanocellulose was almost two orders of magnitude lower than that of SWNT. This highlighted its prominent environmental advantage over other promising nanomaterial(s).